Optical spectroscopy of excitons confined in two-dimensional materials and semiconductor heterostructures

Lorenzo Scarpelli

School of Physcis and Astronomy

Thesis submitted to Cardiff University
for the degree of Doctor of Philosophy

March 2019

Supervisors:
Prof. Wolfgang Langbein
Dr. Egor Muljarov

Declaration and statements

Declaration This thesis has not been submitted in substance for any other degree or award at this or any other university or place of learning, nor is being submitted concurrently in candidature for any other degree or award.

Signed Lorenzo Scarpelli Date 04/02/2019

Statement This thesis is being submitted in partial fulfilment of the requirements for the degree of PhD.

Signed Lorenzo Scarpelli Date 04/02/2019

Statement This thesis is the result of my own independent work/investigation, except where otherwise stated, and the thesis has not been edited by a third party beyond what is permitted by Cardiff University's Policy on the Use of Third Party Editors by Research Degree Students. Other sources are acknowledged by explicit references. The views expressed are my own.

Signed Lorenzo Scarpelli Date 04/02/2019

Statement I hereby give consent for my thesis, if accepted, to be available online in the University's Open Access repository and for inter-library loans after expiry of a bar on access previously approved by the Academic Standards & Quality Committee.

Signed Lorenzo Scarpelli Date 04/02/2019

Abstract

In this thesis we show experiments of optical spectroscopy of excitons confined in two-dimensional materials and semiconductor heterostructures.

We study the exciton and trion density dynamics in monolayers of molybdenum diselenide by resonant three-pulse four-wave mixing spectroscopy, at temperatures from 300 K to 77 K. A multiexponential third-order response function for amplitude and phase of the heterodyne-detected four-wave mixing signal including four decay processes is used to model the data. We provide a consistent interpretation within the intrinsic band structure, not requiring the inclusion of extrinsic effects.

We study the coupling of indium arsenide quantum dot excitons to photonic crystal waveguide modes. The coupling efficiency into guided modes, the beta factor, is determined by direct spectral imaging. We find beta factors above 90% over a wide spectral range of 40 meV in the fast light regime, reaching a maximum of 0.99 ± 0.01. All the reported measured beta factors are not corrected for the collection efficiency of free-space and coupler emission, which would increase the beta factor, since the free space emission, according to our simulation, is collected typically twice as efficiently depending on the QD position inside the lattice unit cell. Direct spectral imaging is also used to measure the directional emission of the circularly polarised transitions in a magnetic field, and deduce the mode circularity at the quantum dot sites. We use the emission energy, mode circularity and beta factor to determine the quantum dot position inside the photonic crystal waveguide unit cell, by comparison with finite-difference time-domain simulations.

Finally, we study the spontaneous emission lineshape of indium gallium arsenide quantum dot excitons by photoluminescence spectroscopy. The lineshape is characterised by a spectrally sharp peak, the zero-phonon line, superimposed to a broad emission due to phonon-assisted transitions. We perform measurements of power dependence and fine-structure splitting to individuate exciton, trion and biexciton emission lines. To fit the corresponding lineshapes, we develop a fitting model based on the independent boson model, from which we extract a set of underlying parameters: deformation potentials, QD confinement lengths and phonon temperature. Additionally, using an observed thermal offset around the zero-phonon transition, we are able to separate the homogeneous from the inhomogeneous broadening.

Acknowledgements

First of all, I sincerely thank my main supervisor Prof. Wolfgang Langbein, for sharing with me his passion for physics and for guiding me through all the different aspects of science. I am sure his approach toward research will influence me throughout all my scientific career.
I thank my second supervisor Dr. Egor Muljarov, for generously guiding and developing the theoretical aspects of the experiments I performed.
I thank Dr. Francesco Masia, for the useful discussions, the help and the support he provided throughout all my PhD.
I thank Dr. Benjamin Lang and my fellow PhD student Amy Morreau for their precious help and collaboration in the development of the theory supporting the experiments performed in this work.
I thank all collaborators from University of Manchester, University of Sheffield, University of Bristol, University of Würzburg and University College Cork who provided the investigated samples.

List of publications and conference presentations

Publications

- L. Scarpelli, F. Masia, E. M. Alexeev, F. Withers, A. I. Tartakovskii, K. S. Novoselov, and W. Langbein, Resonantly excited exciton dynamics in two-dimensional $MoSe_2$ monolayers, *Physical Review B* **96** 045407 (2017). doi:https://doi.org/10.1103/PhysRevB.96.045407

- M. A. Becker, L. Scarpelli, G. Nedelcu, G. Raino, F. Masia, P. Borri, M. V. Kovalenko, T. Stöferle, W. Langbein and R. F. Mahrt, Long Exciton Dephasing Time and Coherent Phonon Coupling in $CsPbBr_2Cl$ Perovskite Nanocrystals, *Nano Letters* **2018**, 18 (12), pp 7546-7551. https://pubs.acs.org/doi/pdf/10.1021/acs.nanolett.8b03027.

- T. Jakubczyk, G. Nayak, L. Scarpelli, F. Masia, W.-L. Liu, S. Dubey, N. Bendiab, L. Marty, T. Taniguchi, K. Watanabe, G. Nogues, J. Coraux, V. Bouchiat, W. Langbein, J. Renard and J. Kasprzak, *Coherence and density dynamics of excitons in a single-layer* MoS_2 *reaching the homogeneous limit*, ACS Nano 2019, 13, 3, 3500-3511 https://pubs.acs.org/doi/10.1021/acsnano.8b09732.

- L. Scarpelli, B. Lang, F. Masia, D. Beggs, E. Muljarov, A.B. Young, R. Oulton, S. Höfling, C. Schneider and W. Langbein *Propagation loss in photonic crystal waveguides embedding InAs/GaAs quantum dots determined by direct spectral imaging*, Proc. SPIE 10916, Ultrafast Phenomena and Nanophotonics XXIII, 1091617 (27 February 2019); doi:10.1117/12.2510478.

- L. Scarpelli, B. Lang, F. Masia, D.M. Beggs, E.A. Muljarov, A.B. Young, R. Oulton, M. Kamp, S. Höfling, C. Schneider and W. Langbein, *99% beta factor and directional coupling of quantum dots to fast light in photonic crystal waveguides determined by hyperspectral imaging* (submitted).

- L. Scarpelli, A. Morreau, S. Moroni, F. Masia, E. Pelucchi, E. Muljarov and W. Langbein, Fit of phonon assisted sidebands allows extraction of the Lorentzian dephasing and localization length of quantum dot excitonic transitions (*in preparation*).

Conference presentations

- Exciton dephasing and decay in two-dimensional $MoSe_2$ layers, Symposium on Frontiers in Polaritonics, 14-17 March 2016, Grasmere, Cumbria, UK (*contributed talk*).

- Exciton dephasing and decay in two-dimensional $MoSe_2$ layers, Solid State Quantum Photonics 2016, 22 March 2016, Sheffield (*poster contribution*).
- Resonantly excited exciton dynamics in two-dimensional $MoSe_2$ layers, TMD-UK 2016, 1-2 September 2016, Bath (*contributed talk*).
- Resonantly excited exciton dynamics in two-dimensional $MoSe_2$ layers, Third South West Quantum Technologies workshop: Quantum Materials, 19-20 January 2017, Cardiff (*contributed talk*).
- Resonantly excited exciton dynamics in two-dimensional $MoSe_2$ monolayers, International Conference on Optics of Excitons in Confined Systems, 10-15 September 2017, Bath (*contributed talk*).
- High beta factors and directional coupling of InAs/GaAs quantum dots to photonic crystal waveguides determined by direct spectral imaging, International Conference on Optics of Excitons in Confined Systems, 10-15 September 2017, Bath (*poster contribution*).
- Disentangling spectral diffusion and blinking from intrinsic line-shapes in single quantum dot photoluminescence by non-negative matrix factorization, Bio-Nano-Photonics Symposium 2017, 18-19 September 2017, Cardiff (*poster contribution*).
- High beta factors and directional coupling of InAs/GaAs quantum dots to photonic crystal waveguides determined by direct spectral imaging, Quantum Dot Day 2018, 24 January 2018, Sheffield (*contributed talk*).
- High beta factors and directional coupling of InAs/GaAs quantum dots to photonic crystal waveguides determined by direct spectral imaging, Quantum Dot 2018, 25-29 June 2018, Toronto (*poster contribution*).
- High beta factors and directional coupling of InAs/GaAs quantum dots to photonic crystal waveguides determined by direct spectral imaging, Photon 2018, 3-6 September 2018, Birmingham (*contributed talk*).

Introduction

An exciton is a bound state of an electron and a hole which are attracted to each other by Coulomb interaction. Excitons can couple to electromagnetic fields. The interaction with the vacuum field is responsible for the spontaneous emission of a photon due to exciton recombination. On the other hand, an external electromagnetic field can excite or de-excite an exciton, by absorption and stimulated emission of a photon respectively, or alternatively be scattered either elastically or inelastically. Optical spectroscopy of excitons is the study of signals produced when excitons interact with an electromagnetic field. Excitons show up as distinct emission lines in absorption and photoluminescence (PL), and they determine the optical properties near the fundamental band edge. When confined in semiconductor nanostructures, the exciton motion is reduced by the confinement, while the Coulomb attraction between the electron and the hole is nearly unaltered. As a consequence, the exciton binding energy is strongly enhanced, and excitonic effects become more relevant, enabling the possibility to investigate the interaction mechanisms between a single exciton with the surrounding environment. Therefore, semiconductor nanostructures are an excellent playground for excitonic physics, both at the fundamental level and for applications, and on the other hand, optical spectroscopy is a powerful tool to investigate such a playground in most of its aspects. In this thesis, we investigate excitons confined in monolayer (ML) of molybdenum diselenide ($MoSe_2$), in indium arsenide (InAs)/gallium arsenide (GaAs) quantum dots (QDs) embedded in photonic crystal waveguides (PCWGs) and in indium gallium arsenide (InGaAs)/GaAs pyramidal quantum dots (PQDs), by optical spectroscopy. We dedicate Ch. 1 to review the theory necessary to understand the experiments presented in this work, and Ch. 2 to detail the spectroscopy techniques we use.

Semiconductor transition metal dichalcogenides (TMDs) have attracted lot of attention, since the demonstration, in 2010, of the indirect-to-direct bandgap crossover when reaching the ML limit, with the direct bandgap located at the $\pm$ K points of the first Brillouin zone. Due to the two-dimensional (2D) confinement, reduced dielectric screening and large electron and hole effective masses, excitons confined in the ML have binding energies of the order of hundreds meV, and they dominate the band-edge optical properties. Additionally, the spin-orbit (SO) interaction and the lack of inversion symmetry result in a spin splitting of the electron and hole bands at the two non-equivalent valleys $\pm$K, linking the circular polarisation of the transition to the valley index $\pm$. To investigate this complicated band structure, time-resolved measurements of the exciton density dynamics are widely used. The majority of the works which aim to describe and interpret the density dynamics in TMDs are based on non-resonantly excited PL or pump-probe, where the influence of excitons distributed over and relaxing across the large variety of dark states onto the bright states is measured. In Ch. 3, we show measurements of density dynamics by heterodyne detected transient four-wave mixing (FWM) spectroscopy. Heterodyne detected FWM can distinguish pump and probe also for degenerate resonant

excitation, allowing to probe the initial dynamics of the optically coupled states, including their dephasing, and provides a well-defined initial exciton distribution for the subsequent density dynamics.

With photonic crystal nanostructures, the light-matter interaction strength can be engineered, allowing many quantum electrodynamics experiments, useful both at the fundamental level as well as for applications. In particular, QDs embedded in PCWGs are of particular interest. Contrary to photonic crystal cavities, they are open systems, and photons, after interaction with the QD exciton, can be directly coupled to a propagating mode. Nevertheless, strong coupling effects are still observable, thanks to the waveguide mode dispersion and confinement. Additionally, the coupling also depends on the mode field polarisation at the QD location, and it is responsible for chiral effects, like directional emission of photons. One of the most important figures of merit of the QD-waveguide coupling is the beta factor, which describes the probability that a spontaneously emitted photon from the QD couples to a waveguide mode. All previous works measured the beta factor from lifetime measurements, assuming that the radiative decay of the QD into non-guided modes Γ_{ng} is independent from the QD position inside the lattice unit cell. But the strong modification of the local dielectric surrounding in PCWG structures, located in the QD near-field, is expected to modify Γ_{ng} significantly. Therefore, the analysis reported in these works is expected to result in significant systematic errors in the determined factor. In Ch. 4 we show how we use direct spectral imaging to measure the emitted powers, from which we determine the beta factor avoiding assumption on decay rates. This technique also allows us to observe directional emission of photons, from which we obtain the waveguide mode circularity at the QD location. These measurements altogether are used to estimate the most likely QD position within the lattice unit cell.

InGaAs/GaAs PQDs are grown by metalorganic vapor phase epitaxy (MOVPE). They are deterministically positioned and possess high crystal symmetry, which make them ideal for single-photon and entangled-photon sources. Although many studies of single QD spectra have been reported, they were mainly focused on the attribution of the observed emission lines to specific excitonic states, like exciton, biexciton and trion, and little has been said about exciton-phonon interactions. The coupling of the exciton with the continuum of acoustic phonons is responsible for a characteristic lineshape, given by a spectrally sharp peak named the zero-phonon line (ZPL), and sidebands due to phonon assisted transitions. In the time domain, sidebands give a very fast inital decay of the exciton first-order polarisation, i.e., coherence loss. Exciton-phonon coupling is therefore usually unwanted, and lot of effort has been invested trying to suppress it. On the contrary, in Ch. 5 we show that exciton-phonon coupling can be used to estimate different parameters. In particular, by fitting the emission lineshape, we extract deformation potentials, QD in-plane and out-of-plane confinement lengths and the phonon temperature. Additionally, we show that the fit, combined with an observed thermal offset, can be used to separate the homogeneous from inhomogeneous broadening of the emission line, similar to FWM spectroscopy and speckle analysis.

Acronyms

2D two-dimensional

CB conduction band

COM centre of mass

DOS density of states

EEA exciton-exciton annihilation

FCC face-centred cubic

FSS fine-structure splitting

FDTD finite-difference time-domain

FWM four-wave mixing

FWHM full width at half maximum

HWP half waveplate

hh heavy hole

IBM independent boson model

lh light hole

MBE molecular beam epitaxy

ML monolayer

ML-TMD monolayers of transition metal dichalcogenide

MO microscope objective

MOVPE metalorganic vapor phase epitaxy

NA numerical aperture

Nd:YAG neodymium-doped yttrium aluminum garnet

OBE optical Bloch equation

PBC periodic boundary condition

PCWG photonic crystal waveguide

PL photoluminescence

PML perfectly matched layer

PQD pyramidal quantum dot

QD quantum dot

QW quantum well

QWP quarter waveplate

RMSE root mean square error

RWA rotating wave approximation

SE spontaneous emission

SEM scanning electron microscopy

SO spin-orbit

SSI summed spectral image

TI-FWM time integrated four-wave mixing

Ti:Sa titanium-sapphire

TMD transition metal dichalcogenide

TR-FWM time resolved four-wave mixing

TLS two-levels system

VB valence band

WL wetting layer

ZPL zero-phonon line

CaF_2 calcium fluoride

CdSe cadmium selenide

GaAs gallium arsenide

hBN hexagonal boron nitride

InAs indium arsenide

InGaAs indium gallium arsenide

MoS_2 molybdenum disulfide

$MoSe_2$ molybdenum diselenide

SiO_2 silicon dioxide

ZnS zinc sulfide

Contents

Chapter 1

Theoretical background

1.1 Electronic properties of III-V semiconductors

In this section, the electronic properties of III-V semiconductors are presented, and the corresponding optical selection rules explained. The effect of carrier confinement is discussed, restricted to the one-dimensional and three-dimensional confinement, as these are the cases relevant to this work.

1.1.1 Crystal structure

Most III-V semiconductors are characterised by the zinc-blende crystal structure. This consists of two face-centred cubic (FCC) Bravais lattices shifted by a quarter of the diagonal of the cube along the diagonal itself. The structure is given in Fig. 1.1(a). The primitive vectors are $\boldsymbol{a}_1 = \frac{a}{2}(\hat{x} + \hat{y})$, $\boldsymbol{a}_2 = \frac{a}{2}(\hat{x} + \hat{z})$ and $\boldsymbol{a}_3 = \frac{a}{2}(\hat{y} + \hat{z})$, with a the lattice constant. For GaAs $a = 5.6533\,\text{Å}$ and for InAs $a = 6.0583\,\text{Å}$ [2]. The crystal basis is formed by two atoms, with the III group atom located at (0,0,0) and the V group atom at $\frac{a}{4}(1,1,1)$.

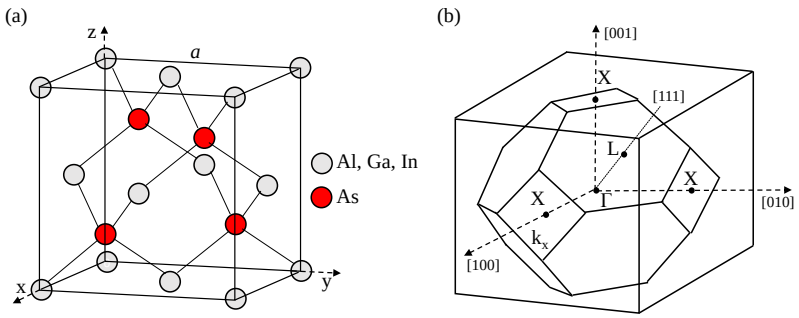

Figure 1.1: Crystal structure of III-V semiconductors. (a) Crystal structure; (b) corresponding first Brillouin zone. Some of the main symmetry points are labelled. Images are reproduced from Ref. [1]

1.1.2 Electronic band structure and selection rules

Before introducing the effect of carrier confinement in semiconductor quantum wells (QWs) and QDs, we review the basic electronic properties of the bulk material close to the centre of the Brillouin zone, i.e. at the Γ-point (see Fig. 1.1)(b) [1]. These properties are similar in most III-V compounds. Similarly to the silicon crystal, the top of the valence band (VB) states arises from hybridisation of p-like orbitals, and the bottom of the conduction band (CB) states from s-like orbitals [5]. The bands are described using VB and CB Bloch functions $|u_{\mathrm{v,c}}\rangle$ which preserve the symmetry of the corresponding atomic orbitals and include the electron spin. The corresponding band structure is sketched in Fig. 1.2(a). From standard $\boldsymbol{k}\cdot\boldsymbol{p}$ theory, the electron dispersion around the Γ point of the CB is found to be parabolic, and it is determined by its effective mass m_{c}. Importantly, the dispersion is isotropic, with constant energy surfaces which are spherical [3]. For GaAs (InAs), $m_{\mathrm{c}} = 0.067\,(0.026)\,m_0$, as determined from experiments, with m_0 the mass of a free electron. For the VB the situation is more complicated, due to SO interaction. In this case, the states are classified in terms of eigenstates of the total angular momentum J and the projection J_z along an arbitrary quantisation direction z, chosen such that $k = k_z$, with the resulting bands respecting the same symmetry. The bands with $J = 1/2, 3/2$ are split by the SO coupling by E_{SO}, which is in the range of few hundreds of meV, with the $J = 1/2$ band, called the split-off band, at lower energies in the VB. The split-off band is usually neglected in practical applications, due to the large energy difference with the band-edge states. On the other hand, the $J = 3/2$ band is fourfold degenerate at $k = 0$, due to the different spin projections along z. Again using $\boldsymbol{k}\cdot\boldsymbol{p}$ theory, one can demonstrate that the degeneracy is partially lifted at $k \neq 0$, resulting in two, twofold degenerate, bands, called the heavy hole (hh) band, with $|J_z| = 3/2$, and light hole (lh) band, with $|J_z| = 1/2$. Their respective effective masses are m_{hh} and m_{lh}, with $m_{\mathrm{hh}} > m_{\mathrm{lh}}$. As in the CB, the hole dispersion is still parabolic. But contrary to the CB, the VB effective masses at the Γ-point are not isotropic, or in other words, the constant energy surfaces are not spherical. For simplicity of discussion, one often considers the VB at the Γ-point as isotropic, with effective masses given by the average over all possible directions. For GaAs (InAs), $m_{\mathrm{hh}} = 0.53\,(0.4)\,m_0$ and $m_{\mathrm{lh}} = 0.08\,(0.026)\,m_0$ [3].

In optical experiments, electrons are excited from the VB to the CB by absorption of a photon. The probability for this to occur is proportional to the matrix element $\langle u_{\mathrm{v}}|\,\boldsymbol{p}\,|u_{\mathrm{c}}\rangle$, with $\boldsymbol{p}$ the momentum operator, according to Fermi golden rule [6]. Only when angular momentum is conserved the above matrix element is not zero. If light is propagating along the z direction, right (left) handed circularly polarised light carriers photons which have angular momentum -1 (+1) along the propagation direction. Therefore, when an electron is promoted from the VB to the CB, it must lose (acquire) a unit of angular momentum upon absorption of a circularly polarised photon. In Fig. 1.2(b), the relevant selection rules

[1] The discussion assumes inversion symmetry. While this is true for diamond-type semiconductors, it is an approximation for zince-blend-type semiconductors [3]. The full and correct calculation is performed by Cardona et al. [4].

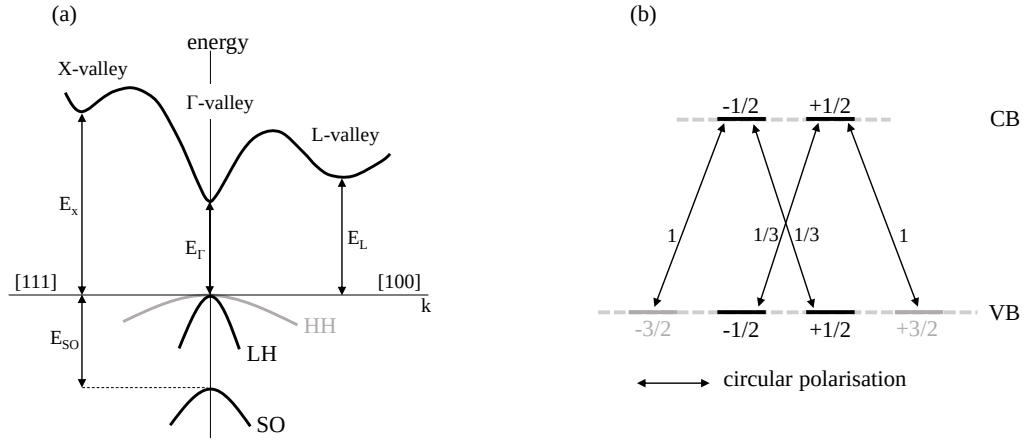

Figure 1.2: (a) Sketch of the band structure of III-V semiconductors along the directions [111] and [100] of the Brillouin zone. The image is reproduced from Ref. [2] (b) Optical selection rules at the Γ point.

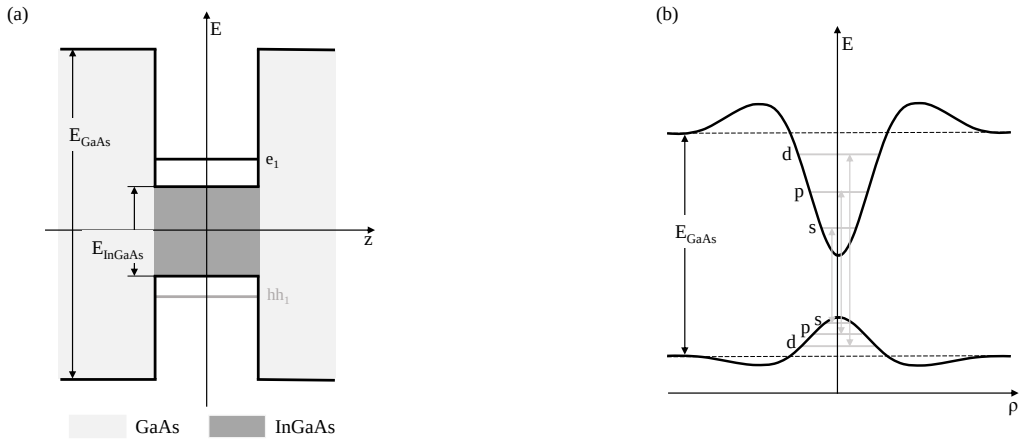

Figure 1.3: Sketch of the potential landscape describing carrier confinement in InGaAs/GaAs heterostructures. (a) QW 1D confinement potential. The potential barrier for the holes is lower than for the electrons due to the band alignment [7]. The first electron (e_1) and heavy hole (hh_1) states are indicated. (b) QD in-plane confinement potential in the harmonic approximation. The states are called s, p, d... in analogy with the atomic states. Image reproduced from Ref. [8].

at the Γ point are shown. The number next to the arrows indicate the relative oscillator strength of the transitions determined by the Clebsch-Gordan coefficients of the involved states.

1.1.3 1D quantum confinement: quantum well

When two materials, like InGaAs (A) and GaAs (B) are sandwiched epitaxially to form a B-A-B structure, a 1D confinement potential for the carriers is created along the growth direction z, due to the different energy band gap E_g of the two materials, forming a QW. A sketch of the QW potential is shown in Fig. 1.3(a). In the sketch, only the lowest energy electron state and the highest energy hh state are given. The energy of the lh states depends on the amount of compressive strain [9] in the QW, which depends on the indium

concentration [10]. This discussion is out of the purpose of this work. For further details, we refer to Ref. [11]. To deal with the carrier confinement within a QW, the envelope wavefunction approximation is widely used. In this approximation, the state of confined electrons and holes close to the Γ point is generally written as a product between the Bloch function $|u_{\mathrm{v,c}}\rangle$ and an envelope function $|\xi_{\mathrm{v,c}}\rangle$, with the latter which satisfies a Schrödinger equation where the free electron mass is substituted with the effective mass:

$$\left(-\frac{\hbar^2}{2m_{\mathrm{v,c}}}\nabla^2 + V(\boldsymbol{r})\right)\xi_{\mathrm{v,c}}(\boldsymbol{r}) = E\xi_{\mathrm{v,c}}(\boldsymbol{r}) \ , \tag{1.1}$$

with $V(\boldsymbol{r})$ the confinement potential. Within the envelope wavefunction approximation, the motion of the electron and the hole in a QW is decomposed in the in-plane motion with momentum $k_{\parallel}$, and the motion along the growth direction with momentum $k_{\perp}$. Due to the confinement, the latter takes values $k_{\perp} = n\pi/L$, with $n = 1, 2, \ldots,$ L the thickness of the A layer and where an infinite barrier potential is assumed. This constraint strongly modifies the energy dispersion. Therefore, by modelling the QW potential as an infinite potential well, the single particle energy can be written as:

$$E_n^{\mathrm{v,c}}(k_{\parallel}) = \frac{\hbar^2}{2m_{\mathrm{v,c}}}\left[\left(\frac{n\pi}{L}\right)^2 + F_{\parallel}^{\mathrm{v,c}}(k_{\parallel})\right] \ , \tag{1.2}$$

with $F_{\parallel}^{\mathrm{v,c}}$ a function describing the in-plane dispersion of electrons and holes. Therefore, carriers are confined to move along a series of subbands, labelled by the index n. The energy $E^{\mathrm{v,c}} = \frac{\hbar^2}{2m_{\mathrm{v,c}}}\left(\frac{\pi}{L}\right)^2$ is the confinement energy and its main effect is to increase the effective bandgap with respect to bulk. Together with strain effects [11], it also induces a splitting $\Delta_{\mathrm{lh-hh}}$ between the lh and hh bands. The electrons in the CB have $F_{\parallel}^{\mathrm{c}} = k_{\parallel}^2$, i.e. they have a parabolic dispersion as in bulk material. On the other hand, $F_{\parallel}^{\mathrm{v}}$ is far more complex. Away from the zone centre, the hh-lh band mixing generates a dispersion which highly deviates from the bulk parabolic dispersion, as calculated by Bastard et al. [12]. For further details on explicit expressions of $F_{\parallel}^{\mathrm{v}}$, we refer the reader to Ref. [3].

The optical selection rules for quantum confined states are dictated by the product of the matrix elements $\langle u_{\mathrm{v}}|\,\boldsymbol{p}\,|u_{\mathrm{c}}\rangle$ and $\langle\xi_{\mathrm{v}}|\xi_{\mathrm{c}}\rangle$, assuming that $\xi_{\mathrm{v,c}}$ are constant within the crystal unit cell [5]. Therefore, the scenario presented in Fig. 1.2(b) is still valid for QW at $k_{\parallel} = 0$, but each allowed transition has to be additionally waited by a term which depends on the electron and hole envelope functions in the quantised direction. Importantly, $\langle\xi_{\mathrm{v}}|\xi_{\mathrm{c}}\rangle \neq 0$ only if ξ_{v} and ξ_{c} have the same parity. Due to the lh-hh splitting $\Delta_{\mathrm{lh-hh}}$, usually the hh states dominate the optical properties close to the gap. This is even more true for in-plane polarisation (i.e the excitation is along the growth direction), in which case hh states have a larger oscillator strength than lh states (see Fig. 1.2(b)).

1.1.4 3D quantum confinement: quantum dot

When an additional in-plane confinement is added to a QW, carriers are confined in all three directions. Such a structure is called a QD. Typically, InAs/GaAs QDs grown by self-assembly have heights in the range of 1-10 nm, while the in-plane sizes are in the range of 10-70 nm. The shape of the QD confinement potential, and the resulting level structure, varies depending on the fabrication process. A commonly adopted description is given by an infinite potential well along the growth direction z, and a 2D harmonic potential for the in-plane confinement, sketched in Fig. 1.3(b) [13, 14, 15, 16]. The quantisation energy $E_n^{\mathrm{v,c}}$ in the z direction is typically one order of magnitude larger than for the lateral confinement, therefore only the 1st QW subband is usually considered. The in-plane harmonic potential creates additional sublevels, whose energies are given by $E_{j,i}^{\mathrm{v,c}} = \hbar\omega_{\mathrm{v,c}}\,(i+j+1)$, with $i,\, j = 1, 2, ...$ The levels separation in the CB and VB depends on the respective effective masses as well as on the confinement length. For InGaAs QD, typical confinement lengths are of the order of 5 nm. For the hh states, the resulting levels separation is $\hbar\omega_{\mathrm{v}} \sim 10$ meV and for the electron states in the CB $\hbar\omega_{\mathrm{c}} \sim 50$ meV [17]. These levels are named s, p, d... in analogy to the atomic shells. The total single particle energy can be finally written as:

$$E_{n,i,j}^{\mathrm{v,c}} = E_n^{\mathrm{v,c}} + E_{j,i}^{\mathrm{v,c}} \quad . \tag{1.3}$$

The optical selection rules are still determined by the symmetry of Bloch functions $|u_{\mathrm{v,c}}\rangle$ in bulk and the electron-hole overlap which depends on the corresponding envelope functions. Therefore, similar to QW, $\langle \xi_{\mathrm{v}}^i | \xi_{\mathrm{c}}^j \rangle \neq 0$ only when ξ_{v} and ξ_{c} have the same parity. Although hh states usually dominate the optical properties, it is worth to note that these selection rules can be relaxed by lh-hh band mixing, described in the QW section. Indeed, even if lh and hh bands are split by $\Delta_{\mathrm{lh-hh}}$, strain [18, 19] and in-plane QD asymmetry [20] can still induce a coupling between the bands.

1.2 Electronic properties of monolayers of transition metal dichalcogenides

In this section, we review the main electronic and optical properties of monolayers of transition metal dichalcogenides (ML-TMDs). When exfoliated to a single ML, TMDs behave like 2D materials. Therefore, the electronic properties of ML-TMD already take into account the quantum confinement effects.

1.2.1 Crystal structure

The crystal structure of ML-TMDs is trigonal prismatic. Six chalcogenide atoms (X=S, Se) are organized around the central metal atom (M=W, Mo) defining the vertexes of a triangular prism, as shown in Fig. 1.4(a). Each chalcogen atom is in turn bounded to three metal atoms such that the triangular prisms are interconnected to form the ML structure,

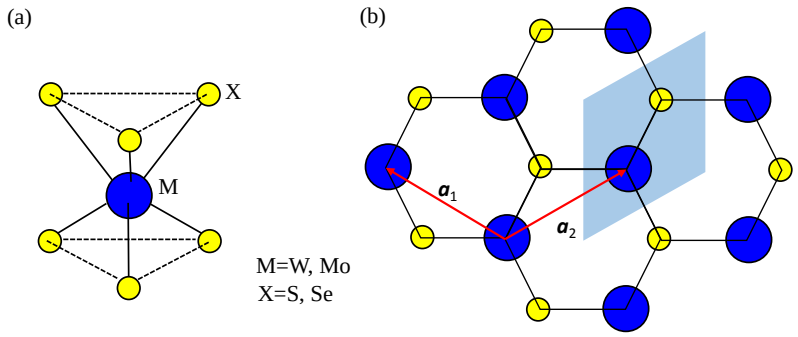

Figure 1.4: Crystal structure of TMDs. (a) Perspective; (b) Top view. $\boldsymbol{a}_1$ and $\boldsymbol{a}_2$ are the lattice vectors and the blue shaded area is the crystal unit cell.

with a typical thickness of 1 nm [21]. Seen from the top, the ML has a honeycomb crystal structure similar to graphene, as shown in Fig. 1.4(b). In variance to graphene, the unit cell contains two different species of atoms, as highlighted in Fig. 1.4(b), breaking the inversion symmetry which strongly affects the electronic band structure. The intra-layer interaction is of covalent-ionic type, while the inter-layer interaction is of van der Waals type. Therefore, ML-TMDs can be stacked together to form bulk TMD in different phases. For details on the multiple bulk phases of TMDs, we refer to the review by Chhowalla et al. [21]. Although the inter-layer interaction is quite weak, it is responsible for an indirect to direct bandgap transition when bulk material is exfoliated down to the ML limit [22]. In ML-TMDs, the direct bandgap is located at the $\pm K$ points of the first Brillouin zone, as shown in Fig. 1.5.

1.2.2 Electronic band structure and selection rules

As already mentioned in the previous subsection, when exfoliated down to the ML limit, TMDs show a direct bandgap located at the $\pm K$ points of the Brillouin zone. We will now focus on the electronic properties at these points, called valleys, which are dominated by the metal atom d orbitals. In particular, it has been demonstrated that the VB maximum wavefunction is mainly composed by the orbitals $d_{x^2-y^2}$ and d_{xy}, while the CB minimum wavefunction is mainly composed by the orbital d_{z^2} [23, 24]. For symmetry reasons, the $d_{x^2-y^2}$ and d_{xy} orbitals hybridise in two orthogonal linear combinations. One of the resulting states has energy above 1 eV from the CB minimum, and it can be neglected [24]. Importantly, the role of these states is inverted for $\pm K$ valleys. In order to qualitatively describe the band-edge physics of ML-TMDs, one can make use of a simple two-band $\boldsymbol{k}\cdot\boldsymbol{p}$ model based on the following basis functions ϕ [25]:

$$|\phi_\mathrm{c}\rangle = |d_{z^2}\rangle\,, \qquad |\phi_\mathrm{v}^\tau\rangle = \frac{1}{\sqrt{2}}\left(|d_{x^2-y^2}\rangle + i\tau\,|d_{xy}\rangle\right)\,, \tag{1.4}$$

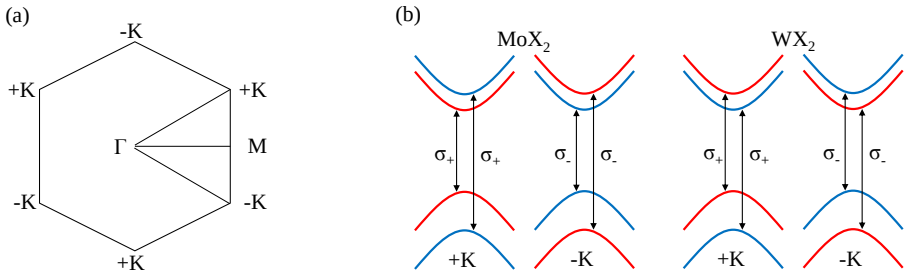

Figure 1.5: (a) First Brillouin zone of ML-TMDs. (b) Optically allowed transition for Mo and W-based TMDs. The red bands are spin up and the blue bands are spin down.

with c and v which label the CB and VB respectively, $\tau = \pm 1$ is the valley index. The corresponding Hamiltonian, to first-order, reads as [25, 26]:

$$H_\tau = \hbar \begin{pmatrix} \hbar\Delta/2 & v_\mathrm{D}\left(\tau k_x - i k_y\right) \\ v_\mathrm{D}\left(\tau k_x + i k_y\right) & -\hbar\Delta/2 \end{pmatrix} \quad , \tag{1.5}$$

with v_D the Dirac velocity. The splitting of the VB and CB states at the $\pm K$ points is $\hbar\Delta$, which corresponds to the energy bandgap E_g. Although very simplified, this simple Hamiltonian allows us to introduce the valley dependent optical selection rules. The coupling to a $\sigma_\pm$ polarised field is measured by the squared modulus of $P_\pm(\boldsymbol{k}) = P_x(\boldsymbol{k}) \pm iP_y(\boldsymbol{k})$, with $P_\alpha(\boldsymbol{k}) = \frac{m_0}{\hbar}\langle\phi_\mathrm{c}|\frac{\partial H}{\partial k_\alpha}|\phi_\mathrm{v}^\tau\rangle$ [25]. Using Eq. 1.5, we find, at $\boldsymbol{k} = 0$:

$$|P_\pm|^2 = m_0^2 v_\mathrm{D}^2 \left(1 \pm \tau\right)^2 \quad . \tag{1.6}$$

Therefore, σ_+ light couples the states $|\phi_\mathrm{v}\rangle$ and $|\phi_\mathrm{c}\rangle$ in the $+K$ valley, but not the states in $-K$ valley. The opposite is true for σ_- light, such that circular excitation can be used to selectively inject carriers in the $\pm K$ valleys. It is worth to note that the physics discussed up to now relies only on symmetry consideration. Indeed, also MLs of graphene with a staggered sublattice potential [25, 27, 28] and graphene bilayers [29] have a finite bandgap at the $\pm K$ points due to sublattice symmetry breaking. It is only when SO interaction is considered that TMDs reveal new exciting properties. The SO coupling, proportional to $\boldsymbol{L} \cdot \boldsymbol{S}$, is expected to be very strong because of the d orbitals and the rather heavy metals used. When considering this coupling, the VB states with opposite spins are split by about 200 meV, with opposite sign in the two valleys, creating a spin-valley locking [25]. The splitting is indeed large enough to selectively excite only one spin component in each valley. Furthermore, it has been shown that also the CB states are split by the SO coupling, with a splitting Δ_cb of the order of 20 meV [24, 30]. Interestingly, the splitting in the CB has opposite signs in Mo and W-based TMDs.

The optically allowed transitions are sketched in Fig. 1.5(b). Importantly, the correlation between valley and spin degrees of freedom, together with the selective excitation of $\pm K$ valleys using circularly polarised light, lies at the heart of new interesting effects, like the valley Hall effect [31].

1.3 Excitons

When an electron is promoted to the CB, a hole is left in the VB. The two particles bind together, with a binding energy E_b which is determined by their Coulomb interaction. This two-particles system is called exciton. Excitons are usually distinguished in two classes: Frenkel excitons [32] and Wannier-Mott excitons [33, 34]. In a Frenkel exciton, the exciton radius (i.e. the electron-hole separation) is so small that the envelope function approximation breaks down. For Wannier-Mott exciton the situation is reversed. In inorganic semiconductor, excitons usually extend over tens of lattice constants, and the Wannier-Mott description can be used. Electron and holes are described with effective masses which depend on the material. We will only deal with Wannier-Mott excitons in the following.

1.3.1 Bulk excitons

In bulk, the Coulomb interaction between an electron and a hole can be treated similar to the interaction of an electron with the proton in a hydrogen atom. The exciton binding energy is then [35]:

$$E_\mathrm{X} = \frac{\mu}{m_0}\frac{1}{\epsilon_\mathrm{r}^2}R \ , \tag{1.7}$$

where μ the exciton reduced mass calculated as $1/\mu = 1/m_\mathrm{c} + 1/m_\mathrm{v}$, ϵ_r the relative dielectric constant of the material and R the atomic Rydberg constant equal to 13.6 eV. For GaAs, for example, $\mu \sim 0.06\, m_0$ using the hh bulk effective mass and $\epsilon_\mathrm{r} \sim 12.3$. This gives an exciton binding energy of about 5 meV, which is approximately 4 times smaller than the room temperature thermal energy $k_\mathrm{B}T \sim 26$ meV. This means that excitonic effects are small at room temperature, as the bound state dissociates into a free electron and a free hole. Importantly, the reduced binding energy for bulk semiconductors with respect to the atomic counterpart is due to a larger screening of the electron-hole Coulomb interaction due to the higher dielectric constant, and the much smaller reduced mass. The exciton Bohr radius a_X can be written in terms of the atomic Bohr radius a_B=0.0529 nm according to [35]:

$$a_\mathrm{X} = \frac{m_0\epsilon_\mathrm{r}}{\mu}a_\mathrm{B} \ , \tag{1.8}$$

with e the electron charge. For GaAs, the bulk exciton Bohr radius is about 10 nm, which is about 18 lattice constants.

1.3.2 Two-dimensional excitons

When excitons are confined within a layer of a thickness comparable to or smaller than their bulk Bohr radius, quantum confinement effects dominate the optical properties. It is instructive at this point to make a comparison between excitons in III-V QW and excitons in TMD materials. As a general remark, the reduced dimensionality in a 2D system reduces the exciton kinetic energy, bringing the electron and the hole of an exciton closer.

As a consequence, in 2D systems, the binding energy is larger than in bulk. For ideal 2D systems, the exciton binding energy E_B^{2D} is [35]:

$$E_{\mathrm{X}}^{2\mathrm{D}} = 4E_{\mathrm{b}} \ , \tag{1.9}$$

and the exciton Bohr radius $a_{\mathrm{B}}^{2\mathrm{D}}$ is [35]:

$$a_{\mathrm{X}}^{2\mathrm{D}} = \frac{a_{\mathrm{X}}}{2} \ . \tag{1.10}$$

Therefore, in the ideal 2D limit, the binding energy is enhanced by a factor of four with respect to the bulk binding energy, and the exciton Bohr radius is reduced by a factor of two. The question arises whether a system can be considered close to the 2D ideal limit. A good measure is the ratio between the bulk binding energy and the confinement energy [36], which is much smaller than one in the ideal 2D limit. This condition is satisfied in ML-TMDs, as typical thickness quantisation energies are of the order of 0.75-1 eV, therefore much larger than the bulk exciton binding energy of few tens of meVs according to Eq. 1.7. In GaAs QW the discussion is more complicated, as the binding energy depends not only the QW thickness, but also on the height of the barrier which determine the extension of the envelope function in the confinement direction [37]. Further details on this topic can be found in Ref. [38]. The binding energy in ML-TMDs is strongly enhanced with respect to III-V semiconductors because of the larger effective masses of both electron and hole. For ML-TMDs, $m_{\mathrm{c}} \sim m_{\mathrm{v}} \sim 0.5\, m_0$ [39], giving a reduced mass $\mu \sim 0.25\, m_0$, which is more than a factor of four larger than III-V semiconductors [40]. Furthermore, the electron-hole Coulomb interaction field is subject to a lower screening when penetrating in vacuum or in a medium which has a much lower dielectric constant than the confining layer [36, 41], enhancing the exciton binding energy. Note that this effect sums up with the effect of the reduced dimensionality, as of different nature. Indeed, for a fixed confinement thickness, the binding energy can be strongly enhanced by decreasing the dielectric constant of the surrounding medium [42]. In ML-TMDs, which have $\epsilon_{\mathrm{r}} \sim 10$ [40] and are usually exfoliated onto a quartz substrate ($\epsilon_{\mathrm{r}} \sim 2.25$) or encapsulated in hexagonal boron nitride (hBN) layer (ϵ_{r} =3.24 [43]), this effect is much stronger than in GaAs QW, for which $\epsilon_r \sim 12.3$ for GaAs. All these observations explain why excitons in ML-TMDs have an extremely large binding energy, of the order of 500 meV [44, 45, 46, 47], which is about 50 times larger than for excitons confined in GaAs QW.

Beside the binding properties which are determined by the relative motion of the electron and the hole, excitons in QWs have the parabolic dispersion in their centre of mass (COM) sketched in Fig. 1.6, which is given by their COM $M^* = m_{\mathrm{c}} + m_{\mathrm{v}}$. The blue shaded area represents the light cone, defined as the region $|\boldsymbol{K}_{\parallel}| < K_0 = n\omega/c$, where n is the refractive index of the surrounding medium. In absence of disorder (as assumed in the following discussion), exciton states are eigenstates of $\boldsymbol{K}_{\parallel}$, and their properties can be characterised in terms of their in-plane wavevector. Excitons within the light

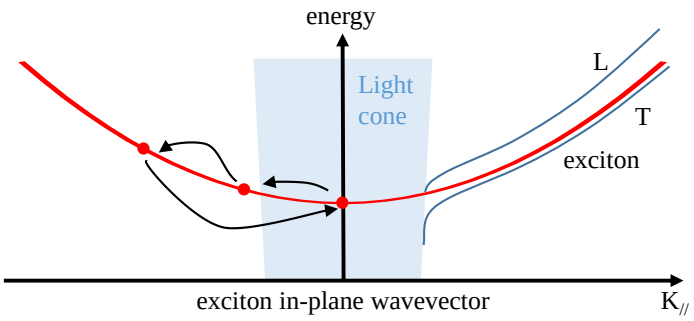

Figure 1.6: Sketch of the exciton COM dispersion, and phonon-assisted scattering between inside and outside the light cone. The splitting between longitudinal (L) and transverse (T) polaritons is also shown. Image taken from Ref. [48].

cone are referred to as "slow", and they can couple to external light fields, as known from QW excitons [38, 49]. On the other hand, excitons can acquire in-plane momentum by scattering with phonons, other excitons and charge carriers, such that $\boldsymbol{K}_{\parallel} > K_0$, as sketched in Fig. 1.6. These excitons are called "fast" here. Fast excitons are dark, as they can not couple to external fields. On the other hand, they can still couple to fields that are evanescent in the direction orthogonal to the ML, to form surface polariton eigenstates with transverse (T) and longitudinal (L) linear polarisations with respect to $\boldsymbol{K}_{\parallel}$, as shown in Fig. 1.6. This behaviour is known from QW excitons [50] and it has been discussed also in ML-TMDs [51, 52].

1.3.3 Zero-dimensional excitons

In QDs, the exciton is confined in all the three dimensions. In this case, we can introduce the notion of confinement regime [53]. In the strong confinement regime, the exciton's wavefunction is factorised into an electron and a hole parts. The direct and exchange Coulomb interaction terms are then introduced as a perturbation of the electron and hole quantum confined states [54]. Although weak, both terms are essential in order to understand optical spectra at low temperatures. Excitons can capture additional carries leading to charged excitonic complexes. The corresponding transitions are usually observed in optical spectra, resulting in a series of peaks with different binding energies, as a consequence of the Coulomb interaction [55, 56]. Furthermore, exchange terms combined with QD shape anisotropy strongly affect the optical selection rules, as it will be explained later in more detail [57]. The strong confinement approach is valid only when the electron and the hole wavefunctions extend less than the exciton Bohr radius in bulk. When this is not the case, the QD can either be in the intermediate or weak confinement regimes. In this case the electronic energy-levels spacing is comparable with the Coulomb interaction energies. Coulomb correlations between electrons and holes can not be treated as a perturbation. This leads to a complex scenario, dominated by the interplay of Coulomb and confinement energies, whose explanation goes beyond the purpose of this work.

1.4 Four-wave mixing spectroscopy

In Ch. 3, experiments of FWM spectroscopy on TMDs will be shown. This section is therefore dedicated to an overview of the technique.

1.4.1 Four-wave mixing in context

FWM is a powerful spectroscopy technique to investigate the coherent properties of individual quantum systems (i.e. qubits). When talking about coherence, we refer to the ability of the quantum system to maintain a well defined spatio-temporal phase relation with the exciting electromagnetic field. Such an ability lies at the heart of any quantum information processing applications, as well as of optoelectronic devices. In this context, dephasing (or decoherence) is the mechanism that leads to the loss of coherence, limiting the time window within quantum operations can be performed. In solid state systems, like semiconductor quantum dots or TMD materials, dephasing occurs because of the coupling of the qubit to the surrounding environment [58, 59, 60]. At cryogenic temperatures, the effects of the environment can be strongly suppressed, down to a regime where phase coherence is only limited by the intrinsic radiative decay of the qubit - the qubit excited state is depopulated by emission of a photon [36, 61, 62]. The population lifetime is conventionally called T_1, to distinguish it from the dephasing time, conventionally called T_2. T_2 is inversely proportional to the energy full width at half maximum (FWHM) of the homogeneous absorption spectral lineshape γ, with $\gamma = 2\hbar/T_2$. In time domain, T_2 corresponds to the decay time of the first-order linear polarisation $p^{(1)}$. One main limitation in measuring the dephasing time using standard linear optics techniques, is the inhomogeneous broadening σ, which describes the distribution of transition frequencies of an ensemble of qubits. The destructive interference of the linear polarisations from different qubits leads to an effective decay time $T_2^* \propto 1/\sigma$. When $\sigma \gg \gamma$, a deconvolution of the inhomogeneous broadening is not possible, and the intrinsic dephasing of the qubit cannot be reliably determined. Even when a single qubit is isolated, the measured first-order polarisation is strongly affected by background light transmitted or reflected in the same direction. This last issue has been overcome by measurements of PL and resonant Rayleigh scattering. From PL experiments, in 1996 Gammon et al. measured the homogeneous linewidth of a single QD [63]. Although very powerful, single QD PL measurements are limited to systems where blinking and spectral diffusion are negligible compared to the homogeneous linewidth. In colloidal systems this is usually not the case. Indeed, because of the quantum-confined Stark effect, the absorption resonance of the qubits randomly shifts due to fluctuating electric fields in the local environment, irreversibly affecting its lineshape [64, 65].

FWM spectroscopy is a powerful non-linear optics technique which is able to overcome the above complications. Similar to the refocusing of the spin magnetisation in nuclear magnetic resonance and magnetic resonance imaging, transient FWM spectroscopy relies on the rephasing of the third order polarisations $p^{(3)}$ of an ensemble of qubits, allowing

for the extraction of the intrinsic dephasing even in the presence of large inhomogeneous broadening. This technique has been successfully applied to measure the dephasing on many inhomogeneously broadened systems, such as InGaAs QDs [66], lead sulfide [67] and cadmium selenide (CdSe)/zinc sulfide (ZnS) colloidal QDs [68], CdSe nanoplatelets [36] and recently also in TMDs [62].

1.4.2 Principles of non-linear optical spectroscopy

In a non-linear process, the nth-order interaction with the electromagnetic field $\boldsymbol{\mathcal{E}}$ generates a macroscopic non-linear polarisation $P^{(n)}$ [69]. This term acts as a source in the Maxwell equations, and it is therefore responsible for the emission of the non-linear field. By writing the electromagnetic field $\boldsymbol{\mathcal{E}}$ as a set of M fields with different wavevector $\boldsymbol{k}$, frequency ω and temporal and spatial profile

$$\mathcal{E}(\boldsymbol{r},t) = \sum_{i=1}^{M} \boldsymbol{\mathcal{E}}_i(\mathbf{r},t) e^{i(\mathbf{k}_i\cdot\mathbf{r}-\omega_i t)} \quad , \tag{1.11}$$

the corresponding non-linear polarisation, in the most general case, is given by

$$P^{(n)} = R^{(\boldsymbol{N})} \boldsymbol{\mathcal{E}}_1^{a_1} \boldsymbol{\mathcal{E}}_1^{b_1 *} \boldsymbol{\mathcal{E}}_2^{a_2} \boldsymbol{\mathcal{E}}_2^{b_2 *} \cdots \boldsymbol{\mathcal{E}}_M^{a_M} \boldsymbol{\mathcal{E}}_M^{b_M *} \quad , \tag{1.12}$$

with $a_1 + a_2 + \cdots a_M + b_1 + b_2 + \cdots b_M = n$ which sets the order of the polarisation. $R^{(\boldsymbol{N})}$ is the non-linear response function of the system, with the vector $\boldsymbol{N} = (a_1 - b_1, \cdots, a_M - b_M)$ which is related to the emission direction of the non-linear field, in a manner that will become clear later. FWM is a third-order process, and we are therefore interested on $P^{(3)}$ only. Between the different combinations of interactions that could generate $P^{(3)}$, we are interested in the process with $\boldsymbol{N} = (-1, 1, 1)$, the so called photon-echo. The connection between the microscopic properties of a two-levels system (TLS) and the macroscopic third-order polarisation lies in the corresponding response function $R^{(\boldsymbol{N})}$. A calculation of the response function is therefore necessary in order to interpret FWM experiments. This can be done in the framework of the well known optical Bloch equations (OBEs), which describe the evolution of a TLS following excitation by an electromagnetic field.

1.4.3 Optical Bloch equations

The are many text books which contain detailed derivations of the OBEs, like Ref. [70] or Ref. [71]. In the next subsection, the main equations are given, which are necessary for the understanding of transient FWM experiments.

In absence of interaction, the system is described by the Hamiltonian $\hat{H}_\mathrm{S} = \hbar\omega_\mathrm{e}\hat{\sigma}_\mathrm{ee} + \hbar\omega_\mathrm{g}\hat{\sigma}_\mathrm{gg}$, where $\hbar\omega_\mathrm{g}$ and $\hbar\omega_\mathrm{e}$ are the energies of the ground state $|g\rangle$ and of the excited state $|e\rangle$ respectively, and $\hat{\sigma}_\mathrm{gg}$, and $\hat{\sigma}_\mathrm{ee}$ indicate the operators $|g\rangle\langle g|$ and $|e\rangle\langle e|$ respectively. In the semiclassical approximation, the interaction of a radiation field with the TLS is

described by the dipole interaction Hamiltonian

$$\hat{H}_{\mathrm{I}} = -\hat{\mu} \cdot \boldsymbol{\mathcal{E}}(0,t) \ , \tag{1.13}$$

where $\hat{\mu} = -e\hat{r}$ is the dipole operator, $\hat{r}$ is the position operator, e the electron charge and $\boldsymbol{\mathcal{E}}(0,t)$ is the electric field vector evaluated at the position of the dipole (assumed to be at the origin of the reference system). The expression of the interaction is already given in the "long wavelength approximation", which assumes the extension of the states is much smaller than the wavelength of the radiation field. The dipole operator is an odd operator and it connects states with opposite symmetry. Therefore, the following relations are valid:

$$\langle g|\,\hat{\mu}\,|g\rangle = 0 \qquad \langle g|\,\hat{\mu}\,|e\rangle = -e\boldsymbol{r}_{\mathrm{ge}} = -e\boldsymbol{r}^*_{\mathrm{eg}} \tag{1.14a}$$

$$\langle e|\,\hat{\mu}\,|g\rangle = -e\boldsymbol{r}_{\mathrm{eg}} \qquad \langle e|\,\hat{\mu}\,|e\rangle = 0 \ . \tag{1.14b}$$

In this way, the dipole operator can be represented as:

$$\hat{\mu} = -e\left(\boldsymbol{r}_{\mathrm{ge}}\hat{\sigma}_{\mathrm{ge}} + \boldsymbol{r}_{\mathrm{eg}}\hat{\sigma}_{\mathrm{eg}}\right) \ , \tag{1.15}$$

where $\hat{\sigma}_{\mathrm{ge}} = |g\rangle\langle e|$ and $\hat{\sigma}_{\mathrm{eg}} = |e\rangle\langle g|$. With this at hand, the interaction Hamiltonian can be written in the form:

$$\hat{H}_{\mathrm{I}} = e\left(\boldsymbol{r}_{\mathrm{ge}}\hat{\sigma}_{\mathrm{ge}} + \boldsymbol{r}_{\mathrm{eg}}\hat{\sigma}_{\mathrm{eg}}\right)\left(\boldsymbol{\mathcal{E}}(0,t) + \boldsymbol{\mathcal{E}}^*(0,t)\right) \ . \tag{1.16}$$

In the present case, monochromatic excitation is assumed, such that the incident laser can be written as $\boldsymbol{\mathcal{E}}_{\mathrm{L}}(0,t) = \boldsymbol{\mathcal{E}}_{\mathrm{L}}(0)e^{-i\omega_{\mathrm{L}}t}$, with ω_{L} the laser frequency and $\boldsymbol{\mathcal{E}}_{\mathrm{L}}(0)$ its amplitude. By defining the Rabi frequency $\Omega_{\mathrm{R}} = e\boldsymbol{r}_{\mathrm{eg}} \cdot \boldsymbol{\mathcal{E}}_{\mathrm{L}}(0)/\hbar$ and $\Omega_{\mathrm{NR}} = e\boldsymbol{r}_{\mathrm{eg}} \cdot \boldsymbol{\mathcal{E}}^*_{\mathrm{L}}(0)/\hbar$, and using equations Eq. 1.14, equation Eq. 1.16 can be written in the extended form:

$$\hat{H}_{\mathrm{I}} = \hbar\left(\Omega^*_{\mathrm{R}}\hat{\sigma}_{\mathrm{ge}}e^{i\omega_{\mathrm{L}}t} + \Omega_{\mathrm{R}}\hat{\sigma}_{\mathrm{eg}}e^{-i\omega_{\mathrm{L}}t} + \Omega^*_{\mathrm{NR}}\hat{\sigma}_{\mathrm{ge}}e^{-i\omega_{\mathrm{L}}t} + \Omega_{\mathrm{NR}}\hat{\sigma}_{\mathrm{eg}}e^{i\omega_{\mathrm{L}}t}\right) \ . \tag{1.17}$$

By moving to the interaction representation, $\hat{\sigma}_{\mathrm{eg}} \to \hat{\sigma}_{\mathrm{eg}}e^{i\omega_0 t}$ and $\hat{\sigma}_{\mathrm{ge}} \to \hat{\sigma}_{\mathrm{ge}}e^{-i\omega_0 t}$. The two terms containing the Rabi frequency in equation Eq. 1.17 have terms oscillating at $\omega_0 - \omega_{\mathrm{L}}$, while the two terms containing Ω_{NR} have terms oscillating at $\omega_0 + \omega_{\mathrm{L}}$. Within the rotating wave approximation (RWA), terms oscillating at $\omega_0 + \omega_{\mathrm{L}}$ in Eq. 1.17, which on resonance is twice the optical frequency, are neglected, as their contribution averages to zero when considering observation time longer than $2\pi/\omega_{\mathrm{L}}$. For excitation in the visible, $2\pi/\omega_{\mathrm{L}} \sim 10^{-15}$ s. In the RWA, the interaction Hamiltonian can be written as:

$$\hat{H}_{\mathrm{I}} = \Lambda\hat{\sigma}_{\mathrm{eg}} - \Lambda^*\hat{\sigma}_{\mathrm{ge}} \ , \tag{1.18}$$

with $\Lambda = \hbar\Omega_{\mathrm{R}}e^{-i\omega_{\mathrm{L}}t}$. The total coherent Hamiltonian of the TLS is therefore $\hat{H}_{\mathrm{coh}} = \hat{H}_{\mathrm{S}} + \hat{H}_{\mathrm{I}}$, and it describes the coherent evolution of the system in response to an incident

field.

In order to describe a real scenario, decoherence effects have to be introduced. While the unitary evolution under a hermitian Hamiltonian can accurately be described by the time evolution of the state vector (or wavefunction), the dissipative dynamics are captured by the master equation for the system density matrix $\hat{\rho}_{\mathrm{s}}$:

$$i\hbar\frac{d\hat{\rho}_{\mathrm{s}}}{dt} = \left[\hat{H}, \hat{\rho}_{\mathrm{s}}\right] \quad , \tag{1.19}$$

with $\hat{H} = \hat{H}_{\mathrm{coh}} + \hat{H}_{\mathrm{R}}$ and $\hat{H}_{\mathrm{R}}$ the relaxation Hamiltonian describing decoherence effects. Although precise theoretical calculations have been performed to introduce relaxation mechanisms, here we rather use a phenomenological approach [72], by writing the commutators for the relaxation Hamiltonian as follows:

$$\left[\hat{H}_{\mathrm{R}}, \hat{\rho}_{\mathrm{s}}\right]_{ee} = -\hat{\rho}_{\mathrm{ee}}/T_1 \qquad \left[\hat{H}_{\mathrm{R}}, \hat{\rho}_{\mathrm{s}}\right]_{eg} = -\hat{\rho}_{\mathrm{eg}}/T_2 \quad , \tag{1.20}$$

where T_1 accounts for population decay and T_2 for dephasing. By defining $n = \hat{\rho}_{\mathrm{ee}}$, $\hat{\rho}_{\mathrm{gg}} = 1 - n$ and $p = \hat{\rho}_{\mathrm{eg}}$, and calculating the matrix element using Eq. 1.19, one obtain the OBEs [72]:

$$\dot{n} + \frac{n}{T_1} + \frac{i}{\hbar}\left(\Lambda p^* - p\Lambda^*\right) = 0 \tag{1.21}$$

$$\dot{p} + \left(i\omega_0 + \frac{1}{T_2}\right) + \Lambda\left(1 - 2n\right) = 0 \quad . \tag{1.22}$$

These equations represent the best knowledge that we can have about a TLS coupled to an external reservoir.

1.4.4 Transient four-wave mixing response function

In this subsection, we follow the discussion presented in Ref. [72] and in the supplementary material of Ref. [36].

The OBEs described in the previous subsection can be expanded in a Taylor series and truncated to the desired order. In order to do this, the electric field has to be considered as a small perturbation, i.e. $\boldsymbol{\mathcal{E}} \to \alpha\boldsymbol{\mathcal{E}}$, with α an arbitrary small parameter. Both polarisation and population terms can also be expanded in a Taylor series:

$$p = p^{(0)} + \alpha p^{(1)} + \alpha^2 p^{(2)} + \alpha^3 p^{(3)} + \cdots \tag{1.23}$$

$$n = n^{(0)} + \alpha n^{(1)} + \alpha^2 n^{(2)} + \alpha^3 n^{(3)} + \cdots \quad . \tag{1.24}$$

By grouping the terms of the same order in α, one finds the following equations, up to

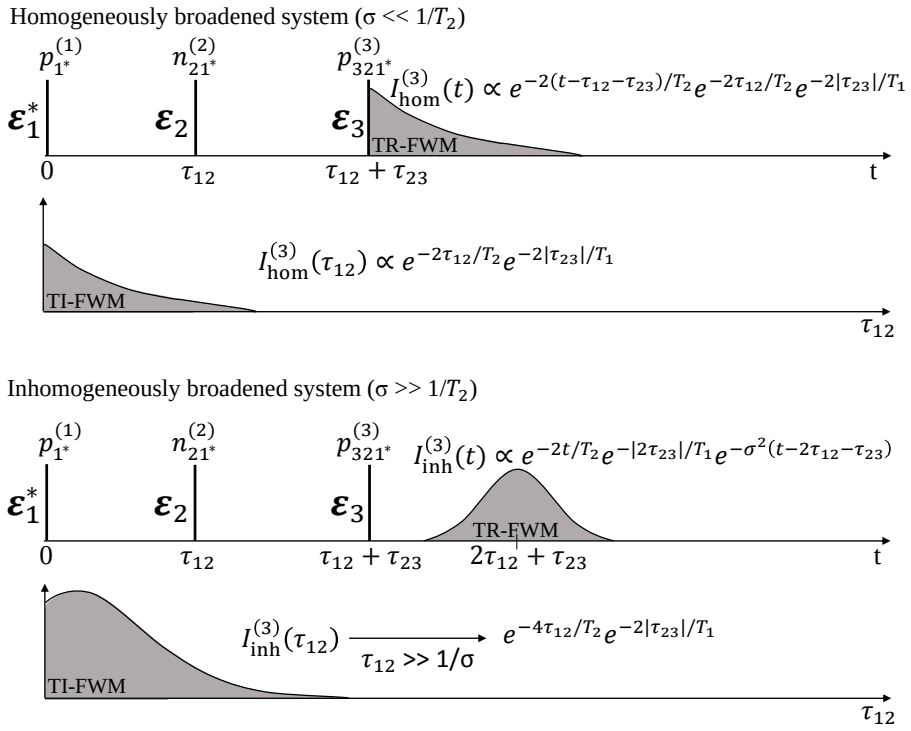

Figure 1.7: Sketch of three beams degenerate transient FWM for the case $\tau_{13} > \tau_{12}$: the first interaction with the pulse $\boldsymbol{\mathcal{E}}_1^*$ generates a first order polarisation $p_{1^*}^{(1)}$; the second interaction with $\boldsymbol{\mathcal{E}}_2$ converts $p_{1^*}^{(1)}$ into population $n_{21^*}^{(2)}$ and the third interaction with $\boldsymbol{\mathcal{E}}_3$ creates a third order polarisation $p_{321^*}^{(3)}$ which emits the FWM signal. The TR-FWM and TI-FWM intensities are shown for both a homogeneously broadened and an inhomogeneously broadened systems. The figure is reproduced from Ref. [73], and adapted to the case of three-beams transient FWM.

third-order:

$$\begin{aligned} &\dot{p}^{(1)} + (i\omega_0 + 1/T_2)\, p^{(1)} + \frac{i}{\hbar}\Lambda = 0 \\ &\dot{n}^{(2)} + \frac{n^{(2)}}{T_1} + \frac{i}{\hbar}\left[\Lambda p^{(1)*} - \Lambda^* p^{(1)}\right] = 0 \\ &\dot{p}^{(3)} + (i\omega_0 + 1/T_2)\, p^{(3)} - \frac{2i}{\hbar}\Lambda n^{(2)} = 0 \ . \end{aligned} \tag{1.25}$$

To obtain the above equations in this form, it is assumed that both polarisation and population terms are zero at $t = 0$, i.e. $p(0) = n(0) = 0$. As a consequence, also $p^{(0)} = n^{(0)} = 0$, which means that without interaction with the electromagnetic field (the zero-order) we do not have any intrinsic polarisation and population in the material. In a three-pulses degenerate FWM, the electric field can be written in the following way:

$$\boldsymbol{\mathcal{E}}(\boldsymbol{r}, t) = \boldsymbol{\mathcal{E}}_1(\mathbf{r}, t)e^{i(\mathbf{k}_1\cdot\mathbf{r}-\omega t)} + \boldsymbol{\mathcal{E}}_2(\mathbf{r}, t-\tau_{12})e^{i(\mathbf{k}_2\cdot\mathbf{r}-\omega t)} + \boldsymbol{\mathcal{E}}_3(\mathbf{r}, t-\tau_{13})e^{i(\mathbf{k}_3\cdot\mathbf{r}-\omega t)} \ . \tag{1.26}$$

Assuming δ-pulses, i.e. $\boldsymbol{\mathcal{E}}_i(t) = \boldsymbol{\mathcal{E}}_i\delta(t)$, the time-ordering of the interactions is defined by the three time delayed pulses, and an analytical solution of Eq. 1.25 is possible. For the photon-echo non-linearity, we are interested in the system third-order polarisation term $p_{321^*}^{(3)}$, which is responsible for the emission of the FWM in the phase matched direction

$\boldsymbol{k}_3+\boldsymbol{k}_2-\boldsymbol{k}_1$. The emitted field is proportional to $P^{(3)}_{\mathrm{FWM}} = \mu p^{(3)}_{321^*}$, where μ is the projection of the dipole onto the electric field polarisation (assuming co-polarised exciting fields), which reads as:

$$P^{(3)}_{\mathrm{FWM}} \propto \mu^4 \mathcal{E}_1^*(\mathbf{r})\mathcal{E}_2(\mathbf{r})\mathcal{E}_3(\mathbf{r})\theta(\tau_{12})\,\theta(\tau_{13})\,\theta(t-\tau_>) \times e^{-g(t-\tau_>)}e^{-|\tau_{23}|/T_1}e^{-g^*\tau_<} \quad , \tag{1.27}$$

where $\tau_{23} = \tau_{13} - \tau_{12}$, $\tau_< = \min(\tau_{13}, \tau_{12})$, $\tau_> = \max(\tau_{13}, \tau_{12})$ and $g = i\omega_0 + 1/T_2$. The time resolved four-wave mixing (TR-FWM) field amplitude from a single TLS is therefore proportional to the fourth power of the dipole moment, it decays exponentially with a time constant T_2 both with $t - \tau_>$ and with $\tau_<$, and it is non-zero only when $\tau_{12} > 0, \tau_{13} > 0$ and $t > \tau_>$. This behaviour is sketched in the top part of Fig. 1.7, for the case $\tau_{13} > \tau_{12}$. The corresponding time integrated four-wave mixing (TI-FWM) intensity as a function of τ_{12} is also shown. Importantly, the two exponential terms in Eq. 1.27 containing the g terms are phase conjugated. At $t = \tau_> + \tau_< = \tau_{12} + \tau_{13}$, the exponential simplifies to $e^{-2\tau_</T_2 - |\tau_{23}|/T_1}$ and it is independent of ω_0. The importance of the phase conjugation becomes evident when considering an ensemble of N TLSs. The ensemble is characterised by inhomogeneous broadening σ. When $N/T_2 \gg \sigma$, we can describe the ensemble by a Gaussian distribution G of transition frequencies ω_0':

$$G(\omega_0') = \frac{1}{\sigma\sqrt{2\pi}} e^{-\frac{(\omega_0'-\omega_0)^2}{2\sigma^2}} \quad . \tag{1.28}$$

The response of the ensemble is therefore a sum over all the possible transition frequencies. The interference between signals resulting from the superposition of the N third-order polarisations is constructive only for $t = \tau_> + \tau_<$, resulting in the photon echo. In formula, for the resonant excitation case $\omega = \omega_0$:

$$\int_{-\infty}^{\infty} N P^{(3)}_{\mathrm{FWM}}(\omega_0', t) G(\omega_0') d\omega_0' = N P^{(3)}_{\mathrm{FWM}}(\omega_0, t) e^{-\frac{\sigma^2(t-\tau_<-\tau_>)^2}{2}} \quad . \tag{1.29}$$

The FWM signal is therefore an echo in real time, with the echo shape determined by the ensemble inhomogeneous broadening, as sketched in the bottom part of Fig. 1.7, for the case of $\tau_{13} > \tau_{12}$. In this case, the TI-FWM intensity as a function of τ_{12}, for delay times $\tau_{12} \gg 1/\sigma$, decays exponentially with a decay constant which is proportional to T_2 and from which the dephasing time can be extracted. Note that from the formulas given in Fig. 1.7, one can see that by analysing the TI-FWM intensity as a function of τ_{23}, one can also extract the population lifetime.

1.5 Photoluminescence

In the experiments shown in Ch. 4 and Ch. 5 we measure the PL emission from single InAs and InGaAs QDs. In PL experiments, the excitation energy is generally higher than

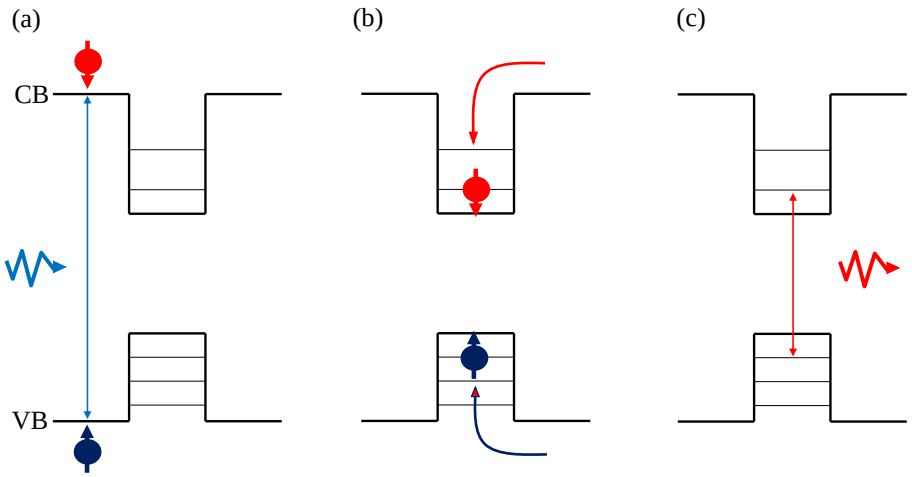

Figure 1.8: Sketch of a PL measurement. (a) Generation of free electrons and holes via above bandgap excitation; (b) carriers relaxation into the QD ground state via phonon emission; (c) recombination of bounded electron-hole pairs by emission of a photon.

the energy bandgap of GaAs. Therefore, free electrons and holes are generated in the GaAs matrix, before they relax to the QD ground state by phonon emission and then recombine. The recombination can either be radiative, where the electron-hole excitation energy is transferred to the emitted photon, or non-radiative, where the electron-hole energy is dissipated into other types of energy. A sketch of a PL measurement is shown in Fig. 1.8. The relaxation process can be quite involved, and it strongly depends on the environment surrounding the QDs and on the excitation density, by the presence of trap states and defects [74, 75]. The relaxation timescales can be similar or substantially longer than the radiative lifetimes, thus affecting measured PL decay times. In CdSe nanoplatelets, for example, the difference between the decay time measured by resonant FWM and non-resonant PL decay times is of two orders of magnitude[36].

1.6 Photonic crystal waveguides

As in this work we perform experiments with QDs embedded in PCWGs, this section is used to give an introduction to the topic.

The structure used in this work is a photonic crystal slab with a line defect. Let us first consider the case of a slab without the line defect. The 2D photonic crystal of the slab is composed of an hexagonal pattern of air holes on a layer of GaAs, distributed in the xy plane, as shown in the top inset in the left panel of Fig. 1.9. The 2D periodicity opens a photonic bandgap that prohibits light with a certain frequency to propagate in the xy plane. This is in analogy with semiconductors, where the periodicity of the Coulomb potential creates the semiconductor bandgap. The photonic band structure of the photonic crystal slab is shown in the left panel of Fig. 1.9, along the relevant directions of the hexagonal Brillouin zone (bottom inset). The mirror symmetry with respect to the $z = 0$ plane allows to classify the guided modes as transverse electric (TE)-like (electric

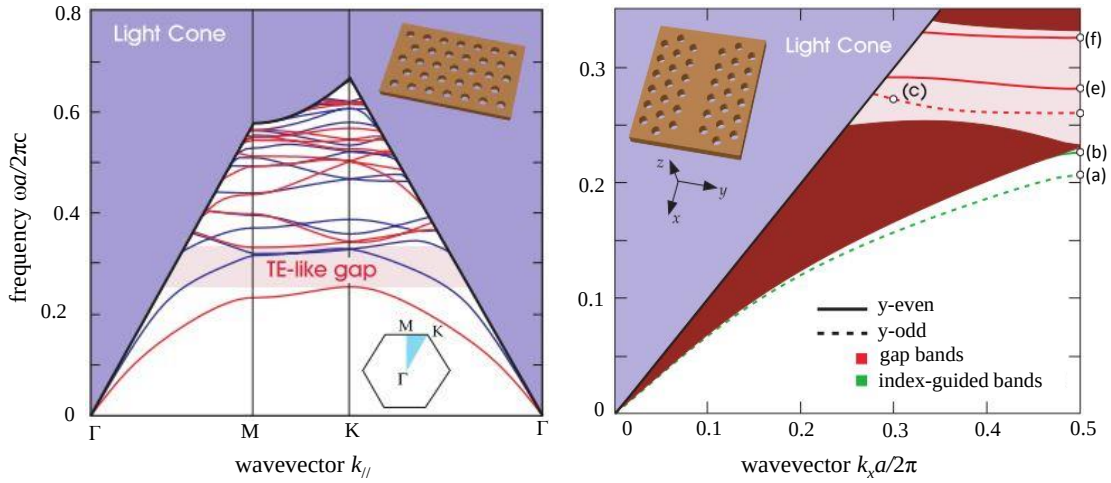

Figure 1.9: Left: band structure of a photonic crystal slab suspended in air with an hexagonal pattern of holes (top inset). Blue/red lines indicate TM/TE-like modes. The TE-like bandgap is highlighted in pink. The blue region is the light cone. The hexagonal Brillouin zone of the crystal is given in bottom inset. The triangular irreducible Brillouin zone is even shown. Right: projected band structure for TE modes of a photonic crystal slab suspended in air plus a line defect. The light cone is given in blue. The dark red region describes extended states in the crystal; y-even modes are indicated by red solid lines, y-odd by dashed lines. The bandgap is highlighted in pink. Index guided modes in all the directions are given in green. The figures are adapted from Ref. [76].

field polarised in the xy plane), and transverse magnetic (TM)-like mode (magnetic field polarised in the xy plane at $z = 0$). The non-zero field components, strictly on the plane $z = 0$, are (E_x, E_y, H_z) for TE-modes and (H_x, H_y, E_z) for TM-modes [76]. For a photonic crystal made of holes, the bandgap opens only for TE-like modes [77], as highlighted in the figure, while TM modes form a continuum of states. Due to the finite thickness of the slab, the continuous translational symmetry in the z-direction is broken. Therefore, for a given in-plane wavevector $k_{\|}$, there can be a continuous set of eigenfrequencies ω that are larger than $ck_{\|}$, as k_z can assume any real value. The line $\omega = ck_{\|}$ defines the light cone. Modes whose eigenfrequency lies above the light cone at a given $k_{\|}$ are not guided as the functional expression of the mode in the z direction is an harmonic function. This region is indicated in blue in Fig. 1.9. For eigenfrequencies below the light cone k_z is imaginary. The corresponding mode is therefore confined in the slab by index guiding, i.e., total internal reflection.

The introduction of a line defect (in this case a line of missing holes), increases the average dielectric constant of the crystal. As a consequence, modes from the upper edge of the photonic bandgap reduce their eigenfrequency and are moved into the photonic bandgap [76]. The corresponding band diagram for this structure is given in Fig. 1.9 right. Because translational symmetry is preserved only along the propagation direction x, the band structure is one dimensional and is given as a function of k_x. As it is possible to see, a series of discrete modes (red lines) lie within the bandgap. These modes are confined in the plane by the photonic bandgap, and in the out-of-plane direction by index guiding. The green lines indicate modes that are confined in all the directions by index guiding.

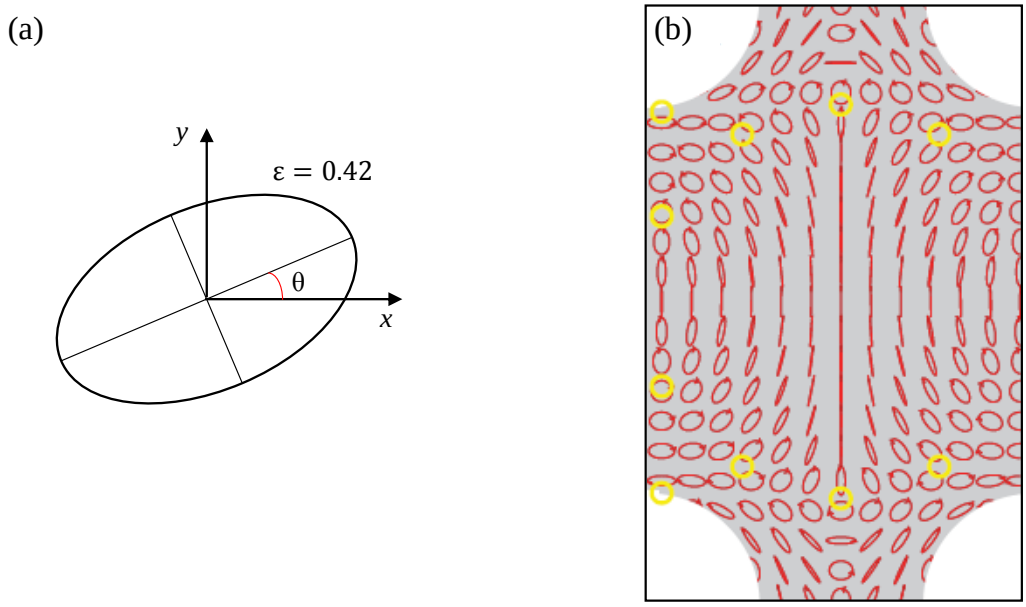

Figure 1.10: (a) A general polarisation ellipse with orientation θ and ellipticity $\varepsilon = 0.42$. According to the given reference system, x is the propagation direction and y the transverse direction. (b) Polarisation ellipses of the field polarisation at the $z = 0$ plane in a PCWG. For ellipticity $\varepsilon = 0$ the polarisation is linear (red line); for $\varepsilon = \pm 1$, the polarisation is circular (highlighted by the yellow circles, called C-points). The figure is adapted from Ref. [78].

The mirror symmetry with respect to the plane $y = 0$ (according to the reference system given in Fig. 1.9(b)), allows to classify the modes as even or odd in response to mirror operation. In particular, for an even (odd) mode E_y (E_x) $= 0$ along the x axis.

Because of the strong confinement created by the 2D photonic bandgap, the field propagates with both longitudinal and transverse components. The spatial dependence of the relative amplitude and phase of the components defines the polarisation state of the electromagnetic field at each position inside the PCWG. The field polarisation can be represented by a polarisation ellipse as shown in Fig. 1.10(a), with an orientation θ and an ellipticity ε defined as follow:

$$\begin{aligned} \theta &= \frac{1}{2}\arctan\left(\frac{S_2}{S_1}\right) \\ |\varepsilon| &= \sqrt{\frac{2}{\sqrt{S_1^2 + S_2^2} + 1} - 1} \\ \varepsilon &= |\varepsilon|\mathrm{sgn}(S_3) \quad , \end{aligned} \tag{1.30}$$

where $S_1 = (|E_x|^2 - |E_y|^2)/S_0$, $S_2 = 2\mathrm{Re}(E_x^* E_y)/S_0$ and $S_3 = 2\mathrm{Im}(E_x^* E_y)/S_0$ and $S_0 = |E_x|^2 + |E_y|^2$ are the Stokes parameters [79] and sgn is the sign function. E_x and E_y are the longitudinal and transverse field components respectively, at the plane $z = 0$, where $E_z = 0$. Throughout this work, E_x and E_y are always considered at this symmetry plane. L-points are locations where the field polarisation is linear, i.e. $|\varepsilon| = 0$, C-points are locations where the field polarisation is circular, i.e. $|\varepsilon| = 1$ (highlighted in Fig. 1.10(b) by

the yellow circles).

1.6.1 Purcell factor

The Purcell factor F_P was introduced by E. M. Purcell in 1946 [80] when studying the coupling of a two-levels atom to a cavity mode. It is defined as the maximum ratio of the spontaneous emission (SE) rate of a dipole into a cavity mode, Γ_cav, and the SE rate of the same dipole into free space, Γ_free. In formula:

$$F_\mathrm{P} = \frac{\Gamma_\mathrm{cav}}{\Gamma_\mathrm{free}} \ . \tag{1.31}$$

The Purcell factor is defined in the weak coupling regime, which is verified when the coupling rate of the emitter with the cavity mode is smaller than the rate at which photons are lost out of the cavity. Emission of photons is therefore irreversible, as in a SE process in free space, although in this case the SE rate is affected by the cavity. In the weak coupling regime, the effect of the cavity can be treated as a perturbation, and the SE rate in the cavity mode can be calculated using the Fermi's golden rule. Considering a TLS with the ground state $|g\rangle$ and the excited state $|e\rangle$, the SE rate Γ can be written as [81]:

$$\Gamma = \frac{2\pi}{\hbar} \left|\boldsymbol{\mathcal{E}}(\boldsymbol{r}_\mathrm{d}) \cdot \langle e|\hat{\mu}|g\rangle\right|^2 \rho(\hbar\omega) \ , \tag{1.32}$$

with $\boldsymbol{\mathcal{E}}(\boldsymbol{r}_\mathrm{d})$ the vacuum field at the dipole position $\boldsymbol{r}_\mathrm{d}$. For free space, it has been calculated $\Gamma_\mathrm{free} = (\mu_\mathrm{eg}^2\omega^3)/(3\pi\varepsilon_0\hbar c^3)$, with $\boldsymbol{\mu}_\mathrm{eg} = -e\boldsymbol{r}_\mathrm{eg}$ and c the speed of light [81]. In order to calculate the SE rate into the cavity, we need an expression for the cavity density of states. This is assumed to be Lorentzian, with a linewidth (full width at half maximum (FWHM)) given by γ_cav centred at the resonance frequency ω_cav, such that the cavity quality factor is $Q = \omega_\mathrm{cav}/\gamma_\mathrm{cav}$. With these definitions, the SE rate into the cavity can be written as [81]:

$$\Gamma_\mathrm{cav} = \frac{2Q\mu_\mathrm{eg}^2}{\hbar\varepsilon_0 V_0}\xi^2 \frac{\gamma_\mathrm{cav}^2}{4\left(\omega_0 - \omega_\mathrm{cav}\right)^2 + \gamma_\mathrm{cav}^2} \ , \tag{1.33}$$

with

$$\xi = \frac{|\boldsymbol{\mathcal{E}}(\boldsymbol{r}_\mathrm{d}) \cdot \boldsymbol{\mu}_\mathrm{eg}|^2}{|\boldsymbol{\mathcal{E}}(\boldsymbol{r}_\mathrm{d})|^2 |\boldsymbol{\mu}_\mathrm{eg}|^2} \tag{1.34}$$

the normalised dipole orientation factor, V_0 the cavity mode volume, ϵ the dielectric constant of the material within the cavity and ω_0 the transition frequency of the TLS. Finally, using Eq. 1.31, the Purcell factor is found to be [81, 82]:

$$F_\mathrm{P} = \frac{3}{4\pi^2}\left(\frac{\lambda}{n}\right)^3 \frac{Q}{V_0} \cdot \left|\frac{\mathcal{E}(\boldsymbol{r}_\mathrm{d})}{\mathcal{E}_\mathrm{max}}\right|^2 \cdot \xi^2 \cdot \frac{\gamma_\mathrm{cav}^2}{4\left(\omega_0 - \omega_\mathrm{cav}\right)^2 + \gamma_\mathrm{cav}^2} \ , \tag{1.35}$$

with $\mathcal{E}_\mathrm{max}$ the maximum field amplitude in the cavity, and where we substituted c/ω with $(\lambda/n)/2\pi$, with λ the wavelength in vacuum and n the refractive index of the medium inside the cavity. For a dipole on resonance with the cavity ($\omega_0 = \omega_\mathrm{cav}$), located at the

field antinode ($\mathcal{E}(\boldsymbol{r}_\mathrm{d}) = \mathcal{E}_\mathrm{max}$) and orientated along the cavity mode field polarisation ($\xi = 1$), the Purcell factor is maximum and equal to:

$$F_\mathrm{P}^\mathrm{max} = \frac{3}{4\pi^2}\left(\frac{\lambda}{n}\right)^3 \frac{Q}{V_0} \ . \tag{1.36}$$

High Purcell factors require high quality factors and small mode volumes.
The Purcell factor for a dipole confined in a PCWG can be defined similarly to the Purcell factor for a cavity, and it describes the enhancement of the SE rate of the dipole into a waveguide mode Γ_wg, with respect to its SE rate in a homogeneous medium Γ_hom. By introducing the effective mode volume per unit cell defined as $V_\mathrm{eff}^{-1} = \max\left[\epsilon_\mathrm{r}(\boldsymbol{r})|\boldsymbol{e}_{k_\omega}(\boldsymbol{r})|^2\right]$ and the function $f(\boldsymbol{r}) = \epsilon_\mathrm{r}(\boldsymbol{r})|\boldsymbol{e}_{k_\omega}(\boldsymbol{r})|^2 V_\mathrm{eff}$, the Purcell factor can be written as [6, 83, 84]:

$$F_\mathrm{p} = \frac{3}{4\pi n}\left(\frac{\lambda}{n}\right)^2 \frac{1}{V_\mathrm{eff}/a} \cdot f(\boldsymbol{r}_\mathrm{d}) \cdot |\hat{e}(\boldsymbol{r}_\mathrm{d}) \cdot \hat{\boldsymbol{n}}|^2 \cdot n_\mathrm{g}(\omega) \ , \tag{1.37}$$

with $\boldsymbol{e}_{k_\omega}(\boldsymbol{r}) = e_{k_\omega}(\boldsymbol{r})\hat{e}(\boldsymbol{r})$ the Bloch mode, polarised along $\hat{e}$, with wavevector k_ω, a the lattice constant, $n_\mathrm{g}(\omega) = c/v_\mathrm{g}(\omega)$ the group index, and $v_\mathrm{g}(\omega)$ the group velocity defined as $v_\mathrm{g} = \partial\omega/\partial k$. The Bloch mode is normalised such that $\int_\mathrm{cell} \epsilon_\mathrm{r}(\boldsymbol{r})|\boldsymbol{e}_{k_\omega}(\boldsymbol{r})|^2 \mathrm{d}\boldsymbol{r} = 1$, with the integral calculated over the unit cell. Eq. 1.37 is very similar to Eq. 1.35: the Purcell factor depends on the projection of the Bloch mode onto the dipole and on the magnitude of the field amplitude at the dipole location. One can also define a quality factor for the waveguide, as $Q = \pi a n_\mathrm{g}(\omega)/\lambda$, in order to recover Eq. 1.36. In the case of a dipole aligned along the Bloch mode and located at the field antinode ($f(\boldsymbol{r}) = 1$), Eq. 1.37 has the same expression of Eq. 1.36. Therefore, as in the case of the cavity, the Purcell factor is increased for small mode volumes and high Q factors. The mode volume can be reduced by reducing the pitch a of the PCWG. The quality factor is instead determined by the group index. As pointed out by Manga Rao and Hughes in 2007 [84], although the similarity in the final expressions, it is important to note that while the cavity is a closed system and it deals with standing waves, the waveguide is an open system, and it deals with propagating waves.

Chapter 2

Experimental methods

For the experiments shown in this work, two different setups have been used. In this chapter, both of them are explained. We start with the description of the transient FWM setup, which is also used to measure the sample extinction. We then describe the micro-spectroscopy setup, which is used to measure PL, to perform Fourier spectroscopy, and to do white light imaging.

2.1 Transient four-wave mixing spectroscopy setup

Traditionally, the detection of transient FWM relied on the directional selectivity imposed by the phase-matching condition. Such a method necessitates of beams propagating with different wavevectors, and it is not suited to study systems where co-linear propagation is needed, like waveguides. To overcome this issue, heterodyne detection has been proposed [85] and implemented [86]. Relying on the time invariance of the system, the experiment is repeated with different relative phases between the exciting beams. The resulting FWM signal is therefore modulated at a defined beating frequency, which can be detected using lock-in amplifiers. Within this context, the research group I worked with during my PhD, leaded by Prof. W. Langbein and Dr. P. Borri, played a significant role in further developing the heterodyne detection scheme [87, 88, 89]. They made use of dual-phase lock-in amplifier combined with a balanced detection scheme to measure FWM signal both in amplitude and phase [48]. In 2005, W. Langbein and B. Patton developed the heterodyne spectral interferometry technique [90, 91, 92]. This elegant and powerful spectroscopy tool has been successfully used to measure transient FWM on individual exciton [91] and the coherent non-linear response of a generic exciton-biexcion system [93], to demonstrate the coherent coupling in small sets of individual excitons [94] and to provide evidence for the quantised character of the strong light-matter coupling in a solid [95].

In order to measure three-beam transient FWM, the experimental arrangement in Fig. 2.1 is used. For a more detailed sketch and explanation of the setup, we refer the reader to the supplementary material of Ref. [36]. For a detailed explanation of the sample mounting, we refer the reader to Ref. [96]. In this subsection, we discuss the main elements

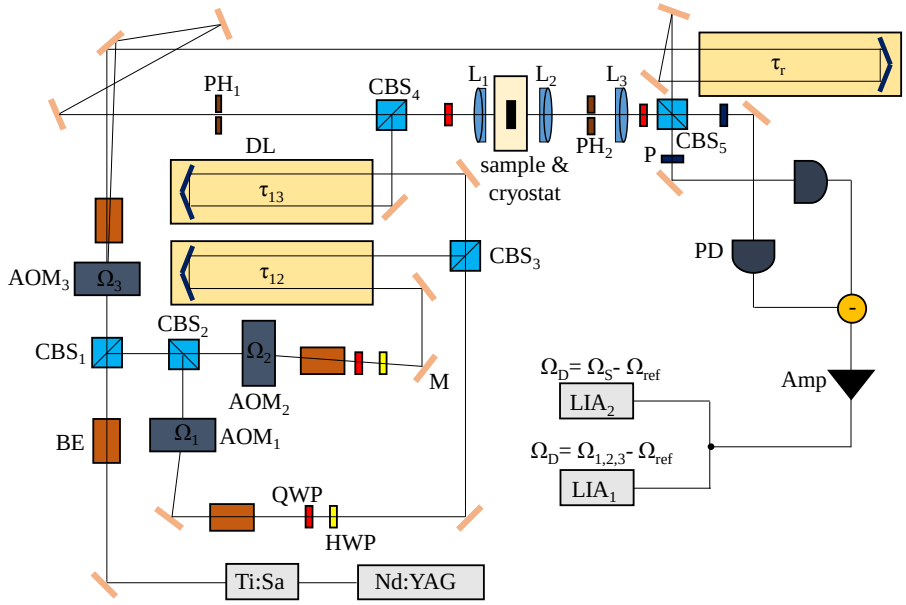

Figure 2.1: Sketch of the transient FWM setup. BE: beam expander; CBS: cube beam splitter; AOM: acousto-optic modulator; QWP: quarter waveplate; HWP: half waveplate; DL: delay line; M: mirror, PD: photodiode; Amp: amplifier, PH: pinhole; L: lens; P: polariser LIA: lock-in amplifier.

that allow the reader to understand how the FWM signal is detected.

The train of pulses is generated by a titanium-sapphire (Ti:Sa) laser pumped by an intracavity frequency doubled neodymium-doped yttrium aluminum garnet (Nd:YAG) laser pumped by a semiconductor diode laser. The pulses have an intensity FWHM of 100-120 fs, and a repetition rate of 76 MHz, corresponding to a time separation between consecutive pulses of about 13 ns. Two cube beam splitters (CBS_1 and CBS_2) are used to generate three trains of pulses, two pumps and a probe beams, which are passed through the corresponding acousto-optic modulators (AOMs). The beam expander (BE) is used to reduce the size of the input beam to match the AOM aperture. The effect of the AOM is to deflect a fraction of the input beam by Bragg diffraction, with frequency shift Ω_i and an amplitude given by the carrier frequency and the amplitude of the electrical drive respectively. The deflected beams are passed through BEs which are used to adjust the beams divergence and size, and they are called P_1, P_2 and P_3 in the following, which are pump one, pump two and the probe respectively, with the corresponding optical frequencies upshifted by Ω_1, Ω_2 and Ω_3, respectively. For the experiments performed in this work, we use $\Omega_1/2\pi = 80\,\text{MHz}$, $\Omega_2/2\pi = 79\,\text{MHz}$ and $\Omega_3/2\pi = 78.6\,\text{MHz}$. The polarisation of P_1 and P_2 is adjusted with combinations of quarter waveplate (QWP) and half waveplate (HWP). P_3 is horizontally linearly polarised after the CBS_4, and can be converted to circular polarisation by rotating the QWP in front of L_1. P_2 is delayed by τ_{12} with respect to P_1 using a delay line (DL) made of a linear stage and a retro-reflector. After recombining at the CBS_3, both P_1 and P_2 are delayed by τ_{13} with respect to P_3 using a second delay line. Pumps and probe finally recombine at CBS_4 and are then focused by the lens L_1 on the sample plane, to a spot size of about 16 µm intensity FWHM at 740 nm. The sample

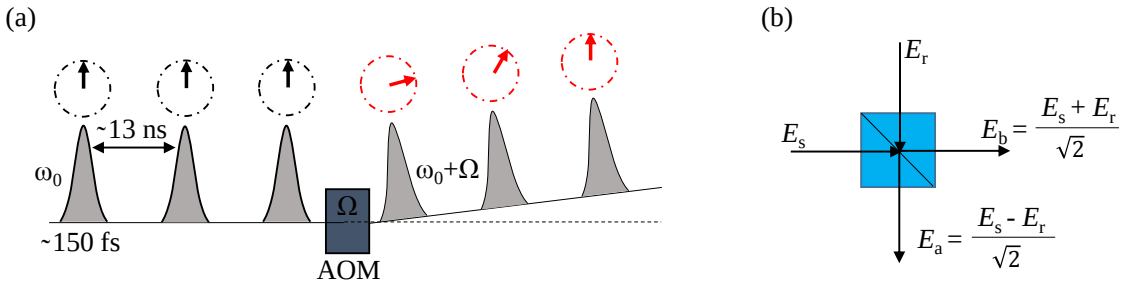

Figure 2.2: (a) Effect of the AOM on the relative phases of consecutive pulses within the same train of pulses. Image reproduced from Ref. [97]. (b) Interference of the FWM signal and the reference field at the 50:50 recombining beam splitter. Image reproduced from Ref. [98].

is mounted into a cold finger helium flow cryostat, which allows cooling down to 4 K. The transmitted field is imaged by L_2 onto the pinhole PH_2, which is used to block spurious reflections. L_3 collimates the beam, and another QWP converts the circular polarisation back to linear.

The undeflected part of P_3 is used as a reference field for the employed heterodyne detection scheme. This is delayed by τ_r with respect to the FWM signal using the corresponding delay line. The FWM and reference fields recombine and interfere at the CBS_5. The two output beams are then projected onto horizontal polarisation by polarisers (P), and detected by photodiodes (PD). In order to better understand how the detection works, we need to introduce some formalism.

A train of pulses with a repetition rate $\Omega_p = 2\pi/T_p$ and vibrating at the optical frequency ω_0 can be written as a Fourier series:

$$E(t) = \boldsymbol{\mathcal{E}}(t) + c.c, \quad \boldsymbol{\mathcal{E}}(t) = e^{-i\omega_0 t} \sum_{n\in\mathbb{Z}} A_n e^{-in\Omega_p t} \ , \tag{2.1}$$

where A_n are the Fourier coefficients describing each pulse. We now analyse the effect of the AOM, with the electrical drive frequency fixed to Ω_{AOM}, on this pulse train. Under the condition that the pulse duration is much smaller than the AOM period, or $\Delta \gg \Omega_{AOM}$ with Δ the spectral width of the envelope of $|A_n|^2$, the effect of the AOM is to change the relative phases between consecutive pulses, without affecting the phase within each pulse. This effect is schematically represented in Fig. 2.2(a). Although quite simple, this behaviour is the basic principle of the heterodyne detection of transient FWM. Because the AOMs fix the relative phases of P_1, P_2 and P_3, the excitation is modulated in time according to the temporal interference of the corresponding pulses. Therefore, as a defined phase relation in real space leads to emission of FWM signal in the phase matched direction $\boldsymbol{k}_s = \boldsymbol{k}_3 + \boldsymbol{k}_2 - \boldsymbol{k}_1$, a defined phase relation in time lead to emission of FWM signal at the beating frequency $\Omega_s = \Omega_3 + \Omega_2 - \Omega_1$. Continuing this analogy, as directional selection requires translational invariance of the system, temporal selection requires time invariance of the system, i.e., the system response does not change with time. Therefore, at the recombining beam splitter CBS_5, two trains of pulses interfere: the one of the FWM

signal which is frequency shifted by Ω_s and the one of the reference field which is not shifted and is delayed by τ_r:

$$\mathcal{E}_\mathrm{r}(t) = e^{-i\omega_0(t-\tau_\mathrm{r})} \sum_n A_n^\mathrm{r} e^{-in\Omega_\mathrm{p}(t-\tau_\mathrm{r})} \tag{2.2}$$

$$\mathcal{E}_\mathrm{s}(t) = e^{-i(\omega_0+\Omega_\mathrm{s})t} \sum_n A_n^\mathrm{s} e^{-in\Omega_\mathrm{p}t} \quad . \tag{2.3}$$

The effect of the 50:50 recombining beam splitter is shown in Fig. 2.2(b). Each photodiode generates a photo-current which is proportional to the squared of the incoming field. With the employed balanced detection scheme, we measure a photo-current I_D which is proportional to $E_\mathrm{b}^2 - E_\mathrm{a}^2$ integrated over the response time T_det of the diodes. This is given by:

$$\begin{aligned} I_\mathrm{D} \propto \int_{T_\mathrm{det}} dt \left(E_\mathrm{b}^2 - E_\mathrm{a}^2\right) \propto \int_{T_\mathrm{det}} dt E_\mathrm{r} E_\mathrm{s} = \int_{T_\mathrm{det}} \Big[\\ e^{-i(2\omega_0+\Omega_\mathrm{s})t + i\omega_0\tau_\mathrm{r}} \sum_{n,m} A_n^\mathrm{s} A_m^\mathrm{r} e^{-i(n+m)\Omega_\mathrm{p}t + im\Omega_\mathrm{p}\tau_\mathrm{r}} \\ + e^{-i\Omega_\mathrm{s}t - i\omega_0\tau_\mathrm{r}} \sum_{n,m} A_n^\mathrm{s} A_m^{*\mathrm{r}} e^{-i(n-m)\Omega_\mathrm{p}t - im\Omega_\mathrm{p}\tau_\mathrm{r}} + c.c \Big] \quad . \end{aligned} \tag{2.4}$$

As $T_\mathrm{det} \gg 2\pi/\omega_0$, terms in Eq. 2.4 oscillating at $2\omega_0$ average to zero over the detection time. On the other hand, terms oscillating at $\Omega_\mathrm{s} + (n-m)\Omega_\mathrm{p}$ can be resolved. We choose to measure the terms with $m - n = 1$ by fixing the detection frequency to $\Omega_\mathrm{D} = \Omega_\mathrm{s} - \Omega_\mathrm{p}$. The detected signal is then given by:

$$I_\mathrm{D} \propto e^{-i(\Omega_\mathrm{s}-\Omega_\mathrm{p})t} \sum_n A_n^\mathrm{s} A_{n+1}^{*\mathrm{r}} e^{-in\Omega_\mathrm{p}\tau_\mathrm{r}} \quad , \tag{2.5}$$

with the integration time T_det which is included in the proportionality constant as terms oscillating at $\Omega_\mathrm{s} - \Omega_\mathrm{p}$ are slowly varying over T_Det. Because $\Delta \gg \Omega_\mathrm{AOM}$, $A_{n+1}^{*\mathrm{r}} \approx A_n^{*\mathrm{r}}$. This means that we detect the cross-correlation $C(\tau_\mathrm{r})$ between the complex fields of the reference and the signal. We detect real and imaginary parts of $C(\tau_\mathrm{r})$ with a dual-phase lock-in amplifier, i.e., we resolve the FWM signal both in amplitude and phase. The signal to detect is selected by the detection frequency Ω_D which is used as the reference signal of the lock-in amplifier. To detect FWM, we set $\Omega_\mathrm{D}/2\pi = (\Omega_3 + \Omega_2 - \Omega_1 - \Omega_\mathrm{p})/2\pi = 1.6\,\mathrm{MHz}$. Analogously, by setting $\Omega_\mathrm{D} = \Omega_j - \Omega_\mathrm{p}$, one can detect the excitation pulses, which is important to set the zero time of the experiment. In particular, $(\Omega_1 - \Omega_\mathrm{p})/2\pi = 4\,\mathrm{MHz}$, $(\Omega_2 - \Omega_\mathrm{p})/2\pi = 3\,\mathrm{MHz}$ and $(\Omega_3 - \Omega_\mathrm{p})/2\pi = 2.6\,\mathrm{MHz}$. Care must be taken in order to suppress signals oscillating at undesired frequencies. The minimum frequency separation that we need to be able to resolve is of the order 400 kHz, set by the differences between the detection frequencies of P_2 and P_3. For this purpose, we used a 24 dB filter in the lock-in amplifier. This has a time constant τ_LI=10 ms and the frequency response function $F(\omega) = (\omega\tau_\mathrm{LI} + i)^{-4}$, which enables to suppress signals at 16 kHz frequency separation by

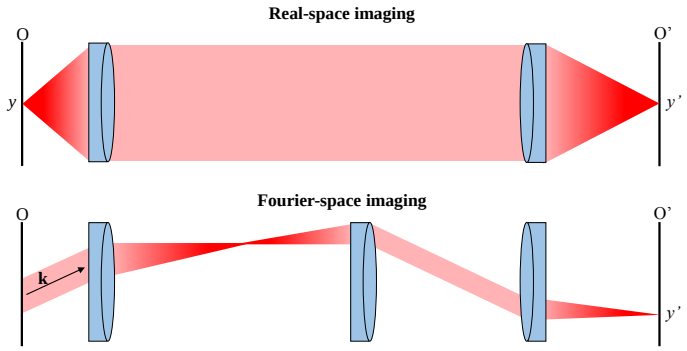

Figure 2.3: Real-space imaging: a position at the object plane corresponds to a position at the imaging plane. Fourier-space imaging: a direction at the object plane corresponds to a position at the imaging plane.

8 orders of magnitude.

2.1.1 Extinction measurements

In order to perform resonant excitation, we need to know the absorption energy of the investigated sample. The extinction of the sample is measured using white light transmission. We use a Meiji Techno FL150 Fiber Optic Illuminator with 21V 150W halogen bulb with a colour temperature of 3250 K as a white light source. This is placed in front of the 1 mm diameter pinhole PH_1 in Fig. 2.1. PH_1 is imaged on the sample plane, with a magnification of about 0.09, as determined by the distance between PH_1 and the sample plane of approximately 550 mm, and the focal length f=40 mm of L_1. In these conditions, only a region of about 90 µm is illuminated. We then adjust the cryostat and the XYZ translational stages of L_1, to illuminate only the region of interest. PH_2 is at about 150 mm from the sample plane. The sample plane is then imaged, by L_2 with f=25.4 mm, onto PH_2, with a magnification of about 4. When measuring the extinction, PH_2 is substituted with a Thorlabs step-index multi-mode optical fiber, with a numerical aperture (NA)=0.39 and a core diameter of 200 µm, connected to a spectrum analyser with an internally adjustable resolution. Using its XYZ translational stages, L_2 is adjusted in order to couple the region of interest to the fibre, which collects light transmitted by a sample region of about 50 µm. The corresponding spectrum is called I_s. In order to reference the extinction, we shift the cryostat to a region where only the substrate is present, and collect the spectra I_{ref}. The extinction A is calculated as:

$$A = -\ln\left(\frac{I_s}{I_{ref}}\right) \quad . \tag{2.6}$$

2.2 Micro-spectroscopy setup

In this section we explain the working principles of the micro-spectroscopy setup, which is used for all the experiments shown in Ch. 4 and Ch. 5. The setup is sketched in Fig. 2.4. It is formed by three imaging systems: two of them image the sample real-space, while the third one the sample directional-space, or Fourier-space. For real-space imaging, the

sample is imaged onto the input slit of a CCD-based spectrometer, and a spectral image is measured. Alternatively, the sample can be simply visualised on the real-space camera display (camera R-S in Fig. 2.4). For directional-space imaging, the sample Fourier-space is visualised on the Fourier-space camera (camera F-S in Fig. 2.4). In this section, we first describe the general imaging properties of the setup. We then dedicate subsections to describe specific experimental techniques relevant for this work.

When analysing the imaging properties of an optical setup, geometric ray optics is very useful [99]. Within this formalism, a ray of light is described by a vector $r = (y, \theta)$, where y and θ indicate the position and propagation angle with respect to the optical axis, at specific imaging planes respectively. The effect of optical elements as well as free space propagation are described by 2x2 matrices. Let us suppose that the matrix M describes the optical setup from the object plane O to the imaging plane O'. After propagation through this setup, a ray which at the plane O is characterised by the vector r, at the plane O' is characterised by the vector $r' = (y', \theta')$ according to the following relation:

$$\begin{pmatrix} y' \\ \theta' \end{pmatrix} = \begin{pmatrix} a & b \\ c & d \end{pmatrix} \begin{pmatrix} y \\ \theta \end{pmatrix} \quad . \tag{2.7}$$

If we want to create an image of the real-space at the plane O, we need to design a setup such that $b = 0$. In this case, a position at the plane O corresponds to a position at the plane O', and the corresponding magnification is given by $y'/y = a$. On the other hand, if we want to create an image of the directional-space at the plane O, we need to design the setup such that $a = 0$. In this case, $y' = b\theta$, which means that a ray direction (or k vector) at the plane O corresponds to a position at the plane O'. In general, one can go from real-space to directional-space by adding only one lens in the optical path, owing to the Fourier properties of a lens. This behaviour is schematically explained in Fig. 2.3. We now turn to describe the imaging properties of the setup shown in Fig. 2.4.

Starting from the sample plane S, the microscope objective (MO), which has a NA of 0.85, and the lens L_2, create an image of the sample real-space at the back focal plane of L_2, where a pinhole (PH) can be used to select the region of interest. At this plane, the size ratio sample to PH is -97.40. After PH, a series of lenses (L_3, L_4, L_5 and L_6) is used to image the sample real-space onto the input slit of an imaging spectrometer, with a size ratio sample to input slit of 31.85. L_6 is mounted on a XY translational stage, in order to optimise the coupling and the focus with respect to the input slit. Alternatively, when both the removable mirrors (RM_1 and RM_2) are not in place, the sample real-space can be visualised on the display of the camera R-S. The camera is always used at infinity focus, and it has an internal zoom that we use to set the magnification at the desired value. Finally, when only RM_2 is in place, the lenses L_8 and L_9 image the Fourier-space at PH (and so the sample Fourier-space) onto the camera F-S, which also has an internal adjustable zoom. Aside from general techniques, like white light and spectral imaging which are explained in the next subsections, real-space and Fourier-space imaging can

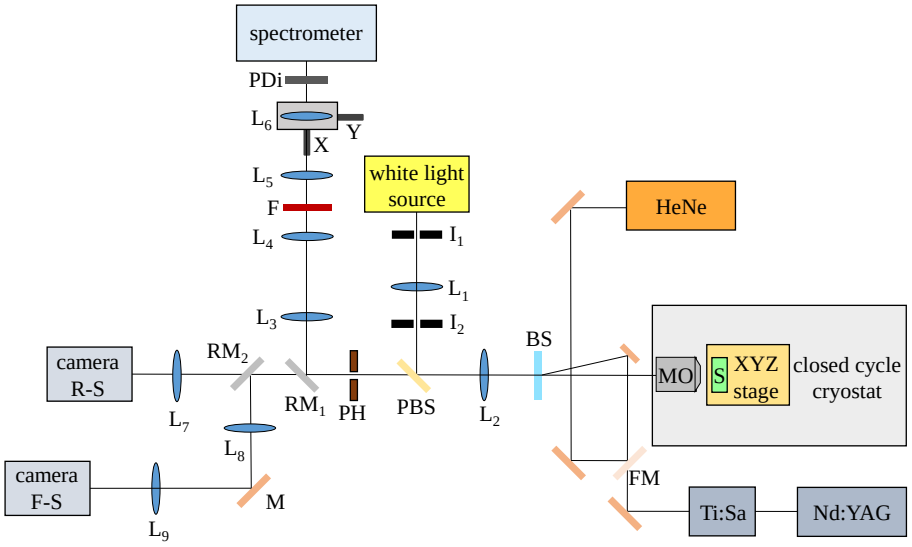

Figure 2.4: Sketch of the imaging setup. MO: microscope objective; BS: 96:4 beam splitter; PBS: pellicle beam splitter; L: lens; I: iris; PH: pinhole; M: mirror; FM: flip mirror; RM: removable mirror; PDi: polarisation displacer; R-S: real-space; F-S: Fourier-space.

be also performed using optical pulses coming from the Nd:YAG and TI:Sa laser system shown in Fig. 2.4. As in the present work this technique is specifically used to measure the dispersion of photonic crystal waveguides, it is explained in the corresponding chapter.

2.2.1 White light imaging

To perform white light imaging, the sample plane illumination is set to form a Khöler illumination setup. This configuration allows even illumination of the sample. At the same time, it assures that an image of the light source is not visible on the imaging plane. We use a Meiji Techno FL150 Fiber Optic Illuminator with 21V 150W halogen bulb with a colour temperature of 3250 K as a white light source. The source is placed on the back focal plane of the lens L_1. The distance between L_1 and L_2 is chosen such that, together with the MO, they form a system characterised by $a \approx 0$, meaning that a point from the lamp is imaged onto a direction at the sample plane. Using the iris I_1 we can control the directional range of the illumination. In order to change the field of view, a second iris I_2 is placed on the back focal plane of L_2 (which is also the Fourier-plane of L_1), such that it is imaged onto the sample plane. The white light source enters the main optical setup by a removable pellicle beam splitter PBS. The image is visualised on the R-S camera and can be recorded on a digital 8 tape and transferred to the computer.

2.2.2 Spectral imaging of photoluminescence

Spectral imaging is used to detect the PL emission from single InGaAs/GaAs and InAs/-GaAs QDs. The excitation source is a Helium-Neon (HeNe) laser, with a wavelength $\lambda = 633\,\text{nm}$. After being reflected by a series of mirrors, the excitation laser beam is sent to the MO by a 96:4 beam splitter (BS), which reflects 4 % and transmit 96 % of the

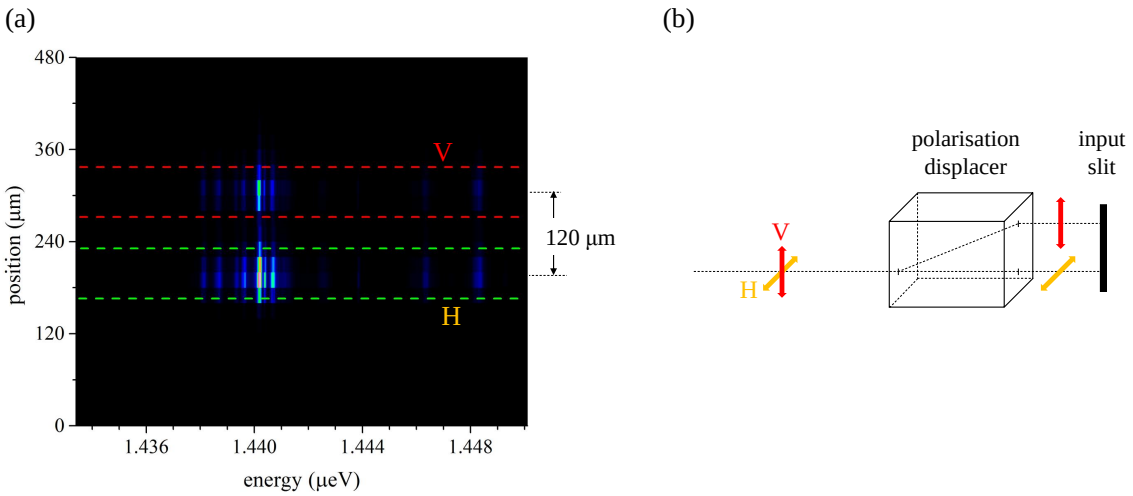

Figure 2.5: (a) An example of polarisation resolved spectral image, intensity scale in arbitrary units. The y axis covers 24 pixels of the CCD camera chip, corresponding to 480 μm.

incident light. The corresponding excitation energy of 1.9587 eV is generally much higher than the energy bandgap of GaAs near normal incidence. Therefore, electron-hole pairs are created in the GaAs matrix, before they relax to the QD ground state by phonon emission and then recombine.

In PL experiments, the sample real-space is therefore given by the SE emission of QDs. The latter is imaged onto the input slit of the imaging spectrometer, allowing to spectrally and spatially resolve the emission along the horizontal and vertical axes of the CCD camera respectively. The emission is filtered with a long-pass colour filter RG680 (F) with a cutoff wavelength of 680 nm, positioned between L_4 and L_5, which is a collimated beam path. In order to perform polarisation resolved measurements, we use a calcite polarisation displacer (PDi), with a thickness of 1 mm. The calcite crystal split the incoming beam into two, parallel-propagating, cross-polarised beams, due to the birefringence. By placing the displacer in front of the input slit of the spectrometer, we vertically displace the vertical (V) and horizontal (H) polarisation components, as sketched in Fig. 2.5(b). The polarisation components are imaged onto the input slit at different heights, and they are therefore separated along the vertical direction on the CCD camera by approximately 120 μm (i.e. 6 pixels). The corresponding polarisation resolved spectral image is shown in Fig. 2.5(a).

The spectral resolution is achieved using the imaging spectrometer sketched in Fig. 2.6(a). This spectrometer has been designed and built by Wolfgang Langbein and Stephan Schneider [100]. It has a focal length of 1.9 m, a 1200 l/mm blazed holographic grating of (120 x 140) mm^2 size and 900 nm blaze wavelength. A CCD (Roper Pixis) of 1340 x 100 square pixels of 20 μm size is used as a detector. The corresponding, nominal, resolution for the different diffraction orders is shown in Fig. 2.6(b). The resolution for the wavelength of interest has been also measured, and it is found to be consistent with the nominal one. Additionally, the wavelength calibration has been performed using reference calibration

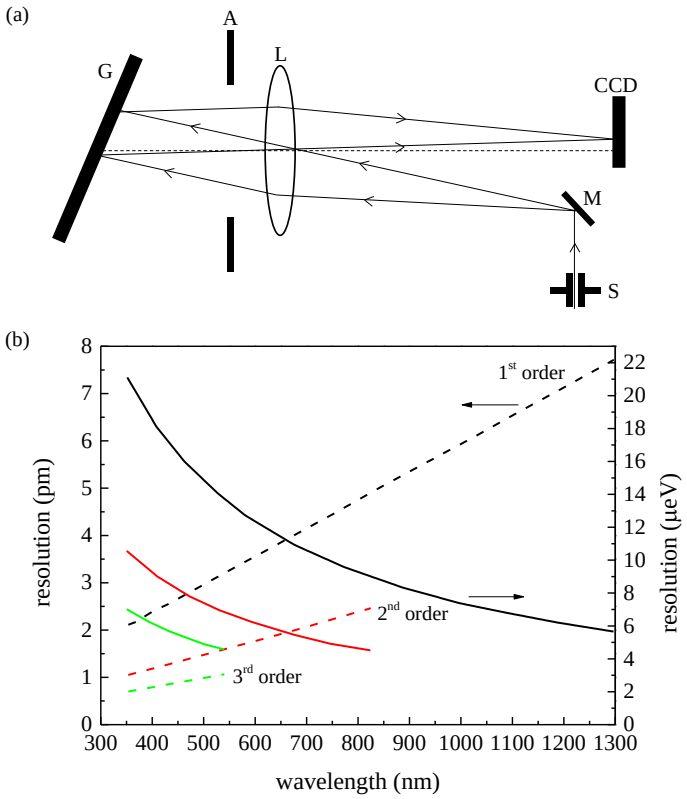

Figure 2.6: (a) Sketch of the IRIS spectrometer. G: diffraction grating; A: aperture; L: lens; S: input slit; M: mirror; CCD: charge-coupled device. (b) Spectral resolution of the spectrometer for different diffraction orders, as a function of wavelength. The image is reproduced from Ref. [100].

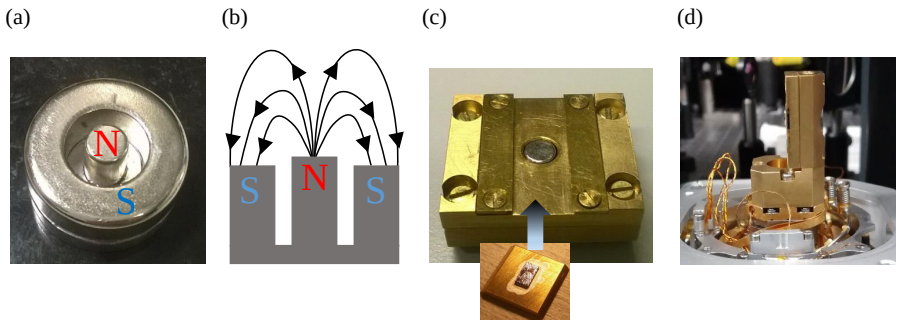

Figure 2.7: (a) Picture of the magnetic field sample holder. (b) Sketch of the magnetic field lines for the construction in (a). (c) Picture of the sample holder. The top part of the inner magnetic cylinder is visible in the centre. The sample is glued on a brass plate, which is screwed onto the sample holder. (d) The sample holder is screwed on a brass platform, which is screwed on the XYZ piezo stage of the cryostat.

lamps.

2.2.3 Sample mounting

The sample is firstly glued on a brass plate using conductive silver varnish. The plate is then fixed to the sample holder using the four internal screws in Fig. 2.7(c). A permanent magnet is placed at 0.4 mm of distance from the back surface of the sample. The magnet is

made by a neodymium cylinder mounted at the centre of a neodymium ring, with opposite polarities, as shown in Fig. 2.7(a). The corresponding magnetic field lines are sketched in Fig. 2.7(b). At the center of the cylinder, we measure, using a Gauss meter, a magnetic field of B=0.45 T, orthogonal to the plane of the sample. The sample holder is made by a front and a back brass bases. The front base is screwed to the back base using the four external screws visible in Fig. 2.7(c). Additionally, it can also rotate by few degrees around the cylinder of the magnet, allowing for fine adjustment of the sample orientation. The back base is then screwed vertically on a brass platform, which is screwed on a XYZ piezo stage (Attocube) of a low vibration closed cycle cryostat (Montana Cryostation), as shown in Fig. 2.7(d). The spatial resolution of the stage is around 0.1 mm, allowing focusing and lateral alignment with respect to the MO. The MO is mounted inside the cryostat on the cold shield, having a temperature of about 30 K when the sample is cooled down at 5 K. This avoids sample heating by thermal radiation.

Chapter 3

Four-wave mixing spectroscopy on monolayers of transition metal dichalcogenides

This chapter is dedicated to present our experiments of FWM spectroscopy on ML of TMDs, specifically on $MoSe_2$. A novel fitting routine for the density dynamics is presented, which makes use of a complex multi-exponential third-order response function of the heterodyne-detected FWM signal, including four decay processes. We provide a consistent interpretation of the dynamics within the intrinsic band structure presented in Ch. 1 and further extended in Sec. 3.5, not requiring the inclusion of extrinsic effects, like defect states or traps. Additionally, we show that exciton-exciton annihilation is not relevant in the observed dynamics, in variance from previous finding under non-resonant excitation.

3.1 Sample description

The sample investigated in this work is a ML of $MoSe_2$ transferred onto a hBN layer on a 1-mm-thick c-cut quartz substrate. This sample was fabricated by F. Wither and K.S. Novoselov from Manchester University. A reflection image is shown in Fig. 3.1, for different magnifications. Different regions are highlighted. The region of interest for FWM experiments has a size of about 50 x 70 µm, and is labelled as ML-$MoSe_2$/hBN/Quartz. The sample is covered by a second 1-mm-thick c-cut quartz substrate to provide thermal radiation screening and mechanical protection. The layer of hBN separates the substrate and the ML by a distance of the order of few tens of nanometers. The effect of charge impurities coming from the silicon dioxide (SiO_2) is therefore strongly reduced, resulting in very sharp excitonic features in PL spectra. Indeed, recently, different research groups have been interested in the studies of van der Waals heterostructure of TMDs [101]. Deterministic methods of assembly have been developed [102] and applied to assemble ML-TMDs sandwiched between two layers of hBN. The excitonic linewidth in these heterostructures

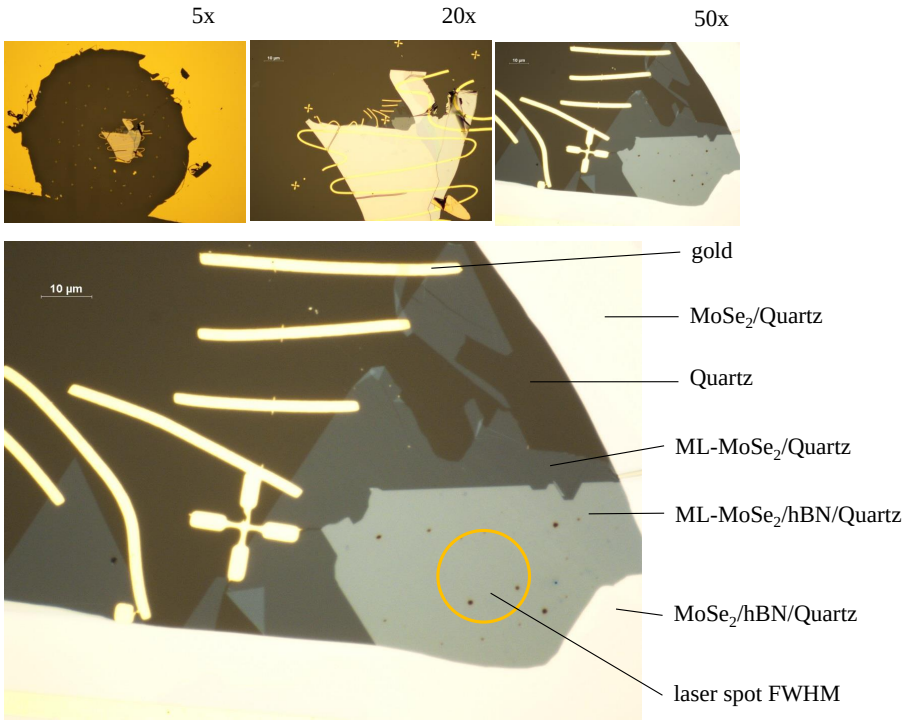

Figure 3.1: Reflection image of the sample, taken with a 0.8 numerical aperture. The different regions are labelled. Image published also in Ref. [48].

has been shown to approach the homogeneous limit [103, 104, 105], although the inhomogeneous broadening can not be fully suppressed [106].

3.1.1 Polarisation properties of the substrate

In order to perform polarisation-resolved FWM, it is crucial to characterise the polarisation response of the sample substrate, in this case c-cut quartz windows. The main reason for using quartz is because is a crystal, so it has high heat conductivity compared to glass, which is needed for low temperature measurements; secondly, it is robust, due to the complicated crystal structure, not exhibiting cleavage planes, as compared to cubic calcium fluoride (CaF_2) which easily cleaves under stress; thirdly, because it is an uniaxial material, where the optical axis is the c-axis, which corresponds to the z axis in Fig. 3.2. All the directions perpendicular to the c-axis are optically equivalent. Light whose linear polarisation lies in a plane perpendicular to the c-axis sees an ordinary refractive index n_o. On the other hand, light whose linear polarisation lies along the c-axis sees an extraordinary refractive index n_e. For the case of quartz $n_o = 1.54422$ and $n_e = 1.55332$ [107]. Therefore, quartz linear birefringence is uniaxial positive, given by $n_e - n_o = 0.0091$. A c-cut quartz window is obtained by slicing quartz along the plane perpendicular to the c-axis, as shown in Fig. 3.2(b). When linearly polarised light propagates perpendicularly to the window surface, it is not affected by linear birefringence. From this point of view, c-cut quartz windows well suit the polarisation selectivity of the optical excitation in a FWM experiment. On the other hand, it is known that quartz is a chiral medium along

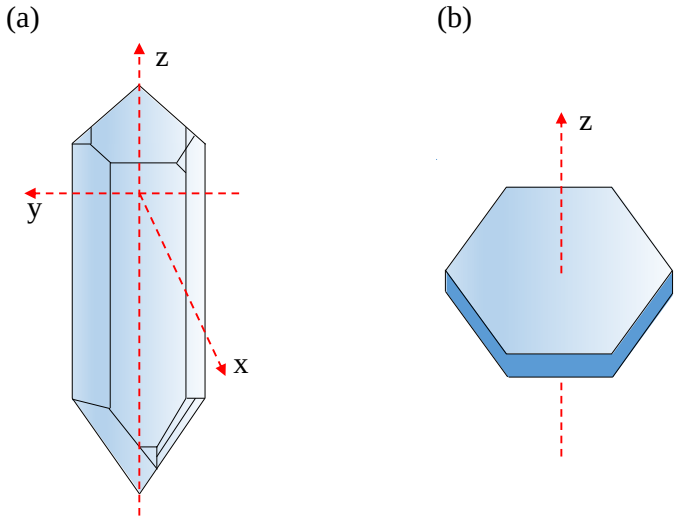

Figure 3.2: (a) Sketch of the quartz crystal structure. (b) c-cut quartz.

the c-axis. Therefore it shows circular birefringence, meaning that right-handed (σ_+) and left-handed (σ_-) polarised light propagating along the c-axis of the crystal experience different refractive indexes. After propagation through the window, the two polarisation components acquire a relative phase of

$$\phi = \frac{2\pi L}{\lambda_0}\Delta n \ , \tag{3.1}$$

where $\Delta n = n_+ - n_-$ is the difference between refractive indexes of σ_+ and σ_- light respectively, L is the thickness of the window and λ_0 is the wavelength of the light in vacuum. As a consequence, a linearly polarised plane wave propagating along the c-axis is rotated by the angle [108]

$$\psi = \frac{\pi L}{\lambda_0}\Delta n \ . \tag{3.2}$$

Circular birefringence is quantified by the optical activity coefficient ρ_{A}, which describes the rotation per unit length of the input linear polarisation. Therefore,

$$\rho_{\mathrm{A}} = \frac{\psi}{L} = \frac{\pi}{\lambda_0}(\Delta n) \ . \tag{3.3}$$

The microscopical origin of the light handedness dependence of the quartz refractive index can be understood in terms of the coupled oscillator model introduced by Chandrasekhar in the 1961. Details of the model can be found in the works [109] and [110]. To the purpose of the present discussion, it is important to report the main result of the model, that is the wavelength dependence of the optical activity. Chandrasekhar finds out the following expression for ρ_{A}:

$$\rho_{\mathrm{A}} = \frac{k\lambda^2}{(\lambda^2 - \lambda_{\mathrm{P}}^2)^2} \ , \tag{3.4}$$

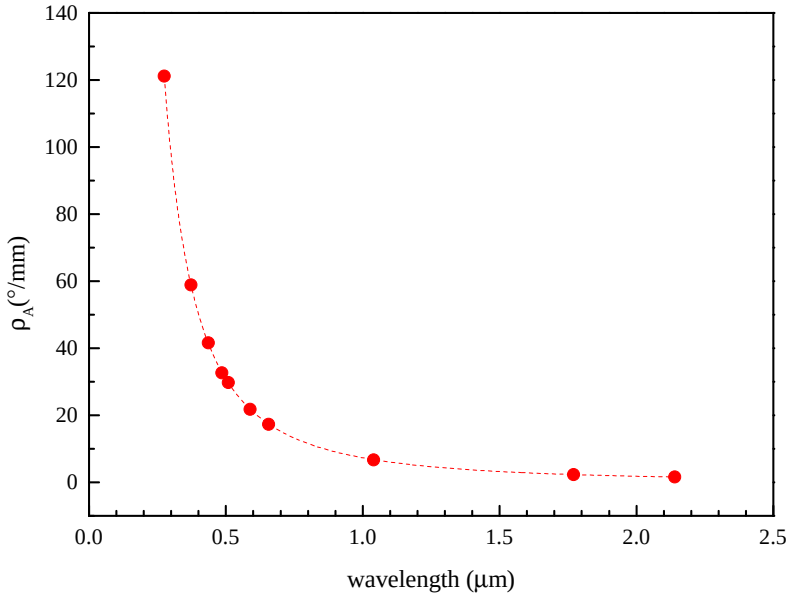

Figure 3.3: Optical activity of quartz as a function of the wavelength. The experimental points are taken from [107]; dashed line: trend described by Eq. 3.4, with $k = 7.19$ and $\lambda_P = 0.0926283\,\mu$m, as given in [110].

where k and λ_P are two parameters whose values depend by the considered crystal. For quartz it has been shown that $k = 7.19$ and $\lambda_P = 0.0926283\,\mu$m allow a good fit for a wide range of the spectrum [110]. In Fig. 3.3, experimental quartz optical activity and the fit according to equation Eq. 3.4 are shown. The k and λ_P values reported above have been used to fit. The experimental points are taken from Ref. [107].

Setup The polarisation response of the window to polarised light is measured using the setup sketched in Fig. 3.4. A collimated mode-locked laser beam, with a pulse repetition rate of 76 MHz has been used. The spectrum of each pulse is characterised by a central wavelength of $\lambda_0 = 743$ nm and a bandwidth of about 5 nm. The train of pulses is generated by a Ti:Sa laser pumped by a intracavity frequency doubled Nd:YAG laser pumped by a semiconductor diode laser. The laser beam is modulated with an optical chopper at a frequency of 70 Hz. Its polarisation is parallel to the optical table, set by the Ti:Sa crystal Brewster angle. The orientation of the linear polarizer P_1 set the plane of the input polarisation. In order to do not lose power, P_1 is chosen to be co-polarised with the laser polarisation. Circularly polarised excitation (i.e. circularly polarised light on the sample) is set by a Casix WPA1212 700-1000 nm QWP (WP_1 in Fig. 3.4). On the other hand, for linearly polarised excitation WP_1 is a Casix WPA1212 700-1000 nm HWP. The beam is focused on the quartz window sample (S) by the lens L_1, and collimated again by the lens L_2. The window is mounted on a sample holder that can be easily inserted in between L_1 and L_2. A second QWP (WP_2) is used to set the polarisation again to linear. In the case of linearly polarised excitation WP_2 is not needed. The detected polarisation is set by the polariser P_2. Finally, the beam is focused by the lens L_3 on the photodetector PD. The generated current is amplified and detected with a lock-in amplifier whose reference

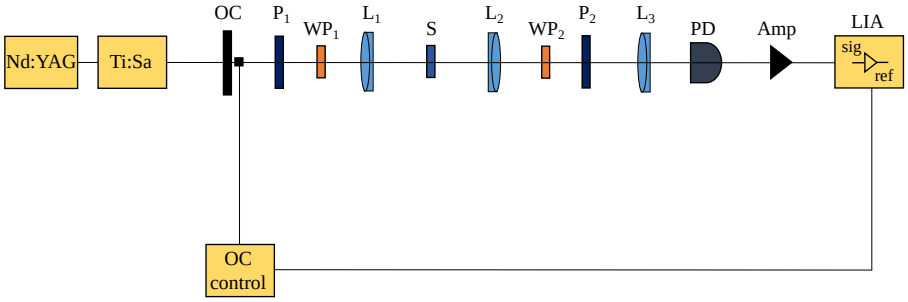

Figure 3.4: Sketch of the experimental setup used for the characterisation of c-cut quartz windows. OC: optical chopper; P: polariser; WP: waveplate; L: lens; S: quartz window sample; PD: photodiode, Amp: amplifier; LIA: lock-in amplifier.

channel is connected to the output signal of the chopper controller. The lock-in time constant has been set to 10 ms and a filter of order n=2 has been used.

Linear polarisation In order to detect quartz induced changes on the linearly polarised excitation, P_1 and P_2 are co-polarised. To co (cross)-polarise the excitation polarisation with respect to P_2, the WP_1 has been used. In this way, a maximum (minimum) signal of 91 (1.1) mV with a gain G=10^3 (10^5) is measured. The degree of polarisation suppression of such configuration is characterised by the polarisation extinction ratio (PER), defined as

$$\mathrm{PER} = 10\log\left(\frac{\mathrm{V_{co}}}{\mathrm{V_{cross}}}\right) \ , \tag{3.5}$$

where $V_{\mathrm{co(cross)}}$ is the signal measured with co-(cross-) polarised excitation with respect to P_2. Therefore, the obtained PER is about 39 dB, against 50 dB obtained by cross-polarising P_1 and P_2. When the quartz window is inserted at the sample plane S, a minimum signal of 8.3 mV is recovered by a 6° compensation with WP_1. The measurement is performed at room temperature for a quartz window with a nominal thickness of 1 mm (see Table 3.1a). Importantly, this corresponds to a rotation of the excitation polarisation of about 12°, in agreement with what expected from the plot shown in Fig. 3.3. In Table 3.1 measurements for two windows with different thickness are shown. The rotation of the excitation polarisation scales linearly with the thickness of the window, as expected.

Circular polarisation In order to detect quartz induced changes on the circularly polarised excitation, P_1 and P_2 are co-polarised. Circularly polarised excitation is set by minimising the signal using the WP_1 when neither the window and WP_2 are present. In this condition, a signal $V = 43$ mV with a gain $G = 10^3$ has been measured (see Table 3.2). To recover co(cross)-polarised linear polarisation with respect to P_2, WP_2 is used. A maximum (minimum) signal of 84 (4.9) mV with $G = 10^3$ (10^5) is measured. The corresponding PER of such configuration is 32 dB. When the quartz window is inserted at the sample plane, a minimum signal of 6.3 mV is measured, without need of compensation with WP_2. The measurements are performed at room temperature for a window with 1 mm of nominal thickness. In Table 3.2, the measurements performed with both right-handed and left-handed circular polarisation are shown.

G	θ_1 (Deg)	Quartz window A	V (mV)
10^3	271	no	91
10^5	316	no	1.1
10^5	310	yes	8.3

(a) Thickness of 1.03 ± 0.01 mm

G	θ_1 (Deg)	Quartz window B	V (mV)
10^3	268	no	86
10^5	313	no	1.1
10^5	310	yes	9

(b) Thickness of 0.54 ± 0.01 mm

Table 3.1: Measurements of the quartz induced polarisation changes on linearly polarised light. Colour legend: black (blue) indicates the signal is a maximum (minimum). Label legend: yes (no) quartz window in place (removed).

G	θ_1 (Deg)	θ_2 (Deg)	Quartz window A	V (mV)
10^3	134	no	no	43
10^3	224	314	no	84
10^5	134	224	no	4.9
10^5	134	224	yes	6.3
10^3	224	no	no	43
10^5	224	134	no	6.5
10^5	224	134	yes	7.2

Table 3.2: Measurements of the quartz induced polarisation changes on circularly polarised light, for window A. Analogous results are obtained for window B (not shown) Colour legend: black indicates the signal is a maximum, blue (red) indicates the signal is minimum for left (right)-handed circularly polarised light. Label legend: as in Table 3.1.

3.1.2 Extinction

The extinction of the sample is measured using white-light transmission, referenced to the quartz region adjacent to the investigated flake, as explained in Ch. 2. The sample was stored in vacuum at $P = -740$ mmHg, and measured 6 months after preparation ("fresh"), and 3 months afterwards, after a few thermal cycles ("aged"). The extinction of the fresh sample as a function of temperature during the first cooldown is given in Fig. 3.5(a). Already at room temperature, two spectral lines are observed. These are the exciton transitions between the lower CB and higher VB valleys, which is called A exciton (X_A), and the transition between the higher CB and lower VB, which is called B exciton (X_B). The energy separation between X_A and X_B is about 200 meV, consistent with what expected from the VB and CB energy splitting [111]. The lines shift to higher energy when the temperature is decreased, as expected from the bandgap shift [112]. At T=77 K, an additional peak below the X_A transition is observed. This peak is attributed to a trion, i.e. an electron-hole pair plus an additional carrier. Although negatively and positively

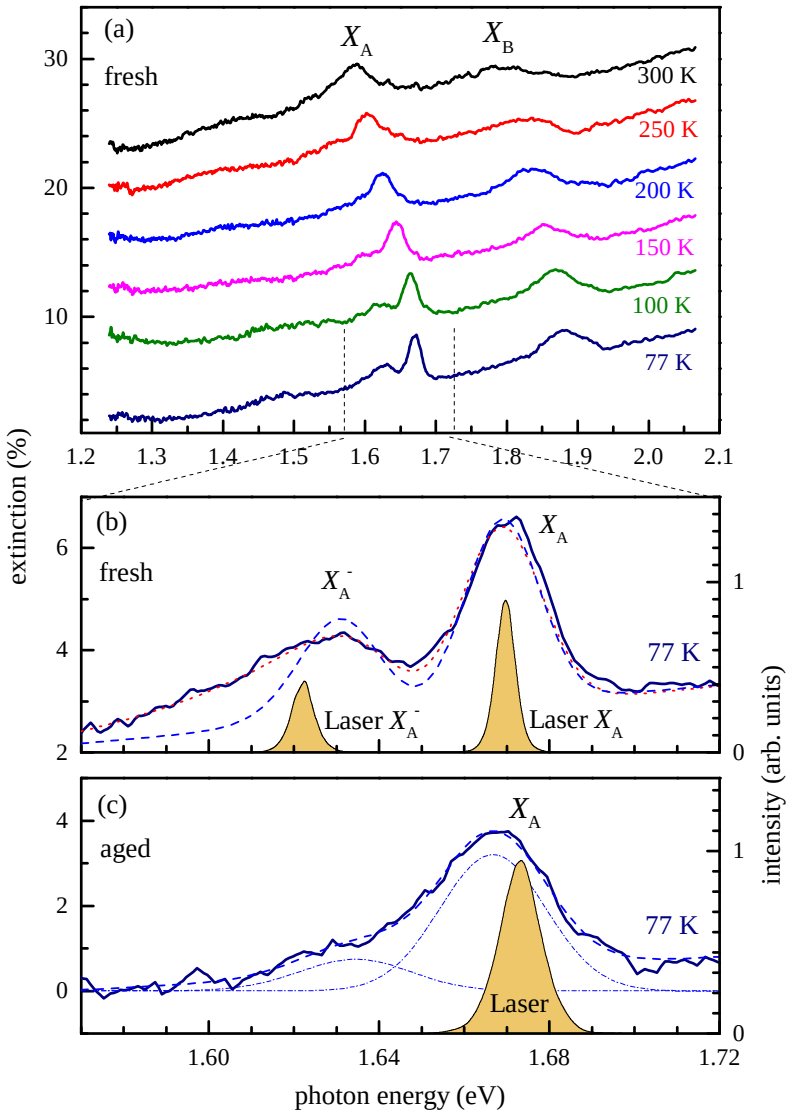

Figure 3.5: Sample optical characterisation and excitation laser spectra. (a) Extinction of the fresh sample as function of temperature, vertically offset for clarity. (b) Zoom of extinction at $T = 77\,\mathrm{K}$, together with the excitation laser spectrum used in FWM experiments. (c) as (b), but for the aged sample. Dashed lines are fits of the data (see text). Figure published also in Ref. [48].

charged trions have very similar binding energies [113], we call the trion here X_A^-, assuming a negative charge due to the additional electron. The trion absorption is possible due to the presence of electrons at the edge of the CB. An important difference between the X_A and the X_A^- is the low energy tail that is clearly observed for the trion and not for the exciton, as shown in Fig. 3.5(b). This reflects the thermal distribution of electrons in the CB, which defines the initial state of the optical transition. When a trion with energy $E_T = E_{0,T} + \hbar^2 K_T^2/2M_T$ is generated from an electron with energy $E_{\mathrm{el}} = \hbar^2 k_{\mathrm{c}}^2/2m_{\mathrm{c}}$ after absorption of a photon with energy $\hbar\omega$, energy and momentum conservation rules state

that:

$$\hbar\omega = E_{0,T} + \frac{\hbar^2 K_T^2}{2M_T} - \frac{\hbar^2 k_\mathrm{c}^2}{2m_\mathrm{c}} \tag{3.6}$$

$$\boldsymbol{k}_\mathrm{c} = \boldsymbol{K}_T \equiv \boldsymbol{Q} \ , \tag{3.7}$$

with m_c the effective mass of the electron with wavevector $\boldsymbol{k}_\mathrm{c}$, and $M_T = 2m_\mathrm{c} + m_\mathrm{v}$ the effective mass of the trion with center of mass wavevector $\boldsymbol{K}_T$ and relative motion energy $E_{0,T}$. The energy conservation rule describes the "recoil" effect of the electron, which gives part of its kinetic energy to the trion. The probability of having an electron with energy E_el as initial state of the optical transition is given, in the low density limit, by the Boltzmann distribution $f(E) = \exp(-E_\mathrm{el}/k_\mathrm{B}T)$. The corresponding trion absorption rate is given by [114]:

$$\begin{aligned} R(\hbar\omega) &= \int d\boldsymbol{Q} \exp\left(-\frac{\hbar^2 Q^2}{2m_\mathrm{c} k_\mathrm{B} T}\right) |M(\boldsymbol{Q})|^2 \times \delta\left(\hbar\omega - E_{0,T} + \frac{\hbar^2 Q^2}{2m_\mathrm{c}} \frac{M_X}{M_T}\right) \\ &\propto |M(\boldsymbol{Q})|^2 \exp\left(-\frac{\epsilon}{k_\mathrm{B}T} \frac{M_T}{M_X}\right) \Theta(\epsilon) \ , \end{aligned} \tag{3.8}$$

where $\epsilon = E_{0,T} - \hbar\omega$, Θ the Heaviside function, $M_X = M_T - m_\mathrm{c} = m_\mathrm{c} + m_\mathrm{v}$ the exciton effective mass and $M(\boldsymbol{Q})$ the optical matrix element. A similar expression is also used for PL spectra [113, 115]. In order to fit the trion lineshape, we convolve R with a Gaussian profile. Using a Gaussian assumes that the absorption lineshape is dominated by the inhomogeneous broadening, which is confirmed by the measured homogeneous broadening (see Sec. 3.2). We fit the exciton lineshape using a Gaussian profile. We use the same inhomogeneous broadening σ for exciton and trion, since the influence of the electron on the exciton wavefunction is small, as shown by the electron binding energy in the trion being an order of magnitude below the exciton binding energy. The resulting fitting function for the absorption lineshape $A(\hbar\omega)$ is given by the following expression:

$$\begin{aligned} A(x) =& C_0 + C_1 x + A_X \exp\left[-\left(\frac{x - E_X}{\sqrt{2}\sigma}\right)^2\right] + \\ &+ \frac{A_T}{2}\left[1 - \mathrm{erf}\left(\frac{x - E_{0,T}}{\sqrt{2}\sigma} + \frac{C\sigma}{\sqrt{2}k_\mathrm{B}T}\right)\right] \times \exp\left[C\frac{x - E_{0,T}}{k_\mathrm{B}T} + \left(\frac{C\sigma}{\sqrt{2}k_\mathrm{B}T}\right)^2\right] \ . \end{aligned} \tag{3.9}$$

C_0 and C_1 provide a baseline, A_X is the amplitude of the Gaussian exciton peak of position E_X, A_T is the amplitude of the trion lineshape of position $E_{0,T}$, and $C = M_T/M_X$ is the ratio between the trion effective mass and the exciton effective mass. Using the electron effective mass [39] $m_\mathrm{e}^* = 0.53\, m_0$ and the hole effective mass $m_\mathrm{h}^* = 0.65\, m_0$, we find $C \approx 1.45$. For simplicity, we have neglected the optical matrix element $M(\boldsymbol{Q})$. A fit to the extinction of the fresh sample (see blue dashed line Fig. 3.5(b)), with $C = 1.45$ shows that the resulting low energy tail of the trion is less extended than observed, for reasons that are not fully understood. We find a trion binding energy of $E_X - E_{0,T} \approx 34\,\mathrm{meV}$

and a FWHM of the exciton peak of $2.355\sigma \approx 20$ meV. Leaving C as free parameter (see red dotted curve), a good fit is obtained, yielding $C = 0.18$, a trion binding energy of 27 meV and a FWHM of 22 meV. On the other hand, a fit to the extinction of the aged sample (see blue dashed line in Fig. 3.5(c)) with $C = 1.45$ shows good agreement with the data, providing a trion binding energy of 28 meV and a FWHM of 29 meV. The retrieved trion binding energies are consistent with previous reports [62, 113, 116, 117, 118]. The aged sample shows a larger linewidth and a smaller trion contribution. This is about 25% of the exciton peak area, against 63% for the fresh sample using the fit with $C = 1.45$. The microscopic origin of the change is unknown. One could speculate that it is due to a wrinkling of the sample after thermal cycling, which creates a larger strain inhomogeneity and different dielectric environments. We exclude oxidation as possible deterioration mechanism as the sample was kept in vacuum between the two measurement sessions. An inhomogeneous distribution of strain and trion concentration was recently shown on ML-$MoSe_2$ on Si/SiO_2 substrates [62]. It is worth to note that the observation of the low energy tail in the trion absorption depends on how large is the thermal energy k_BT with respect to the line broadening. For example, the trion absorption has been studied by Sidler et al. [119] in a charge-tunable structure at $T = 4$ K. The corresponding thermal energy is $k_BT \approx 0.34$ meV, which is much smaller than the line broadening, and such a tail is not observed. In our case, we measure the trion absorption at $T = 77\,K$, and $k_BT \approx 6.6$ meV is comparable with the line broadening and thermal effects are therefore relevant.

3.2 Exciton and trion dephasing

In this section, measurements of exciton and trion dephasing are shown. The analysis of TI-FWM is detailed in the Supplementary Material of [36] and in [96].

The dephasing of X_A and X_A^- is measured by FWM, with the polarisation configuration of P_1, P_2, P_3 and detection given by $(\rightarrow, \rightarrow, \uparrow, \uparrow)$, where the four symbols, in this order, abbreviate for cross-linear polarisation of $P_{1,2}$ to P_3 and detection. The measurements are performed only on the fresh sample. The same power P has been used for the three excitation beams, therefore the power of only one beam is specified. The measured photon echo field amplitude versus τ_{12} is shown in Fig. 3.6. The echo amplitude is characterised by a rapid decay with τ_{12}. The photon echo duration, in this case, is defined by the laser pulse width. Indeed, the laser spectrum is narrower than the broadening of the transitions, as shown in Fig. 3.5(b), and, as a consequence, only a fraction of transitions frequencies is probed. As one can deduce from the formula given in Fig. 1.7, the TI-FWM field amplitude is proportional to $\exp(-2\tau_{12}/T_2)$. To extract the dephasing time T_2, we therefore use this expression to fit the data. In particular, we start the fit beyond the time range of pulse overlap $\tau_{12} > 0.5$ ps, which we determine from a measurement of the pulses cross-correlation (not shown). From the fits, shown as dashed lines in Fig. 3.6, we obtain for X_A at T=77 K a dephasing time T_2 of (386 ± 16) fs for P=100 µW and of (359 ± 3) fs

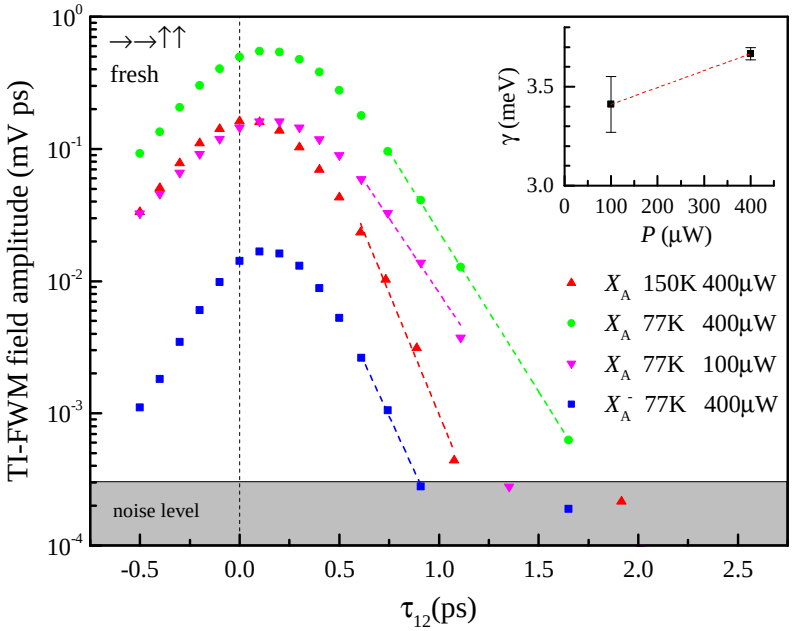

Figure 3.6: X_A and X_A^- TI-FWM field amplitude as a function of τ_{12} for different temperatures and excitation powers and τ_{23} of 1 ps and 1.2 ps respectively, measured for the fresh sample. The dashed lines are exponential fits to the data. The inset shows the extracted power dependence of the X_A homogeneous linewidth γ at $T = 77$ K. Figure published also in Ref. [48].

for P=400 µW. At 150 K and for P=400 µW we obtain a T_2 of (237 ± 18) fs. The data for 150 K is close to the limit of the time-resolution of the experiment. From T_2, we extract the homogeneous linewidth as $\gamma = 2\hbar/T_2$. In the inset of Fig. 3.6, we show γ as a function of the excitation power, for the X_A and at T=77 K. The exciton dephasing in ML-$MoSe_2$ is affected by radiative decay, and scattering by phonons and charge carriers. Although the power dependence is weak, the increasing of the homogeneous linewidth with increasing of the excitation power is expected. At larger power, the density of optically excited carriers is higher, and the probability of scattering events with charge carriers increases, leading, in average, to a faster dephasing time. By fitting the power dependence using $\gamma = \gamma_0 + \gamma_P P$, we extrapolate a zero-density homogeneous linewidth γ_0 of 3.3 meV and $\gamma_P \approx 1$ meV/mW.

The trion absorption found in Sec. 3.1.2 shows the presence of charge carriers, which create an additional dephasing and relaxation channel for excitons. In Ref. [120], the temperature dependent linewidth (FWHM) of the X_A resonance in reflection was fitted with

$$\gamma(T) = \gamma_0 + \frac{A}{e^{E_A/k_B T} - 1} \quad , \tag{3.10}$$

using $A = 72$ meV and $E_A = 30$ meV. This width includes homogeneous and inhomogeneous broadening. The phonon activated term, representing a homogeneous broadening, amounts to 33 meV at $T = 300$ K, 7.8 meV at $T = 150$ K, and 0.79 meV at $T = 77$ K. In Ref. [62] an additional linear term of 0.03 meV/K was found, and a homogeneous broadening of about 3.5 meV at 77 K, which is consistent with our finding.

The trion X_A^- shows a faster dephasing than X_A, with $T_2 = (266 \pm 13)$ fs at $T = 77$ K,

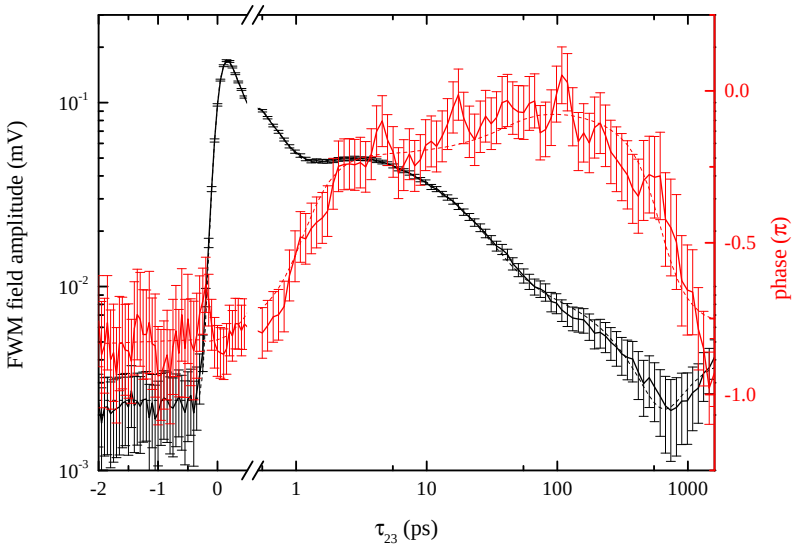

Figure 3.7: Example of FMW signal in amplitude and phase as function of τ_{23}. The dashed line are the result of the complex fit.

corresponding to a homogeneous broadening of (5.0 ± 0.3) meV. This is attributed to the additional carrier, the charged character, and the lower binding energy, increasing the scattering rate.

3.3 Complex fit of the density dynamics

In this section, details on the fitting model applied to quantitatively analyse density dynamics data measured by FWM spectroscopy is presented. This model is a significant improvement of the previously applied fitting routine, which was considering only the FWM field amplitude, assuming the phase to be constant during the dynamics. The author has applied, successfully, the new fit on ML-$MoSe_2$ [48], ML-molybdenum disulfide (MoS_2) [106], an also on cesium lead halide perovskite nanocrystals [121]. In the following, we first present the fitting model, together with some technical details. We then dedicate a final subsection to highlight the implications of the model.

3.3.1 The model

In this section, we describe in details the FWM response function, and the corresponding fitting function, we use to model density dynamics data. We first recall that the lock-in amplifier measures the real part X and the imaginary part Y of the FWM field. The FWM field amplitude is calculated as $R_s = \sqrt{(X - X_0)^2 + (Y - Y_0)^2}$ and FWM field phase as $\psi_s = \text{atan2}((Y - Y_0), (X - X_0))$, where X_0 and Y_0 describe the lock-in offset. An example of FWM data both in amplitude and phase is shown in Fig. 3.7, together with the fit and the error bars. To quantitatively analyse the data, we use a fit with the complex

multi-exponential response function

$$R(\tau) \propto A_{\mathrm{nr}} e^{i\varphi_{\mathrm{nr}}} \delta(\tau) + \sum_n A_n \theta(\tau) \exp\left(i\varphi_n - \frac{\tau}{\tau_n}\right) \quad , \tag{3.11}$$

where A_n, φ_n, and τ_n are amplitude, phase, and decay time of the n-th decay process and A_{nr} is a non-resonant instantaneous component such as Kerr effect or two-photon absorption. Eq. 3.11 describes the FWM complex field as a coherent superposition of exponentially decaying components. The measured phase contains an additional slow drift, which is caused by temperature drift of the setup, changing the relative phase of reference and probe pulses over the time t of the measurement of a few minutes. This phase drift has been modelled in the fitting procedure in a prefactor $\exp(i(\varphi_0 + \varphi_0' t))$ using a linear time dependence. The response is convoluted with a periodic Gaussian to reflect the excitation pulses of FWHM $2\sqrt{\ln 2}\tau_0$ in amplitude, and repetition period T_{r}, yielding the fit function

$$\begin{aligned} F(t,\tau) = \exp(i(\varphi_0 + \varphi_0' t)) \Bigg\{ & A_{\mathrm{nr}} \exp\left(i\varphi_{\mathrm{nr}} - \frac{\tau^2}{\tau_0^2}\right) \\ & + \sum_n A_n \left[\frac{1}{e^{\frac{T_{\mathrm{r}}}{\tau_n}} - 1} + \frac{1}{2}\left(1 + \mathrm{erf}\left(\frac{\tau}{\tau_0} - \frac{\tau_0}{2\tau_n}\right)\right)\right] \\ & \times \exp\left(i\varphi_n + \frac{\tau_0^2}{4\tau_n^2} - \frac{\tau}{\tau_n}\right)\Bigg\} \quad , \end{aligned} \tag{3.12}$$

which includes the pile-up of signal due to the finite T_{r}. The pile-up term takes into account the signal from previous pulses. The signal just before the arrival of the next pulse sequence is proportional to $e^{-T_{\mathrm{r}}/\tau_n}$. As each data point is an average over many pulse sequences responses, the contribution before the j_{th} pulse sequence is proportional to $(e^{-T_{\mathrm{r}}/\tau_n})^{j-1}$. By summing the responses of an infinite number of pulse sequences, a geometric series is obtained, which explains the pile-up term given in Eq. 3.12. We note that at the arrival of the first pulses sequence, the pile-up signal is not present. Therefore the summation is performed starting from j=2. Only the longer timescales give a measurable pile-up, while the shortest ones give a negligible contribution.

3.3.2 Measurement time

As explained in the previous subsection, the fit requires a calculation of the time of the measurement which corresponds to each value of τ_{23}. First the velocity v of the delay stage has been determined by measuring the time it takes to move of a τ_{23} interval $\Delta\tau_{23}$. A $v = 0.03$ s/$\Delta\tau_{23}$ has been estimated, as shown in Fig. 3.8(a). Then we take into account the acquisition time of each data point. The acquisition time can be written as the number of reads N for each data point times the sum of the reading time (t_{Read}=0.09 s) and time waited after every read (t_{WAR}=0.3 s). If one defines the i_{th} time step in unit of τ_{23} as $S_i = \tau_{23}[i] - \tau_{23}[i-1]$, then the real time of the measurement t_i which corresponds to $\tau_{23}[i]$

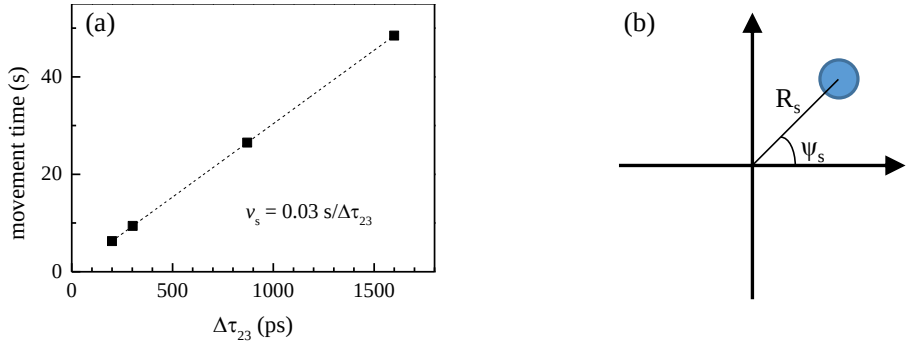

Figure 3.8: (a) Stage movement time t as a function of $\Delta\tau_{23}$, with $\Delta\tau_{23} = 0$ at $\tau_{23} = 0\,\mathrm{ps}$. A velocity of $0.03\,\mathrm{s}/\Delta\tau_{23}$ is measured. (b) Sketch of the complex FWM signal with the uncertainty circle.

can be written as:

$$t_i = t_{i-1} + S_i * v + N(t_{\mathrm{WAR}} + t_{\mathrm{Read}}) + t_{\mathrm{WAM}} \ , \tag{3.13}$$

where t_{WAM}=0.5 s describes the time waited after the movement of the delay stage in order to stabilise the vibration after stopping the motion.

3.3.3 Errors for weighted fit

In the plot of Fig. 3.7, error bars for both amplitude and phase are shown. These errors are used to perform a weighted fit. The errors on the amplitude ΔR_{s} are given by

$$\Delta R_{\mathrm{s}} = \sqrt{\sigma_{\mathrm{sn}}^2 + (\kappa R_s)^2} \ , \tag{3.14}$$

where σ_{sn} describes the shot noise, which is has been measured to be of about 1-3 µeV. The second term is due to laser intensity fluctuations. For all the fits shown in this work, the factor κ assumes values between 1% and 5%. On the other hand, the error on the phase $\Delta\psi_{\mathrm{s}}$ is given by

$$\Delta\psi_{\mathrm{s}} = \sqrt{\left(\frac{\Delta R_{\mathrm{s}}}{\sqrt{R_s^2 + \sigma_{sn}^2}}\right)^2 + \psi_{\mathrm{dr}}^2} \ , \tag{3.15}$$

where ψ_{dr} describes classical phase fluctuations (i.e. phase drift), and it is of the order of $0.05\,\pi$. The idea behind these expressions is that the an error on the amplitude ΔR_{s} produces an uncertainty on the phase $\Delta\psi_{\mathrm{s}} = \Delta R_{\mathrm{s}}/R_{\mathrm{s}}$, defining, unless than shot noise and phase drift terms, an uncertainty circle in the complex plane, as shown in Fig. 3.8(b).

3.3.4 Discussion of the model

It is important at this point to specify the connection between the technique of heterodyne detection of FWM, described in Ch. 2, and the fitting model explained above.

First of all, we recall that the interference between P_1 and P_2 generates a density

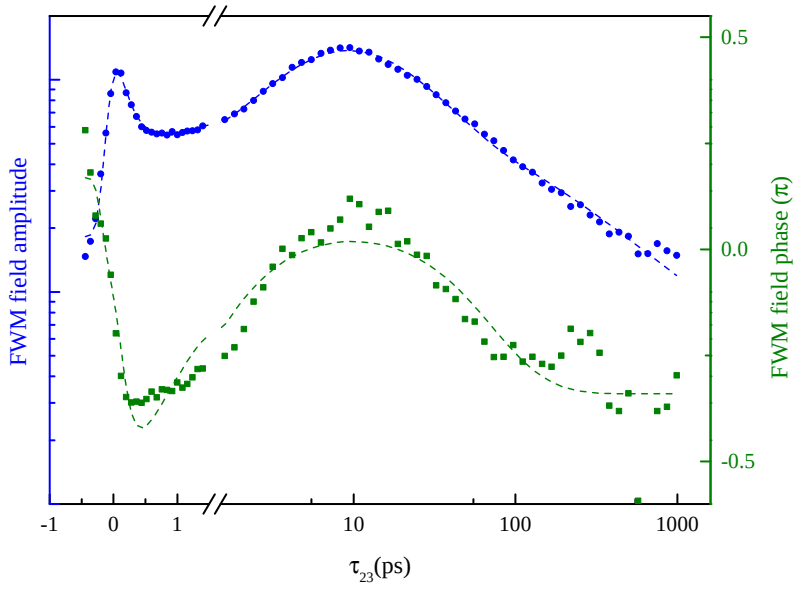

Figure 3.9: Example of FWM field amplitude and phase as a function of τ_{23}, measured on MoS_2. The image is adapted from Ref. [106].

modulation frequency of $(\Omega_1 - \Omega_2)/(2\pi) = 1\,\mathrm{MHz}$, which provides a single pole high-pass filter for the response, with a cut-off at lifetimes of $1/(\Omega_1 - \Omega_2) \sim 160\,\mathrm{ns}$, which is larger than the repetition period of the laser T_r=13 ns. This means that variations of population density which occur on timescales comparable or longer than the modulation period are suppressed in the signal. The probe pulse, delayed by τ_{23}, generates the FWM signal, which probes the density dynamics by inferring the amplitude and the phase of the resulting modulation of the excitonic response, which are responsible for absorption dynamics and refractive index dynamics, respectively. In the first case, the amplitude of the third-order polarisation $P^{(3)}$ is proportional to the excitonic density of optically bright states at the time of the probe arrival. In the second case, the transition energy E of optically bright states is modified by the renormalisation $E \to E + \delta$, caused by their interaction, like static dipole-dipole or exchange interaction, with other states, modifying the phase of $P^{(3)}$. The scenario is similar to the biexcitonic coupling demonstrated by Kasprzak et al. [94], where the presence of an exciton changes the transition energy of a spatially closed exciton. Therefore, using a complex fit takes into account the different phases of the decay components, given by the relative effect on absorption and refractive index explained above. The resulting interference between different components is responsible for an unusual dynamic, which could generate signal rise as the one shown in Fig. 3.9. In this case, the fit, performed by the author, contains also a power law term which is not included in Eq. 3.12. For details we refer to Ref. [106].

Heterodyne detected FWM is therefore directly sensitive to population of dark states, through their interaction with optically bright states. This is a significant advantage with respect to PL experiments, which are indirectly sensitive to dark states, through the use of sophisticated models.

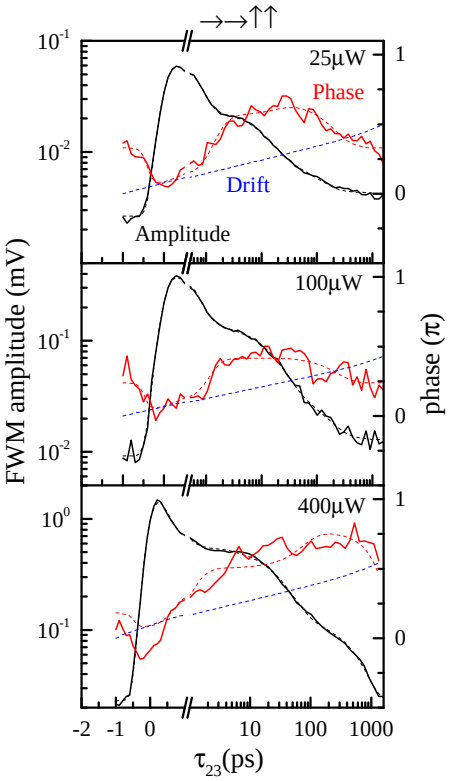

Figure 3.10: Density dynamics of the fresh sample. FWM field amplitude (black solid line) and phase (red solid line) as function of the delay τ_{23} for different excitation powers P as given and cross-linear polarisation configuration $(\rightarrow, \rightarrow, \uparrow, \uparrow)$. The dashed lines are fits to the data. The fitted phase drift (blue dashed line) has been subtracted from the data. Excitation resonant to X_A at T=77 K. Figure published also in Ref. [48].

3.4 Exciton density dynamics

In this section, data of exciton density dynamics are shown, for different excitation powers and temperatures. All the data are fitted with the model presented in Sec. 3.3, using four components $n = 1..4$. We fix the phase of the fastest component to $\varphi_1 = 0$ so that the phases of the other components represent the relative phases to the first component. We note that an absolute phase is present in the phase drift factor, such that setting $\varphi_1 = 0$ is removing this degeneracy of parameters. The fit parameters are summarised and then interpreted in Sec. 3.5.

3.4.1 Density dependence

In Fig. 3.10 density dynamics measurements at 77 K for different excitation powers are shown for the fresh sample, using the polarisation configuration $(\rightarrow, \rightarrow, \uparrow, \uparrow)$. The resulting fits are also shown. The measurements, see for example P=100 μW in Fig. 3.11, show a characteristic change of the phase versus time: the phase at negative delays is similar to the phase of the resonantly generated signal after pulse overlap, at $\tau_{23} > 100$ fs. This component decays in the first picoseconds after which a phase change of about $\pi/2$ is

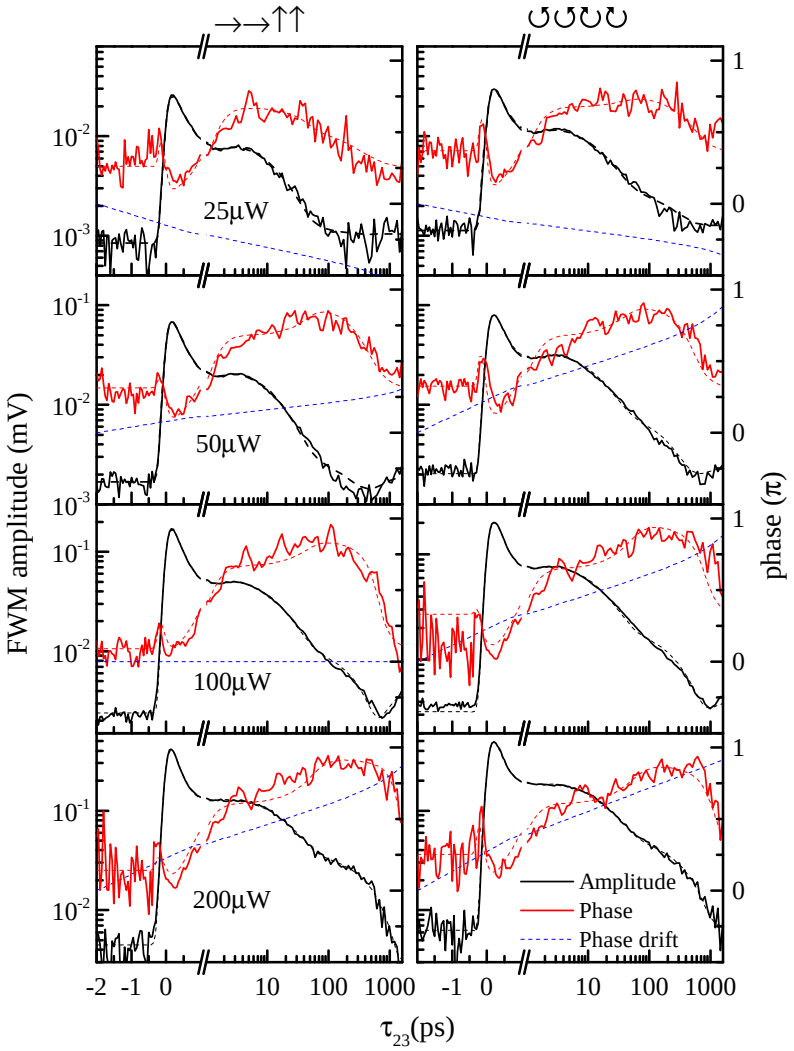

Figure 3.11: As Fig. 3.10, but for the aged sample and two polarisation configurations, cross-linear $(\rightarrow,\rightarrow,\uparrow,\uparrow)$ and cross-circular $(\circlearrowleft\circlearrowleft\circlearrowright\circlearrowright)$. Figure published also in Ref. [48].

observed together with a slower dynamics. After around 20 ps a second, a somewhat smaller phase shift is seen, and later, around 1 ns, the phase starts to shift back to its initial value. The phase data are corrected for the fitted phase drift, which is also shown in Fig. 3.10, in blue dashed lines. In Fig. 3.11, data for the old sample are shown in a similar way, for both polarisation configurations $(\rightarrow,\rightarrow,\uparrow,\uparrow)$ and $(\circlearrowleft\circlearrowleft\circlearrowright\circlearrowright)$. All the fit parameters, which include decay times τ_n, amplitudes A_n and phases φ_n, are summarised in Fig. 3.12. The amplitudes are shown normalised to the scaling $P^{3/2}$ expected for a $\chi^{(3)}$ process. The fastest component with $\tau_1 \sim 0.6$ ps represents the dominating amplitude A_1, about 5 times larger $(A_1/A_2 \sim 5)$ than the second component with $\tau_2 \sim 20$ ps and a phase of $\varphi_2 \sim \pi/2$. The next component with $\tau_3 \sim 400$ ps has an amplitude A_3 which is again about 4 times lower than A_2, $(A_2/A_3 \sim 4)$, and a phase of $\varphi_3 \sim \pi$, i.e. it is out of phase to the first component. The fourth component with $\tau_4 \sim 20..100$ ns has an amplitude which is about 10 times lower than A_3, $(A_3/A_4 \sim 10)$. It is longer than T_r, and

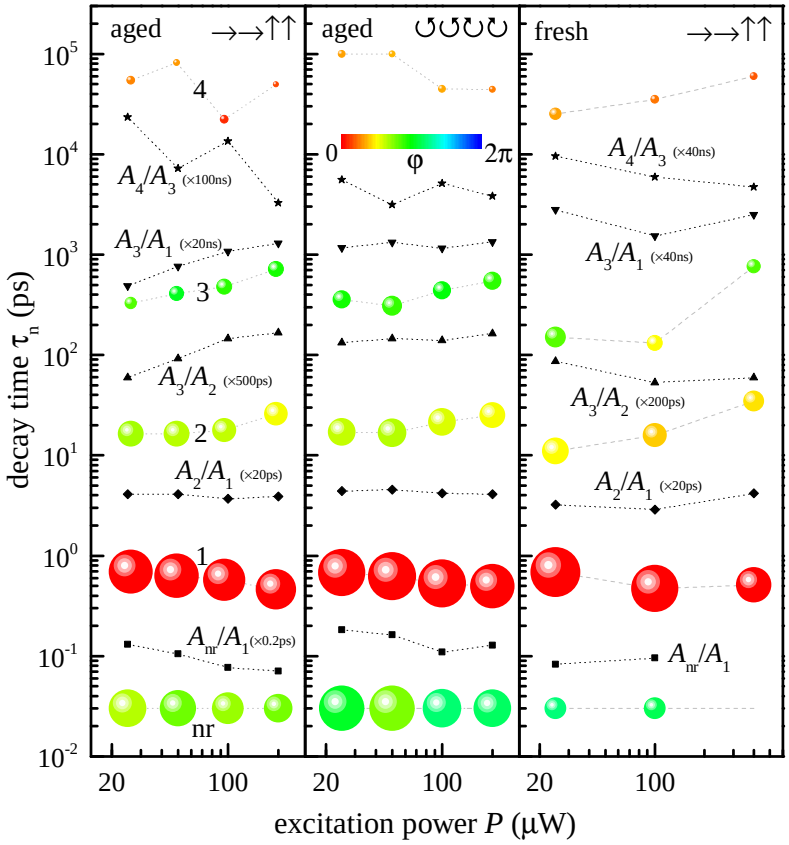

Figure 3.12: Results of the fit of Eq. 3.12 to the data shown in Fig. 3.10 and Fig. 3.11. The amplitudes A_n, normalized to the third-order scaling $P^{3/2}$ with the excitation power, are given by the volume of the symbol (diameter proportional to $A_n^{1/3}P^{-1/2}$, and for absolute scaling $A_1 = 40\,\mu$V at $P = 25\,\mu$W for the aged $(\rightarrow, \rightarrow, \uparrow, \uparrow)$ sample, and 108 μV for the fresh sample). The phases φ_n are given by the symbol colour according to the colour map. A_{nr} is shown at a decay time of 30 fs. Selected amplitude ratios, scaled as labelled, are given as symbols. Dotted lines are guides for the eye. Figure published also in Ref. [48].

it is therefore responsible for the signal at negative delay due to a pile-up term. It has a phase $\varphi_4 \sim 0..\pi/4$, i.e. similar to the initial component. We observe a weak dependence of the dynamics on the excitation power. With P increasing over an order of magnitude, τ_1 is decreasing by a few 10%, and τ_2 and τ_3 are increasing by about a factor of 2. The dominant amplitude A_1 is scaling as expected for a third-order process, as seen by the near constant symbol size versus P, apart from the highest powers used. The ratio A_2/A_1 does not change with P, but the ratio A_3/A_2 is increasing by a factor of 2 for the cross-linear aged case, near constant for the cross-circular aged case and slightly decreasing for the cross-linear fresh case. For the longest component, the values of τ_4 and A_4 are partially correlated since the signal measured at negative delay is given by a combination of both, and at the maximum positive delay of 1.6 ns a part of component 3 still is remaining.

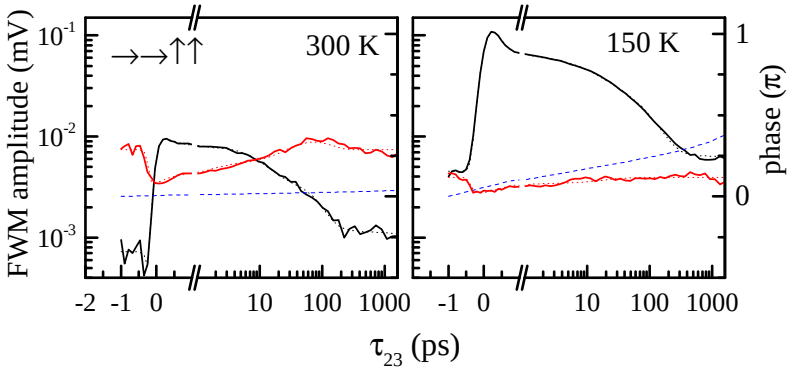

Figure 3.13: Density dynamics of the fresh sample for different temperatures as indicated. FWM field amplitude and phase as function of the delay τ_{23} for $P = 100\,\mu$W, cross-linear ($\rightarrow\rightarrow\uparrow\uparrow$) polarisation configuration, and excitation resonant to X_A. Figure published also in Ref. [48].

3.4.2 Temperature dependence

To investigate the influence of phonon-scattering and thermal distribution across states, we measure the density dynamics for different temperatures. Additionally to the $T = 77\,$K data shown in Fig. 3.10, for which the thermal energy k_BT is about 6.6 meV, we show data for 150 K and 300 K, corresponding to k_BT of 13 meV and 26 meV, respectively. A power $P = 100\,\mu$W was used, allowing for sufficient dynamic range while limiting the density induced effects. The resulting dynamics is given in Fig. 3.13. The excitation pulse center wavelength was tuned to match the X_A for each temperature, in order to compensate the temperature dependence of the energy bandgap, according to the results shown in Fig. 3.5. We find that with increasing temperature, the main effect is a reduction of the decay in the first picosecond, while the subsequent dynamics is changing in a more subtle way. The results of a fit of the data with the multi-exponential decay model are given in Fig. 3.14. We see the reduction of A_1 with increasing temperature as expected, and also an acceleration of the third component from $\tau_3 \sim 130\,$ps at 77 K to 55 ps at 300 K.

3.5 Interpretation of the exciton density dynamics

In order to interpret the exciton dynamics data, we need to extend further the discussion presented in Sec. 1.3.2 about excitons confined in 2D systems. In the next, this extension is presented in two steps: first we describe effects which are inherited from QW excitons, then we describe properties, in particular dark states, which are specific for the peculiar band structure of ML-$MoSe_2$.

3.5.1 Analogies with quantum well excitons

3.5.1.1 Effect of disorder

In Sec. 1.2, the basic electronic properties of TMD materials are shown. Additionally, excitons confined in ML-$MoSe_2$ are 2D, and they are characterised by the parabolic exciton

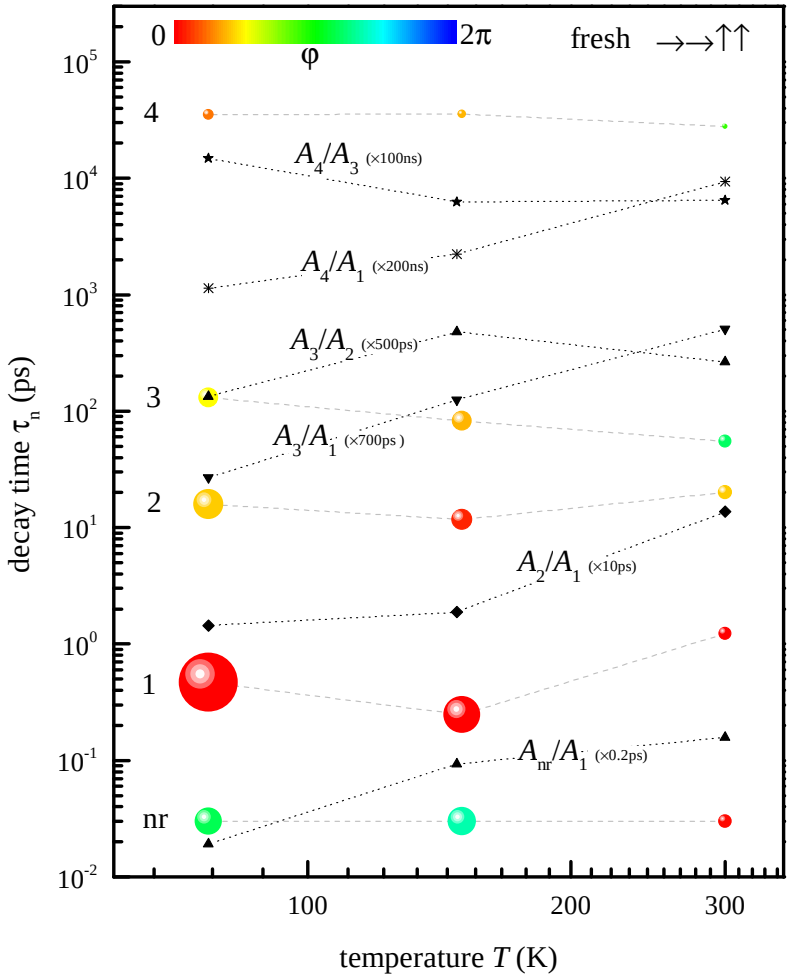

Figure 3.14: As Fig. 3.12, but for the fresh sample only, as function of temperature for $P = 100\,\mu$W and cross-linear ($\rightarrow\rightarrow\uparrow\uparrow$) polarisation configuration. Figure published also in Ref. [48].

center of mass dispersion shown in Fig. 1.6. In that section, we consider excitons as eigenstates of $\boldsymbol{K}_{\parallel}$, meaning that the exciton wavefunction has an infinite in-plane extension. This picture is altered when disorder is included, as exciton eigenstates have a finite width in $\boldsymbol{K}_{\parallel}$ [122]. In real-space, the weaker is the disorder, the larger is the exciton coherence volume. In k-space this means that the exciton eigenstates are more confined within the light cone, increasing their oscillator strength (it is important to note the large variety of different exciton wavefunctions, which leads to a statistical distribution of oscillator strength [123]). Viceversa, the stronger is the disorder, the more the exciton wavefunction extends outside the light cone, resulting in a longer radiative lifetime τ_r [122]. In radiatively limited systems, such a correlation between disorder and τ_r is also reflected in a correlation between disorder and dephasing time, with the latter which increases when the former increases. These correlations have been clearly demonstrated using FWM spectroscopy, both in W-based [124] and Mo-based [106] ML-TMDs.

3.5.1.2 Effect of thermalisation

The exciton radiative lifetime within the radiative cone scales with the square of the exciton oscillator strength, and is about 10 ps in the classical 2D system, like GaAs QWs [125]. The large exciton binding energy in ML-$MoSe_2$ leads to a faster lifetime, in the sub-picosecond regime [52, 62, 126, 127]. The scenario is similar to the fast radiative lifetimes in the 1 ps range observed in 2D CdSe platelets [36], which also show exciton binding energies of the order of 100-300 meV. In presence of in-plane disorder, the eigenstates have a finite width in $\boldsymbol{K}_{\parallel}$, yielding longer minimum radiative lifetimes, as explained above. Additionally, scattering between slow and fast excitons can occur by interaction with phonons, excitons, and charge carriers. Assuming thermal equilibrium within the exciton dispersion, one can define [52, 125] an effective radiative decay time of

$$\tau(T) = \frac{3k_{\mathrm{B}}T}{4E_0}\tau_{\mathrm{r}}\,, \text{ with } E_0 = \frac{\hbar^2 K_0^2}{2M_X}\ , \tag{3.16}$$

with the exciton kinetic energy at the edge of the light cone $E_0 = 4.5\,\mu$eV. This expression yields the values $\tau(77\,K) \approx 1100\,\tau_{\mathrm{r}} \approx 440$ ps, $\tau(150\,K) \approx 2150\,\tau_{\mathrm{r}} \approx 860$ ps, and $\tau(300\,K) \approx 4310\,\tau_{\mathrm{r}} \approx 1.7$ ns, using [126] $\tau_{\mathrm{r}} = 0.4$ ps.

In order to have thermalisation, the scattering has to be much faster than τ_{r}. An estimate of the scattering time is given by the dephasing time. In our case, we measured, at $T = 77$ K, a dephasing time of about 0.36 ps (see Sec. 3.2), which is comparable with the expected sub-picosecond radiative lifetime in ML-$MoSe_2$. We therefore expect at this temperature a two components decay: first the fast radiative decay of the initially excited slow excitons, and later a decay of the fast excitons, via scattering to the slow excitons and subsequent radiative emission. The decay dynamics we observe is characterised by more than two decay processes. This behaviour can be explained by the population of intrinsic dark states, which are described below. On the other hand, at room temperature the phonon scattering is likely to be sufficiently fast to allow thermalisation. Accounting for disorder, leading to in-plane localisation, the maximum radiative rate of the exciton states decreases [122, 123], allowing for better thermalisation.

3.5.2 Excitonic landscape in monolayer of molybdenum diselenide

Beside these general properties, the ML-TMDs electronic structure allows formation of different dark excitons. In particular, the exciton has different spin and valley states [25, 128], as sketched in Fig. 3.15. We denote these states as $X_{i_{\mathrm{e}}i_{\mathrm{h}}}^{s_{\mathrm{e}}s_{\mathrm{h}}}$ where i_{e} and i_{h} are the valley index $+$ or $-$, and s_{e} and s_{h} are the spin $\uparrow$ or $\downarrow$, of the electronic state, of electron and hole, respectively. The optical transitions are circularly polarised according to the valley index, and conserve spin and valley index. We call an exciton state spin-allowed for $s_{\mathrm{e}} = s_{\mathrm{h}}$, and spin-forbidden otherwise. Furthermore, an exciton which has equal valley index $i_{\mathrm{e}} = i_{\mathrm{h}}$ is called direct, and indirect otherwise. The direct spin-allowed states $X_{++}^{\uparrow\uparrow}$ and $X_{--}^{\downarrow\downarrow}$ couple to external light and thus have a radiative decay, and the polariton

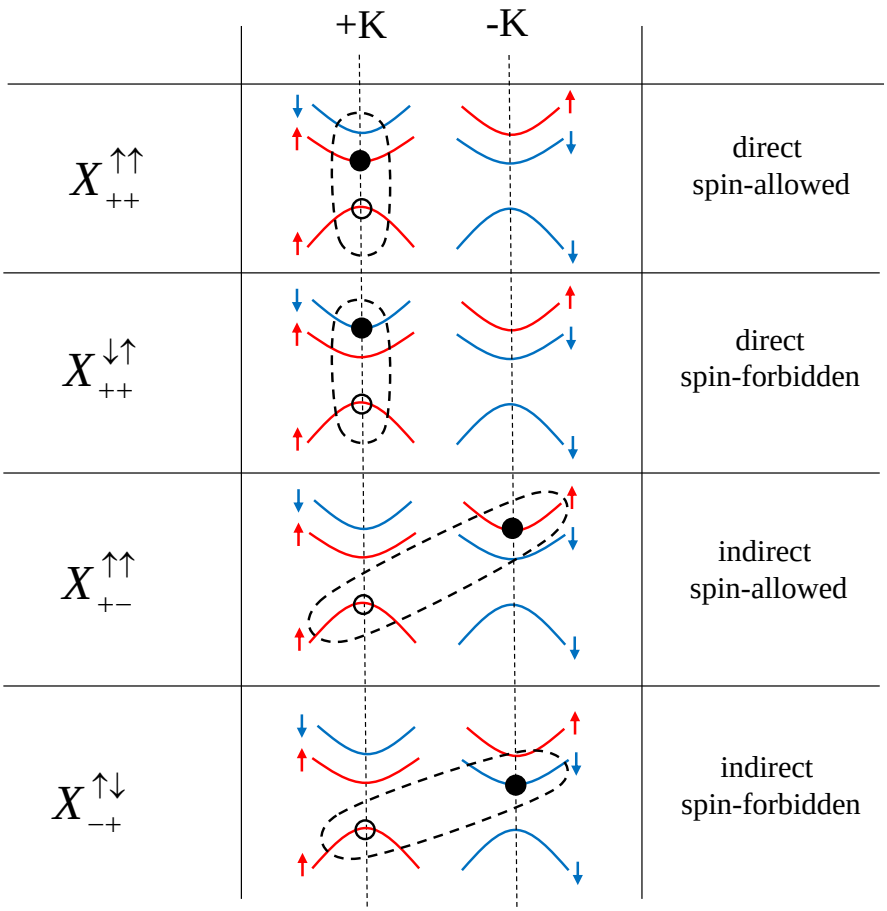

Figure 3.15: Possible electron-hole combinations in the single-particle electronic band structure forming the exciton. An occupied (unoccupied) electron state is represented by full (empty) black circle, with a red/blue vertical arrow indicating the corresponding electron spin. The nomenclature and properties of each exciton state is given. The lower energy valence band with opposite spin is not shown due to its large energy splitting of about 200 meV. Each state shown has a degenerate partner (not shown) with inverted indices, e.g. $X^{\uparrow\uparrow}_{++}$ and $X^{\downarrow\downarrow}_{--}$. Figure published also in Ref. [48].

features discussed in Sec. 1.3.2. Notably, the polariton self-energy couples these two states to form linearly polarised superpositions of L and T states, with an energy splitting, which depends on $\boldsymbol{K}_{\parallel}$, of a few meV for the fast excitons [51]. For each $\boldsymbol{K}_{\parallel}$, the energy splitting corresponds to a different oscillation period between $X^{\uparrow\uparrow}_{++}$ and $X^{\downarrow\downarrow}_{--}$ on the picosecond timescale. The spin memory is therefore lost within this timescale, which can explain the measured fast spin relaxation [117, 129, 130]. The superposition of the oscillations coming from excitons with different $\boldsymbol{K}_{\parallel}$, is responsible for a fast decay, instead of a beating, of the FWM signal. The coupling strength between L and T states is indicated by γ_{LT}. The direct spin-forbidden states $X^{\downarrow\uparrow}_{++}$ and $X^{\uparrow\downarrow}_{--}$ are assumed to be at higher energy due to the CB splitting Δ_{cb}. The direct spin-forbidden states $X^{\uparrow\downarrow}_{++}$ and $X^{\downarrow\uparrow}_{--}$ are not considered in this discussion as they are hundreds of meV above the direct spin-allowed states due to VB splitting.

The presence of the intrinsic dark states described above, open up the possibilities of

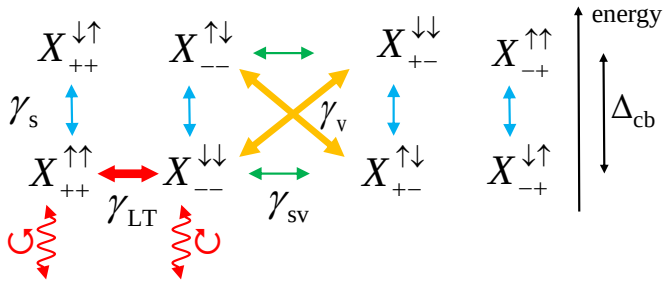

Figure 3.16: Sketch of the scattering rates between the exciton states, as explained in text. Δ_{cb} is the energy splitting between CB and VB. Wavy red lines indicate radiative recombination with emission of circularly-polarised light. Figure published also in Ref. [48].

multiple scattering channels, which we summarise in in Fig. 3.15(c). As already mentioned, the states $X^{\uparrow\uparrow}_{++}$ and $X^{\downarrow\downarrow}_{--}$ are coupled by the L-T polariton splitting, with coupling strength γ_{LT}. Other scattering mechanisms can occur via emission or absorption of phonons. In general, a scattering process that changes the valley index only is indicated with γ_v, the spin only with γ_s and both valley and spin with γ_{sv}. The scattering rate depends on the availability of phonons with a certain energy and momentum. In particular, γ_{sv}, which couples the energy degenerate direct spin-allowed and indirect spin-forbidden states, is expected to be small. Indeed, such a process would need a phonon with approximately zero energy which is at the same time able to provide the wavevector difference between the two valleys, which is given by the K point of the lattice, and this is very unlikely since there are not phonons with these properties. γ_s connects direct spin-allowed and spin-forbidden states, which are split by Δ_{cb}, but have equal wavevector. In this case, there are Γ points phonons with the right energy, which can make the scattering process more likely. In particular, as shown in Ref. [39], the mode E'' and the mode A' at the Γ point have energies of about 20 meV and 30 meV respectively, which are comparable with the CB splitting. On the other hand, the scattering process requires also an electron spin flip, which can not be provided by phonons as they do not couple to spin. Spin-orbit interaction can induce a spin-flip event, although we are not aware of explicit calculations and we do not further comment on this point. Finally, γ_v connects the direct spin-allowed with the indirect spin-allowed state, and the direct spin-forbidden with the indirect spin-forbidden state. Both states have an energy difference given by the CB splitting Δ_{cb}, and a momentum difference between the -K and +K point. Because there are modes matching the energy and momentum required for these transitions, we expect γ_v to be the largest of all three rates.

3.5.2.1 Effect of the exchange interaction

In the sketch shown in Fig. 3.15, the $X^{\uparrow\uparrow}_{++}$ and $X^{\downarrow\downarrow}_{--}$ states are considered degenerate, as well as the $X^{\downarrow\uparrow}_{++}$ and $X^{\uparrow\downarrow}_{--}$ states coming from the higher CB. The exchange interaction could, in principle, modify this scenario. In particular, excitons in ML-TMDs are affected by the short and long range exchange interaction. Because of its electrodynamic nature,

long range exchange interaction affects only the bright excitons, mixing direct spin-allowed states of opposite valleys. Together with the polariton features described above, this could be the reason of the observed fast spin relaxation [117, 129, 130]. On the other hand, the short range exchange interaction affects both bright and dark states, changing their energy. Overall, the electron-hole exchange interaction is expected to lead to an energy splitting of the degenerate direct spin-allowed and indirect spin-forbidden excitons, and also a change of the splitting between direct spin-allowed and direct spin-forbidden. The sign and the amount of the splittings are still under debate in literature [131, 132], and they will not be discussed further.

3.5.3 Interpretation

To interpret the results, we remind ourselves that the strong exciton binding energy of a few hundred meV, combined with resonant excitation of the lowest exciton X_{A}, leads to a dominating role of excitons in the carrier dynamics. Free electron-hole pairs are expected to play a minor role, even at room temperature. Furthermore, for the same reason, the lower spin-split valence band, with a splitting energy of about 200 meV, involved in X_{B}, is also expected to be not relevant. In the presence of extrinsic carriers, due to defects or doping, the resulting electron or hole density leads to the formation of trion states. These will be considered later. In view of the intrinsic properties of the excitonic states in ML-$MoSe_2$ which we described above, we now discuss the observed FWM density dynamics, starting with the data at $T = 77\,\mathrm{K}$.

The optical excitation populates the direct spin-allowed exciton, with $\boldsymbol{K} \sim 0$, therefore close to the center of the radiative cone. When linear polarisation is used, a superposition of direct spin-allowed states in the two opposite valleys is populated. On the other hand, for circular excitation only the direct spin-allowed state from one of the two valleys is populated. Regardless of the polarisation of the excitation, direct spin-allowed states are expected to show a fast radiative recombination time τ_{r}, of the order of 0.5 ps [62, 126]. This is consistent with the decay time we found for the first component, which is about 0.6 ps for both polarisations, which is therefore attributed to radiative recombination. A competing process could be the phonon-assisted formation of a trion, although in ML-$MoSe_2$ it has been measured a trion formation time from the exciton in the 1-2 ps range [133], which is not consistent with our findings. τ_1 slightly decreases with the power, and the reason could be exciton-exciton scattering into the fast states or other spin-valley states. Once the initially excited population of slow spin-allowed excitons is gone, the remaining fast excitons would be expected to have an effective radiative decay at least a thousand times slower, as calculated earlier, in the order of 500 ps. The fast excitons show, as discussed before, a large LT splitting, which is mixing the $X_{++}^{\uparrow\uparrow}$ and $X_{--}^{\downarrow\downarrow}$ states. The memory of the initially excited state, which is different for circularly and linearly polarised excitation, is therefore lost in the fast direct states within the first picoseconds. The subsequent dynamics is expected to be independent of the excitation polarisation configuration, consistent

with our observations, see e.g. Fig. 3.11. The dynamics given by the second component with times τ_2 of about 20 ps is attributed to scattering of the fast spin-allowed states into the indirect spin-forbidden states, possibly via the indirect spin-allowed states involving the rates γ_v and γ_s. Because the latter is the smaller rate, it is expected to dominate the observed timescale. The resulting change of their interaction with the probed slow direct spin-allowed states changes the phase of the signal. Notably, the indirect spin-allowed and direct spin-forbidden states at about 20 meV higher energy will not carry a significant population at T=77 K, considering the Boltzmann factor $\exp(-20/6.6) \approx 0.05$ - they are thus only intermediate states facilitating the transfer between direct spin-allowed and indirect spin-forbidden state. Once the population of the fast direct spin-allowed exciton states and indirect spin-forbidden excitons have thermalised by this scattering process, the exciton density is decaying by scattering back to the direct spin-allowed state, or non-radiative processes. This process is attributed to the third component with $\tau_3 \approx 300$ ps, which is consistent with the decay time of a thermalised distribution of excitons as predicted by Eq. 3.16. The different FWM signal phases of the components can accordingly be attributed to the somewhat different exciton-exciton interactions with the slow direct spin-allowed states, which are carrying the FWM polarisation. Component 1 is due to the interaction within these states, component 2 due to the interaction with fast direct spin-allowed states, and component 3 due to the interaction with indirect spin-forbidden excitons. According to this attribution, the phase of the process included in the fit is mainly determined by the interaction of slow direct spin-allowed states with the excitonic states which are initally populated when the corresponding decay process starts to dominate the dynamics. Notably, the amplitudes of the components are scaling approximately with their decay rate, as would be expected for this picture of three exciton reservoirs with bidirectional scattering. The increasing amplitude of the third process with the excitation power could accordingly be related to exciton-exciton scattering from the direct spin-allowed to the indirect spin-forbidden state, which requires exchange of electron or hole in the process $X^{\uparrow\uparrow}_{++} + X^{\downarrow\downarrow}_{--} \longrightarrow X^{\uparrow\downarrow}_{+-} + X^{\downarrow\uparrow}_{-+}$. This could increase also the radiative decay by a faster scattering into the slow spin-allowed excitons. The weak fourth component with an amplitude A_4 around 1% of A_1 has a time-constant in the tens of nanoseconds and decreases its relative amplitude with increasing fluence. It could be related to thermalisation of existing unpaired charge carriers after the optical excitation.

We now turn to the interpretation of the temperature dependence. With increasing temperature, the scattering rates γ_s and γ_v are expected to increase, due to the larger population factor of phonons which make the processes possible. We can therefore expect that at 150 K and 300 K, these two rates are dominating the dynamics, providing a faster thermalisation between the various exciton states. At 150 K, this leads to an increased amplitude and reduced decay time of the third component. At 300 K, the overall signal is reduced, due to the homogeneous broadening of the exciton of about 40 meV, superseeding the inhomogeneous broadening (see also Fig. 3.5). This also means that the slow direct spin-allowed excitons are scattered within the pulse duration towards the other

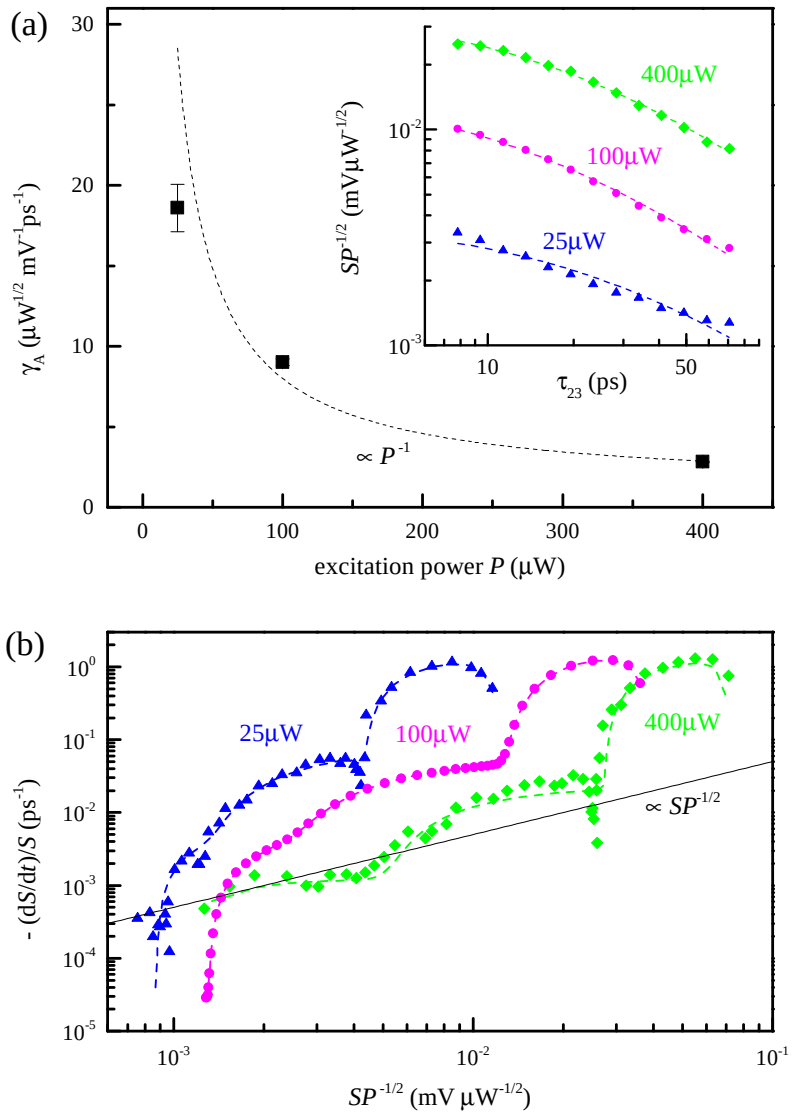

Figure 3.17: Exciton-exciton annihilation analysis. (a) Inset: normalised FWM field amplitude $S/\sqrt{P}$ (symbols) as function of τ_{23} for different powers P as indicated, and fits (dashed lines) according to Eq. 3.18. Main: γ_A values (squares) determined by the fit; dashed line: P^{-1} dependence. (b) Logarithmic decay rate of the FWM field amplitude S versus $S/\sqrt{P}$ for different P as indicated. Symbols: measurements for $\tau_{23} \geq 0.3$ ps; dashed lines: fits shown in Fig. 3.10; the solid line shows a dependence proportional to $S/\sqrt{P}$. Figure published also in Ref. [48].

exciton states, and the dynamics is dominated by a single decay time around 30 ps. At this temperature, the mobility of excitons in the sample could also allow the excitons to recombine non-radiatively at defects. However, in Ref. [134], a similar sample did not show a strong variation of the non-resonantly excited PL intensity for $T > 100$ K, indicating that diffusion to defects and subsequent non-radiative decay is not significant.

3.5.4 Exciton-exciton annihilation

Observation of exciton-exciton annihilation (EEA) in ML-TMDs has been proposed to interpret carrier dynamics in WSe_2 [135], MoS_2 [136] and $MoSe_2$ [137], using largely varying

EEA rates, and rates affected by the substrate [138], while there are also reports where EEA was not invoked [139, 140]. In all these works, non-resonant optical excitation leading to free electron-hole pairs has been used, and the dynamics can be strongly affected by the relaxation process. Considering the already quite intricate scenario which involves many dark states, such an additional decay channel would make the interpretation of density dynamics data extremely ambiguous. In the following, we demonstrate that EEA can not describe the observed dynamics. To evaluate whether EEA has a role in the dynamics we measure, we follow the analysis in Ref. [137]. In this paper, Kumar et al. show that EEA is the dominating decay mechanism in the delay range from 5 ps up to 60 ps. Therefore, we first try to understand if this is true also in our data.

The EEA rate equation describing the density decay is given by [137]

$$\frac{dN}{dt} = -\frac{N}{\tau} - \frac{\gamma_A}{2}N^2 \ , \tag{3.17}$$

with the density of excitons N, the low-density decay rate τ, and the EEA rate γ_A. The EEA is expected to be dominant at higher density and we can therefore neglect the low density decay rate. Within this approximation, the solution of Eq. 3.17 is given by

$$N(t) = \left(N_0^{-1} + \gamma_A t/2\right)^{-1} \ , \tag{3.18}$$

where N_0 is the initial exciton density. We note that in Ref. [137], Eq. (3), a factor 1/2 is missing. In our experiments, the exciton density is expected to be proportional to $S/\sqrt{P}$ where S is the FWM field amplitude. Indeed, S is proportional to the third power of the electric field, the exciton density to the squared of the electric field and $\sqrt{P}$ to the electric field. We therefore fit $S/\sqrt{P}$ as shown in the inset of Fig. 3.17 (a) for delays τ_{23} from 5 ps to 55 ps, using Eq. 3.18. The resulting rates γ_A are given in Fig. 3.17 (a). We find that γ_A is strongly varying, being approximately inversely proportional to the power P. This finding is in contradiction with Eq. 3.17, which assumes a constant value for γ_A. In order to extend the analysis over the full time range of our experiments, we decide to avoid the approximation of negligible low density rate used in Ref. [137]. By dividing Eq. 3.17 by $-N$, we obtain a linear dependence on N: $-dN/(dtN) = \tau^{-1} + \gamma_A N/2$. As a consequence, we expect $-(dS/dt)/S$ to be linear with $S/\sqrt{P}$. In Fig. 3.17(b), we show $-(dS/dt)/S$ versus $S/\sqrt{P}$, for $\tau_{23} \geq 0.3$ ps, together with the same quantity deduced from the fit Eq. 3.12 to the data shown in Fig. 3.10. The linear dependence predicted by Eq. 3.17 does not describe the data. Furthermore, the data for different P do not overlap, as would be predicted by Eq. 3.17. Similar results were found for the aged sample using the data from Fig. 3.11, whose EEA analysis is not shown here. We therefore conclude that EEA is not relevant to explain the observed dynamics.

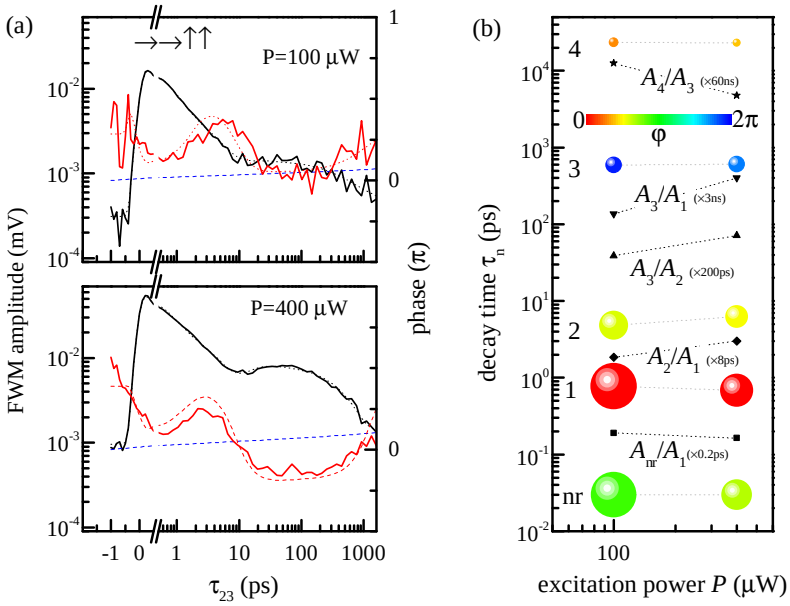

Figure 3.18: Density dynamics of the fresh sample for excitation resonant to X_A^- at T=77 K. (a) FWM field amplitude and phase as function of the delay τ_{23} for two excitation powers P as given and cross-linear polarisation configuration $(\rightarrow,\rightarrow,\uparrow,\uparrow)$. The fitted phase drift (blue dashed line) has been subtracted from the data shown. (b) Results of a fit to (a), formatted as Fig. 3.12. For absolute scaling $A_1 = 24\,\mu$V at $P = 100\,\mu$W. Figure published also in Ref. [48].

3.6 Trion population dynamics

3.6.1 Density dependence

In order to investigate the trion X_A^- dynamics, we measured the population dynamics resonantly exciting and probing the X_A^- transition (see Fig. 3.5(b)) using cross-linearly polarized pumps at T=77 K. The data are shown in Fig. 3.18(a) for two different powers. As in Sec. 3.4, we fitted the data using Eq. 3.12 with four decay processes, and the resulting decay times, amplitudes and phases are shown in Fig. 3.18(b). We find an initial fast decay of $\tau_1 \approx 1$ ps similar to the exciton-resonant dynamics. The instantaneous response A_{nr} is stronger relative to A_1, and it is π-shifted with respect to A_1 ($\varphi_{nr} \approx \pi$). The stronger relative weight is expected considering that the X_A^- has a weaker absorption than the X_A and A_1 is about five times smaller for a given power. The second timescale $\tau_2 \approx 5$ ps is shorter than for the exciton-resonant dynamics where $\tau_2 \approx 20$ ps, and has a larger relative amplitude compared to A_1. The later dynamics determined by τ_3 and τ_4 instead are similar to what is found for the exciton-resonant excitation. We do not observe a significant variation of the timescales with power, in difference to what has been recently reported [118] and interpreted as saturation of defect states. The amplitudes slightly decrease with increasing power. All the amplitude ratios seem to increase with the power, with the exception of A_4/A_3. The phase evolution is quite different from the exciton-resonant data. Indeed, we find $\varphi_2 \approx \pi/2$ while $\varphi_3 \sim 2\pi$, which is equivalent to zero. φ_4 is slightly less then $\pi/2$.

3.6.2 Interpretation

Concerning the initial dynamics, we note that exciton to trion conversion has been recently investigated [133]. As already mentioned, according to this paper the exciton to trion conversion occurs within 1-2 ps at T=13 K. At this temperature, the trion, which has a binding energy of 30 meV, is not thermally excited, so that the time measured is the trion formation time. We emphasise that the rate of the corresponding process exciton plus electron gives trion plus phonon is expected to be proportional to the electron density, and the latter was not specified in Ref. [133]. The reported timescale should therefore be taken only as a possible value, which can vary strongly depending on the electron density. In our experiment we initially excite X_A^-, and we are therefore measuring, as initial process, the thermal excitation of the trion within its dispersion, and its ionisation into a free electron and an exciton. The radiative recombination of trions is expected to be much slower than the slow bright excitons, due to the momentum distribution of the remaining electron after the decay [115]. We therefore attribute the first timescale τ_1 to trion thermalisation within its dispersion. Trion ionisation is not expected to be efficient at $T = 77$ K, due to the large trion binding energy of 30 meV compared to the thermal energy. The second timescale τ_2 can then be attributed to trion ionisation, a process which was recently observed in PL [141]. After ionisation, the dynamics are expected to be similar to the case of the exciton. Consistently with this interpretation, the similarity of the τ_3 and τ_4 values to the exciton-resonant results indicates that after about 100 ps, the initially excited X_A^- are thermalised with X_A, and thus the memory of the initially excited transition is lost. The phases differ somewhat due to the difference in energy of the probed optical response.

3.7 Conclusions

We presented experiments of FWM spectroscopy on ML-$MoSe_2$. Our work is the first study specifically dedicated to the understanding of the exciton density dynamics, measured under resonant excitation, in contrary to previous works that all made use of a non-resonant excitation scheme. We presented a new fitting model based on a complex multi-exponential response function, which describes the FWM signal as a coherent superposition of exponential decay processes. Such a model allows fitting both in amplitude and phase. The fit shows that the phase evolution, contrary to the constant phase approximation previously adopted, is responsible for destructive and constructive interference between different decay process, and is the origin of surprising rises of the FWM signal, which are not expected by simple rate equations models. The density dynamics, both for exciton and trion, is interpreted within the intrinsic band structure, without introducing other extrinsic effects. Additionally, we show that exciton-exciton annihilation is not relevant for the description of the observed dynamics.

As an outlook, we believe the complex fitting routine can be further extended. In

particular, it would be interesting to connect the macroscopic phases φ_n that we give to each decay process included in the fit, to microscopic quantities such the strength of the exchange and dipole-dipole interactions.

Chapter 4

Spontaneous emission properties and directional emission of quantum dots in photonic crystal waveguides

The work presented in this chapter is part of the GW4 project, a collaboration between University of Bath, University of Bristol, Cardiff University and University of Exeter. The aim of the alliance is to address key national and global challenges of different type. Among the numerous GW4 communities, the Southwest Quantum Technologies group focuses its research to advance the development of new quantum technologies. In this context, our work focuses on InAs/GaAs self assembled QDs embedded in PCWGs. Such a system has been shown to have very promising properties for scalable, on chip, quantum photonics [6]. The ability to tailor light-matter interaction enables to control the SE properties of single QDs, owing to the Purcell effect [83, 84]. Additionally, it has been shown that a QD couples to a waveguide mode with near-unity coupling efficiency [142], which makes the system ideal for single photon source application. On the other hand, recently also chiral effects has been explored. Depending on the mode field polarisation at the QD site, the SE becomes direction dependent [143]. This exciting property can play an important role in the context of spin-photon interfaces [144, 145, 146].

In this work, we use direct spectral imaging to measure the coupling efficiency, known as the beta factor, of InAs/GaAs QD to the guiding modes of a PCWG. In contrast to previous works based on lifetime measurements, spectral imaging is a direct measurement of the beta factor. Additionally, we use the observed directional emission to quantify the mode field circularity at the QD site. Beta factor, mode polarisation and QD energy uniquely define the QD position inside the lattice unit cell. We compare our data with finite-difference time-domain (FDTD) simulations, from which we are able to estimate the most likely position of the QD inside the lattice unit cell.

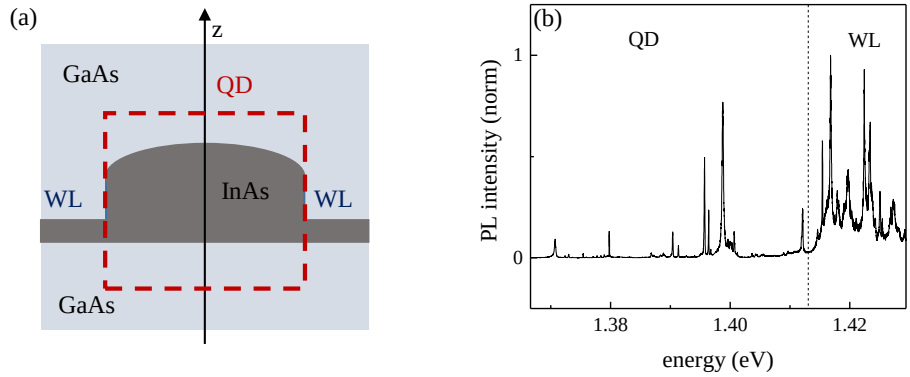

Figure 4.1: (a) Sketch of an InAs/GaAs self-assembled QD. (b) Characteristic PL spectrum from an ensemble of InAs/GaAs QDs measured on one of the waveguide sample investigated in this work.

4.1 Self-assembled InAs/GaAs quantum dots

The sample investigated in this work embeds InAs/GaAs QDs. They are grown by molecular beam epitaxy (MBE) and from the Stransky-Krastanov method, in which QDs form by self assembly, through a strain-driven nucleation process [147, 148] caused by the lattice mismatch between the GaAs and InAs lattices. QDs made by this process have generally a lens-shaped structure, which forms on the top of a 2D InAs wetting layer (WL) [149], as shown in Fig. 4.1(a). The QDs have a typical diameter of the order of 20 nm and height of 5 nm [59]. In Fig. 4.1(b) we show a characteristic PL spectrum of an ensemble of InAs/GaAs QDs measured in this work. For energies smaller than about 1.41 eV, single sharp lines are observed, which are due to recombination, from the s-shell, of electron-hole pairs confined in different QDs. Above 1.41 eV, we observe also sharp lines, but on the top of the broader emission, which is given by recombination of the electron-hole pairs confined in the WL. The sharp lines in this case are due to localised excitons.

4.2 Quantum dots embedded in photonic crystal waveguides

Combining Sec. 4.1 and Sec. 1.6, we now look at the light-matter interaction between QDs coupled to a PCWG mode. In this context, we are mainly interested in the beta factor and in the directional emission of photons, which are described in the following.

4.2.1 Beta factor

The beta factor β describes the probability that a spontaneously emitted photon from a QD couples to a waveguide mode. In contrast to the Purcell factor, the beta factor considers also the radiative decay rate of the QD into non-guided modes Γ_{ng} and the

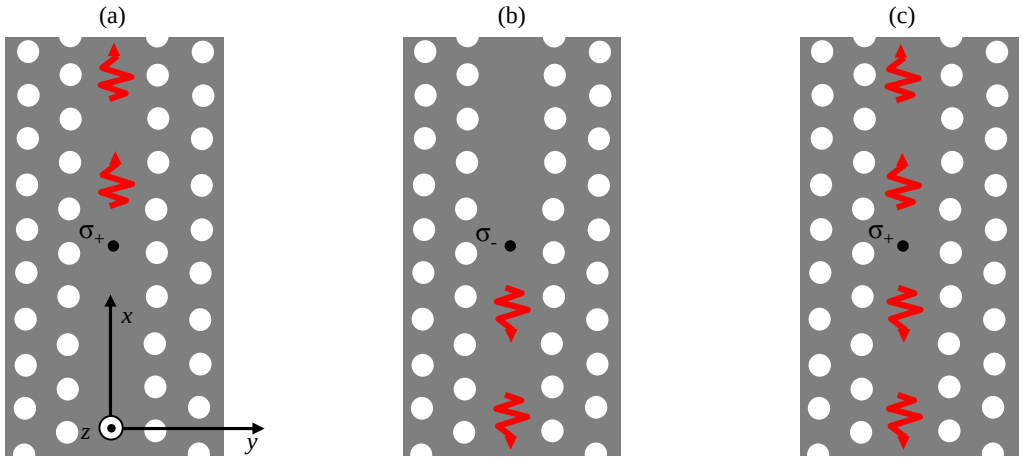

Figure 4.2: A σ_+ (a) and a σ_- (b) dipoles, at the same C-point, emit photons in the opposite propagation directions, $+x$ and $-x$ respectively. (c) A σ_+ dipole at a L-point emits photon in both the $+x$ and $-x$ directions.

intrinsic non-radiative decay rate Γ_{nr}. It is defined as:

$$\beta = \frac{\Gamma_{\mathrm{wg}}}{\Gamma_{\mathrm{wg}} + \Gamma_{\mathrm{ng}} + \Gamma_{\mathrm{nr}}} \quad . \tag{4.1}$$

Importantly, high Purcell enhancement does not imply high beta factor and vice versa, high beta factor does not occur only at region of high Purcell enhancement [84].

In previous works, the beta factor was estimated using lifetime measurements [142, 150, 151, 152, 153, 154]. The challenge in these measurements is to determine all three decay rates. A common approach assumed Γ_{wg} to be given by the difference between the decay rate of a QD coupled to a waveguide mode, Γ_{c}, and the decay rate of similar QDs not coupled to the waveguide, Γ_{nc}, so that $\Gamma_{\mathrm{wg}} = \Gamma_{\mathrm{c}} - \Gamma_{\mathrm{nc}}$, and also used $\Gamma_{\mathrm{ng}} + \Gamma_{\mathrm{nr}} = \Gamma_{\mathrm{nc}}$. This approach assumes that both QDs have the same decay rate into non-guided modes, and the same non-radiative decay. The non-radiative decay Γ_{nr} is depending on QD charging and local defects and is thus determined by properties beyond the photonic environment. Assuming no influence of local defects or tunneling, it is negligible for neutral excitons in InAs QDs, and even in charged excitons, where Auger processes provide a non-radiative decay, they have a rate in the order of $1\,\mu\mathrm{s}^{-1}$ [155], thus three orders of magnitude below typical radiative decay rates of $1\,\mathrm{ns}^{-1}$ [156]. Considering the radiative decay into other modes Γ_{ng} instead, the strong modification of the local dielectric surrounding in PCWG structures, located in the QD near-field, is expected to modify Γ_{ng} significantly, as recent calculations [157] have highlighted. Therefore, the analysis reported in these previous works is expected to result in significant systematic errors in the determined β factor.

4.2.2 Directional emission

Directional emission is a very interesting phenomena, where the direction of spontaneously emitted photons from a quantum emitter depends on the polarisation state of the elec-

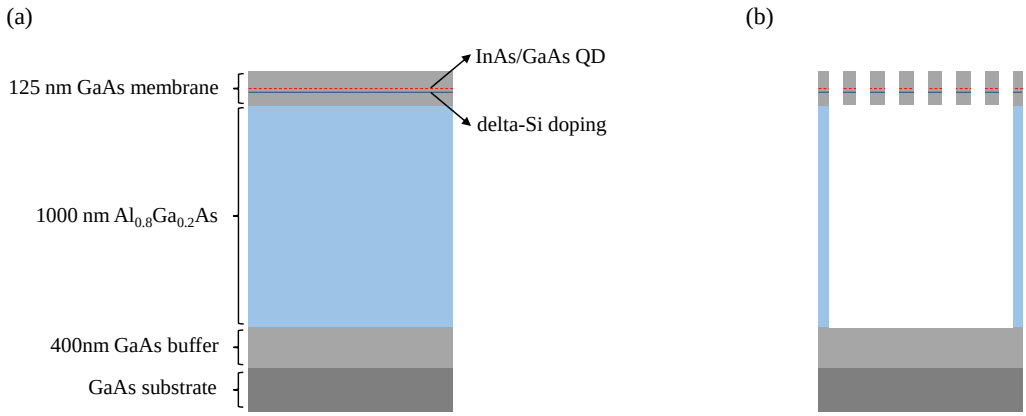

Figure 4.3: Sample side view. (a) Layer structure as grown by MBE. (b) Creation of a free-standing GaAs membrane, by removing of the $Al_{0.8}Ga_{0.2}As$ sacrificial layer with hydrofluoric acid.

tromagnetic field at the quantum emitter position [143]. This mechanism is schematically reproduced in Fig. 4.2. If a right-handed circularly polarised dipole on a C-point emits photons in one direction, a left-handed circularly polarised dipole on the same C-point emits photons in the opposite direction, owing to time-inversion symmetry [143]. Directional-dependent SE of photons has been observed in PCWG [145, 158] and more recently also in topological photonic states [159]. Although in this work we exploit directional emission only through the SE from QDs, chiral properties also affect resonant transmission and reflection [160], with strong implications in quantum technology applications[144].

4.3 Sample description

The sample was grown by members of Christian Schneider's group in Würzburg University. A sketch of the side view is shown in Fig. 4.3(a). The layered structure is growth by MBE and consists of a GaAs substrate, a 400 nm-thick GaAs buffer, a sacrificial layer of $Al_{0.8}Ga_{0.2}As$ 1000 nm-thick and a final layer of GaAs, forming a membrane, 125 nm-thick. In the middle of the latter, a layer of InAs is deposited in order to form InAs/GaAs QDs by self assembly, with a density of roughly $10^9\,cm^{-2}$. Delta-doping of n-type is provided by silicon atoms deposited 10 nm underneath the QDs layer, with a doping density which is 8 times the QDs density. With electron-beam lithography the periodic pattern of air holes forming the PCWG is transferred from the photo resist to the GaAs membrane and to the sacrificial layer. The latter is removed by high selective etching with hydrofluoric acid. The resulting structure side view is shown in Fig. 4.3(b). A free-standing GaAs membrane is formed, with a layer of InAs/GaAs QDs in the middle. For more details on the sample fabrication process, we refer to Ref. [82].

The photonic crystal, in all the analysed waveguides, has an hexagonal unit cell with two primitive vectors of equal magnitude a, as shown in Fig. 4.4(a). Two different PCWGs (called WG_A and WG_B) have been analysed. They differ by their hole radius to period ratio r/a, being 0.24 and 0.26, respectively. The PCWGs are both $100a$ long and $12a$

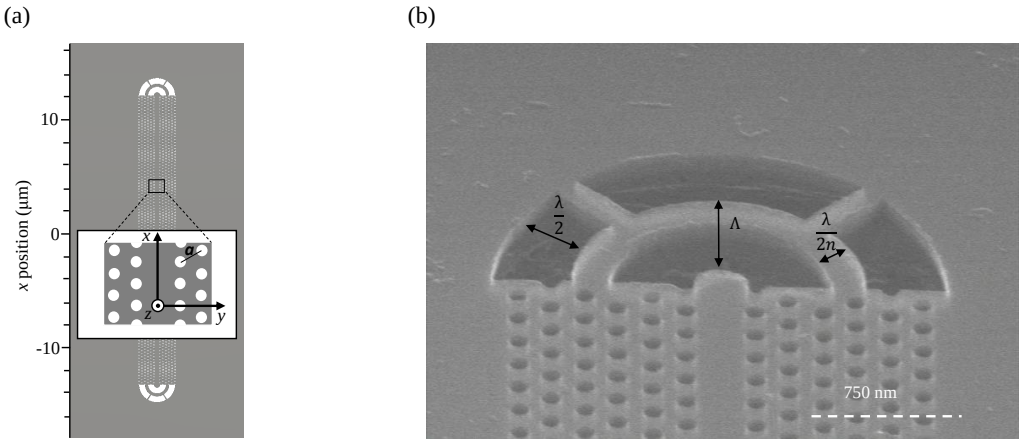

Figure 4.4: (a) Sketch of the PCWG, terminated by grating out-couplers; inset: lattice structure. (b) SEM image of the grating out-coupler.

wide, with $a = 260\,\text{nm}$. The PCWGs are terminated, on both sides, by second-order Bragg reflectors, which couple light propagating in the PCWG to free space [161]. A scanning electron microscopy (SEM) image is shown in Fig. 4.4(b). The working principle of the grating is based on the scattering laws:

$$\begin{aligned} \boldsymbol{k}_{\text{out}} &= \boldsymbol{k}_{\text{in}} - \boldsymbol{K} \\ \omega_{\text{in}} &= \omega_{\text{out}} \quad , \end{aligned} \tag{4.2}$$

where $\boldsymbol{k}_{\text{in}}$ and $\boldsymbol{k}_{\text{out}}$ are the wavevectors of the incoming light and scattered light respectively, with the corresponding angular frequencies ω_{in} and ω_{out} and $\boldsymbol{K}$ the out-coupler wavevector. The grating are designed with a total period $\Lambda = \lambda$, such that $K_x = K_y = 2\pi/\Lambda = 2\pi/\lambda$. Light emitted from the end of the waveguide has also a wavevector $k_x = 2\pi/\lambda$. Therefore, $k_{\text{out},x} = 0$. Conservation of energy dictates that light has to be scattered in the out-of-plane direction. Because of the spherical symmetry of the grating out-couplers, this effect is true for all the incoming wavevectors in the plane of the waveguide.

4.4 Measurement of the waveguide dispersion

Determining the photonic band structure of the investigated sample is crucial for a quantitative comparison with numerical simulations. In the literature, near-field scanning optical spectroscopy [162], combined with interferometric techniques [163] have been used to determine the guided mode dispersion in PCWGs. In other cases, a measurement of the dispersion has been circumvented by measuring the transmitted intensity as a function of energy, and by adjusting the simulation parameters to match the measured transmission window [164]. The latter lacks of sharp edges, and the matching criteria are usually ill defined or not defined at all. An alternative method made use of Fabry-Pérot resonances to calculate the group index of the guided mode [142]. Here, we use Fourier-space imaging

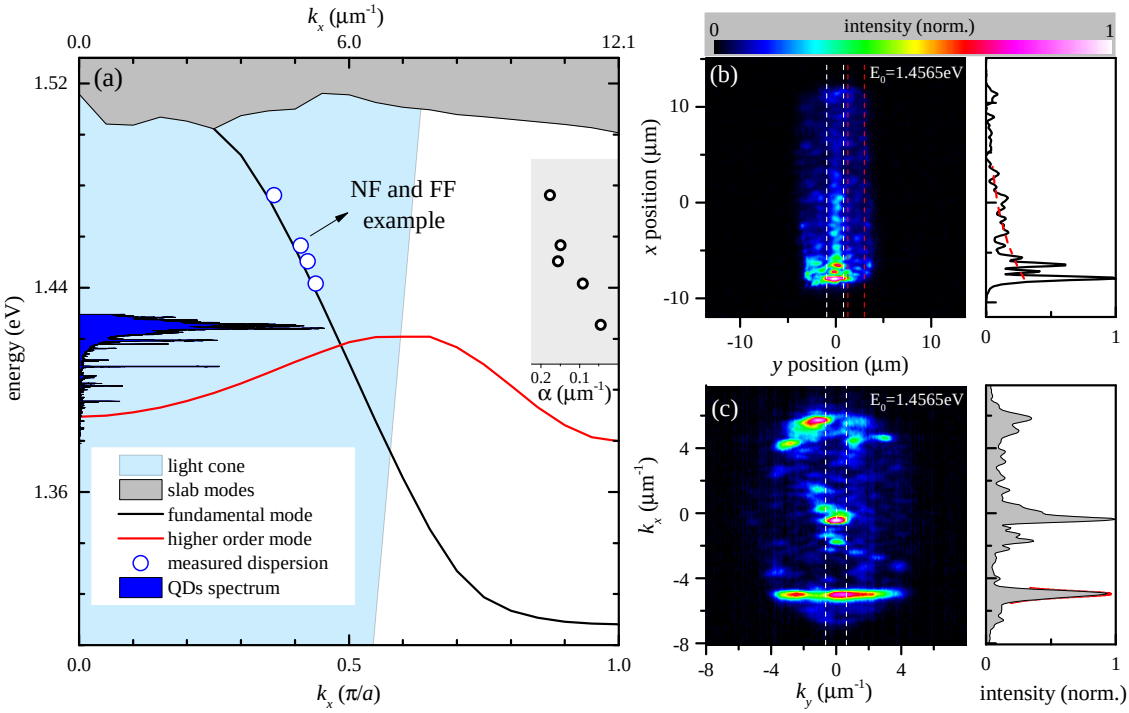

Figure 4.5: Photonic band structure and real-space and Fourier-space imaging. (a) Simulated photonic band structure of WG_A; dark-blue shaded area: QDs emission spectrum; blue circles: measured dispersion from Fourier-space imaging; inset: loss coefficient obtained from real-space imaging. (b) Main panel: real-space imaging; right panel: real-space intensity profile obtained as the difference between a cut along the waveguide and a reference side cut (white dashed lines and red dashed lines in the main panel, respectively). Red dashed line: exponential fit. (c) Main panel: Fourier-space imaging; right panel: Fourier-space intensity profile obtained from a cut highlighted by white dashed lines in the main panel. Red solid line: Lorentzian fit. Benjamin Lang built and run the model to generate the data of the simulated dispersion; plot produced by the author.

[165, 166] to directly measure the band dispersion within the light cone [167].

The simulated dispersion for the WG_A is shown in Fig. 4.5(a), with the fundamental and the higher order mode given in black and red solid lines respectively. A characteristic QD spectrum is also shown in dark-blue shaded area in the figure. The light cone is given by the light-blue shaded area. The blue and the dark circles are the result of the Fourier-space and real-space measurements respectively, which are explained in the following.

In order to measure the real-space and Fourier-space intensities of radiation losses, we use optical pulses generated by the Nd:YAG and Ti:Sa laser system shown in the sketch of Fig. 2.4. The reason why optical pulses are used is because they have shorter coherence length with respect to continuous wave excitation, and interference effects from background scattering are reduced. The spectral width of the excitation pulses limits the resolution of the Fourier-space measurements, as shown later, although this is not critical for our purposes. The excitation pulses are coupled to the waveguide by focussing onto the bottom grating out-couplers. The laser polarisation is set orthogonal to the PCWG direction, in order to mainly select the fundamental mode (see Sec. 4.8). To suppress the reflection of the excitation laser, we use a rectangular aperture of (8.7,19.0) µm in the

intermediate image plane, centred on the PCWG. The image of this aperture is clearly visible in Fig. 4.5(b). We tune the energy of the excitation pulses in the energy range 1.44-1.48 eV, within the light cone. In this way, the sample plane is filled with the radiation losses from the waveguide. The corresponding real-space and Fourier-space intensities are imaged onto the real-space and Fourier-space cameras respectively (see Sec. 2.2). The real-space measurement for the laser energy $E_{\mathrm{L}} = 1.45648\,\mathrm{eV}$ is shown in the main panel of Fig. 4.5(b) and the corresponding Fourier-space in the main panel of Fig. 4.5(c). To obtain the images, the original data are subtracted with a background image, taken individually for the two different cameras. All the images, including the background, are the sum of 100 frames exported from the corresponding 4 s long video.

4.4.1 Real-space imaging

We now discuss the real-space measurements shown in Fig. 4.5(b). According to the scale of the "x position" axis given in the figure, which is calibrated using the position of the grating couplers (a reference measurement is taken without the rectangular aperture), the bottom out-coupler is located at -13 µm, and the top out-couplers at +13 µm. Light is therefore propagating from the bottom coupler towards the top coupler. Importantly, propagation losses are directly observed as the decrease of the out-of-plane emission as a function of distance. The real-space intensity profile along the PCWG shows significant fluctuations, reflecting the coherent nature of the emission. It can be fitted with an exponential decay, as shown in the right panel of Fig. 4.5(b), which allows us to obtain the losses per unit distance, described by the coefficient α. The fitted curve has been derived as the difference between the emission profile along the waveguide and a reference profile next to the waveguide. Each profile is averaged over 1.7 μm along the "y position" axis, as highlighted in Fig. 4.5(b) with the white and red dashed lines respectively. We repeat the measurements at different energies, and the results are summarised in the inset of Fig. 4.5(a). At E_{L}=1.42525 eV, we find $\alpha = 0.047 \pm 0.008\,\mu\mathrm{m}^{-1}$, while at E_{L}=1.47613 eV, $\alpha = 0.184 \pm 0.023\,\mu\mathrm{m}^{-1}$. The increasing of α at higher energies is expected, for two main reasons. According to the dispersion shown Fig. 4.5(a), at higher energies the propagation wavevector k_x is reduced, going deeper within the light cone, where radiation losses increase. At the same time, also the WL absorption is expected to increase at higher energy. In order to separate the two contributions, we perform simulations without including the WL. In Sec. 4.8.2, we discuss propagation losses in more details.

4.4.2 Fourier-space imaging

We now turn to the discussion of the Fourier-space measurements (Fig. 4.5(c)). We note that the accessible range of the in-plane wavevector $\mathbf{k}$ is limited by the NA of the MO to $|\mathbf{k}| < k_0\mathrm{NA}$, with the free-space wavevector $k_0 = 2\pi/\lambda$. The resulting cut-off is visible in the figure and from this we can calibrate the k-space of our measurements. In particular, we measured the Fourier-space intensity of the transmission from the top coupler for

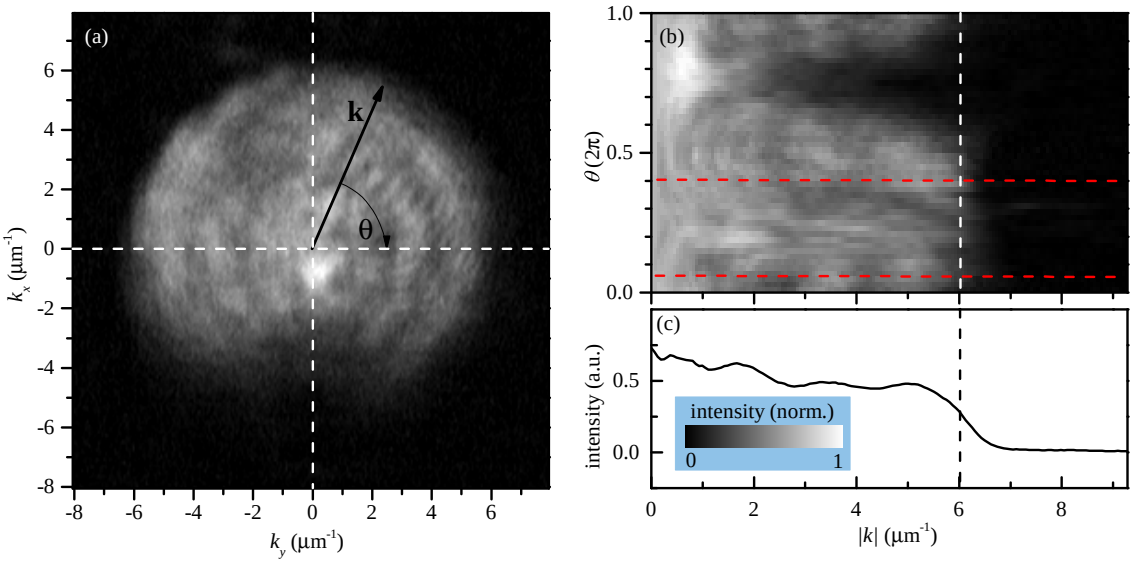

Figure 4.6: NA calibration. (a) Fourier-space intensity of the PCWG transmission coupled out by the top coupler at E=1.4102 eV. (b) Azimutal cuts taken from (a). (c) Profile taken as average of the region delimited by horizontal dashed lines in (b). Vertical dashed lines in (b) and (c) indicate the radius of the NA in k-space.

E_{L}=1.4102 eV, as shown in Fig. 4.6(a). To use the known NA of the objective for calibration, we determine the cut-off radius, using the polar coordinate representation of the data shown in (b). We adjusted the centre of the coordinate system to obtain a constant maximum radius, shown by the vertical dashed line. We average on the region in between the two horizontal dashed lines in Fig. 4.6(b), to get the profile shown in Fig. 4.6(c). We take the NA radius to be the value of k at half step height, and calibrate this radius to $k_0\mathrm{NA} = 6.076\,\mu\mathrm{m}^{-1}$. The measured Fourier-space pattern shows a stripe at k_x around -5 µm^{-1}, elongated in the k_y direction, which is the PCWG radiation loss. The mode wavevector along the waveguide is given by k_x, and the large extension in the k_y is due to the small spatial extension of the PCWG mode in y direction in real-space. As the light is propagating in the positive x direction in the PCWG, it is in first place surprising that it has a negative wavevector k_x, but is just evidence of the negative group velocity of the PCWG mode, i.e. group and phase velocity are opposite to each other. To better clarify on this point, in Fig. 4.7 we show a sketch of the actual scenario. When coupling the light from the bottom out-coupler, we automatically select a propagation direction, in this case the positive x direction, which is also the direction of the group velocity v_{g}. Because of the translational invariance along x, the mode field builds up in different mode replica, separated, in k-space, by a reciprocal lattice vector G. In the present case, all the replicas with propagation wavevector in the same direction as the group velocity, lie outside the light cone. Therefore these replicas do not radiate in the out-of-plane direction and we do not measure them. On the other hand, the replica inside the light cone has radiation losses. In particular, the propagation wavevector of this replica has opposite sign with respect to v_{g} (as shown in Fig. 4.7(a)), resulting in the observed negative group

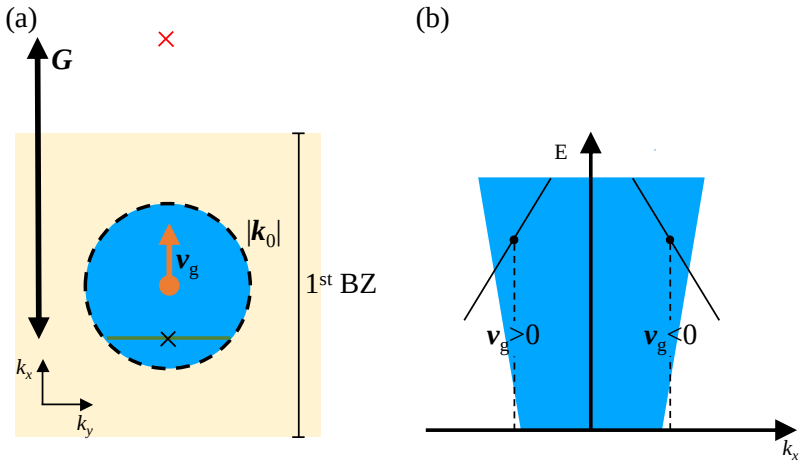

Figure 4.7: Negative group velocity dispersion. (a) A pulse propagates with group velocity v_g (orange arrow) pointing along the positive k_x direction. The mode replica within the light cone (black cross) has opposite sign with respect to v_g, resulting in a phase velocity which is opposite to the group velocity. The Fourier-space profile of this replica is shown by the green line. One of the replica propagating with positive k_x, obtained by adding a reciprocal lattice vector $\boldsymbol{G}$, is given by the red cross. BZ: Brillouin zone. (b) By imposing a propagation direction, we select either the positive or negative k_x directions of the dispersion.

velocity dispersion. We note that by imposing the propagation direction, we select either the positive or negative (mirror symmetric around $k_x = 0$) k_x directions of the dispersion, as shown in Fig. 4.7(b). We determine the propagation wavevector of the replica inside the light cone by fitting the Fourier-space profile with a Lorentzian, as shown in the right panel of Fig. 4.5(c). The profile is obtained by averaging over a k_y range of about $1.2\,\mu\mathrm{m}^{-1}$ centred around $k_y = 0$, as given by the white dashed lines. The resulting $-k_x(E_\mathrm{L})$ are shown in Fig. 4.5(a), with the blue circles. The reflection symmetry of the PCWG results in a reflection symmetry in the dispersion around $k_x = 0$, allowing to use $-k_x$. The matching criteria we used to calibrate the simulated dispersion to the measured one are explained in details in Sec. 4.8.1.

The Fourier-space profile shown in Fig. 4.5(c), has a finite width, γ_{k_x}, in the k_x direction. There are two contributions to the observed width: the bandwidth of the excitation laser, described by the intensity FWHM γ_laser, and the finite spatial extent of the real-space intensity profile in the x direction. In particular, the latter contribution is determined by the exponential decay of the field amplitude due to radiation losses, and limited by the aperture size. The field is thus proportional to

$$E(x) = \left[\theta\left(x + \frac{L_\mathrm{p}}{2}\right) - \theta\left(x - \frac{L_\mathrm{p}}{2}\right)\right] \exp\left(-\frac{\alpha x}{2}\right) \quad , \tag{4.3}$$

with the aperture size L_p and the Heaviside function θ. Fourier-transforming and taking the absolute square, we find the corresponding intensity in k-space $I(k)$:

$$I(k) = \frac{2}{k^2 + \frac{\alpha^2}{4}}\left[\cosh\left(\frac{\alpha L_\mathrm{p}}{2}\right) - \cos\left(kL_\mathrm{p}\right)\right] \quad . \tag{4.4}$$

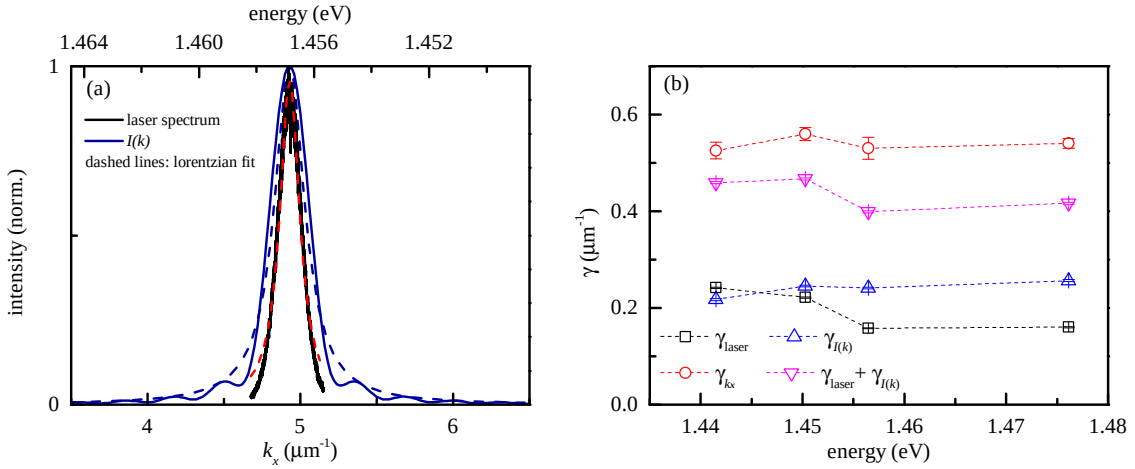

Figure 4.8: (a) Solid lines: laser spectrum and $I(k)$; dashed lines: corresponding fits. (b) Fourier-space intensity width γ_{k_x} in the k_x direction interpreted as the sum of the laser width (γ_{laser}) and the width of $I(k)$ ($\gamma_{I(k)}$). All the γ coefficients are given in intensity FWHM of the corresponding Lorentzian fit.

For $\alpha L_{\text{p}} \gg 1$, $I(k)$ is a Lorentzian, while in the opposite limit, it is a sinc function. We fit the envelope with a Lorentzian function in order to get the corresponding FWHM $\gamma_{I(k)}$. The laser spectrum is converted into k-space using the measured dispersion, which is approximated to a linear function with dispersion -27.3 $\mu\text{m}^{-1}\,\text{eV}^{-1}$ in the energy range considered. The corresponding spectrum and $I(k)$, together with the corresponding Lorentzian fits, are shown in Fig. 4.8(a) for the same energy and losses of Fig. 4.5(b) and (c). According to this description, the width of the Fourier-space profile corresponds to the FWHM of the Lorentzian given by the convolution, in k-space, of the two contributions. This is simply given by $\gamma_{\text{laser}} + \gamma_{I(k)}$. The results of this analysis are shown in Fig. 4.8(b) as a function of the laser energy E_{L}. $\gamma_{\text{laser}} + \gamma_{I(k)}$ does roughly reproduce γ_{k_x}. Defocus in the Fourier-space imaging might explain the additional observed broadening of about 0.1 μm^{-1}.

4.5 Spectral imaging of the spontaneous emission from quantum dots coupled to photonic crystal waveguides

In this section, we show how the spectral imaging technique introduced in Ch. 2 can be applied to measure the SE of QDs coupled to PCWG modes. First, the geometry of the experiment is explained. Second, the method of analysis of spectral images is detailed. Finally, we show that QDs can be excited both locally and non-locally. In particular, non-local excitation can be used to determine the QD position along the waveguide also for strongly coupled QDs, whose emission directly in free space is not visible.

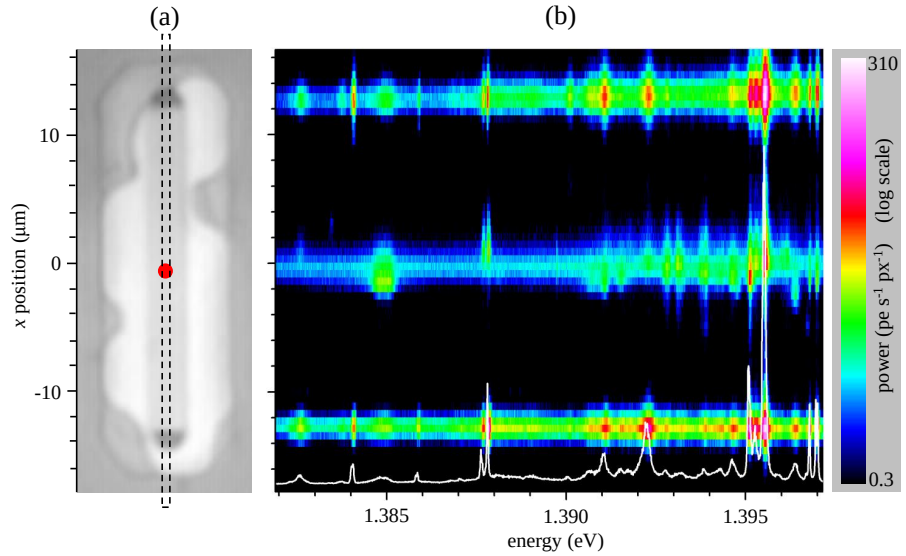

Figure 4.9: (a) White light reflection image of WG_A. The red circle represents the spot of the excitation laser and the black dashed line is the image of the input slit of the spectrometer onto the sample plane, in scale 1:1 with the reflection image. (b) Spectral image from the full CCD camera display, in units of photoelectrons per time and per pixel. The bottom and top spectra are the QD SE into the waveguide mode and coupled to free space by the bottom and top grating couplers respectively. The central spectrum is the direct free space emission from the QDs. White line: spectrum emitted from the bottom grating couplers.

4.5.1 Geometry of the experiment

In Fig. 4.9(a) a white light reflection image of WG_A is shown. The red spot represents the HeNe excitation laser, positioned approximately at the centre of the PCWG ($x = 0\,\mu m$). The PCWG is clearly visible on the top of the GaAs membrane, and it is terminated by the bottom and the top grating out-couplers. The excitation above the GaAs bandgap induce the radiative emission of the excited QDs. The SE of the QDs, which fills the sample real-space, is imaged onto the input slit of the imaging spectrometer, indicated in scale as black dashed line in Fig. 4.9(a). Importantly, the waveguide has been aligned along the slit, in order to collect and image the emission from the whole waveguide and the grating couplers. The SE spectrum from the QDs is therefore detected spatially resolved along the waveguide and spectrally resolved, as exemplified in Fig. 4.9(c), covering an energy range of about 15 meV for a single spectrometer centre position. The signals around $x = \pm 13\,\mu m$ show the QD SE into the waveguide mode and coupled to free space by the bottom and top grating out-couplers respectively. The spectrum indicated as a white line is integrated over 6 pixels, from -14.3 µm to -11.4 µm, covering the emission from the bottom coupler. The signal around the excitation position $x = 0\,\mu m$ is due to QD SE into the non-guided modes, which are excited by the carrier relaxation and diffusion processes. However, we also observed QD emission from positions far away from the excitation spot, which we attribute to an indirect excitation mechanism, as explained in Sec. 4.5.3. In Fig. 4.10 we show two examples of spectral images. In Fig. 4.10(a), three QDs with different coupling strength to the PCWG mode are highlighted by the rectangular contours. In white we give

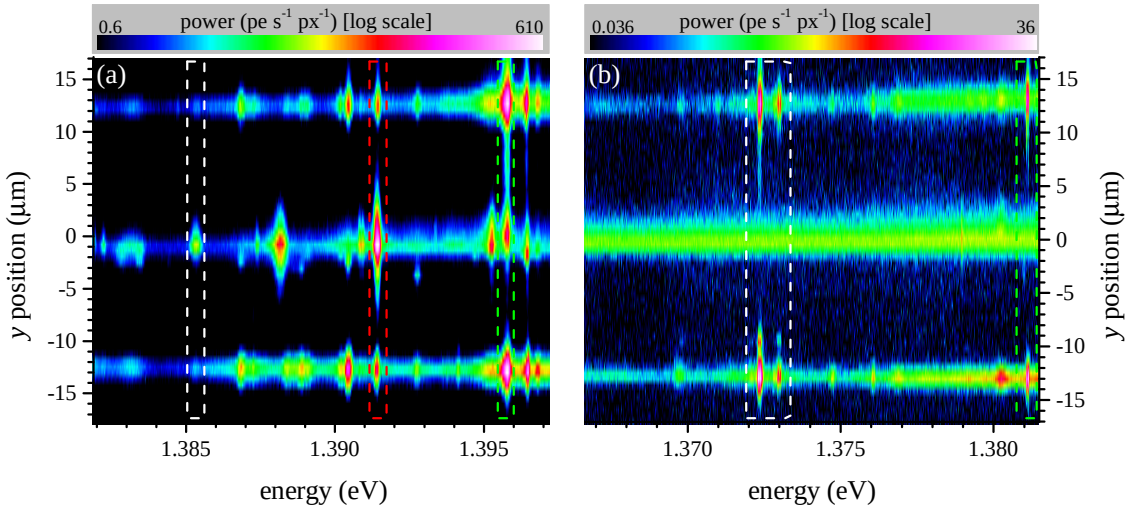

Figure 4.10: Examples of spectral images, showing differently coupled QDs. (a) White, red and green rectangular contours highlight a weakly, intermediate and strongly coupled QDs. (b) QDs indirectly excited. White (green) rectangular contour: QDs with visible (not visible) free space emission.

an example of a QD which is weakly coupled to the PCWG mode, as the emission directly into free space is much more intense than the emission from the grating out-couplers. In red and green we highlight a QD which is weakly coupled and a QD which is strongly coupled, respectively. Fig. 4.10(b), instead, shows cases where non-local excitation occurs, as mentioned above. Although we are exciting at $x = 0\,\mu\text{m}$, the SE into free space is observed at $x = -10\,\mu\text{m}$, together with the SE emitted from the grating out-couplers (white contour). In green we see a case where the SE into free space is not observed at all, and this is true for all the excitation positions along the PCWG (not shown).

4.5.2 Analysis of spectral images

In this section we discuss in detail how the spectral imaging data are analysed to retrieve the emission powers of the QDs. After subtracting the dark background, the data are divided by the integration time and multiplied by the CCD gain of 2 electrons per count, resulting in data as given in Fig. 4.11(a) in photoelectrons per time and pixel (pe $\text{s}^{-1}\text{px}^{-1}$). In order to determine the total detected power from the QD emitted, for example, from the bottom grating out-coupler, the emission is integrated along the waveguide over the number of pixels contained in the region of interest. This region is highlighted in Fig. 4.11(a) with dashed green lines. The lineshape is fitted using a Voigt profile, as shown in Fig. 4.11(c). The analysis is then repeated for the emission from the top coupler, as well as directly from free space, to recover the total emission. When $B_z = 0.45\,\text{T}$, line splitting is observed, as visible in Fig. 4.14. In this case, we first fit the QD direct free space emission using a double Voigt profile, without any constraint on the fit parameters aside that the two lines have the same linewidth parameters. From this fit we use the linewidth and splitting. The emissions from the bottom and top couplers are then fitted

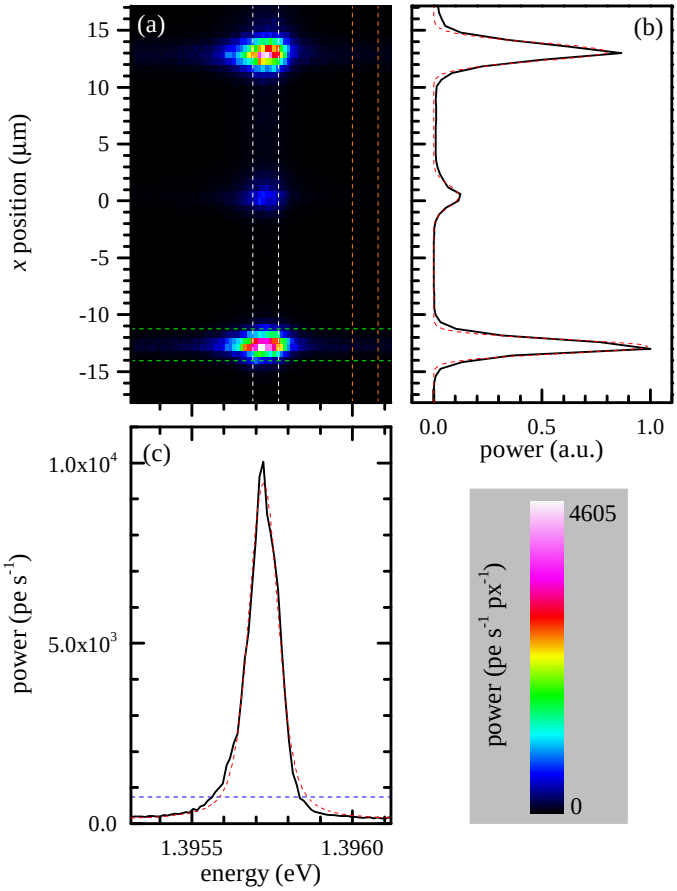

Figure 4.11: (a) An example of spectral image zoomed on a single QD line. (b) QD emission as a function of the position along the PCWG. The curve is obtained as the difference of a spectral average along and next to the waveguide region, as given by the white and orange dashed lines shown in (a). (c) Lineshape of the QD SE emitted from the bottom out-coupler (solid line), calculated as a spatial integral over the region given by the green dashed lines shown in (a); the corresponding background level is given by the blue dashed line; dash dotted lines are fit to the data.

using this linewidth and splitting. In any case, the area of the fitted peak, in units of photoelectrons per time, corresponds to the measured "raw" power P^{raw}. In order to obtain the QD position along the PCWG, the emission is averaged along the energy axis. We separate the QD signal from the excitation background by averaging over two regions: one includes the QD signal and the other only the excitation background (white and orange dashed lines in Fig. 4.11(a) respectively). The latter region is taken very close to the QD under consideration to limit spectral inhomogeneities. We then subtract the excitation background to recover only the signal from the QD. The result is shown in Fig. 4.11(b). We fit the obtained profile using a three gaussian peaks function. From the position of the grating couplers we calibrate the x axis. For most of the QDs, the error resulting from the fit is less than 100 nm (standard deviation). Similarly, by fitting only the excitation background we can determine the excitation position along the waveguide.

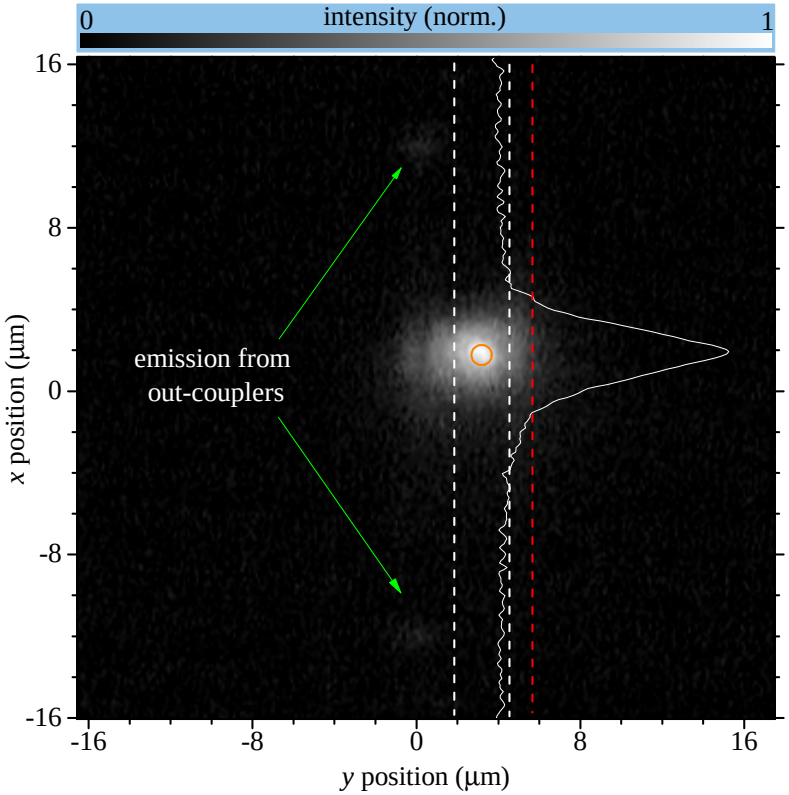

Figure 4.12: SE emission spot corresponding to the carrier diffusion on the photonic crystal membrane. Red dashed line: right edge of the membrane. Carriers reaching the waveguide region excite the QDs, and the corresponding coupled emission is visible from the grating out-couplers, as highlighted. Solid white line: carrier diffusion profile, obtained averaging along the "y position" axis, in the region between white dashed lines. Orange circle: HeNe spot.

4.5.3 Excitation mechanisms

There are two possible mechanisms to excite QDs: direct and non-direct. The direct excitation mechanism is the dominant one. It consists of creation of electron-hole pairs in the GaAs membrane, which are captured by the QDs located within a radius of the order of the carrier diffusion length from the excitation laser. In order to measure the carrier diffusion length in the planar region of the sample, we use direct imaging of the SE on the real-space camera (see Fig. 2.4). This measurement is shown in Fig. 4.12. The HeNe laser was focused sideway with respect to the PCWG, as shown by the orange circle, and filtered out with a long-pass colour filter RG680 (F) with a cutoff wavelength of 680 nm, positioned just in front of the real-space camera. The larger visible spot is due to the SE from the excited QDs, ad its size is determined by the average distance carriers can travel on the GaAs membrane, i.e., the carrier diffusion length. The SE profile, shown along the x direction by the white solid line, is obtained as the average along the "y position" axis over the region between white dashed lines. By fitting the profile with a Gaussian function, we obtain a carrier diffusion length of about 3 µm (considered as the intensity FWHM obtained from the fit). Although the excitation spot is focused next to the PCWG, QDs are excited also in the PCWG region, and the coupled SE is visible from the grating

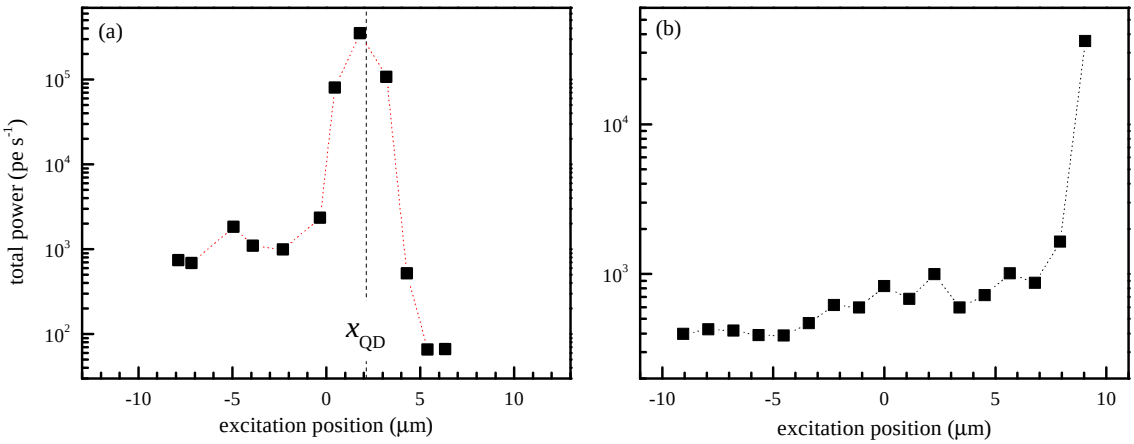

Figure 4.13: (a) Total power of a QD as a function of the excitation position along the waveguide. The black dashed line indicates the deduced QD position from the analysis presented in Sec. 4.5.2. (b) As (a), but for a QD whose direct free space emission in not visible. The trend of the total power allows us to determine the QD position along the waveguide.

out-couplers, as highlighted in Fig. 4.12.

However, as already mentioned, we also observed QD emission from positions far away from the excitation spot. Importantly, these QDs emit between 890 and 900 nm. This is attributed to the indirect excitation mechanism, where the WL emission, which is coupled into the PCWG mode, is absorbed by the QD excited states. Most likely, the WL emission is resonant with the trion p-shell (see Supplementary Material of Ref. [146] and Ref. [168]), which is 35-40 meV above the s-shell, in agreement with the energy separation between the WL emission and the QDs emitting at 890-900 nm. This non-local excitation mechanism which occurs for few QDs, allows us to perform studies as a function of the excitation position along the PCWG, which we describe in the next section.

4.5.4 Scanning the excitation position along the waveguide

The non-local excitation mechanism, which we observe for few QDs, allows us to perform studies as a function of the excitation position along the PCWG. In Fig. 4.13(a) we show the total SE as a function of the excitation position along the PCWG for one specific QD and for a fixed excitation power $P_{\text{exc}} = 0.5\,\mu\text{W}$ given at the sample plane. The total SE is calculated by summing the measured powers from the bottom and top grating couplers and non-guided modes. Notably, the total emission varies over three order of magnitudes when scanning the excitation position along the PCWG. As expected, it shows a maximum when the excitation position is at the QD location. This is highlighted by the black dashed lines given in Fig. 4.13(a), which indicates the QD x position calculated as described in Sec. 4.5.2. Therefore, one can use this property to estimate the QD position along the waveguide also in the case where the QD free space emission is not observed. One of these cases is shown in Fig. 4.13(b). The trend of the total SE suggests that the QD is located closed to the top grating out-coupler.

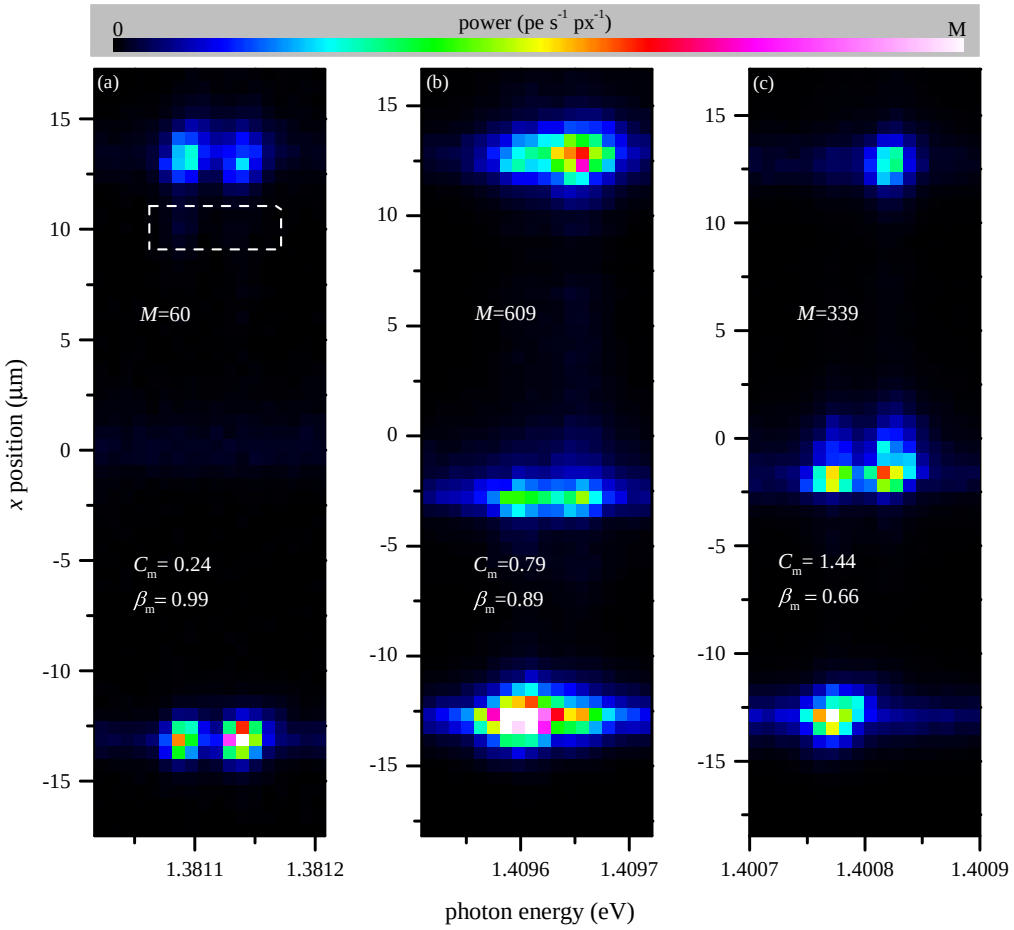

Figure 4.14: Single QD spectral images. (a), (b), (c) Spectral images of three different QDs located at sites with (a) low, (b) intermediate and (c) high waveguide mode circularity C_{m}. The corresponding beta factors β_{m} are given. The weak free space emission of the QD in (a) is highlighted by the rectangle in white dashed line.

4.6 Beta factor and directional emission

In this section we show measurements of the beta factor and waveguide mode circularity.

By zooming a spectral image around the single QD emission, we identify the SE of individual QDs from the top and bottom couplers and from the QD position into non-guided modes. The excitation position is adjusted along the PCWG to maximise the QD emission. The measurements were performed at a low excitation power to avoid multi-exciton emission, and with a magnetic field of 0.45 T in Faraday configuration (i.e. orthogonal to the plane of the PCWG). Examples of the SE detected for three different QDs are shown in Fig. 4.14(a), (b) and (c), covering a small spectral range of 210 μeV suited to contain the QD linewidth and the spin-split doublet created by the magnetic field. For the QDs shown in Fig. 4.14, we measured a spin-splitting $\Delta E_z \sim 50\,\mu$eV. As the exciton has spin projection $S_z = \pm 1$, the Zeeman splitting between these states is given by $\Delta E_z = 2\mu_{\mathrm{B}} g_X B_z$, with μ_B the Bohr magneton. Using $B_z = 0.45\,\mathrm{T}$, we calculate an exciton g-factor $g_X \sim 0.96$, which is similar to what reported in [145].

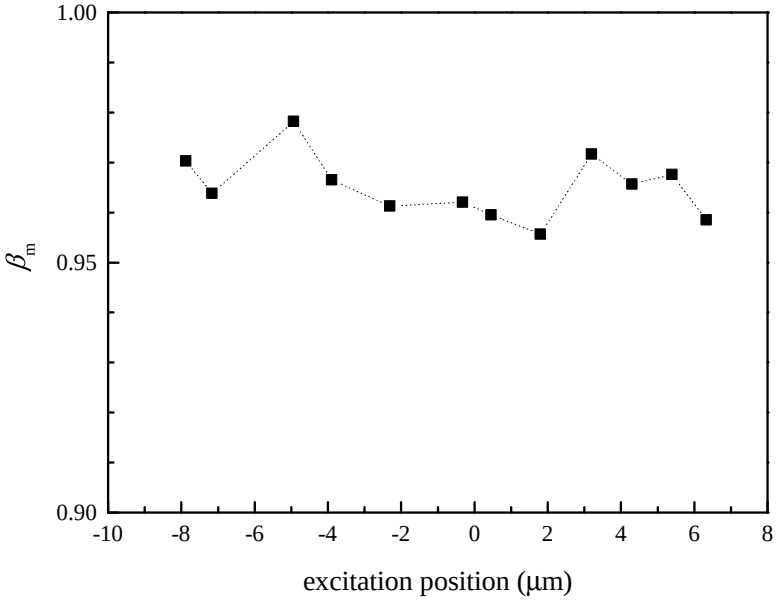

Figure 4.15: β_m of another QD as a function of the excitation position along the waveguide.

From the spectral images shown in Fig. 4.14, the probability that a spontaneously emitted photon couples to the waveguide, i.e. the beta factor, can be calculated as the ratio between the power emitted from the couplers and the total emitted power. In formula:

$$\beta_m = 1 - \frac{\sum_j P_{fs}^j}{\sum_j (P_t^j + P_b^j + P_{fs}^j)} \ , \tag{4.5}$$

where $P_{b,t,fs}$ are the detected SE powers of a single QD from the bottom and top grating out-couplers and at the QD site respectively, corrected for the losses and the gratings relative efficiencies as described in Sec. 4.7, and $j = \pm$ labels the helicity of the QD transition. We note that the β_m values we report are not corrected for the simulated collection efficiency of free-space and coupler emission discussed in Sec. 4.8.4 and Sec. 4.8.3 respectively, which would increase the beta factor, since the free space emission is collected typically twice as efficiently, depending on the QD position. Furthermore, from the spectral images we can determine the QD energy and the QD position along the waveguide, x_{QD}, as explained in Sec. 4.5.2. For the QD shown in Fig. 4.14(a), we evaluate $\beta_m = 0.99 \pm 0.01$. The QD is located close to the top grating coupler, as highlighted in the figure by the white dashed rectangle. This is indeed the same QD shown in Fig. 4.13(b). Importantly, we use the indirect excitation mechanism to verify that the β_m is independent of the excitation position. In Fig. 4.15 we show an example of β_m as a function of the excitation position, and we find that the β_m is constant within fluctuations of the order of 1% standard deviation. This is expected as the relative weights of the QD coupling to the waveguide mode and to free space depend only on the projected local density of optical states at the QD site, and it is therefore independent of the excitation position. This analysis sets a lower limit for the error of β_m. Fig. 4.14(b) and (c) instead show the SE of QDs with

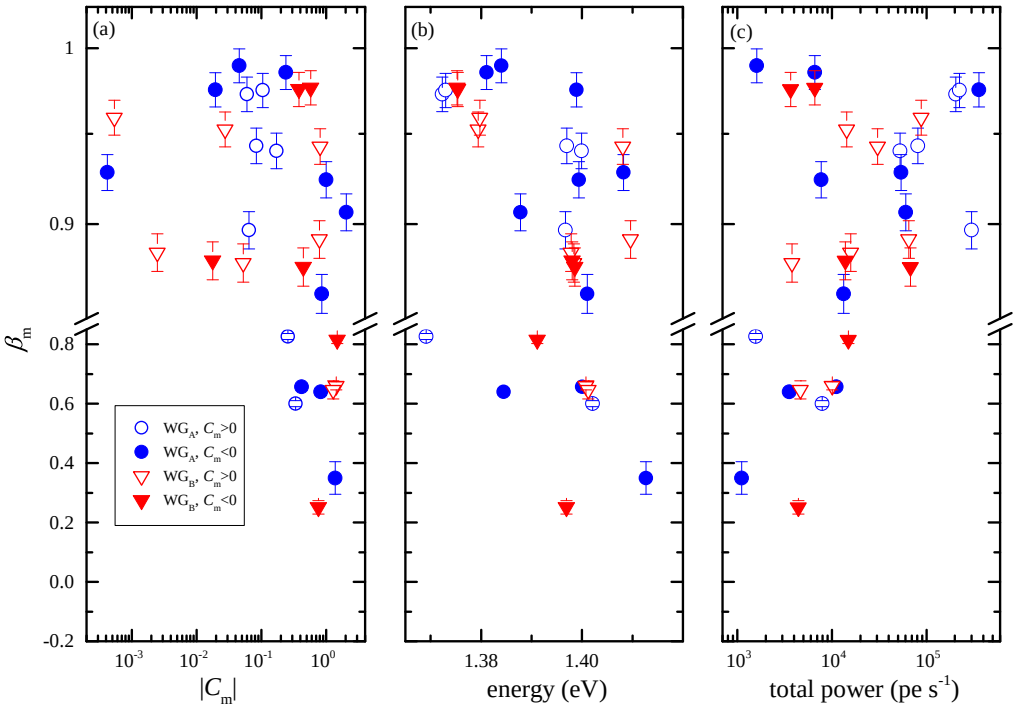

Figure 4.16: (a), (b), (c) Measured beta factor β_m as a function of (a) mode circularity $|C_m|$, (b) QD peak energy and (c) total emission power for local excitation.

$\beta_m = 0.89 \pm 0.01$ and $\beta_m = 0.66 \pm 0.01$, respectively.

The directional emission is evident in the asymmetry of the power from top and bottom couplers. The degree of directionality depends on the waveguide mode circularity C_m at the QD site, which we define here as

$$C_m = \frac{1}{4}\ln\left(\frac{P_t^+ P_b^-}{P_t^- P_b^+}\right) \quad . \tag{4.6}$$

which by taking the dual power ratio is independent of the efficiencies of the grating couplers. It is related to the directionality D used in Ref. [145] by $D = \tanh(C_m)$, making it equal for small circularities but avoiding saturation for high circularities. At a circularly polarised point (C-point), C_m diverges. On the other hand, at a linearly polarised point (L-point) C_m is zero. The images shown in Fig. 4.14 correspond to QDs on a point with low (a), intermediate (b) and high (c) mode circularity. Notably, the QD free space emission increases for larger $|C_m|$, reducing β_m. To provide a statistically relevant result, the circularity and β_m have been determined for 31 QDs, in WG_A and WG_B, as shown in Fig. 4.16(a). The reduction of β_m for QDs located at points of high circularity is observed for both waveguides. This is expected, as circular points require both transversal and longitudinal fields, and thus do not occur at the mode field antinode. We find positive and negative circularities with almost equal probability, for both the waveguides. Furthermore, we find β_m >0.90 over a range of about 40 meV (see Fig. 4.16(b)). In particular, in the WG_A we find QDs with β_m >0.90 for energies between 1.37234 eV and 1.40822 eV. This

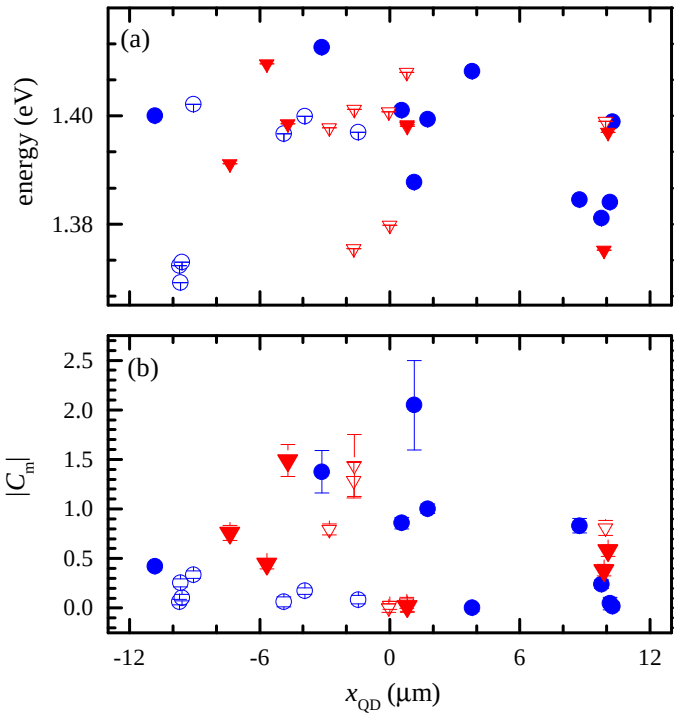

Figure 4.17: Spatial distribution of QD energy (a) and circularity (b) along the PCWG. The error bars result from the fit shown inFig. 4.11(b). Legend as in Fig. 4.16(a).

spectral range corresponds to a region of overlap of the fundamental and the higher order mode. Whether a QD couples mainly to one or the other mode depends not only on the QD energy, but also on its position within the PCWG unit cell, as discussed later. Importantly, these results show that efficient coupling occurs even in region of low group index within the light cone. In Fig. 4.16(c) we plot β_m as a function of the total SE power from the QD when this is locally excited, using for all the QDs the same excitation power $P_{exc} = 0.5\,\mu W$, given at the sample plane. We find β_m >0.90 over three order of magnitudes in the total emission, showing that the β_m is uncorrelated to the total SE from the QDs. This indicates that the emission power is dictated by the local carrier capture dynamics, which depends on the disorder landscape in the WL close to the QDs. Therefore, we attribute such a wide range of intensities to the different carrier capture efficiencies of the QDs, which depends on the local disorder. Additionally, one would expect that there is no correlation of energy and WG mode circularity with the QD position along the PCWG. The experimental data are given in Fig. 4.17, and exhibit a random distribution of energy and circularity along the QD position, consistent with this expectation.

4.7 Discussion of the systematic errors

At this point, it is important to discuss the complications and limits of determining the beta factor and mode circularity using spectral imaging. All the experimental graphs shown in this chapter show β_m and C_m, which are calculated from the raw QD powers

corrected for the propagation losses, for the relative efficiencies of the grating out-couplers and for the coupling efficiency into the spectrometer slit.

There are different factors that make the raw powers different from the true powers emitted by the QDs, which are the ones we need to have an accurate estimate the beta factor and the mode circularity.

First of all, the grating out-couplers can have different relative extraction efficiencies due to fabrication imperfections. This affects only the measured β_{m}, while it does not affect C_{m}, as the grating efficiencies simplify according to the definition given in Eq. 4.6.

On the other hand, propagation losses affect both. The two corrections are discussed in details in Sec. 4.7.1.

The coupling efficiency into the spectrometer slit might be different for the grating out-couplers, modifying the effective collection efficiencies.

Residual reflections from the grating couplers might limit the maximum value of C_{m}, and leave unchanged the β_{m}. This systematic is discussed in Sec. 4.7.2.

Another source of error is the different collection efficiencies of the direct free space emission from the QDs, and of the emission from the grating out-couplers. The collection efficiency is determined by the far-field profile at the plane of the MO and the corresponding real-space profile at the plane of the input slit of the spectrometer. Although both the far-field and real-space profiles from the grating out-couplers and free space are simulated with FDTD simulations (this is discussed in Sec. 4.8), the correction can not be directly applied to the experimental data. Indeed, the free space far-field profile depends on the position of the QDs within the lattice unit cell, and this is not known a priori. Therefore, we apply the opposite approach: we first correct the simulations in order to make them as close to the experimental data as possible; then, comparing experimental data with simulations, we determine the most likely QD position within the lattice unit cell. The corrections applied to the simulations are explained in details in Sec. 4.9.2.

4.7.1 Losses model

In this section we discuss how we determine the relative efficiencies of the two grating out-couplers, including also the coupling efficiency into the spectrometer slit, as well as propagation losses, from the spectral images.

The analysis has been applied to the data taken with B_z=0.45 T. For a given excitation position along the PCWG, we call L_{t} and L_{b} the distances between the excitation position x and the top and bottom couplers respectively, as given in the inset of Fig. 4.18(a). In the following t, b label the top and bottom couplers respectively. In this way, $L_{\frac{\mathrm{t}}{\mathrm{b}}} = L/2 \mp x$, with L the length of the waveguide. Using a simple Lambert-Beer extinction model, the SE powers emitted from the top and bottom couplers are proportional to $\eta_i \exp(-\alpha L_i)$ with $i = \mathrm{t}, \mathrm{b}$. η_i includes the relative extraction efficiencies of the couplers as well as the coupling into the spectrometer slit. On the other hand, α is a parameters describing the propagation losses. The present model assumes that most of the emission is locally excited,

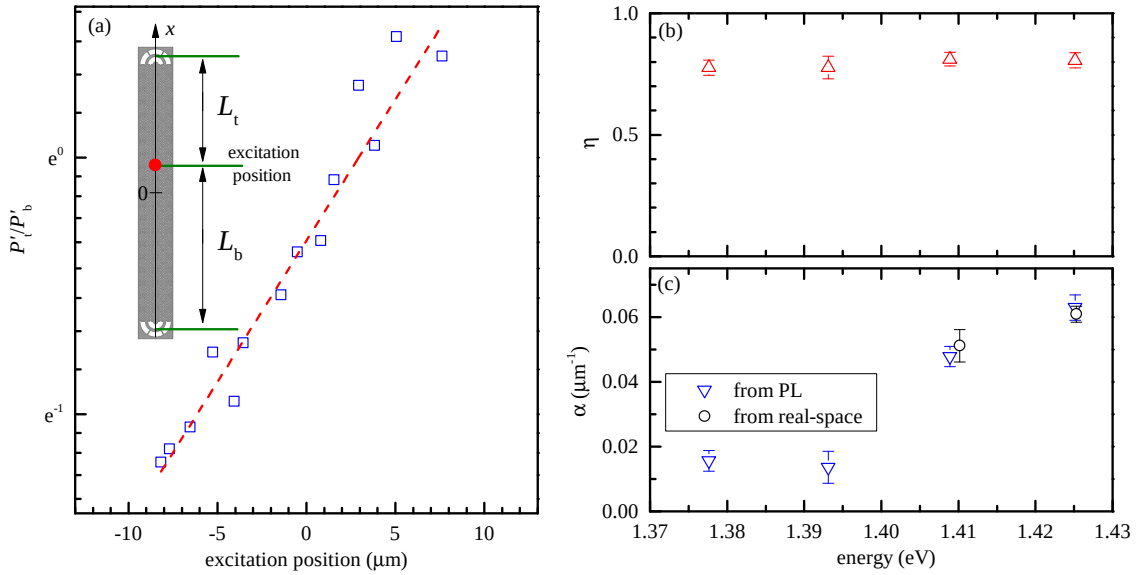

Figure 4.18: Loss coefficient from SE measurements. (a) Ratio P'_t/P'_b as a function of the excitation position for the spectral range centred at $E_0 = 1.4251\,\text{eV}$. Inset: model applied to calculate the loss coefficient. (b) Grating relative efficiency as a function of energy; an average value $\eta = 0.79 \pm 0.02$ is found. (c) Triangle: losses coefficient as a function of energy. Circle: losses coefficient calculated from real-space imaging, as described in Sec. 4.4.1.

which is consistent with the experimental findings of the imaging along the PCWG, as discussed in Sec. 4.5.3. To apply the model, we integrate the PL emissions from the bottom and top couplers over the full spectral range covered by the CCD camera (about 15 meV), to average over the directionality of individual QDs. Calling P'_b and P'_t the spectrally integrated measured emission, we then calculate the ratio P'_t/P'_b and plot it as a function of the excitation position x. According to the above model, the ratio is given by

$$\frac{P'_t}{P'_b} = \eta e^{2\alpha x} \quad , \tag{4.7}$$

with $\eta = \eta_t/\eta_b$. The result and the corresponding fit is shown in Fig. 4.18(a) for the spectral range centred at E_0=1.4251 eV for WG_A. A good agreement between data and fit is observed. We repeat the same analysis for all the 4 spectral ranges considered in the experiment. In Fig. 4.18(b) and (c) we show the ratio η and the losses coefficient α determined from the fit as a function of energy respectively. Importantly, η is constant, as expected. We calculate an average value of $\eta = 0.79 \pm 0.02$, which we use to correct the emission intensities of all the data taken on this waveguide. The analysis is repeated with WG_B, giving a similar result ($\eta = 0.6 \pm 0.1$, see appendix A). On the other hand, α increases with the energy. Remarkably, the loss coefficient calculated in this way is in good agreement with the one calculated from real-space imaging (shown in black circles in Fig. 4.18(c)), confirming the analysis.

With both η and α at hand, we can correct the experimental data. In particular, being the spectrally integrated emission from the top coupler smaller than the one from

the bottom coupler for central excitation position, the top coupler is less efficient than the bottom one. As this is the case for both the waveguides, the raw powers have been corrected using the following expression:

$$\begin{aligned} P_{\mathrm{b}}^{j} &= P_{\mathrm{b}}^{j,\mathrm{raw}} \exp\left[\alpha\left(L/2 + x_{\mathrm{QD}}\right)\right] \\ P_{\mathrm{t}}^{j} &= \frac{P_{\mathrm{t}}^{j,\mathrm{raw}}}{\eta} \exp\left[\alpha\left(L/2 - x_{\mathrm{QD}}\right)\right] \quad , \end{aligned} \tag{4.8}$$

with P_{b}^{j} and P_{t}^{j} the power used in Eq. 4.5 and Eq. 4.6.

4.7.2 Reflection coefficient

In order to understand if reflections are affecting the observed waveguide mode circularity, we consider the measured powers of the QD with the highest mode circularity we found. To first order in the reflection coefficient R, the measured power from top coupler, $P_{\mathrm{t}}^{j,\mathrm{raw}}$, should be subtracted by the reflection of the raw power from the bottom coupler, $P_{\mathrm{b}}^{j,\mathrm{raw}}$, to give $A_j \approx P_{\mathrm{t}}^{j,\mathrm{raw}} - RP_{\mathrm{b}}^{j,\mathrm{raw}}$, and vice versa, $B_j \approx P_{\mathrm{b}}^{j,\mathrm{raw}} - RP_{\mathrm{t}}^{j,\mathrm{raw}}$. Requiring that these powers are positive, we find from the measured powers of all investigated QDs shown in Fig. 4.16 an upper limit for R of about 3-5 %. The reflection leads to a systematic underestimation of the absolute circularity, and for 5 % is limiting the measured circularity to $|C_{\mathrm{m}}|<1.8$. The dynamic range of our experimental data is sufficient to measure $|C_{\mathrm{m}}|$ above 4, and is thus not limiting the results presented.

4.8 Simulations

In this section, we present FDTD simulations that are performed to quantitatively interpret the experimental data. The simulations have been implemented by Benjamin Lang and collaborators. Benjamin Lang run the model to generate all the simulated data.

4.8.1 Simulation parameters

The first thing we do is to adjust the sample parameters in the simulations to match the measured dispersion of the fundamental mode, shown in Fig. 4.5(a). We start using exactly the nominal sample structure, which has a lattice constant $a = 260\,\mathrm{nm}$, hole radius $r = 0.24$ ($r = 0.26$) a for $\mathrm{WG_A}$ and $\mathrm{WG_B}$ respectively, membrane thickness of 125 nm, and six layers of air holes place on both side of the line defect forming the PCWG. The membrane thickness and hole diameters have been measured by SEM, and they are found to be approximately equal to the nominal parameters. Also, from the SEM images we find that the grating period has a negligible fabrication error. The implemented simulation geometry is the following: along x, which is the propagation direction, we use periodic boundary conditions (PBCs), in the $\pm z$ simulation facets (with z the out-of-plane direction) we use perfectly matched layer (PML), and in the $\pm y$ simulation facets we use adiabatic absorbers [169] to absorb light escaping in this direction. The simulations are

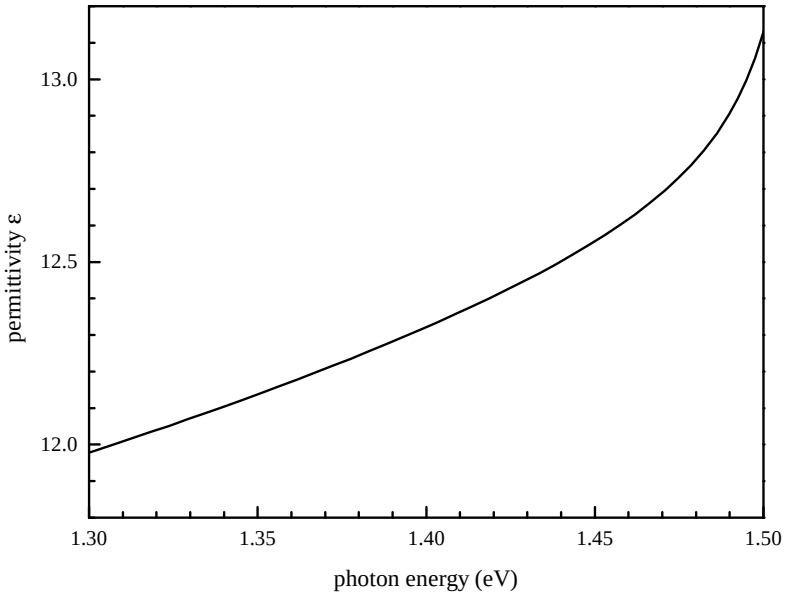

Figure 4.19: Dependence of the GaAs permittivity ε on the photon energy used in the calculations. Data from the material implementation of Eq. 4.9 in FDTD. Benjamin Lang built and run the model to generate the simulated data; plot produced by the author.

performed over a single unit cell, using a randomly located source. By Fourier transforming the time domain data, we extract the mode resonances. We note that the refractive index of GaAs has previously been used as adjustable parameter, set to $\sqrt{12}$ in [84], n=3.5 at T=15 K in [153] and n=3.45 K both at 4.2 K and 10 K in [142]. However, the GaAs index is well known, and significantly higher than these values. The refractive index of the slab is therefore taken here as the one of GaAs at the sample temperature of T= 5K, including its dispersion, according to the following formula [170]:

$$\varepsilon(E) = 5.965 + \frac{3.04 \times 10^{-2}}{1.519^2 - E^2} + \frac{33.1494}{2.692^2 - E^2} + \frac{2.38 \times 10^{-3}}{0.0334^2 - E^2} \quad , \tag{4.9}$$

with ε the dielectric constant, expressed in eV. The QD layer embedded in the slab corresponds to less than 1% of its thickness and is made of a similar material as GaAs. It is therefore not having a significant effect on the dielectric environment. In Fig. 4.19 we show the energy dependence of the GaAs at T=5 K according to Eq. 4.9. The simulated dispersion which makes use of the nominal parameters is in disagreement with the measured dispersion, for both WG_A and WG_B, as shown in Fig. 4.20 (a) and (b) respectively. So the question arises of how to properly change the parameters of the simulations to find the best matching. It is known that GaAs oxidises over time [171], and, as a consequence, its refractive index reduces. This can be modelled by using an over-etching parameter t_e, whose effect is to decrease the effective thickness of the membrane t_m such that $t_m \rightarrow t_m - t_e$, as well as increase the effective radius of the holes r such that $r \rightarrow r + t_e$. Additionally, the SEM images we use to measure the sample parameters are taken before the high selective etching which removes the sacrificial layer of AlGaAs below the PCWG

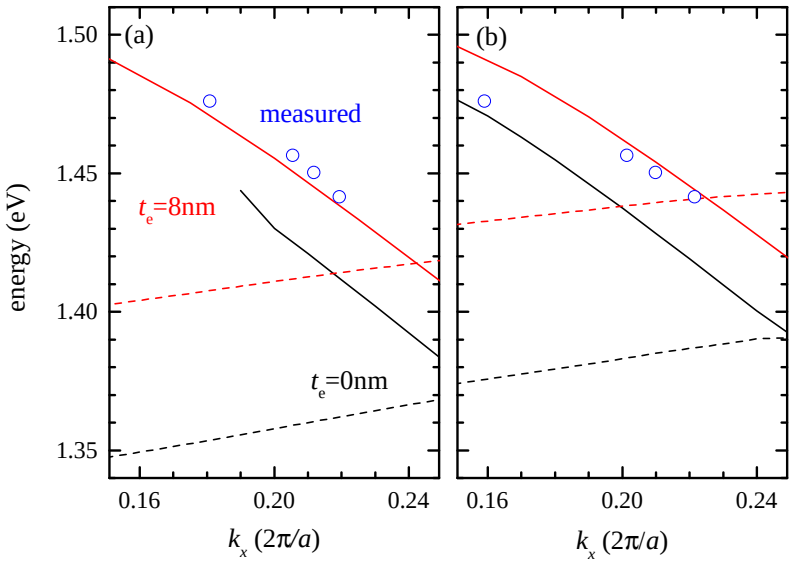

Figure 4.20: Matching simulations to the measured mode dispersion for (a) WG_A and (b) WG_B. Solid lines: fundamental mode; dashed lines: higher-order mode; black lines: $t_e = 0\,nm$; red lines: $t_e = 8\,nm$; Circles: measured (see Fig. 4.5). Benjamin Lang built and run the model to generate the simulated data; plot produced by the author.

membrane. This process also might reduce the membrane thickness and increase the hole radius, and it is therefore included in the over-etching parameter t_e. Because the effects of oxidation and high selective etching should be reasonably homogeneous across the sample chip, we choose t_e to obtain the best matching for both WG_A and WG_B. The results are shown in Fig. 4.20 (a) and (b) respectively, for which we use $t_e = 8\,nm$. For both PCWGs, the simulations match the measured dispersion reasonably well. In Fig. 4.21 we show the corresponding modulus of the electric field amplitude $|E| = \sqrt{|E_x^2| + |E_y^2|}$, and the ellipticity ε and the orientation θ of the polarisation ellipse as defined in Sec. 1.6, in the plane $z = 0$, for WG_A. In this case, in order to collect the field for the fundamental and higher order mode separately, the source position within the unit cell and polarisation is chosen to selectively excite only one of the two modes, owing to the symmetry properties of the structure (see Sec. 1.6). For example, by placing a source polarised along y at $y = 0\,\mu m$ (for a generic x position), only the fundamental mode is excited. The source energy is fixed to $E = 1.39\,eV$. The corresponding propagation wavevectors are indicated in the right inset of Fig. 4.21, with the higher order mode having two branches, propagating inside ($k_x(\pi/a) = 0.05$) and outside ($k_x(\pi/a) = 0.86$) the light cone.

4.8.2 Losses

As shown in Sec. 4.6, a large fraction of QDs show $\beta_m > 0.90$ also when they couple to modes within the light cone, where $\omega > ck_x$. This was surprising to us at first, as we were not expecting to see strongly coupled QD in this spectral region. Therefore, we perform simulations to better understand the origin of propagation losses. They are carried out for WG_A only.

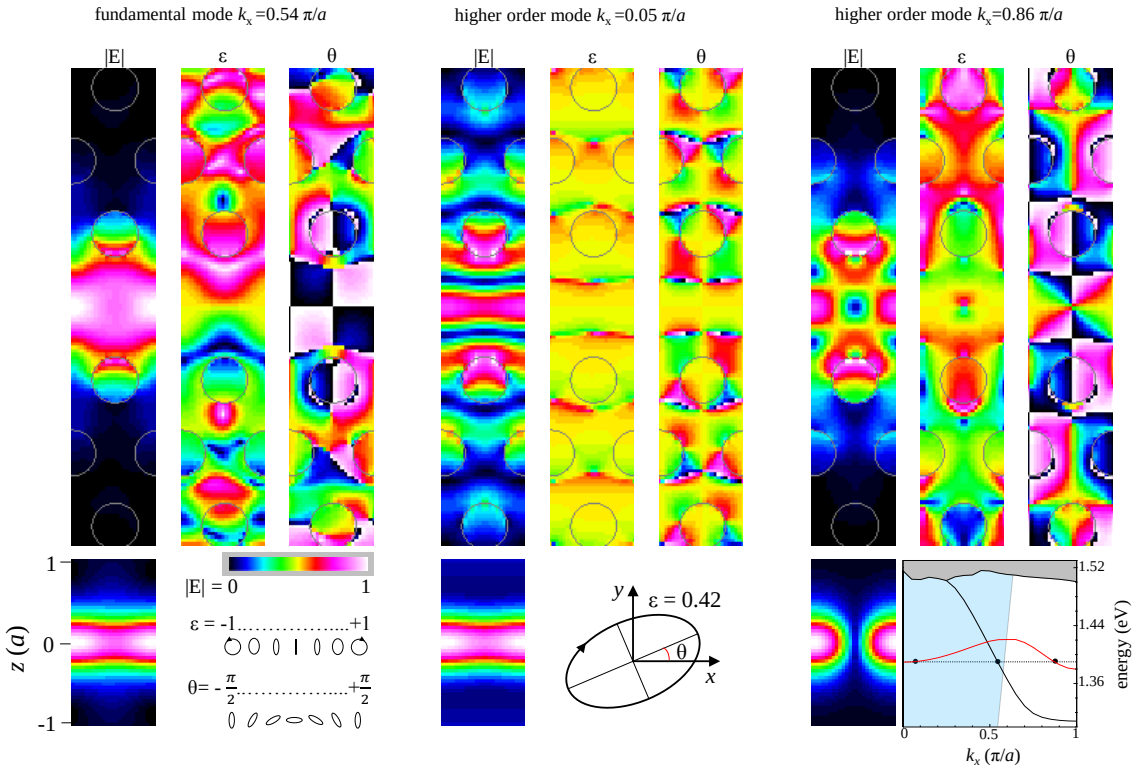

Figure 4.21: Modulus of the electric field amplitude $|E| = \sqrt{|E_x^2| + |E_y^2|}$ and polarisation ellipse ellipticity ε and orientation θ in the plane $z = 0$, for $\mathrm{WG_A}$. θ is defined according to the sketch shown in the central panel. The source energy is $E = 1.39\,\mathrm{eV}$, which corresponds to the indicated propagation wavevectors, according to the dispersion shown in Fig. 4.5(a). Benjamin Lang built and run the model to generate the simulated data; plot produced by the author.

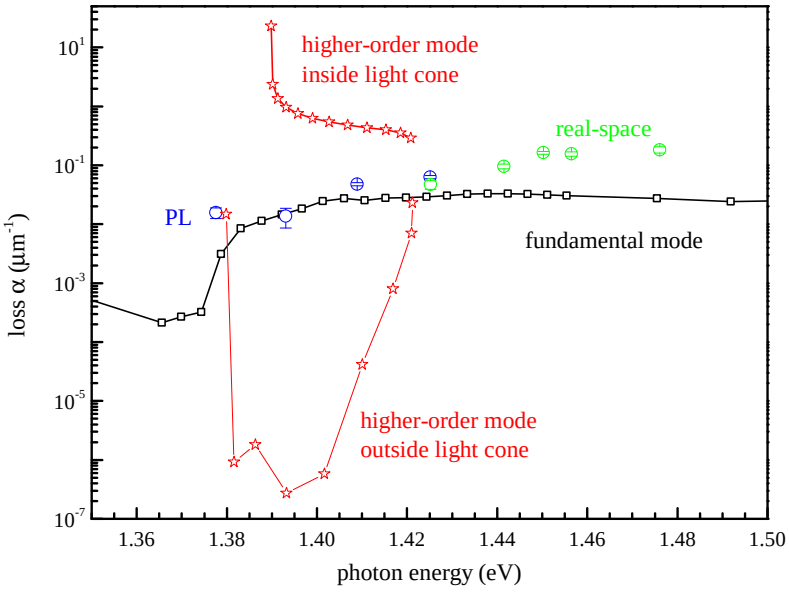

Figure 4.22: Simulated propagation loss of the fundamental mode (black squares) and higher order mode (red stars). Blue circles: loss measured from PL. Green circles: loss measured from real-space imaging. Benjamin Lang built and run the model to generate the simulated data; plot produced by the author.

The loss was simulated with the method described in Sec. 4.8.1, choosing the symmetry of the simulation and source either even or odd to excite only one of the two guided modes, and increasing the height of the simulation to ten unit cells allowing to better separate the out of plane loss from the in-plane propagation. We use a source with a Gaussian time dependence of 29 fs standard deviation, truncated at 5 standard deviations either side of the peak. Assuming that by the simulation's end (1000 time-steps, equivalent to about 870 fs, after the source is switched off) the contribution of unguided modes is negligible, the Poynting vector was calculated, providing the power flux density distribution of the excited mode. This distribution was used to calculate the flux F_z through the $\pm z_s$ planes (out-of-plane loss), F_x through the $+x_s$ plane (along the PCWG) and F_y through the $\pm y_s$ planes (tunnelling through the cladding). The transmission coefficient per unit cell is then given by:

$$T = \frac{F_x}{F_x + F_y + F_z} \quad . \tag{4.10}$$

The loss coefficient α is then determined using the relation $T = \exp(-\alpha a)$, according to a Lambert-Beer model, with $a = 260\,\text{nm}$. We note that α calculated in this way includes both out-of-plane losses (along z) and in-plane losses (along y). The results of the calculations are shown in Fig. 4.22, for both the fundamental mode and the higher order mode, for the energy range relevant for the experiment. Let us first interpret the results for the higher order mode. In this case, two branches are observed (red stars): one branch gives the losses of the mode outside the light cone and the other one inside the light cone. As expected, losses inside the light cone are much higher than outside the light cone. Around $E = 1.38\,\text{eV}$ and $E = 1.42\,\text{eV}$ also the losses of the branch outside the light cone are significant. The reason is that these energies correspond to regions of slow light, where losses are expected to increase due to the longer time light needs to propagate. On the other hand, the fundamental mode (black squares) has only one branch, which is propagating within the light cone for the energies shown in the figure (see also Fig. 4.5(a)). Importantly, the calculated losses are in good agreement with the measured losses up to $E \sim 1.42\,\text{eV}$ (blue and green circles). Above this energy, the measured losses are higher than the simulated one. We attribute this behaviour to the WL absorption and possible fabrication imperfections.

4.8.3 Grating collection efficiency

As discussed in Sec. 4.7, it is very important to determine the collection efficiency of the emission from the grating out-couplers as well as of the free space emission from the QDs. We now discuss both cases.

For this purpose, we perform again FDTD simulations. A map of part of the simulation volume is shown in Fig. 4.23. Two different simulations are needed: a calibration simulation without grating out-coupler (left panel), and a simulation with the grating (right panel). In both cases, the source is placed off the left of the simulation area shown in the figure, at the same distance from the green vertical line. Similar to the simulation of the losses,

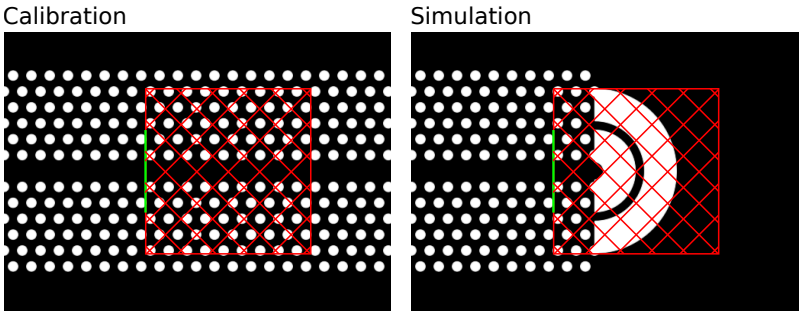

Figure 4.23: Part of the FDTD volume for the calibration and grating simulations. The green line indicates the plane that measures the flux incident on the grating. This same plane measured the grating reflectivity. The red hatched region indicates the area over which the grating flux was measured.

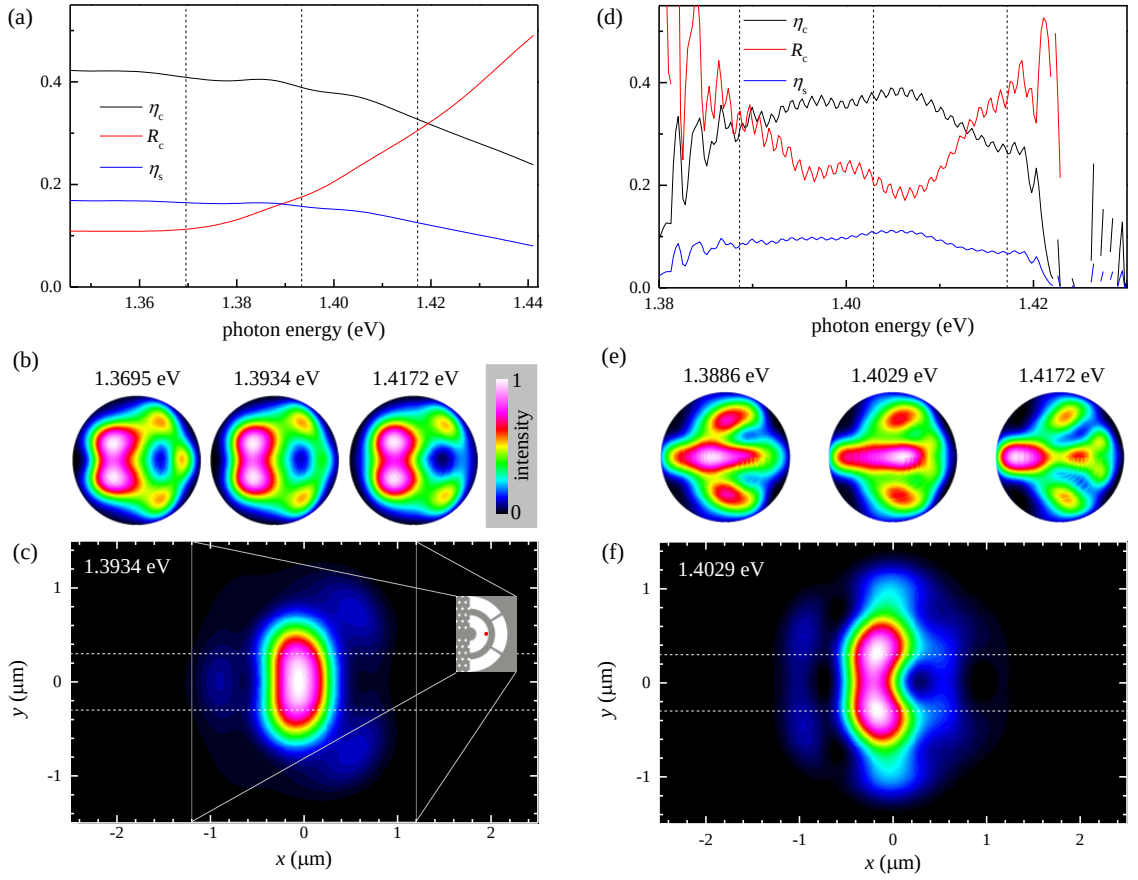

Figure 4.24: (a) The simulated efficiency and reflectivity of the grating for the fundamental mode as a function of energy. The blue line indicates the efficiency of the grating when the effects of the microscope NA and the spectrometer slit are also included. (b) Far-fields radiated from the grating for three choices of frequency; the centre corresponds to vertical emission, the edge to horizontal emission. (c) The real-space profile at $E = 1.3934\,\text{eV}$ (after focusing with a microscope of NA=0.85). The effective size of the spectrometer slit is shown by the white dashed lines. (d), (e), (f) as (a), (b), (c) but for the higher order mode. Benjamin Lang built and run the model to generate the simulated data; plot produced by the author.

the source position within the unit cell and polarisation is chosen to selectively excite only one of the two modes. We use thick layers of adiabatic absorbers placed both off right and left of the simulation area, in order to minimise numerical reflections, also in the case of slow-light modes. The flux radiated toward the grating is measured at the flux plane represented by the green vertical line. The out-of-plane flux radiated from the grating out-coupler is measured at the flux plane represented by the red grid. This flux plane is positioned just above the slab.

The efficiency of the grating is determined by the fraction of power that enters the grating, calculated as the flux through the green vertical line, and the power that escapes the grating in the out-of-plane direction, calculated as the flux through the red grid. Note that the efficiency upward (which is the one we are interested in) is limited to 50% because of the emission in both the $\pm z$ directions. We can also estimate the reflectivity of the grating, as the difference between the net flux toward the grating through the green vertical line and the flux through the same flux plane in the calibration simulation. Efficiency and reflectivity are shown in Fig. 4.24(a) and (d) for the fundamental mode and higher order mode respectively, in the energy range relevant for our experiment. The visible fringes in Fig. 4.24(d) are due to residual numerical reflections coming from the slow-light regions of the higher order mode, which interfere with the incoming field.

Using the same simulations we also collect the far-field profile of the emission from the grating out-coupler. The profiles are shown in Fig. 4.24(b) and (e) for three different energies as indicated, for the fundamental mode and higher order mode respectively. With the far-field at hand, we can calculate the collection efficiency of our setup, which is mainly determined by the objective NA and the input slit of the spectrometer. The collection from the objective is determined by calculating the fraction of far-field contained in the NA. The resulting far-field profiles are then transformed back into real-space profiles, which are shown in Fig. 4.24(c) and (f) for the fundamental and higher order mode respectively, together with the effective size of the spectrometer slit at the sample plane, given by the red lines. In this case, the real-space collection is calculated as the fraction of the real-space image contained by the slit. Far-field and real-space collection efficiencies are then multiplied to find the total collection efficiency, shown in Fig. 4.24(a) and (d) for the two modes, in blue line. Overall, the predicted collection efficiency averages to 14.4 % for the fundamental mode, and it is 10 % at $E = 1.403\,\mathrm{eV}$ for the higher order mode.

By adding a polariser in the real-space, we also resolve the polarisation of the emission from the grating. The effect of a polariser, for example, along x, is introduced by setting $E_y = 0$ and calculating the new fraction of the real-space image contained in the slit. In this way, we find that 81.67 % (73.01 %) of the emission from the grating is polarised along the y (x) for the fundamental (higher order) mode.

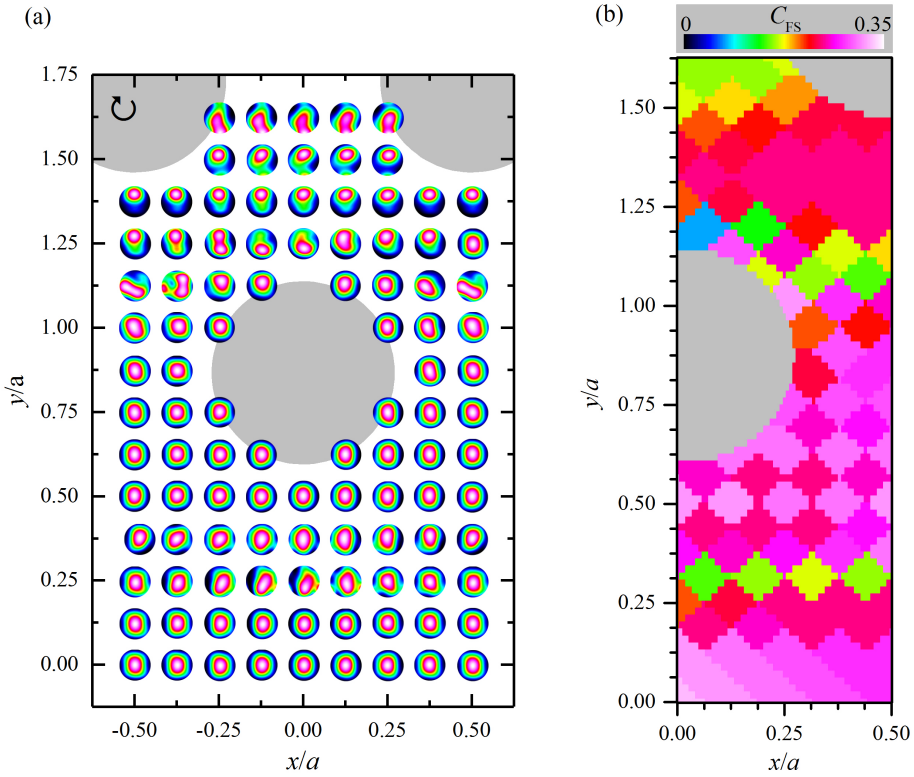

Figure 4.25: (a) Far-field profiles of the free space emission of a right-handed (↻) circularly polarised dipole source with emission energy E=1.3934 eV, as a function of the source position. (b) Corresponding collection efficiency including the objective NA and the input slit of the spectrometer. Light-grey: holes of the photonic crystal. Benjamin Lang built and run the model to generate the simulated data; plot produced by the author.

4.8.4 Free space collection efficiency

In this case, we use again FDTD simulations, but with a different geometry with respect to the simulation for the gratings. From these simulations we also calculate the simulated beta factor β_s and mode circularity C_s, which we discuss in Sec. 4.8.5. Each simulation run makes use of a supercell of size 39a in x, 18a in y, and 5a in z directions. An electrical dipole source with a time-varying current given by $[j_x(t), j_y(t)] \propto [i, 1] \exp(-i\omega t - t^2/(2\Delta_t^2))$ is used. and it is located at a certain position in the unit cell. The source position is varied on a grid formed by two subgrids, one centred at $(0,0)a$, and the other one at $(0.625,0625)a$, and both subgrids use a step of $0.125a$ in both directions, with the total range that varies from $0a$ to $0.5a$ in the x direction and from $0a$ to $1.625a$ in the y direction. This source is activated at an energy E=1.3934 eV, which is roughly the central energy of the measured QD distribution. The source has a duration of $\Delta_t = 50\,a/c \approx 43$ fs standard deviation, which results in a frequency standard deviation of $\Delta_\omega = 2\pi/\Delta_t \approx 10$ meV$/\hbar$, covering the range of QD energies measured experimentally. On both the $\pm x$ sides of the simulation we use $15a$ thick adiabatic absorbers. Therefore, out of the 39 simulated unit cells, only 9 are not inside the absorbers. On the other hand, a $2a$ thick absorber and $1a$ thick PML

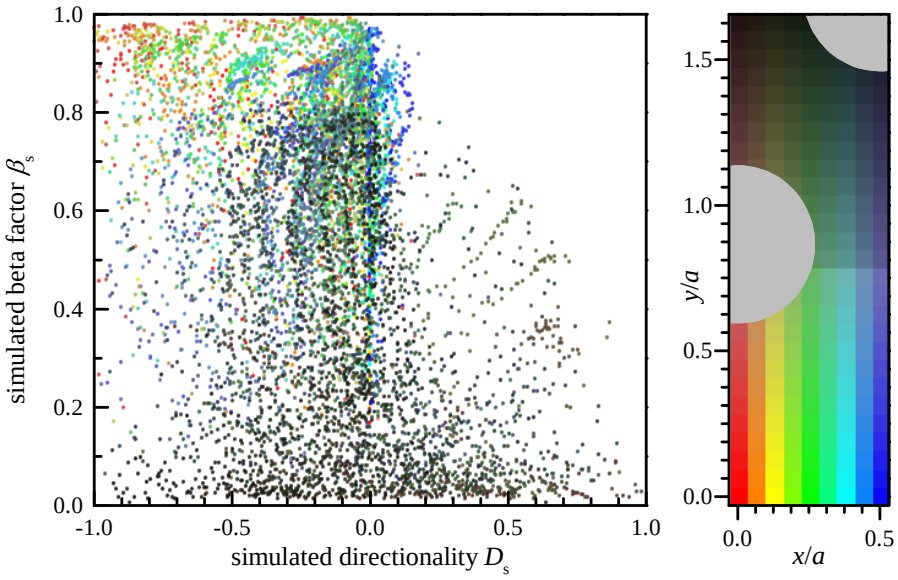

Figure 4.26: (a) Plot of simulated beta factor β_s against simulated directionality D_s for 100 different energies within 1.3457 eV and 1.4411 eV. The colour of the data points corresponds to their locations as shown in the right panel. Positions inside the holes (light grey) are not shown. Benjamin Lang built and run the model to generate the simulated data; plot produced by the author.

layer are used in the $\pm y$ and $\pm z$ simulation facets respectively.

The frequency resolved flux radiated from the source in the out-of-plane direction, which we call F_l, is measured by a flux plane which is doubled to account for the up/down symmetry. The corresponding far-field profiles are shown in Fig. 4.25(a), for the source activation energy E=1.3934 eV. By including the NA of the objective and the input slit of the spectrometer as described in Sec. 4.8.3, we determine the free space collection efficiency C_FS, shown in Fig. 4.25(b) for all the simulated positions. C_FS reaches a maximum of 35 %, and it is, in average, higher that what we calculated for the grating out-couplers. The regions of low values of C_FS in Fig. 4.25(b) correspond to the region where the far-field profile is highly asymmetric (Fig. 4.25(a)), as expected.

4.8.5 Beta factor and mode circularity

In order to calculate the beta factor and the mode circularity, we use the same simulations presented in Sec. 4.8.4. Additionally to the flux F_l, we also measure the total radiated flux forward F_f, and the total radiated flux backward F_b with respect to the circularly polarised source. With these definitions, we determine the simulated beta factor β_s and the directionality factor D_s as:

$$\beta_s = \frac{F_\mathrm{f} + F_\mathrm{b}}{F_\mathrm{f} + F_\mathrm{b} + F_\mathrm{l}} \tag{4.11}$$

$$D_s = \frac{F_\mathrm{f} - F_\mathrm{b}}{F_\mathrm{f} + F_\mathrm{b}} \ . \tag{4.12}$$

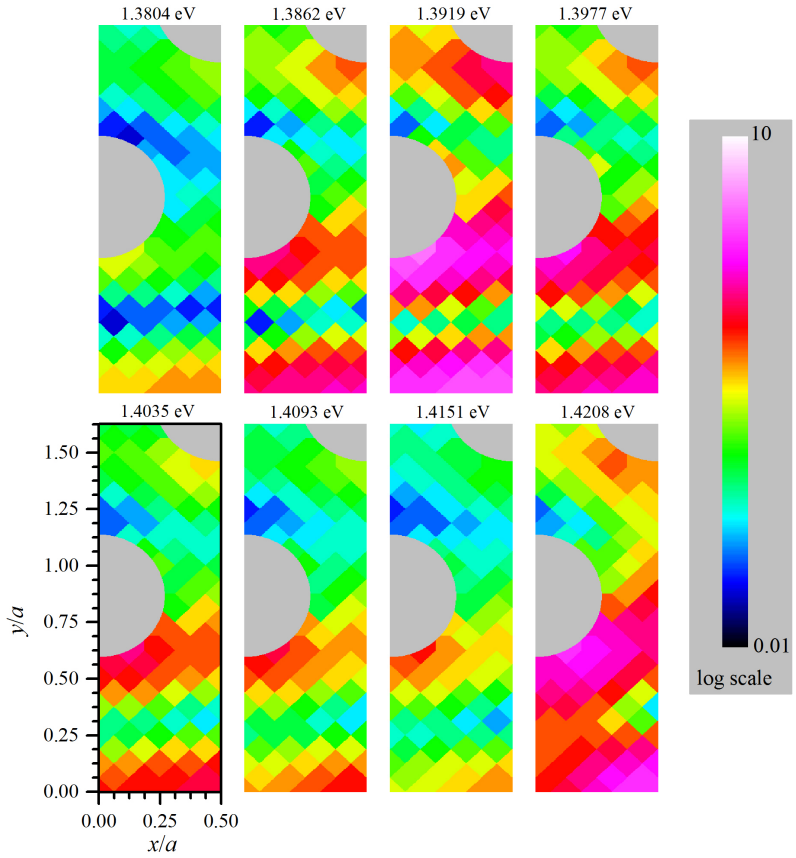

Figure 4.27: The rate of emission into loss (escaping) modes for a circular dipole as a function of location, for different energies as indicated. The rate is expressed in units of Purcell factor (such that 1 indicates a loss rate matching the total decay rate in bulk GaAs). Note the colour scale is logarithmic. Light-grey: holes of the photonic crystal. Benjamin Lang built and run the model to generate the simulated data; plot produced by the author.

Note that in this definition of the β_s we are not able to distinguish what is the contribution of the fundamental and of the higher order modes. Because the majority of the measured QDs have energies in overlap with both modes, this add additional complications when a comparison with the data wants to be carried out. This is discussed in details in Sec. 4.9.1. All the quantities in Eq. 4.11 and Eq. 4.12 are function of x and y positions and energy. For simplicity, we will omit this dependence throughout this section. In a single mode waveguide, D_s, for each energy and location inside the unit cell, is equal to the third Stokes parameter S_3. In multi-mode waveguides D_s is given by an average of the mode S_3's weighted by their densities' of states [78]. For comparison with experiment, D_s can be converted into a circularity value by:

$$C_s = \frac{1}{2}\ln\left(\frac{1+D_s}{1-D_s}\right) \quad . \tag{4.13}$$

In each simulation run, β_s and C_s are extracted as a function of frequency for a given source location. Propagation losses affect both of these quantities.

When performing a simulation run with the source located at a certain location x along the waveguide, the source is closer to one of the two flux planes along this direction. This means that propagation losses affect the fluxes F_f and F_b by a different amount. To compensate for this effect, for each location x, we also simulate the location $-x$, and the final fluxes considered for calculating β_s and C_s are an average between the results of the two simulations. This approach guarantees an accurate calculation of the mode circularity, although the β_s is still affected by losses. In particular, the lossy branch of the higher order mode also radiates in the out-of-plane direction. We decide to not separate its contribution from the direct free space emission of the source, as also in the experimental data we are not able to separate them. The calculated β_s as a function of the directionality D_s are shown in Fig. 4.26. The position of the source is colour coded according to the colour map shown in the right panel. The hue varies along the x direction, while the value along the y direction. As expected, the more the source is located far off the centre of the waveguide in the y direction, the more β_s is reduced. For the directionality, at $D_\mathrm{s} = 0$ (source located on a linear point) we find β_s up to 1. For $D_\mathrm{s} \to +1$, we observe a significant reduction of β_s. For $D_\mathrm{s} \to -1$, we also observe a reduction of β_s, but this time is much smaller and of the order of 0.1%. From these simulations, we can only conclude that small β_s are most likely to correspond to points of high directionality, although β_s of 99% can be also expected at C-points ($D_\mathrm{s} = \pm 1$). Note that the breaking of symmetry in D_s originates from the display of only half the unit cell, with the other half being mirror symmetric, mapping x to $-x$ and D_s to $-D_\mathrm{s}$.

In Fig. 4.27 we show the rate of emission of the circularly polarised dipole source directly into free space (i.e. in the out-of-plane direction) as a function of the source position. The emission is given in units of Purcell factor, such that a value equal to 1 indicates a loss rate equal to decay rate in bulk GaAs. Importantly, the emission varies with the source position inside the lattice unit cell over three order of magnitude, as recently reported [157], which confirms that an estimation of the beta factor from a comparison of the lifetimes of two QDs can be highly inaccurate, as the position of the QDs is not known.

4.8.6 Mode separation

As we will show in the next session (Sec. 4.9), for a proper comparison between simulation and experiment, we need to distinguish the contributions of the fundamental mode and the higher order mode to the fluxes F_f and F_b.

To calculate the mode projections, the electrical field profiles $\mathbf{E}(\mathbf{r}, \omega)$ and group indices $n_\mathrm{g}(\omega)$, extracted from the loss FDTD calculations, are used. The group indices are calculated using the spatially integrated Poynting vector [172]. These are used to calculate the density of states (DOS) into the forwards and backwards directions at each spatial location using the Purcell factor equations presented in [84], adapted to only express the intensity in a given direction. As we are only concerned with ratios between modes at a

shared frequency, these can be simplified to:

$$\begin{aligned} \mathrm{DOS}_{\mathrm{Forwards}} &= |\mathbf{E}(\mathbf{r},\omega)|^2 n_g(\omega)(1+D_{\mathrm{s}})/2 \\ \mathrm{DOS}_{\mathrm{Backwards}} &= |\mathbf{E}(\mathbf{r},\omega)|^2 n_g(\omega)(1-D_{\mathrm{s}})/2 \ . \end{aligned} \tag{4.14}$$

The DOS is therefore proportional to electric field intensity at the position and energy of the source and to the group index $n_{\mathrm{g}} \propto 1/v_{\mathrm{g}}$. Additionally, it depends on the directionality D_{s}, such that for a linearly polarised source (D_{s}=0), the directional DOS is half the one for a circularly polarised source ($D_{\mathrm{s}} = 1$). Using the fields/modes associated with each mode respectively allows us to calculate the fraction of the power emitted forwards that is in the even mode (for some choice of location and frequency). We neglect the lossy branch of the even mode that would be almost entirely lost by the time the light makes it to a grating. Using these fractions, the collection efficiencies of the gratings can be corrected while accounting for the different efficiencies for the two modes

4.9 Determination of the most likely QD position inside the lattice unit cell

In this section, we discuss how, by a comparison of simulations and data, we can determine the most likely QD position inside the lattice unit cell. But first, we need to discuss how the raw simulations data, in particular the fluxes F_{l}, F_{f} and F_{b} presented in section Sec. 4.8.5, have to be corrected in order to be comparable with the corresponding measured quantities. Indeed, because the QDs energies are in overlap with both the fundamental and higher order modes, different fraction of the coupled emission goes in the two modes depending on the density of states defined by each mode at the QD energy. Additionally, the two modes, as explained in Sec. 4.8.3, have different transverse and longitudinal polarisation components after the grating out-couplers. This means that, because of the polarisation response of the spectrometer grating, which is different for the two polarisations, they are detected with different efficiencies. In light of these properties, we now discuss how simulation are corrected.

4.9.1 Correction of simulations

The forward F_{f} and the backward F_{b} propagating fluxes are firstly separated into the fundamental and higher order modes projections as calculated in Sec. 4.8.6. The fluxes of each mode are then multiplied by the corresponding collection efficiencies due to grating out-couplers, NA of the MO and input slit of the imaging spectrometer, using the coefficients given in Sec. 4.8.3. We recall that this collection efficiencies are averaged over the spectral range covered by the simulations. The resulting fluxes from each mode are then separated into transverse and longitudinal polarisation, using the coefficients specified also in Sec. 4.8.3. Finally, we include the polarisation dependent reflection efficiency T_{g} and L_{g} of the spectrometer grating for transverse and longitudinal polarisations respectively.

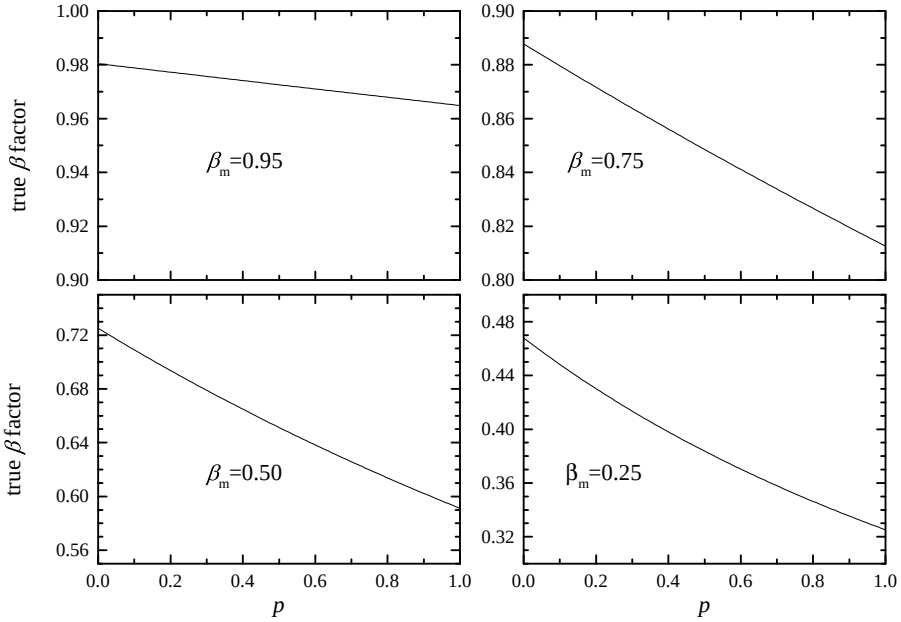

Figure 4.28: True beta factor β_{t} as a function of the mode projection parameter p, for different values of the measured beta factor β_{m}.

The transverse and longitudinal polarised fluxes are multiplied by the coefficients T_{g} and L_{g} respectively, and the resulting fluxes are then summed up, separately for each mode, to obtain the fully corrected flux. T_{g} and L_{g} are determined by measuring the grating polarisation efficiency ratio $R_{\mathrm{g}} = T_{\mathrm{g}}/L_{\mathrm{g}}$, with the normalisation $T_{\mathrm{g}} + L_{\mathrm{g}} = 2$, such that for unpolarised light $T_{\mathrm{g}} = L_{\mathrm{g}} = 1$. We find $T_{\mathrm{g}} \sim 1.24$ and $L_{\mathrm{g}} \sim 0.76$ for energies around the QD emission. On the other hand, for the free space emission we first multiply the out-of-plane flux by the position dependent collection efficiency. In this case the collection efficiency is calculated only for $E = 1.3934\,\mathrm{eV}$. We calculated the energy dependence at one location and we found it to be negligible (not shown). In order to include the polarisation efficiency of the grating spectrometer, we consider the free space emission to be circularly polarised.

Let us give a concrete example of the effect of these corrections. To this purpose, we use a very simplified model, which neglects propagation losses. Let us suppose we measure a beta factor β_{m} from a generic QD. The question we want to answer is: what is the true beta factor of this QD, considering collection and detection efficiencies we simulated? We know that the collection efficiencies of the grating out-couplers, for the fundamental and the higher order modes, are about 14% and 10% respectively. We know also that 81.67 (73.01)% of emission from the grating out-couplers is polarised along the transverse (longitudinal) direction for the fundamental (higher order) mode. The detection efficiencies of transverse polarisation are given above. On the other hand, the average (over position) free space collection efficiency is 24% at $E = 1.3934\,\mathrm{eV}$. Using these values, we find the effective collection efficiency for the fundamental mode is $\kappa_f \approx$16.6%, and for the higher order mode is $\kappa_h \approx$9.1%. The effective collection efficiency of free space remains

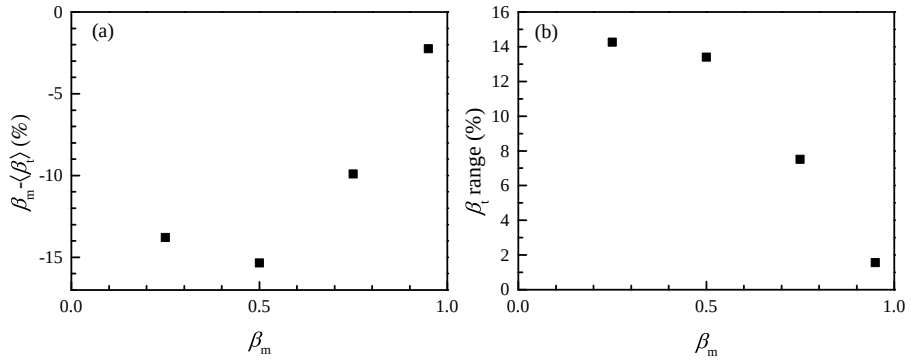

Figure 4.29: (a) Measured beta factor β_m minus average true beta factor β_t and (b) range of β_t, as obtained from plots in Fig. 4.28, as a function of β_m.

$\kappa_\mathrm{fs} = 24\%$, because it is not affected by the polarisation response of the spectrometer grating. The measured beta factor β_m and the true beta factor β_t are related by the following equations:

$$\beta_\mathrm{m} = \frac{\kappa_\mathrm{f} S_\mathrm{f} + \kappa_\mathrm{h} S_\mathrm{h}}{\kappa_\mathrm{f} S_\mathrm{f} + \kappa_\mathrm{h} S_\mathrm{h} + \kappa_\mathrm{fs} S_\mathrm{fs}} \tag{4.15}$$

$$\beta_\mathrm{t} = \frac{S_\mathrm{f} + S_\mathrm{h}}{S_\mathrm{f} + S_\mathrm{h} + S_\mathrm{fs}} \ , \tag{4.16}$$

where S_f, S_h and S_fs are the true emission powers of the QD into the fundamental mode, higher order mode and free space respectively (we indicate the variables of this model with the letter "S" because their use is only limited to this section of the thesis, and they should not be confused with measured and simulated variables that we have already defined). We also introduce the parameter $p \in (0, 1)$ to consider the mode projection, such that $S_\mathrm{f} = pS$ and $S_\mathrm{h} = (1-p)S$. Therefore, when $p = 1$ the emission coupled to the waveguide couples entirely to the fundamental mode, and when $p = 0$ to the higher order mode. Once we set a value also for the measured free space emission $\kappa_\mathrm{fs} S_\mathrm{fs}$, all the true quantities S_f, S_h and S_fs are defined. In Fig. 4.28 we show the true beta factor β_t as a function of the mode projection parameter, for different chosen values of β_m, as indicated in the figure. We summarise the results in Fig. 4.29. In Fig. 4.29(a), we show β_m minus the average (over p) true beta factor $\langle\beta_\mathrm{t}\rangle$, as a function of β_m. Due to the larger collection efficiency from the direct free space emission than from the grating out-couplers, β_m underestimates the true beta factor, resulting in the negative values. The quantity $\beta_\mathrm{m} - \langle\beta_\mathrm{t}\rangle$ is therefore a measure of the error we are making by not correcting experimental data for the collection efficiencies. This error mainly affects low beta factor, while for $\beta_\mathrm{m} > 90\%$, the error is less than 5%. On the other hand, in Fig. 4.29(b) we show the range of β_t (i.e. $\beta_t^\mathrm{max} - \beta_t^\mathrm{min}$) as a function of β_m. In this case, the range is a measure of the effect of the mode projection on β_m. Also in this case the correction mainly affects low beta factors.

From this analysis, we can conclude that the $\beta_\mathrm{m} > 0.90$ shown in Fig. 4.16 are accurate within less than 5%.

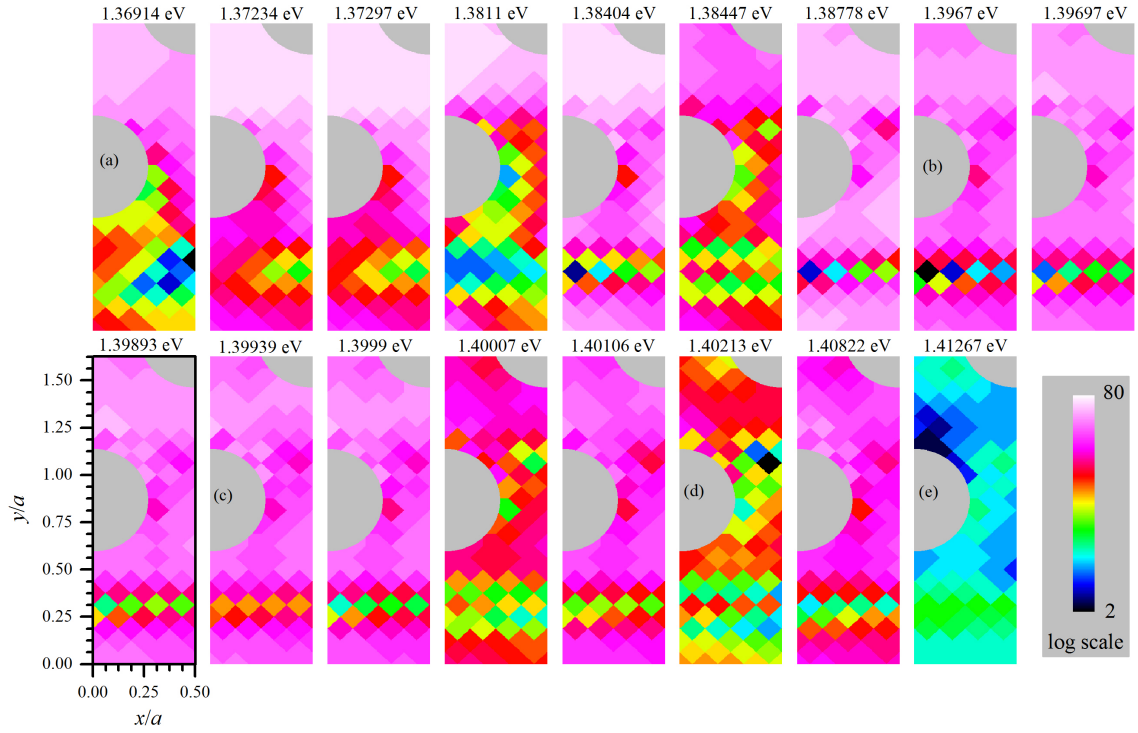

Figure 4.30: Error plots. Residual $\chi(x, y)$ of beta factor and circularity between simulations and experiment (see Eq. 4.17) for WG_A. Positions (x, y) inside the holes are not considered and they are indicated in light grey.

4.9.2 Error plots

The waveguide mode circularity at the QD site, together with the QD beta factor and energy, identifies possible QD positions inside the PCWG unit cell. In order to exploit this property, the FDTD simulations presented in Sec. 4.8.5, and corrected as discussed in Sec. 4.9.1 are compared with the experiment taking into account the experimental errors. In particular, we evaluate the normalized residual $\chi(x, y)$ for each QD using the following expressions:

$$\chi(x,y) = \sqrt{\left(\chi_c^2(x,y) + \chi_\beta^2(x,y)\right)/2} \ , \tag{4.17}$$

with

$$\chi_c(x,y) = \frac{C_m - \tilde{C}_s(x,y)}{\Delta C_m}, \quad \chi_\beta(x,y) = \frac{\beta_m - \tilde{\beta}_s(x,y)}{\Delta \beta_m} \ , \tag{4.18}$$

with ΔC_m and $\Delta\beta_m$ the experimental error (standard deviation) of C_m and β_m respectively, and $\tilde{C}_s$ and $\tilde{\beta}_s$ the simulated mode circularity and beta factor. $\tilde{C}_s$ and $\tilde{\beta}_s$ are calculated using the corrected fluxes described in Sec. 4.9.1. x and y label the simulated positions. Note that according to Eq. 4.17 and Eq. 4.18, a good agreement between simulation and experiment is obtained for χ of the order of unity. In general, the minimum of the residual indicates the most likely QD position inside the unit cell. In Fig. 4.30 the results are shown for all the QDs we have analysed from WG_A, ordered with increasing energies, as labelled. Generally, for each QDs we find residuals on the order of 5 at certain locations

as well as relative minima from which the most likely position of the QD can be found. In particular plots (a), (b), (d) and (e) are nice examples where $\chi \leq 2$, for which the QD position is determined with high probability. Importantly, the corresponding positions are quite distributed over the unit cell, meaning that we are not limited by systematic errors. On the other hand, in plot (c) we find $\chi > 20$ for all the simulated positions. In this case, although relative minima are present, we can not determine the QD position with high accuracy. In particular the stripe at y/a of about 0.25 is a region where both the fundamental and higher order modes are present. It could be that this might result in systematic errors in the numerical simulations. Further investigation is needed.

4.10 Conclusions

In conclusion, we have shown an extensive study on the SE properties of InAs/GaAs QDs embedded in PCWGs. We have shown that direct spectral imaging is a very powerful spectroscopy tool to measure the beta factor, avoiding the systematic errors of previous reports measuring decay rates and assuming that decay rates into non-guided modes is unaffected by the QD position inside the lattice unit cell. Using spectral imaging, we also observe directional emission, which together with the QD beta factor and energy, uniquely define the QD position inside the lattice unit cell. We use Fourier optics to measure the band dispersion of the waveguide, from which we accurately calibrate the simulation parameters to the measured sample. Combining our experimental results with FDTD simulations, we determine the most likely QDs position inside the lattice unit cell.

As an outlook, we would like to measure the waveguide dispersion also for energies confined within the photonic bandgap, using spectral interferometry. This would open the possibility to perform a similar study for the region of the fundamental mode which is confined within the bandgap, which is the most interesting region for quantum technology applications. Once this part of the dispersion has been characterised, it would be interesting to measure the FWM from **QDs!**s (**QDs!**s) coupled to the slow light region of the fundamental mode, to investigate the strong coupling regime.

Chapter 5

Spontaneous emission lineshape of pyramidal quantum dots

5.1 Introduction

A PQD is an interesting system to perform both fundamental and applied physics experiments. The main features are the inherent site-control and the higher crystal symmetry. Site controlled growth of InGaAs/GaAs QDs has been demonstrated by Sugiyama et al., in 1995 [173]. In 1998, Hartmann et al. [174] observed PL emission from an AlGaAs/-GaAs QDs grown in inverted tetrahedral pyramids, which showed the possibility of using PQDs as site controlled sources of quantum fields. A second order correlation function at zero delay ($g^{(2)}(0)$) of 0.25 has been reported by Baier et al. [175], which is a clear signature of the single photon character of the emission. One step further has been the use of PQDs as entangled photons sources, proposed in 2000 by Benson et al. [176], using the exciton (X) - biexciton (XX) cascade. To emit entangled photons, the fine-structure splitting (FSS) of the exciton has to be smaller than the radiative linewidth. In practice, detection of entangled states is mainly limited to QDs with small FSS [177]. Therefore, only few post-growth-selected quantum dots are measured to show entanglement. In 2013, Juska et al. [178] show that growth along the [111]B direction forms PQDs with very high in-plane symmetry, with a FSS below 4 μeV. The high reproducibility of the growth allows formation of QD-arrays of entangled photon emitters, which is an important prerequisite for scalable optical quantum information processing.

Another interesting aspect of PQDs which has been recently exploited, is the possibility to vertically stack multiple QDs within the same pyramidal recess, to form QD molecules [179]. Control over the kinetic parameters during the growth process allows tuning of the distance between two adjacent QDs, from 0.1 nm to 100-1000 nm. This capability opens up the possibility of a large variety of experiments whose aim is to investigate on the coherent coupling between adjacent QDs and on the transition between different coupling regimes: electronic coupling, for distances up to 1 nm, dipole-dipole coupling for distances between 1-10 nm and radiative coupling for distances between 10-100 nm.

Before starting with FWM experiments, a characterisation using linear spectroscopy is necessary, to have an overview of the optical properties of the sample. These measurements revealed a characteristic single QD spectrum, where the intrinsic lineshape of the excitonic transition is broadened by interaction with phonons, resulting in the phonon sidebands. In single QD spectra, phonon sidebands are not easy to observe, due to their weaker signal, 2-3 order of magnitude smaller than the transition where no phonons are involved, and they are usually masked by the noise. In the present case, using high dynamic range measurements, we resolve phonon sidebands in InGaAs/GaAs QDs, in a temperature range from 5 K to 100 K, enabling to investigate the exciton-phonon interaction in detail. In particular, in collaboration with the theory group headed by Dr. Egor Muljarov, we develop a fitting model based on the independent boson model (IBM), from which we extract a set of underlying parameters: deformation potentials, QD confinement lengths and phonon temperature. Additionally, using an observed thermal offset around the zero-phonon transition, we separate the homogeneous from the inhomogeneous broadening, similar to what is achieved using FWM spectroscopy [66] or speckle analysis [165].

5.2 Sample description

A detailed discussion concerning the growth of PQDs is given in Ref. [180]. In this section, the main growth steps are summarised, to introduce the sample's salient features. The growth of a PQD sample can be grouped into three steps: substrate pre-patterning, pyramidal recess filling and back-etching. The three steps are schematically represented in Fig. 5.1.

5.2.1 Substrate pre-patterning

Pre-patterning of the substrate is achieved by photolithography and wet chemical etching. The substrate is a thick layer, typically a few hundred µm, of [111]B gallium arsenide (GaAs). The B prefix indicates a surface which is As-terminated. A positive photoresist is spin-coated on the substrate, and after UV exposure, is developed for about 25 s in order to form an hexagonal lattice of equilateral triangles. In the case of the sample investigated in this work, the pitch of the lattice, as well as the side of the triangles, is 7.5 μm. The pattern is then transferred to the substrate by etching with a solution of bromine and methanol. A side view of a pyramidal recess which forms after the whole procedure is given in Fig. 5.1(a). The three facets of the pyramidal recess are of [111]A, which means they are Ga-terminated [171] [181].

5.2.2 Filling of the pyramidal recess

In order to grow a QD inside a pyramidal recess, MOVPE is performed. Without giving technical details, there are mainly two mechanisms that determine the growth inside a recess: decomposition induced growth rate anisotropy and adatom diffusion. From exper-

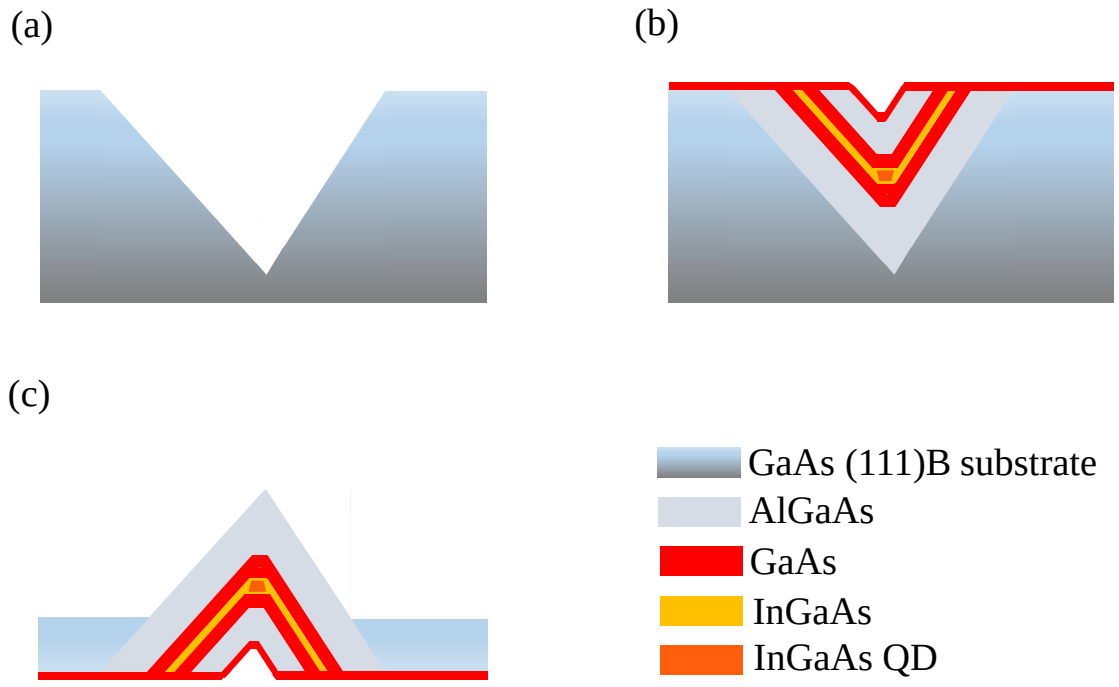

Figure 5.1: Growth of a InGaAs QDs inside a pyramidal recess. (a) Subtrate pre-patterning; (b) filling of the pyramidal recess; (c) back etching.

iments, it is observed that III-V materials tend to grow along the [111]A surfaces due to faster decomposition rates of precursors. Therefore, before full precursor decomposition has occurred, there is a preferential growth along the pyramidal surfaces.

On the other hand, adatom diffusion occurs preferentially towards the centre of the pyramidal recess, due to the curvature of the surface and the resulting step edges. This process favours the growth at the centre of the pyramid, and it becomes the dominant growth mechanism after all the precursors are decomposed. Capillarity action minimises the surface energy and leads to planarization of the recess. When equilibrium between the competing mechanisms is reached, a self-limiting growth profile (SLGP) is obtained [182]. Note that MBE would lead to a preferential growth on the [111]B surface, preventing the formation of the SLGP, which is essential to have control on the position of the grown QD.

Referring to Fig. 5.1(b), first a layer of AlGaAs is grown in the recess (in the following, we omit the compositions 1-x, x for brevity, but the material intended is always stoichiometric, with the same number of group III and group V elements). This layer is used as an etching stop, as it will be explained in the next subsection, and also as additional potential barriers which enhance the capture of carriers into the QD. Then, a thin layer of InGaAs is grown between two barriers of GaAs. An InGaAs/GaAs QD is formed at the centre of the pyramid, together with three InGaAs/GaAs lateral quantum wells (LQWs). Then, everything is covered by another layer of AlGaAs, followed by a cap layer of GaAs. Note that by alternating GaAs barriers and the InGaAs layers, two or more QDs can

growth direction

double quantum dot sample

Layer	Materials	Thickness (nm)
buffer	GaAs	65
etchstop 1	$Al_{0.45}Ga_{0.55}As$	45
etchstop 2	$Al_{0.8}Ga_{0.2}As$	90
barrier 2 down	$Al_{0.55}Ga_{0.45}As$	80
barrier 1 down	GaAs	100
QD 1	$In_{0.25}Ga_{0.75}As$	0.5
spacer	GaAs	**2**
QD 2	$In_{0.25}Ga_{0.75}As$	0.5
barrier 1 up	GaAs	70
barrier 2 up	$Al_{0.55}Ga_{0.45}As$	55
cap	GaAs	1

single quantum dot sample

Layer	Material	Thickness (nm)
Buffer	GaAs	200
etchstop 1	AlAs	50
barrier	GaAs	240
QD	$In_{0.25}Ga_{0.75}As$	0.5
barrier	GaAs	140

Figure 5.2: Epitaxial structure of the dQDs and sQD samples.

be vertically stacked within the same recess, with a distance set by the thickness of the barrier.

One process that has not been considered up to now is segregation [182, 183, 184]. This leads to a much more complicated heterostructure. Indeed, In diffuses more than Ga, which diffuses more than Al. Therefore, the InGaAs (AlGaAs) layer has a higher concentration of In (Ga) at the center of the pyramid, as well as along the corners of the pyramidal recess, because of the minimisation of the surface energy (or by capillarity action in other words). Because the energy band gap of $In_xGa_{1-x}As$ and $Al_{1-x}Ga_xAs$ decreases with increasing x, quantum wires (QWRs) form at the center and at the corners of the pyramidal recess. Furthermore, because of the larger thickness of the AlGaAs layer with respect to the InGaAs one, three vertical AlGaAs QWs (VQWs) are formed. The full heterostructure is sketched in Fig. 5.3(a) and (b).

In this work we report on two different samples: a single QD (sQD) and a double QD (dQD) with 2 nm separation between the QDs. The samples' epitaxial structures are given in Fig. 5.2. The dQD sample is studied with the ultimate goal of demonstrating coherent coupling of two vertically stacked QDs by FWM spectroscopy. The results presented in this thesis are therefore the basis of future FWM experiments.

5.2.3 Back-etching

Referring to the geometry given in Fig. 5.1, the light extraction, when exciting from the top, is not very efficient, due to total internal reflection of the emitted light. It has been shown the configuration with inverted pyramids enhances the light extraction of about three orders of magnitude [183]. In order to obtain such a configuration, all the chip is inverted. The substrate is then etched away, revealing the pyramids. The process of etching is very non-uniform. The substrate is fully removed, partially removed, or not removed at all depending on the exposure time to the chemicals. As a consequence, the pyramids, in white light reflection imaging, seems to have different dimensions, as shown

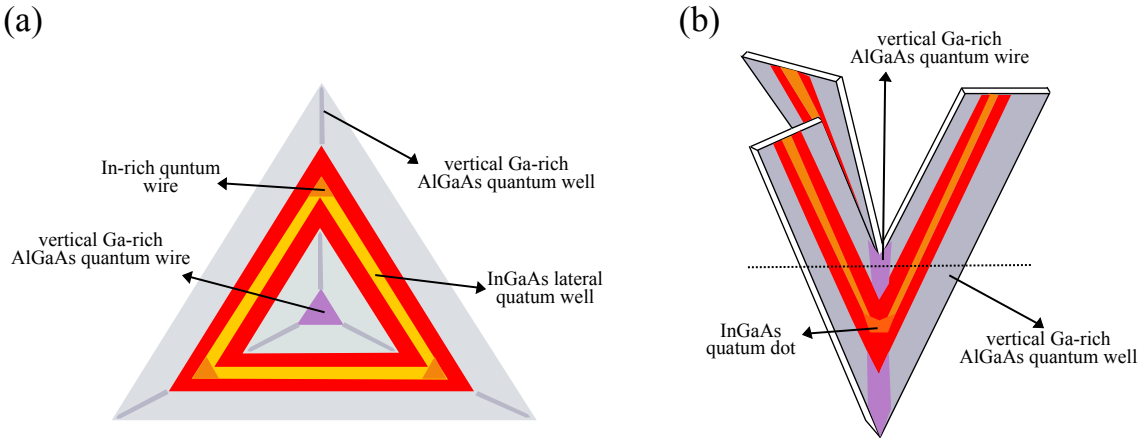

Figure 5.3: Cross-section (from black dashed line in (b)) of the PQD heterostructure formed after filling the pyramidal recess. Colours legend as in Fig. 5.1(d). (a) Top view of pyramidal recess after filling. (b) 3D schematic of the PQD heterostructure that is formed at the corners of the pyramidal recess.

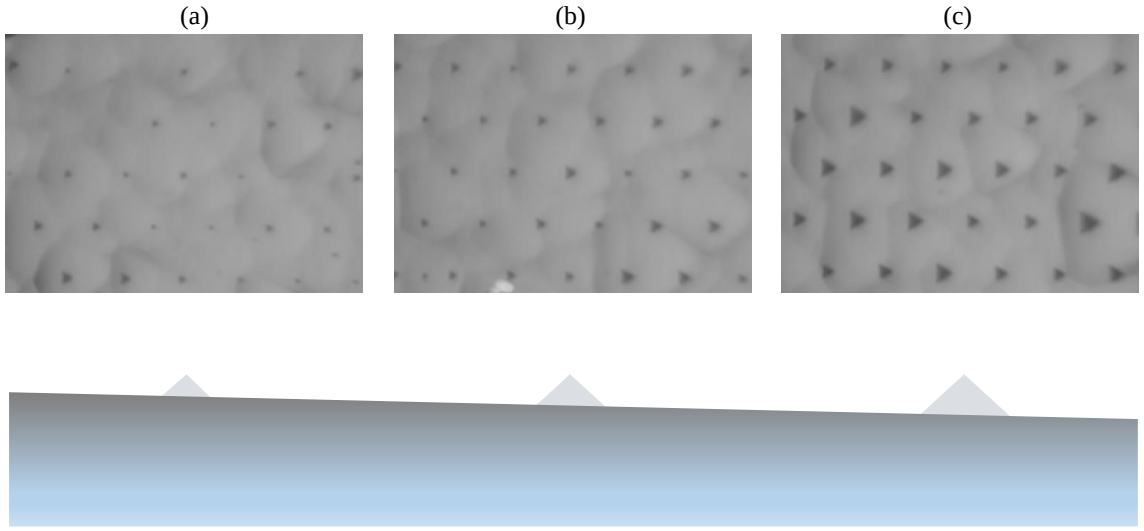

Figure 5.4: (a), (b) and (c): white light images of the dQD sample pictures, at regions with different levels of substrate removal, as sketched.

in Fig. 5.4.

5.3 Theoretical background

In this section, we give some additional theoretical details which are necessary to understand the experiments.

5.3.1 Fine-structure splitting

The FSS results from the electron-hole exchange interaction which couples the electron and hole spins of an exciton state. This coupling can be described in terms of an effective magnetic field generated by the holes which cause the electron spin to precess and

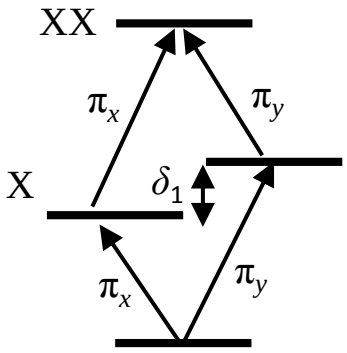

Figure 5.5: X-XX system for elliptical QDs.

viceversa [185]. The corresponding effective Hamiltonian is given by:

$$H_{ex} = -\sum_{i=x,y,z} \left(a_i J_{h,i} S_{e,i} + b_i J_{h,i}^3 S_{e,i} \right) \quad , \tag{5.1}$$

with S_e and J_h the spin of the electron and hole respectively, and a_i and b_i are spin-spin coupling parameters which take into account the symmetry of the QD. Neglecting hh-lh mixing, the band-edge physics is dominated by excitons formed by a hh with $J_h = 3/2$, $J_{h,z} = \pm 3/2$ and an electron with $S_e = 1/2$, $S_{e,z} = \pm 1/2$, where z labels the growth direction. The resulting exciton states have $|M| = 1, 2$, with $M = S_{e,z} + J_{h,z}$. States with $|M| = 2$ are dark as they do not couple to light. On the other hand, states with $|M| = 1$ are bright as they can be optically excited using circularly polarised light. The exchange interaction can be divided in two contributions: the short-range term and the long-range term. The former affects both dark and bright states, as it is a spin-spin interaction. The latter affects only bright states, as it is mediated by the exchange of virtual photons, which do not interact with dark states. Within the subspace described by the exciton bright states $|+1\rangle$ and $|-1\rangle$, the effect of the exchange interaction (both short-range and long-range) is described by the Hamiltonian H_{ex}, which has the following matrix form [57]:

$$H_{ex} = \frac{1}{2} \begin{pmatrix} \delta_0 & \delta_1 \\ \delta_1 & \delta_0 \end{pmatrix} \quad , \tag{5.2}$$

with δ_0 and δ_1 parameters which depend on the QD symmetry [57]. In the case of QDs which are spherical in the plane orthogonal to the growth direction, δ_1=0 and Eq. 5.2 is diagonal, meaning that the states $|+1\rangle$ and $|-1\rangle$ are eigenstates, resulting in two degenerate circularly polarised transitions. In the case of elliptical QDs, $\delta_1 \neq 0$, and the eigenstates of Eq. 5.2 are [57]:

$$\begin{aligned} |L_1\rangle &= \frac{1}{\sqrt{2}} \left(|+1\rangle + |-1\rangle \right) \\ |L_2\rangle &= \frac{1}{\sqrt{2}} \left(|+1\rangle - |-1\rangle \right) \quad , \end{aligned} \tag{5.3}$$

with the corresponding eigenenergies given by:

$$\begin{aligned} E_{L_1} &= \frac{1}{2}\left(\delta_0 + \delta_1\right) \\ E_{L_2} &= \frac{1}{2}\left(\delta_0 - \delta_1\right) \quad . \end{aligned} \tag{5.4}$$

These are two linearly polarised transitions aligned with the principal axis of the QD, split by the FSS δ_1. When considering emission spectra from charged and multi-exciton states, one needs to consider the FSS of both the initial and the final states. The emission from a negative trion, which is composed of two electrons in the s-shell of the CB and one hh in s-shell of the VB, does not show FSS. In the trion state, the two electrons pair together to form a spin singlet, and the resulting exchange interaction with the hole spin is quenched. At the same time, the final state of a trion transition is a single electron, which again does not have FSS. For the biexciton emission the situation is different. The initial state does not have FSS, for the same reason as the trion, but the final state is an exciton, which has the FSS as explained above. The resulting X-XX system is schematically represented in Fig. 5.5, with the X and XX states which have the same magnitude of FSS, but for opposite linear polarisations. The case of a biexciton trion transition is more complicated due to the multiple spin configurations of the final state (the trion excited state). A detailed explanation is beyond the scope of this work, and we refer the reader to more detailed references [56, 186, 187, 188].

5.3.2 Fine-strucutre splitting in presence of a magnetic field

In this work we measured the emission spectra from QDs in the presence of a magnetic field B=0.45 T in Faraday configuration (i.e. aligned along the growth direction). The interaction with the field is described by the Zeeman Hamiltonian H_z, which, if restricted to hh only ($J^2_{h,z} = 9/4$), reads as:

$$H_z = -\mu_\mathrm{B}\left(g_{e,z}S_{e,z} - \frac{g_{h,z}}{3}J_{h,z}\right)B_z \quad , \tag{5.5}$$

where $g_{e,z}$ is the electron g-factor and $g_{h,z}$ is the effective hole g-factor [57]. In the presence of FSS, the total Hamiltonian of the system is then $H = H_{ex} + H_z$. In this case, by defining $\delta_z = \mu_\mathrm{B}\left(g_{e,z} + g_{h,z}\right)B_z$, the states splitting and polarisation degree is determined by the relative strength of the magnetic field and exchange interaction, quantified by the ratio $\kappa = \delta_z/\delta_1$. The eigenstates of the total Hamiltonian are the following:

$$\begin{aligned} |L_1\rangle &= \sqrt{\frac{1}{1+C_+^2}}\left(|{+1}\rangle + C_+\,|{-1}\rangle\right) \\ |L_2\rangle &= \sqrt{\frac{1}{1+C_-^2}}\left(|{+1}\rangle + C_-\,|{-1}\rangle\right) \quad , \end{aligned} \tag{5.6}$$

with $C_\pm = \kappa \pm \sqrt{1+\kappa^2}$. The eigenstates are therefore elliptically polarised, with a degree of ellipticity which depends on the factor C_i. The corresponding eigenergies are given by:

$$\begin{aligned} E_{L_1} &= E_0 + \frac{1}{2}\sqrt{\delta_1^2 + \delta_z^2} \\ E_{L_2} &= E_0 - \frac{1}{2}\sqrt{\delta_1^2 + \delta_z^2} \quad . \end{aligned} \tag{5.7}$$

5.3.3 Exciton-phonon interaction: independent boson model

Phonons, i.e. lattice vibrations, are one of the main mechanisms of coherence loss in a solid state environment. When an exciton is optically excited in a QD, the charge distribution of the system is modified, as an electron is created in the CB and a hole is left in the VB. As a result of the coupling, the exciton polarisation decays in a non-exponential way, which corresponds to a characteristic lineshape in the spectral domain (see Fig. 5.6(b)). The spectrally sharp peak is the ZPL, as the exciton recombination does not involve phonons. The broadband is due to phonon-assisted transitions. In this section, the basic theory of exciton-phonon coupling is presented within the framework of the IBM [189], which is the starting point of different theoretical works on QDs [190, 191]. Importantly, the IBM allows for direct, and quantitative, comparisons with experiments of PL [192, 193, 194] and FWM [195]. Although these comparisons can qualitatively reproduce the experimental data, a fit of the lineshape, using all relevant parameters, has not been reported for QDs, and parameters like the electron-hole deformation potentials and the phonon temperature are usually fixed according to tabulated values and nominal values respectively. On the contrary, a fit has been developed and applied for carbon nanotubes, although it is not a full fit of all parameters [196].

Excitons can couple to acoustic phonons, through both the deformation potential and piezo-electric couplings, and to optical phonons, through the polar coupling [191]. The main contribution to the coupling in InGaAs/GaAs QD is given by the deformation potential D to longitudinal acoustic phonons [60, 197, 198], which describes the modification of the energy bandgap due to local lattice distortion, and we just consider this case in the following. Generally, the valence and conduction bands have different deformation potentials D_v and D_c respectively. In the limit where phonon-assisted transitions to higher QD states are negligible, only the exciton ground state $|1\rangle$ is important. Within this limit, the dynamic of an exciton coupled to a phonon bath is described by the IBM Hamiltonian

$$\begin{aligned} \hat{H} &= \sum_{\boldsymbol{q}} \hbar\omega_{\boldsymbol{q}} \hat{b}_{\boldsymbol{q}}^\dagger \hat{b}_{\boldsymbol{q}} + \hbar\,|1\rangle\langle 1|\left(\omega_{11} + \hat{V}\right) \\ \hat{V} &= \sum_{\boldsymbol{q}} \left(\lambda_{\boldsymbol{q}} \hat{b}_{\boldsymbol{q}}^\dagger + \lambda_{\boldsymbol{q}}^\star \hat{b}_{\boldsymbol{q}}\right) \quad , \end{aligned} \tag{5.8}$$

with $\hbar\omega_{11}$ the bare exciton energy, $\hat{b}_{\boldsymbol{q}}^\dagger$, $\hat{b}_{\boldsymbol{q}}$ the creation and annihilation operators of phonons with momentum $\boldsymbol{q}$ and energy $\hbar\omega_{\boldsymbol{q}}$, respectively, and $\lambda_{\boldsymbol{q}}$ the matrix element describing the exciton-phonon coupling. The IBM Hamiltonian can be solved exactly in different ways.

Here for example, the results are obtained with the linked cluster expansion [189]. From now on in this section, $\hbar$ is assumed to be equal to 1 for simplicity.

The exciton linear polarisation $P_{\mathrm{IBM}}(t)$ after δ-pulse excitation at $t = 0$ is given by the dipole-dipole correlation function $P_{\mathrm{IBM}}(t) = \langle d^\dagger(t) d(0) \rangle$, with $d = |0\rangle\langle 1|$, and $|0\rangle$ the state when no excitons are present. It can be demonstrated that

$$P_{\mathrm{IBM}}(t) = \theta(t) e^{-i\omega_{11}t} e^{K(t)} \ , \tag{5.9}$$

with the cumulant$K(t)$ given by:

$$K(t) = -\frac{1}{2} \int_0^t \mathrm{d}t_1 \int_0^t \mathrm{d}t_2 \langle \mathcal{T} \tilde{V}(t_1) \tilde{V}(t_2) \rangle_{\mathrm{ph}} \ , \tag{5.10}$$

with $\mathcal{T}$ the time-ordering operator a $\tilde{V}$ the phonon coupling term in the interaction picture with respect to the phonon Hamiltonian $\hat{H}_{\mathrm{ph}} = \sum_{\boldsymbol{q}} \hbar\omega_{\boldsymbol{q}} \hat{b}^\dagger_{\boldsymbol{q}} \hat{b}_{\boldsymbol{q}}$. The average is taken over the thermalised phonon bath, described by the density matrix $\hat{\rho}_{\mathrm{ph}}$ given by the following expression:

$$\hat{\rho}_{\mathrm{ph}} = \frac{e^{-\beta \hat{H}_{\mathrm{ph}}}}{\mathrm{Tr}\left\{ \left(-\beta \hat{H}_{\mathrm{ph}} \right) \right\}_{\mathrm{ph}}} \ , \tag{5.11}$$

with $\beta = (k_{\mathrm{B}} T)^{-1}$, k_{B} the Boltzmann constant and T the phonon bath temperature. A calculation of the cumulant requires an explicit expression for the matrix element $\lambda_{\boldsymbol{q}}$. Assuming that the phononic properties of the QD are not significantly different from those of the surrounding material, and the linear dispersion $\omega_q = v_{\mathrm{s}} |\boldsymbol{q}|$ with v_{s} the speed of sound in the material, $\lambda_{\boldsymbol{q}}$ can be expressed as:

$$\lambda_{\boldsymbol{q}} = \sqrt{\frac{q}{2\rho_{\mathrm{m}} v_{\mathrm{s}} V}} D(\boldsymbol{q}) \ , \tag{5.12}$$

with ρ_{m} the mass density of the material and $D(\boldsymbol{q})$ a form factor. Neglecting electron-hole Coulomb correlations, the exciton wavefunction ψ_X is factorisable in the electron and hole wavefunctions ψ_{e} and ψ_{h} respectively as

$$\psi_X = \psi_{\mathrm{e}}(\boldsymbol{r}_{\mathrm{e}}) \psi_{\mathrm{h}}(\boldsymbol{r}_{\mathrm{h}}) \ , \tag{5.13}$$

and the form factor takes the form:

$$D(\boldsymbol{q}) = \int \mathrm{d}\boldsymbol{r} \left[D_{\mathrm{v}} |\psi_{\mathrm{h}}(\boldsymbol{r})|^2 - D_{\mathrm{c}} |\psi_{\mathrm{e}}(\boldsymbol{r})|^2 \right] e^{-i\boldsymbol{q}\cdot\boldsymbol{r}} \ . \tag{5.14}$$

For an isotropic parabolic QD confinement potential, the ground state electron and hole envelope functions are Gaussians:

$$\psi_\alpha(\boldsymbol{r}_\alpha) = \sqrt{\frac{1}{\pi^{3/2} a_\alpha^3}} \exp\left(-\frac{r_\alpha^2}{2a_\alpha^2} \right) \ , \tag{5.15}$$

with α=e,h and a_α the electron and hole confinement lengths. Assuming a_e=a_h=a, the form factor becomes:

$$D(\boldsymbol{q}) = (D_\mathrm{c} - D_\mathrm{v})\exp\left(-\frac{a^2q^2}{4}\right) \ , \tag{5.16}$$

from which the matrix element $\lambda_{\boldsymbol{q}}$ can be simply obtained using Eq. 5.12. We can now introduce a spectral density function $J(\omega)$:

$$J(\omega) = \sum_{\boldsymbol{q}} |\lambda_{\boldsymbol{q}}|^2 \delta(\omega - \omega_{\boldsymbol{q}}) \ . \tag{5.17}$$

In the present case, it takes the form

$$J(\omega) = J_0 \omega^3 e^{-\frac{\omega^2}{\omega_0^2}} \ , \tag{5.18}$$

with

$$J_0 = \frac{(D_\mathrm{v} - D_\mathrm{c})^2}{(2\pi)^2 \rho_\mathrm{m} v_\mathrm{s}^5} \tag{5.19a}$$

$$\omega_0 = \frac{\sqrt{2} v_\mathrm{s}}{a} \ . \tag{5.19b}$$

With these definitions, the cumulant, after performing the double integration in Eq. 5.10, becomes:

$$K(t) = K_\mathrm{p}(t) + (-i\Omega_\mathrm{p} t - S) \ , \tag{5.20}$$

with

$$K_\mathrm{p}(t) = J_0 \int_0^\infty \mathrm{d}\omega \omega e^{-\frac{\omega^2}{\omega_0^2}} \left(N_{\boldsymbol{q}}(\omega) e^{i\omega t} + [N_{\boldsymbol{q}}(\omega) + 1] \, e^{-i\omega t} \right) \tag{5.21a}$$

$$\Omega_\mathrm{p} = J_0 \sqrt{\frac{\pi}{2}} \left(\frac{v_\mathrm{s}}{a} \right)^3 \tag{5.21b}$$

$$S = J_0 \int_0^\infty \mathrm{d}\omega \omega e^{-\frac{\omega^2}{\omega_0^2}} \coth\left(\frac{\omega}{2k_\mathrm{B}T} \right) \ . \tag{5.21c}$$

In these expressions, $N_{\boldsymbol{q}}(\omega) = \langle \hat{b}_{\boldsymbol{q}}^\dagger \hat{b}_{\boldsymbol{q}} \rangle_\mathrm{ph}$ and $N_{\boldsymbol{q}}(\omega) + 1 = \langle \hat{b}_{\boldsymbol{q}} \hat{b}_{\boldsymbol{q}}^\dagger \rangle_\mathrm{ph}$, with $N_{\boldsymbol{q}}(\omega) = 1/[\exp(\beta\hbar\omega_{\boldsymbol{q}}) - 1]$ and $\hbar\omega_{\boldsymbol{q}}$ the energy of the phonon with momentum $\boldsymbol{q}$. Ω_p and S are the polaron shift and the Huang-Rhys factor respectively. In this way, using Eq. 5.9, the polarisation can be written in the following compact form:

$$P_\mathrm{IBM}(t) = \theta(t) e^{-S} e^{-i(\omega_{11} - \Omega_\mathrm{p})t} e^{K_\mathrm{p}(t)} \ . \tag{5.22}$$

The physical meaning of these expressions can be understood by first considering what happens if the exciton interacts with a single phonon. At $t = 0$ (after pulse excitation), the exciton polarisation amplitude $|P_\mathrm{X}|$ is maximum. Because of the exciton-phonon coupling, the exciton exchanges energy with the phonon, to form a polaron state, which

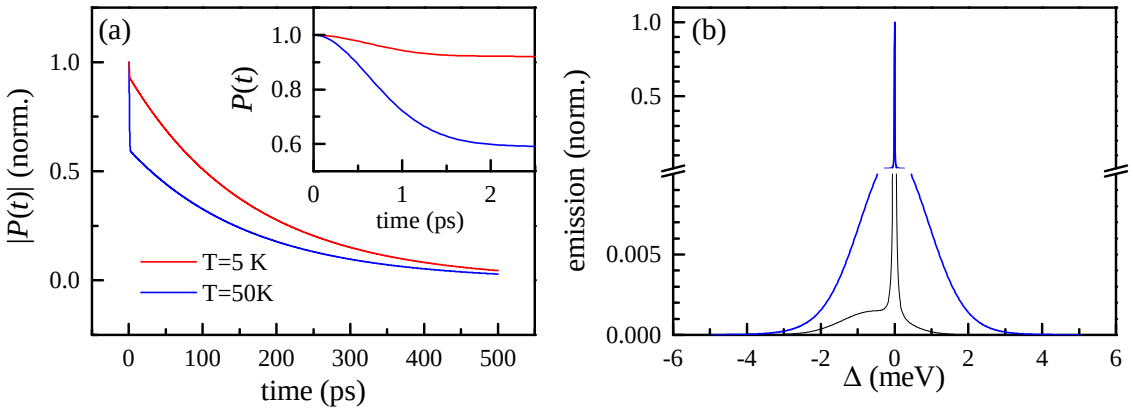

Figure 5.6: (a) Absolute value of the IBM polarisation as a function of time (delta pulse exciting at $t = 0$), for T=5 K (red line) and T=50 K (blue line); the calculation uses a spherically symmetric parabolic confinement potential, a=3.3 nm. $|D_c - D_v| = 6.5\,\text{eV}$, $v_s = 4.6 \times 10^3\,\text{m/s}$, $\rho_m = 5.65\,\text{g/cm}^3$, and a phenomenological Lorentzian decay $\Gamma = 8\,\mu\text{eV}$ (FWHM) is used to model the ZPL broadening. (b) Corresponding emission spectra calculated using Eq. 5.23. Amy Morreau built and run the model to generate the simulated data; plot produced by the author.

is eigenstate of the Hamiltonian Eq. 5.8 in the case of one phonon. An exciton in a QD interacts, with many, independent phonons with different frequencies, to form what is called a polaron cloud, and the exchange of energy occurs with different periods. Therefore, the exciton polarisation amplitude can not come back to its maximum value and is partially lost in the phonon bath. This transient, which describes the formation of the polaron cloud, is described by $K_p(t)$, and it develops on the timescale of a few picoseconds for the QD excitons investigated here [199]. At longer times $K_p(t)$ tends to zero, and the exciton polarisation reaches a stable state, with the residual polarisation amplitude given by $\exp(-S)$, which remains constant in time according to Eq. 5.22. Additionally, the interaction with the polaron cloud shifts the bare exciton frequency by the polaron shift Ω_p. In experiments, it is observed that the exciton polarisation decays exponentially at longer time [66]. We can add this term with the substitution $\omega_{11} \rightarrow \omega_{11} + i\Gamma$ in Eq. 5.22 [200]. The exciton polarisation amplitude as a function of time for $T = 5\,K$ and $T = 50\,\text{K}$ is shown in Fig. 5.6(a), with $\Gamma = 8\mu\text{eV}$. At both temperatures, the dynamics occurs with two different timescales: in the first few picoseconds, the polarisation decays very fast, due to the transient behaviour described by $K_p(t)$ (see inset); at longer times, it decays exponentially with time constant $1/\Gamma$. At $T = 50\,\text{K}$, the amplitude of the polarisation left is smaller than at $T = 5\,\text{K}$, due to the larger Huang-Rhys factor. As a consequence, the ZPL weight is also smaller.

The emission spectrum is given by the real part of the inverse Fourier transform of the polarisation $\alpha(\omega)$:

$$\alpha(\omega) = Re \int_0^\infty \mathrm{d}t P(t) e^{-i\omega t} \quad . \tag{5.23}$$

We use the above equation to calculate the absorption spectra corresponding to the polarisation shown in Fig. 5.6(a). The results are shown in Fig. 5.6(b). The rapid decay is responsible for the ZPL sidebands. The long-time dynamics is instead responsible for the

broadening of the ZPL.

In the limit where one-phonon processes dominate the dynamics, the change of the sidebands lineshape reflects the average phonon occupation number $N_{\boldsymbol{q}}(\omega)$. Indeed, in PL spectra, the low energy sideband is proportional to the probability of emitting a phonon, $N_{\boldsymbol{q}}+1$, and viceversa, the high energy sideband is proportional to the probability of absorbing a phonon, $N_{\boldsymbol{q}}$ [195]. In this context, we define this property as thermal symmetry. At high temperatures, $N_{\boldsymbol{q}}+1 \sim N_{\boldsymbol{q}}$ and the lineshape becomes symmetric around the ZPL. For example, considering a phonon energy of 1 meV, $N = 0.11$ at 5 K and $N = 3.83$ at 50 K. Therefore, while at 5 K the emission sidebands at 1 meV is expected to be 10 times more intense than the absorption one, already at 50 K one would expect to have similar intensities ($(N+1)/N \sim 1.26$ at the considered phonon energy). This behaviour is evident from Fig. 5.6(b). The thermal symmetry can be in principle used as a phonon thermometer, as already suggested by Zimmermann and Muljarov in 2004 [195]. The phonon temperature can be extrapolated from a linear fit of the thermal ratio R_{T}, defined as:

$$R_{\mathrm{T}} = \ln\left(\frac{I(-\hbar\omega)}{I(\hbar\omega)}\right) = \frac{\hbar\omega}{k_{\mathrm{B}}T} \quad , \tag{5.24}$$

with I the intensity of the emission spectrum and $\hbar\omega$ the emission energy, with the ZPL taken as the zero frequency. A similar approach is applied in Raman spectroscopy, where the phonon temperature is determined by the thermally distributed intensity of the Stokes and anti-Stokes signals [201, 202].

5.4 Characterisation of the double quantum dot spectra

In order to characterise the emission spectra from PL experiments, we perform polarisation resolved measurements of power dependence and FSS, using the spectral imaging technique explained in Sec. 2.2.2. All the data presented in this section are taken as a single acquisition ($N = 1$). Before performing any analysis, the raw data from a spectral image, per each polarisation, are integrated over the number of pixels (6 in this case) that contain the signal from each individual polarisation, multiplied by the CCD sensitivity (2 photoelectrons (pe) per count), normalised by the integration time and background subtracted. The background is calculated by averaging over two lines of pixels on the lowest part of the acquired spectral image, where no QD emission is present.

5.4.1 Power dependence

In Fig. 5.7 spectra at $T = 5$ K for different excitation powers P_{exc} are shown, with the QD subject to a magnetic field B=0.45 T in Faraday configuration. A QWP is placed between the 96:4 beam splitter and the lens L_2 shown in Fig. 2.4, in order to project the circularly polarised emission into the vertical (π_V) and horizontal (π_H) polarisation basis of the displacer. In Fig. 5.7, only the spectra from the π_H polarisation projection, which corresponds to ↻, are shown. The indicated excitation power P_{exc} refers to the power

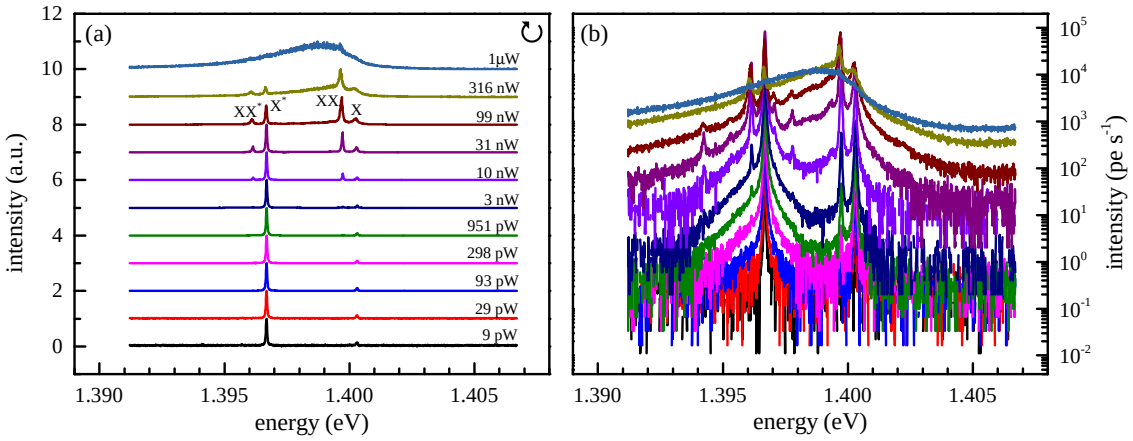

Figure 5.7: (a) ↻ polarised PL spectra for different powers of dQD_1. The spectra are normalised and offset corrected for clarity. The indicated powers are given at the sample plane. Measurements are taken at $T = 5\,\mathrm{K}$. (b) As (a) but data are in units of photoelectrons per second and are not offset corrected.

at the sample plane. Four emission peaks are observed, attributed to: an exciton (X), a biexciton (XX) and a trion (X^*) and the peak named XX^*.

Let us focus on the X-XX system. In Fig. 5.8(c) we show the peak area as a function of P_{exc}. The area is evaluated from fitting the peak using a Voigt profile. As a general note, when fitting single QD spectra, one should take care of the finite offset generated by the phonon sidebands. For the fit shown here, this offset has been included, using a phenomenological model that will be explained later, only in the X^* fit, as this is the only case where phonon sidebands give a significant offset to the ZPL.

The peak area shows a linear dependence for X and a quadratic dependence for XX, as shown by the dashed and dot-dashed lines respectively. Although these are clear hints of an exciton-biexciton system, a power dependence is not enough to exclude multi-charged states as the origin of the observed trend. Indeed, Fig. 5.9(c) shows a similar behaviour for the X^*-XX^* system. FSS measurements are necessary.

5.4.2 Fine-structure splitting

In order to measure the FSS, we performed polarisation resolved measurements without magnetic field. As in this case the emission is expected to be linearly polarised (see Sec. 5.3.1), we change the projections of the emitted polarisation with respect to the π_{H}-π_{V} basis set by the displacer using a HWP placed between the 96:4 beam splitter and the lens L_2 shown in Fig. 2.4.

In Fig. 5.8(a), we show the projection of the PL emission along π_H, as a function of the HWP angle θ_{HWP}. The emission shows periodic oscillations as a function of θ_{HWP} for both the X and XX peaks, with the expected relative π phase shift of an exciton-biexciton system. In order to extract the peak energy at each θ_{HWP}, we fit each individual transition with a Voigt profile. In Fig. 5.8(b) the obtained peak energies, shifted by the energy offset E_0 as given in the figure, as a function of θ_{HWP}, are shown. From the

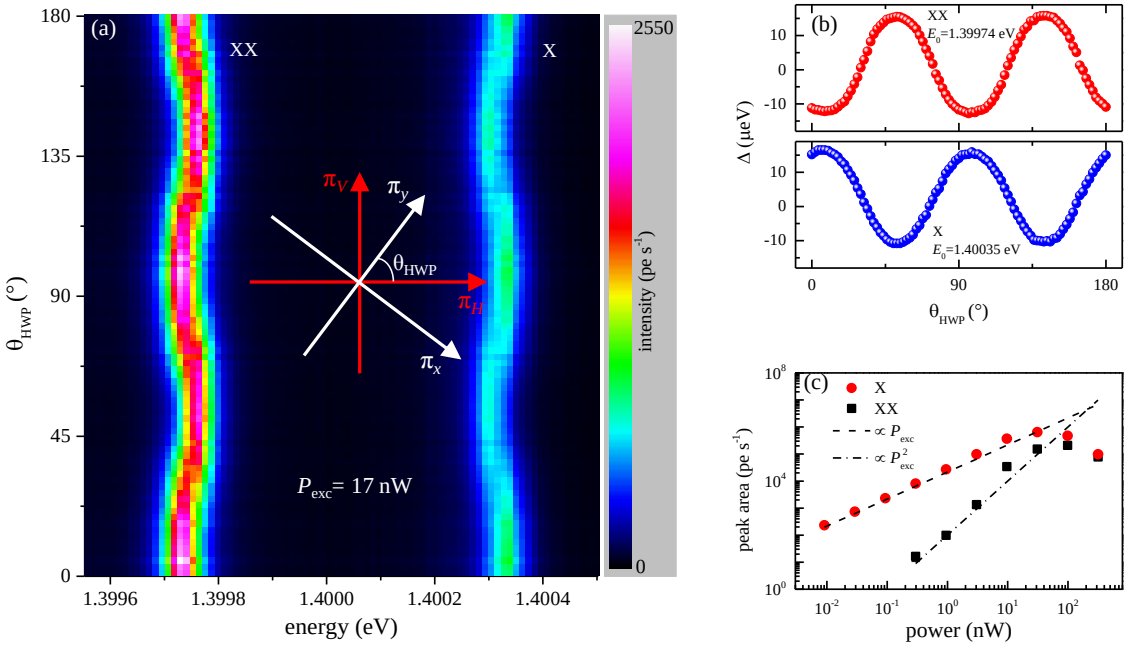

Figure 5.8: FSS on the X and XX emission lines of dQD_1. (a) Projection of the PL emission along the horizontal polarisation π_H, as a function of the HWP angle. Inset: emitted polarisation (white) and detection (red) polarisation basis; the emitted polarisation is rotated by θ_{HWP} with respect to detection basis set by the polarisation displacer. (b) $\Delta = E - E_0$ of X and XX as a function of HWP angle; from the minimum and maximum Δ we find $\delta_1 = 27.3\,\mu\mathrm{eV}$ for X and $\delta_1 = 28.6\,\mu\mathrm{eV}$ for XX. (c) Peak area as a function of power for the X and XX. Dashed (dashed-dot) line is a function proportional to P_{exc} (P^2_{exc}). All the measurements are taken at $T = 5\,\mathrm{K}$.

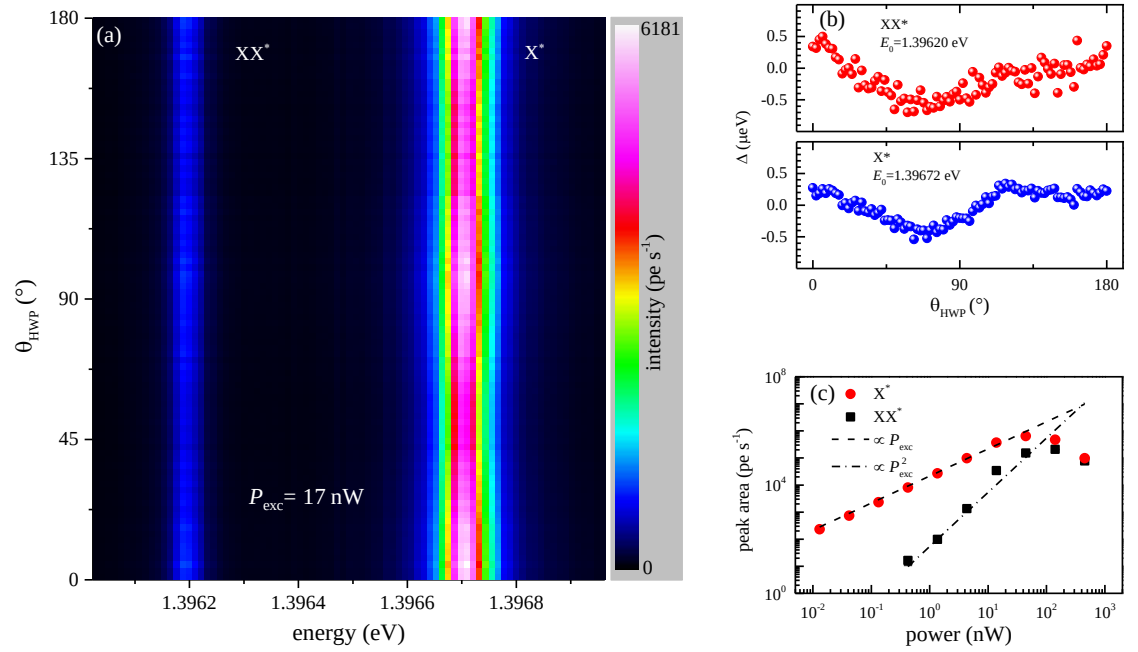

Figure 5.9: FSS on the X^* and XX^* emission lines of dQD_1. (a) As Fig. 5.8(a); (b) X^* and XX^* peak energies as a function of HWP angle, showing no FSS, although a similar energy drift is observed. (c) Peak area as a function of power for the X^* and XX^* states. Dashed (dashed-dot) line is a function proportional to P_{exc} (P^2_{exc}). All the measurements are taken at $T = 5\,\mathrm{K}$.

minimum and maximum of the oscillations we find $\delta_1 = 27.3\,\mu\text{eV}$ for X and $\delta_1 = 28.6\,\mu\text{eV}$ for XX. Therefore, we can conclude that this is indeed an exciton-biexciton system. In Fig. 5.9(a) we show the same analysis performed on the X^* and XX^* transitions. Both X^* and XX^* peaks do not show measurable FSS, as shown in Fig. 5.9(b). On the other hand, they have a similar energy drift, which could be either due to low frequency fluctuations of the spectrometer grating due to change in air humidity during the measurement (as we integrate 5 s per each θ_{HWP}, and we take data at 91 different angles, each measurement last for about 7.5 minutes), either due to the quantum-confined Stark effect. Together with the observed linear dependence of the peak area as a function of power, we can conclude that X^* is a trion transition. The interpretation for XX^* is less obvious. Considering the quadratic power dependence of the peak area, one could attribute this peak to the recombination of a biexciton trion which leaves behind a trion in its excited state (i.e. with a carrier in the p-shell), although it is known that this transition should appear in the form of a doublet due to the exchange interaction, which we do not observe in the measured spectral range [56].

5.4.3 Zeeman splitting

As shown in Sec. 5.4.2, we measure a FSS which is comparable with the Zeeman splitting created by the magnetic field. The eigenstates of the total Hamiltonian are given by Eq. 5.6. Therefore, care must be taken when fitting the single QD spectra shown in Fig. 5.7. In our experiment, we separate the emission from $|+1\rangle$ and $|-1\rangle$ using the QWP and the polarisation displacer. To be sure of that, the QWP orientation is set to separate the Zeeman split lines (i.e. $|+1\rangle$ and $|-1\rangle$ states) of the X^*, which is not affected by the FSS (see Sec. 5.3.1). In Fig. 5.10(a) we show a polarisation resolved spectrum normalised to its maximum intensity. For the X^* and XX^* transitions, $\delta_1 = 0$. Therefore, the two Zeeman split transitions are contributing exclusively to the respective polarisation channels. In order to fit these lines, we performed a global fit using one Voigt profile in each polarisation, with the linewidth used as a global fit parameter. An example of this fit is shown in Fig. 5.10(c). On the other hand, for the X and XX transitions $\delta_z \sim \delta_1$, and both states $|L_1\rangle$ and $|L_2\rangle$, with energies E_{L_1} and E_{L_2} respectively, have a defined non-zero projection onto the circularly polarised states $|+1\rangle$ and $|-1\rangle$. Therefore, for a proper estimate of the Zeeman splitting, this has to be included in the fitting. We therefore define the fitting functions f_+ and f_- for the $|+1\rangle$ state and $|-1\rangle$ states respectively. These can be written as:

$$f_+ = A_+ \left[N_{1,+}P_1 + N_{2,+}P_2\right] \tag{5.25a}$$

$$f_- = A_- \left[N_{1,-}P_1 + N_{2,-}P_2\right] \ , \tag{5.25b}$$

with $N_{i,\pm} = |\langle \pm 1|L_i\rangle|^2$, $i = 1, 2$ and $A_\pm$ overall amplitudes terms. P_i is the lineshape describing the X and the XX transitions. According to this model, for each circular polarisation, we observe two peaks, P_1 and P_2, whose relative amplitudes are fixed by δ_z

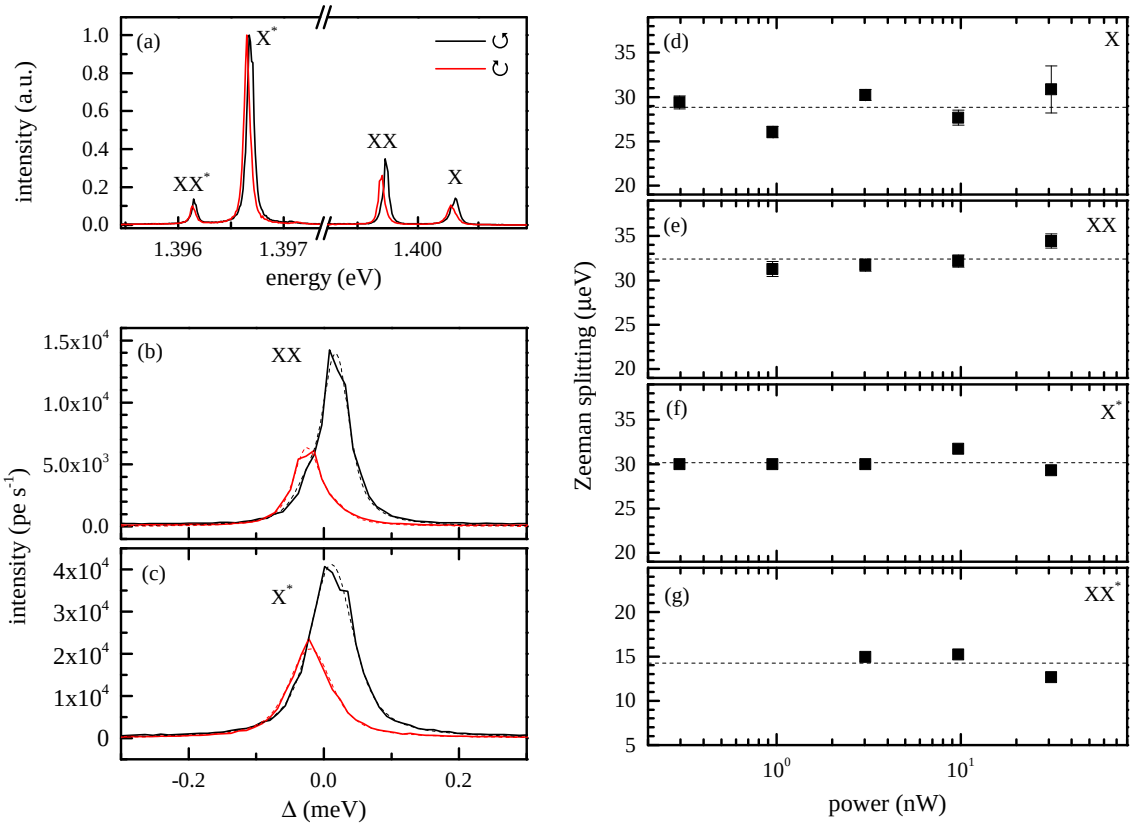

Figure 5.10: (a) Left-handed (↺) and right-handed (↻) circularly polarised spectra over the full spectral range covered by the CCD camera. (b) and (c) Zoom around the XX and X* peaks respectively; dashed lines: fit. (d),(e),(f) and (g): Zeeman splitting of the X, XX, X* and XX* emission lines respectively; dashed lines: average values. All the measurements are performed at $T = 5\,\mathrm{K}$.

and δ_1. We chose P_i to be a Voigt profile with unitary amplitude, peak center E_{L_i} (as defined in Eq. 5.7) and Gaussian and Lorentzian widths which are kept the same for both peaks. With these definitions, we performed a global fit using both the ↻ and ↺ polarised spectra. An example of this fit is shown in Fig. 5.10(b) for the XX transition. The fit works well for both polarisations. A summary of the obtained δ_zs, is shown in Fig. 5.10(d), (e), (f) and (g) as a function of the excitation power, for all the relevant transitions. We find an average Zeeman splitting of 28.84 ± 1.99, 32.41 ± 1.41, 30.20 ± 0.90 and $14.26 \pm 1.41\,\mu\mathrm{eV}$ for the X, XX, X* and XX* respectively. Importantly, δ_z show very similar values for X, XX and X*, as expected [56, 203]. The fact that δ_z for the XX* is quite different from what found for all the other states is a further hint that we are actually looking at a transition where a carrier in the p-shell of the QD is involved, for which a different effective g-factor is expected [56]. We note that when the FSS splitting is neglected, δ_z for the X and XX states was found to be of the order of 40 μeV, about 10 μeV larger than the value for the X*.

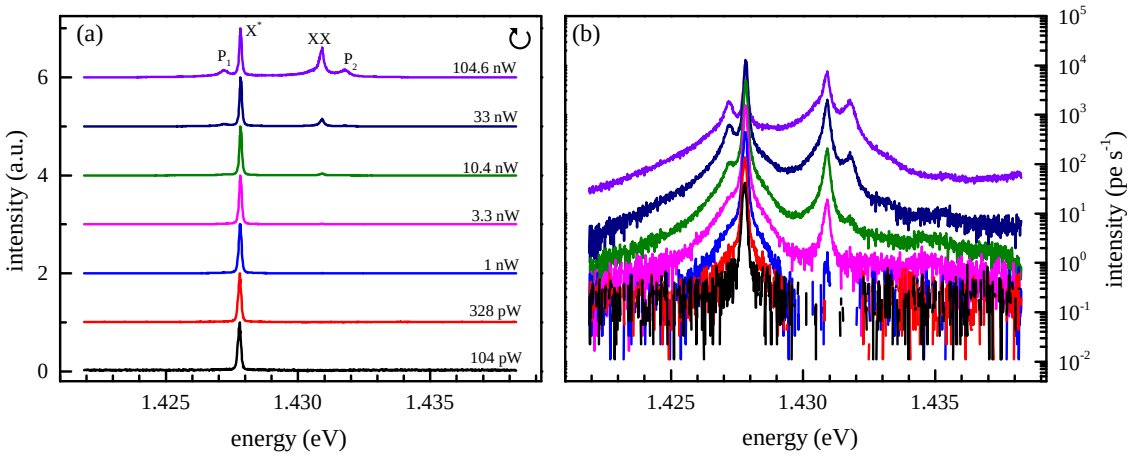

Figure 5.11: (a) ↻ polarised PL spectra for different powers of sQD. The spectra are normalised and offset corrected for clarity. The indicated powers are given at the sample plane. Measurements are taken at $T = 5\,\mathrm{K}$. (b) As (a) but data are in units of photoelectrons per second and are not offset corrected.

5.5 Characterisation of the single quantum dot spectra

In this section, we show the optical characterisation of the sQD sample.

In Fig. 5.11, we show ↻ polarised PL spectra for different excitation powers measured at $T = 5\,\mathrm{K}$. In this case, we observe a trion emission X^* and a biexciton emission XX. The other two peaks, P_1 and P_2, are not conclusively interpreted and they will not be considered in the following. Their broader linewidth points towards the emission of a multiply charged state. We combine a power dependence with measurements of FSS, measured in the same way as for the dQD_1 sample. In Fig. 5.12 we summarise the results. The peak area of X^*, (b), and XX, (c), shows a linear and quadratic dependence with the excitation power respectively. At the same time, the X^* does not show FSS, (f), while the XX shows a FSS of about $5.5\,\mu\mathrm{eV}$, (g). These findings are all consistent with our interpretation.

5.6 High dynamic range measurements for phonon sidebands

In order to measure phonon sidebands with a large signal-to-noise ratio, we perform high dynamic range measurements. All the data shown in this section are taken in presence of a magnetic field B_z=0.45 T in Faraday configuration and the QWP, in the same way as in Sec. 5.4.1. We acquire N polarisation resolved spectral images with the same integration time. To obtain the high dynamic range data, we applied the following procedure: first, we sum all the spectral images corresponding to one particular data to generate the summed spectral image (SSI), after correcting for the shift of the emission spectra along the vertical direction of the CCD camera, caused by laboratory temperature changing during the measurement (>1 hr); we perform this correction by calculation of the position of the

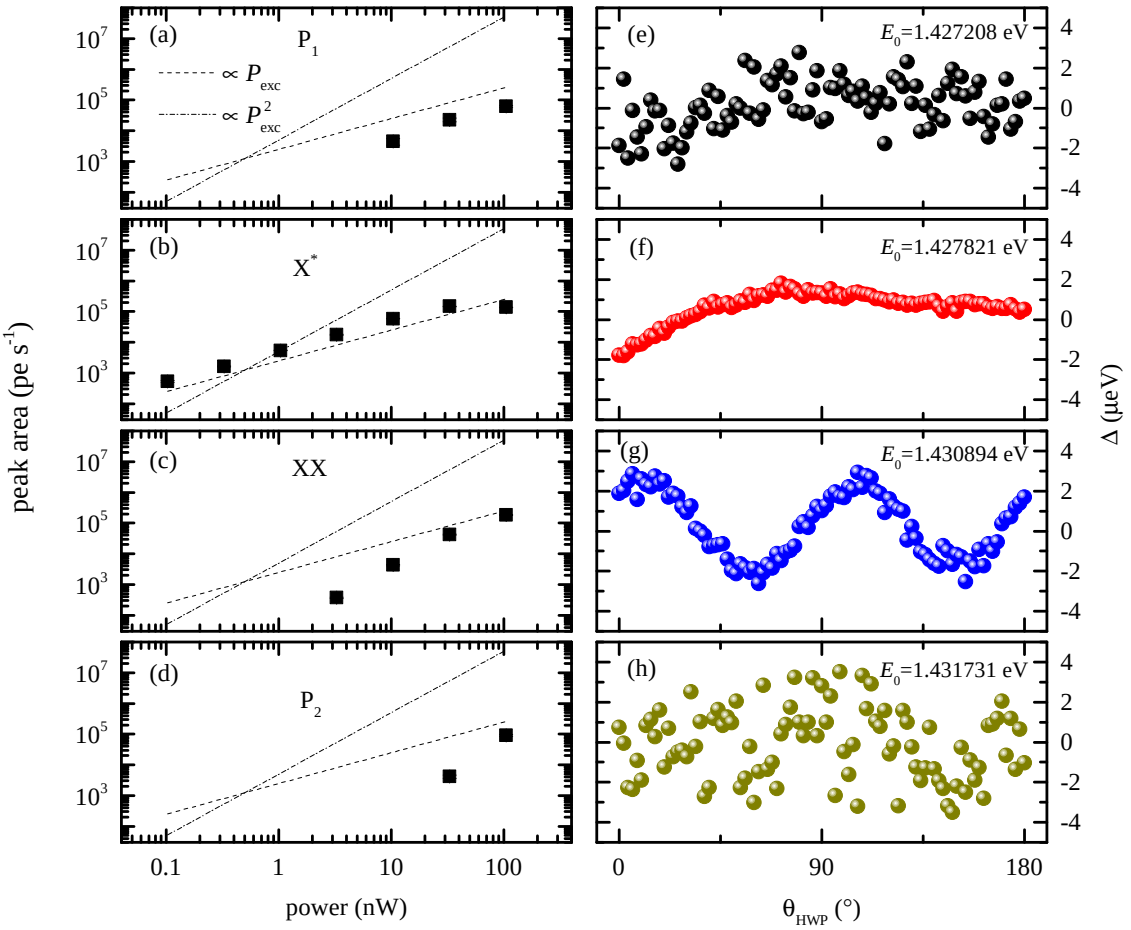

Figure 5.12: Characterisation of the sQD sample. (a), (b), (c) and (d): peak area as a function of power for P_1, X^*, XX and P_2 emission lines; dashed (dashed-dot) line is a function proportional to P_{exc} (P_{exc}^2). (e), (f), (g) and (h): corresponding peak energy as a function of the HWP angle, measured on the π_{H} polarisation component, as in Fig. 5.8; the XX in (g) has been subtracted by the X^* peak energy shown in (f) to remove the drift. From the maximum and minimum Δ we find δ_1=5.5 μeV. All measurements are performed at $T = 5$ K.

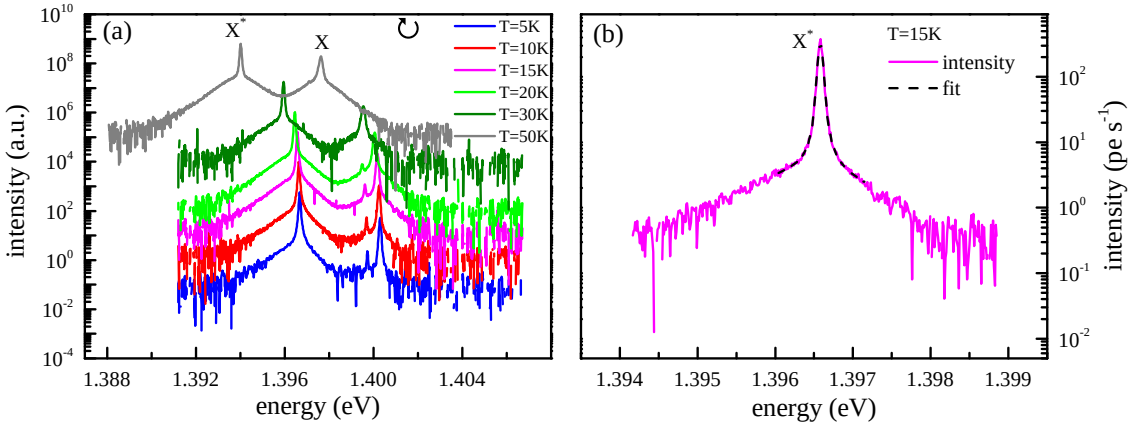

Figure 5.13: (a) High dynamic range data D for dQD_1 as a function of energy, for different temperatures. D is divided by the integration time. Only the ↻ polarisation is shown. (b) Spectrum at T=15 K; dashed line: fit using Eq. 5.27.

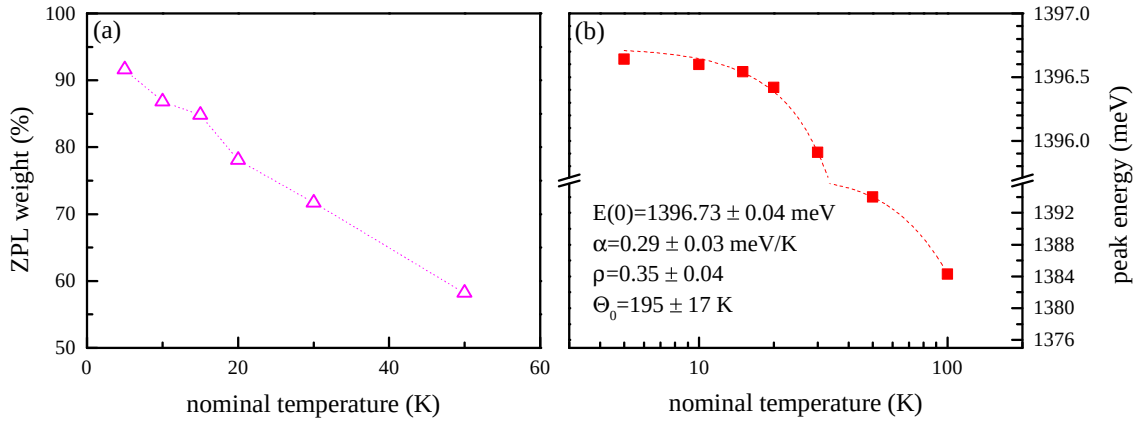

Figure 5.14: ZPL weight (a) and peak energy (b) as a function of the nominal temperature, as obtained from the fit using Eq. 5.27. The dashed line in (b) is a fit according to Eq. (9) of Ref. [112]. The fit parameters are specified in the graph.

maximum along the vertical direction for each spectral image. We then calculate the corresponding mean value and shift all the data such that the new position of the maximum is at the mean value. From the SSI, we calculate the signal S from the polarisation we want to analyse, by integrating over N_s pixels along the y axis containing that polarisation (see also Fig. 2.5) and multiply by the camera sensitivity, fixed to 2 photoelectrons (pe) per count in all the measurements; we generate also the background signal B by integrating over N_b pixels along y axis from a region of the SSI where no signal is present, followed by multiplication of the camera sensitivity; finally, we obtain the final data D, in units of photoelectrons, as:

$$D = N_s \left(\frac{S}{N_s} - \frac{B}{N_b} \right) \quad . \tag{5.26}$$

In Fig. 5.13(a), we show the corresponding spectra from dQD_1 as a function of temperature, for similar excitation powers. Phonon sidebands are visible. The spectral position of both the X and X* emission lines shift to low energy due to the bandgap shift [112]. Additionally, by comparing the spectra, two effects are observed with the increasing temperature: a reduction of ZPL weight, and a change in the sidebands lineshape, which becomes more symmetric around the ZPL. These observations are consistent with the predictions of the IBM, as explained in Sec. 5.3.3. For a more quantitative analysis, we apply a phenomenological model to separate the ZPL from the phonon sidebands. This model makes use of the following fitting function:

$$I = \mathrm{Voigt}(\hbar\omega, E_{\mathrm{ZPL}}, A, w_{\mathrm{G}}, w_{\mathrm{L}}) + \frac{A_1}{2}\left[1 + \mathrm{erf}\left(\frac{E - E_P}{w_1}\right)\right]\exp\left[-\frac{E - E_{\mathrm{P}}}{w_2}\right] \quad . \tag{5.27}$$

Voigt describes a Voigt function, obtained as the convolution of a Lorentzian and a Gaussian functions with widths w_{L} and w_{G} respectively, E_{ZPL} is the peak centre of the ZPL line and A is the ZPL peak area. The error function erf, whose width is w_1, reproduces the low energy sidebands, while the exponential decay, with decay constant w_2, the high

energy ones. E_{P} is the peak centre of the phonon sidebands, which is not necessarily the same as the ZPL peak centre. One fit is shown in Fig. 5.13(b). The fit is applied only to a small range around the ZPL, where the phonon sideband shape is adequately modelled by the fit function. The ZPL weight can be simply calculated as the area of the ZPL obtained from the fit, divided by the total area, including the phonon sidebands, calculated from the integrated intensity, and it is shown as a function of temperature in Fig. 5.14(a). The ZPL weight is about 92 % at $T = 5\,\mathrm{K}$, it then decreases down to 58 % at $T = 50\,\mathrm{K}$. From the phenomenological model, we also obtain the ZPL peak energy as a function of temperature, as shown in Fig. 5.14(b). The dashed line is a fit according to Eq. (9) of Ref. [112], which describes the shift of the excitonic resonance due to the shrinkage of the energy bandgap at higher temperatures. The fit parameters are specified in the graph.

5.6.1 Noise analysis

The high dynamic range measurements presented above are affected by mainly three sources of noise: read noise, camera sensitivity noise and shot noise. All signals are given unitless in number of photoelectrons. Non-linearities of the CCD camera response are below 1% for 100 kHz digitization used in the experiment and are therefore not relevant.

Let us start with the read noise, which is the electronic noise generated by the CCD camera during the reading of the photo-generated electrons. In order to estimate the read noise per single pixel, which we call σ_{r}, we take two background spectra from one line of pixels of the corresponding acquisition. In this case we use short exposure times, such that we can neglect shot noise. We then subtract the two spectra, calculate the standard deviation σ of the resulting spectrum, and finally obtain the read noise as $\sigma_{\mathrm{r}} = \sigma/\sqrt{2}$. In order to get the total read noise from our measurements, we first need to consider that each pixel along the energy axis of both S and B signals has a read noise σ_{S} and σ_{B} respectively, given by:

$$\begin{aligned} \sigma_S &= \sigma_{\mathrm{r}}\sqrt{N \cdot N_{\mathrm{s}}} \\ \sigma_B &= \sigma_{\mathrm{r}}\sqrt{N \cdot N_{\mathrm{B}}} \ . \end{aligned} \tag{5.28}$$

Therefore, using the above equation together with Eq. 5.26, we obtain the final expression for the total read noise $\sigma_{\mathrm{r}}^{\mathrm{m}}$ of our measurement:

$$\sigma_{\mathrm{r}}^{\mathrm{m}} = \sigma_{\mathrm{r}}\sqrt{N \cdot N_{\mathrm{s}}\left(1 + \frac{N_{\mathrm{s}}}{N_{\mathrm{b}}}\right)} \ . \tag{5.29}$$

The camera sensitivity noise results from the different detection sensitivity of different pixels. The resulting fluctuations are particularly visible in the plot of the thermal ratio R_{T} of Fig. 5.15(a). Therefore, we make use of this plot to give an estimate of the standard deviation α of the sensitivity fluctuations. The corresponding noise in a signal I is then given by αI. In order to estimate α, we first remove a linear contribution from R_{T} close to the ZPL, (where the linear behaviour is expected) in order to centre the fluctuations

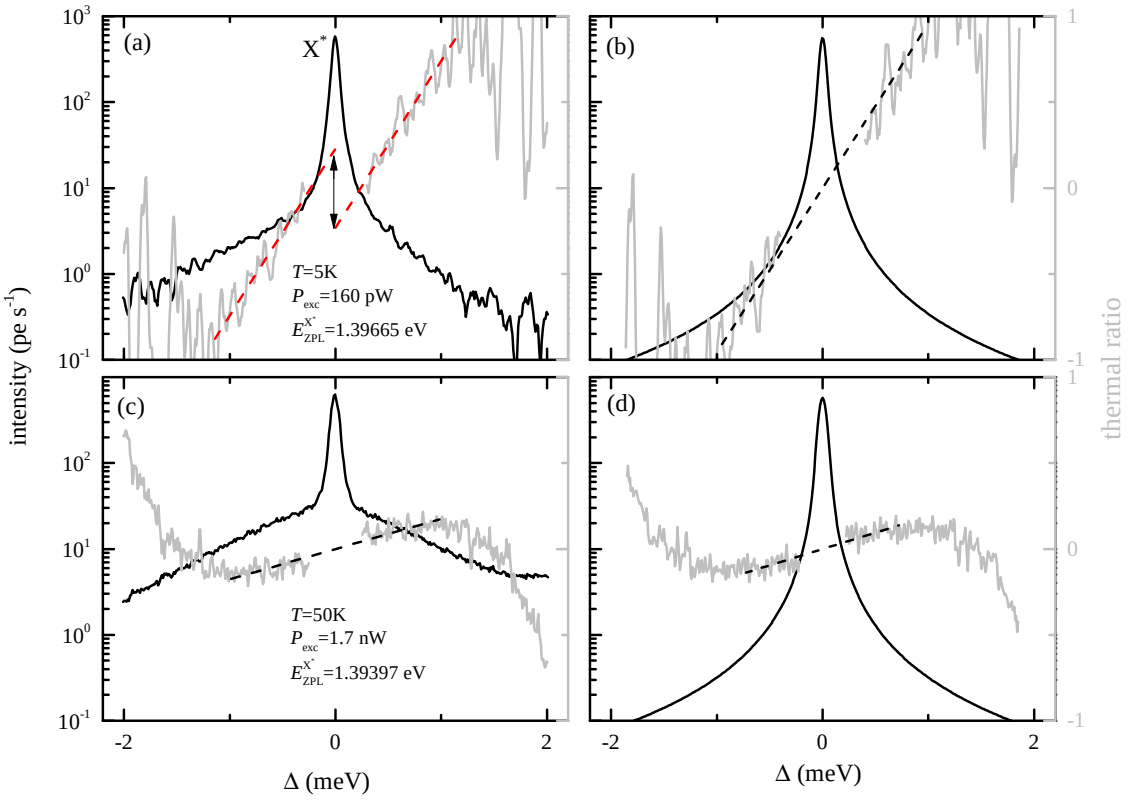

Figure 5.15: (a) Black solid lines: ↻ polarised PL spectrum at $T = 5\,\mathrm{K}$, P_{exc}=160 pW, as a function of $\Delta = E - E^{X^*}_{ZPL}$; light grey solid lines: thermal ratio R_{T} calculated without subtraction of the ZPL contribution. (b) Black solid line: ZPL contribution obtained from the fit with Eq. 5.27; light grey solid lines: thermal ratio calculated after subtraction of the ZPL contribution. (c) and (d): as (a) and (b) respectively, but for T=50 K and $P_{\mathrm{exc}} = 1.7\,\mathrm{nW}$. For all the figures, red dashed line: linear fit including O_{T}; black dashed line: linear fit with $O_{\mathrm{T}} = 0$. All the measurements are performed on dQD_1.

around zero. We then calculate the standard deviation β of the resulting data. Finally, we obtain α as $\beta/\sqrt{2}$.

The shot noise of a signal is well known, and it gives rise to fluctuations characterised by a standard deviation $\sigma_{sn} = \sqrt{I}$, with I the the signal in photoelectrons.

The total noise of the final data D is then calculated by summing all the noise contributions, resulting in the following expression:

$$\sigma_D = \sqrt{(\sigma_r^m)^2 + (\alpha D)^2 + D} \ . \tag{5.30}$$

5.7 Phonon thermometer

In order to calculate the thermal ratio R_{T} and the corresponding phonon temperature, we first consider the spectra shown in Fig. 5.13 around the ZPL of the trion X^*, which shows visible sidebands. In Fig. 5.15 we show the spectrum (black solid lines) at T=5 K (a) and T=50 K, (c). The zero of the energy axis is fixed to the corresponding peak energy of the ZPL (E_{ZPL}), as given in the figure. The thermal ratio is shown by the light grey solid

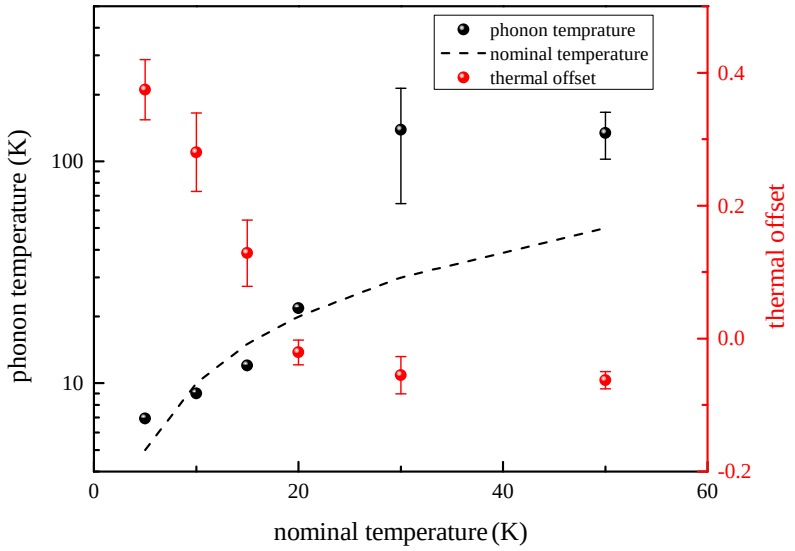

Figure 5.16: Phonon thermometer analysis on dQD_1. Phonon temperature (black symbols) and thermal offset (red symbols) as a function of the nominal temperature. Dashed line: nominal temperature.

line, and it is calculated without removing the ZPL contribution to the data (although the ZPL has been masked in order to better show the linear behaviour). At $T = 50\,\mathrm{K}$ R_T pass through zero at $\Delta = 0$, as shown by the linear fit (with intercept fixed to zero) given in black dashed line. This is the expected behaviour from the phonon thermometer described by Eq. 5.24. At $T = 5\,\mathrm{K}$ a remarkably different behaviour is observed: R_T does not pass through zero at $\Delta = 0$, as highlighted in Fig. 5.15(a). The phonon thermometer is not respected in this case, and the fit (red dashed line) requires a finite intercept (which we call thermal offset O_T). We apply the phonon thermometer analysis by fitting the linear part of the thermal ratio R_T, up to $T = 50\,\mathrm{K}$, including the thermal offset O_T, as exemplified in Fig. 5.15(a) by the red dashed lines. The results are shown in Fig. 5.16. The phonon temperature roughly reproduces the nominal one up to T=20 K. For $T > 20\,\mathrm{K}$, the phonon temperature is overestimated and it has large error bars. This is due to the interference of the sidebands from higher lying X emission, as it is possible to see in Fig. 5.13. We will see that the global fit explained in the next section significantly improve the situation. On the other hand, the thermal offset O_T decreases with the temperature.

To further investigate on the origin of the observed thermal offset, we calculate R_T after having subtracted the ZPL contribution, obtained using the fit with Eq. 5.27, from the measured spectrum. The results are shown in Fig. 5.15(b) and (d), for T=5 K and T=50 K respectively, together with the removed ZPL contribution given in black solid line. At $T = 50\,\mathrm{K}$, R_T respects the phonon thermometer. Surprisingly, this is now the case also at T=5 K. Such observation, brought us to develop the fitting model explained in the next session.

5.8 Fitting model

In this section, we describe in details the model we developed to fit the single QD lineshapes shown in Fig. 5.13. We use a simple microscopic model for the exciton wavefunction, which allows us to calculate the cumulant for an elliptical confinement potential. Then, we include a convolution with the IBM lineshape which allows a fit of the single QD lineshape also in presence of the observed thermal offset. The calculations have been performed by Amy Murreau and Dr. Egor Muljarov, with input from the author, Dr. Francesco Masia and Prof. Wolfgang Langbein. The idea of the model originated from Wolfgang Langbein and the author.

5.8.1 Cumulant for elliptical quantum dots

According to our model, the QD is assumed to generate an anisotropic parabolic confinement potential for both the electron and the hole. Assuming both carriers to be in their ground state, the envelope function takes this form:

$$\psi_a(\boldsymbol{r}_a) = \sqrt{\frac{1}{\pi^{3/2} a_\parallel^2 a_\perp}} e^{-\frac{x_a^2+y_a^2}{2a_\parallel^2}} e^{-\frac{z_a^2}{2a_\perp^2}} \quad , \tag{5.31}$$

with a=e,h and $a_\parallel$ and $a_\perp$ the QD confinement lengths in the plane and along the growth direction respectively. In this simplified model, we assume the same envelope function for electrons and holes. We indirectly take into account electron-hole Coulomb correlations through the confinement lengths $a_\parallel$ and $a_\perp$, which are assumed to be independent parameters for exciton and trion. In the double QD case, the confinement lengths also include the effect of exciton delocalization over the two QDs, as they are expected to be electronically coupled for 2 nm separation. A more accurate model is postponed to future modelling. Using Eq. 5.12, Eq. 5.13, Eq. 5.14 and Eq. 5.17, the spectral density function, using $\hbar = 1$, takes the following form:

$$J(\omega) = J_0 \omega^3 \exp\left(\frac{a_\parallel^2 q_\parallel^2}{4}\right) \exp\left(\frac{a_\perp^2 q_\perp^2}{4}\right) \quad , \tag{5.32}$$

with J_0 as defined in Eq. 5.19a. These expressions are used to calculate the cumulant $K(t)$ as given in Eq. 5.20. In particular:

$$K_{\mathrm{p}}(t) = \mathcal{F}\left[\frac{N_{\boldsymbol{q}} J_0 v_{\mathrm{s}}\sqrt{\pi}}{\sqrt{2\left(a_{\parallel}^2 - a_{\perp}^2\right)}}\eta(\omega)\right] \tag{5.33a}$$

$$\Omega_{\mathrm{p}} = J_0 \frac{\sqrt{\pi}}{2}\frac{v_{\mathrm{s}}^3}{a_{\parallel}^2 a_{\perp}} \tag{5.33b}$$

$$S = \frac{J_0 v_{\mathrm{s}}\sqrt{\pi}}{\sqrt{2\left(a_{\parallel}^2 - a_{\perp}^2\right)}}\int_0^{+\infty} \mathrm{d}\omega\eta(\omega)\coth\left(\frac{\omega}{2k_{\mathrm{B}}T}\right) \quad , \tag{5.33c}$$

with $\mathcal{F}$ indicating the Fourier transform and

$$\eta(\omega) = w\left(\frac{\omega}{\sqrt{2}v_{\mathrm{s}}}\sqrt{a_{\parallel}^2 - a_{\perp}^2}\right)\exp\left(-\frac{a_{\perp}^2\omega^2}{2v_{\mathrm{s}}}\right)\exp\left(-\frac{a_{\parallel}^2\omega^2}{2v_{\mathrm{s}}}\right) \quad . \tag{5.34}$$

w is the Faddeeva function, defined as:

$$w(z) = e^{-z^2}\left(1 + \mathrm{erfi}(z)\right) \quad , \tag{5.35}$$

with $\mathrm{erfi}(z) = -i\mathrm{erf}(iz)$ and erf the error function.

5.8.2 Inclusion of the zero-phonon lineshape

As already discussed in Sec. 5.3.3, the IBM without including the quadratic coupling does not lead to a broadening of the ZPL. The inclusion of the quadratic coupling [200], in the long time limit, naturally introduces an exponential decay term $\propto \exp^{-\Gamma t}$ in the IBM polarisation, describing the homogeneous broadening. On the other hand, the quadratic coupling does not include the inhomogeneous broadening due to spectral diffusion. Therefore, in order to include both homogeneous and inhomogeneous broadening, an exponential and a Gaussian decays of the polarisation is considered phenomenologically, leading to:

$$P(t) = P_{\mathrm{IBM}}(t)e^{-\frac{\gamma_{\mathrm{L}}}{2}t}e^{-\left(\frac{\pi}{2\ln(2)}\gamma_{\mathrm{G}}\right)^2 t^2} \quad , \tag{5.36}$$

with γ_{L} and γ_{g} the FWHM of the corresponding Lorentzian and Gaussian spectral functions. In the frequency domain, Eq. 5.36 corresponds to a convolution of the IBM spectral lineshape, with the Gaussian and Lorentzian spectral functions. The observed thermal offset is created by the mixing of the low energy and high energy sidebands due to the convolution. To verify this behaviour, we calculate the ratio from the data simulated with Eq. 5.36, including only the Lorentzian decay ($\gamma_{\mathrm{G}} = 0$, $\gamma_{\mathrm{L}} = 4\,\mu\mathrm{eV}$) or the Gaussian decay ($\gamma_{\mathrm{L}} = 4\,\mu\mathrm{eV}$, $\gamma_{\mathrm{L}} = 0$), for the same QD parameters given in Fig. 5.6. In both cases, R_{T} is calculated without removing the ZPL lineshape. The results are shown in Fig. 5.17. As it possible to see, the thermal offset is mainly determined by the Lorentzian broad-

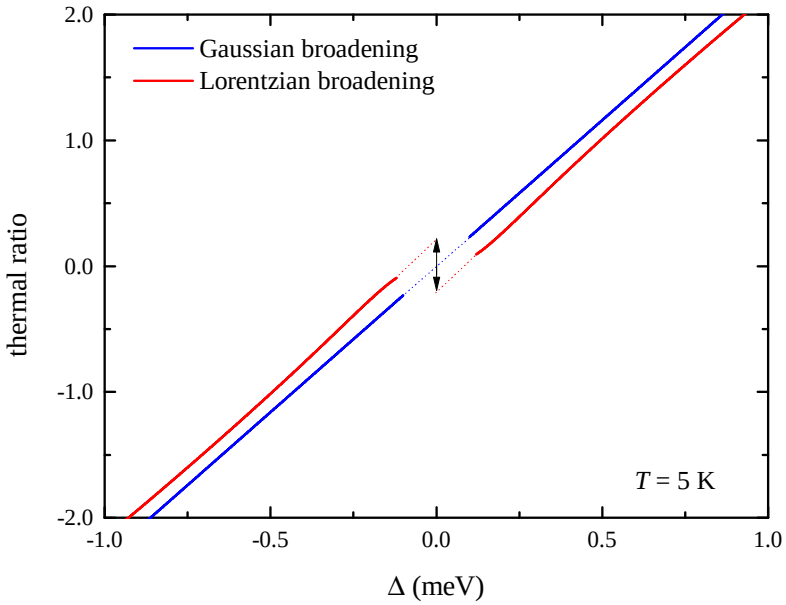

Figure 5.17: Thermal ratio calculated from data simulated with Eq. 5.36, without removing the ZPL lineshape. Red: $\gamma_G = 0$, $\gamma_L = 4\,\mu eV$; blue: $\gamma_L = 4\,\mu eV$, $\gamma_L = 0$. QD parameters as in Fig. 5.6. Amy Morreau built and run the model to generate the simulated data; plot produced by the author.

ening. Indeed, a Lorentzian lineshape has more pronounced tails than the corresponding Gaussian with the same FWHM, and the thermal offset is expected to be dominated by its contribution. We will comment further on this point when discussing the fit results. Therefore, the observed thermal offset can be used to separate the homogeneous and inhomogeneous broadening of the emission lineshape, similarly to FWM spectroscopy [66] and speckle analysis [165].

In order to fit the spectra shown in Fig. 5.13, we include two independent polarisations of the form given by Eq. 5.36, one for the exciton P_X and one for the trion P_{X^*}, by adding their corresponding emission spectra, calculated using Eq. 5.23. Importantly, for QDs where the FSS has been found to be comparable with the Zeeman splitting, we use Eq. 5.25 to fit the exciton peak. Note that in Sec. 5.4.3, Eq. 5.25 was used to perform a global fit using both ↻ and ↺ polarisations, while here only the ↻ polarisation is used.

5.9 Fitting results

To perform the fit, we minimise the weighted mean square deviation weighted with the coefficients $w_i = 1/\sigma_i^2$, with σ_i given by Eq. 5.30. For further details, we refer to Ref. [204]. In Fig. 5.18, Fig. 5.19, Fig. 5.20, Fig. 5.21, Fig. 5.22, Fig. 5.23 and Fig. 5.24 we show the results of the fit performed on the spectra from dQD_1, for ↻ polarisation, from T=5 K to T=100 K as indicated in the figures. Additional data for dQD_2 and sQD are shown in Sec. B.1 and Sec. B.2 of the appendix respectively. In each plot we give the corresponding fit parameters, which are the Lorentzian and Gaussian linewidths γ_L and γ_G respectively,

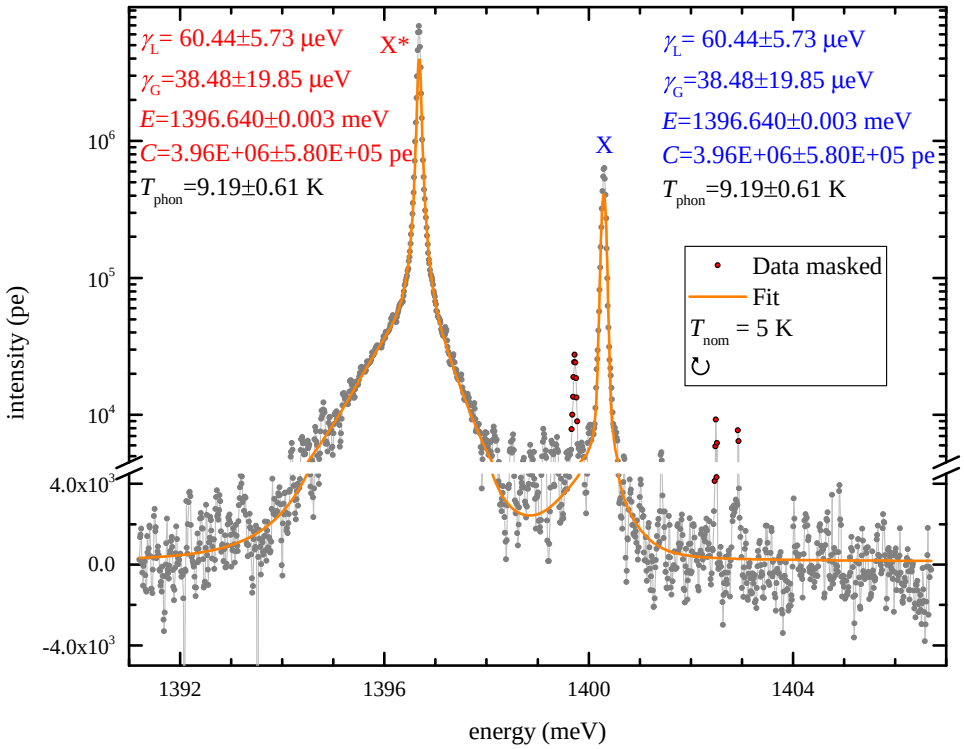

Figure 5.18: Experimental and fitted emission spectra for dQD_1 at the nominal temperature of 5 K, showing data manually excluded from the fit in red symbols. Fit root mean square error (RMSE) = 3.21. Red: fit parameters for X*; blue: fit parameters for X. The phonon temperature (black) is a global fit parameter. Amy Morreau built and run the model to fit the experimental data; plot produced by the author.

the peak energy E and the peak amplitude C, for both the X and the X* transitions. The phonon temperature T is a shared parameters between X and X*. The following procedure is applied: we first perform the fit allowing the parameters to vary independently for both the X and the X* emissions. We then perform a second fit, where $a_{\parallel}$ and $a_{\perp}$ are kept fixed to the weighted average, calculated separately for the X and X*, of the values obtained from the first fit. In particular, by indicating with x_i a general fit parameter with error (standard deviation as obtained from the fit) given by Δx_i, the weighted average is calculated as $(1/N)\sqrt{\sum_{i=1}^{N}(x_i/\Delta x_i)^2/\sum_{i=1}^{N}(1/\Delta x_i)^2}$, with N the number of fitted spectra. We use the same method for the deformation potential parameter $|D_c - D_v|$, but in this case the weighted average is calculated considering the values obtained from all the three QDs, as they all have the same material properties. These fixed parameters are given in the tables of Fig. 5.25, Fig. 5.26 and Fig. 5.27, together with the plots which summarise the results of the fit for the dQD_1, dQD_2 and sQD respectively.

Let us now describe the obtained results. We start from dQD_1. When increasing the temperature from 5 K to 100 K, we observe: for the X* state, a reduction of the Lorentzian linewidth from 60 μeV down to 30 μeV up to 50 K, which then increases up to about 350 μeV at 100 K; an increasing of the Gaussian linewidth from about 35 μeV up to 130 μeV; for the X state, an increasing of the Lorentzian linewidth from 15 μeV

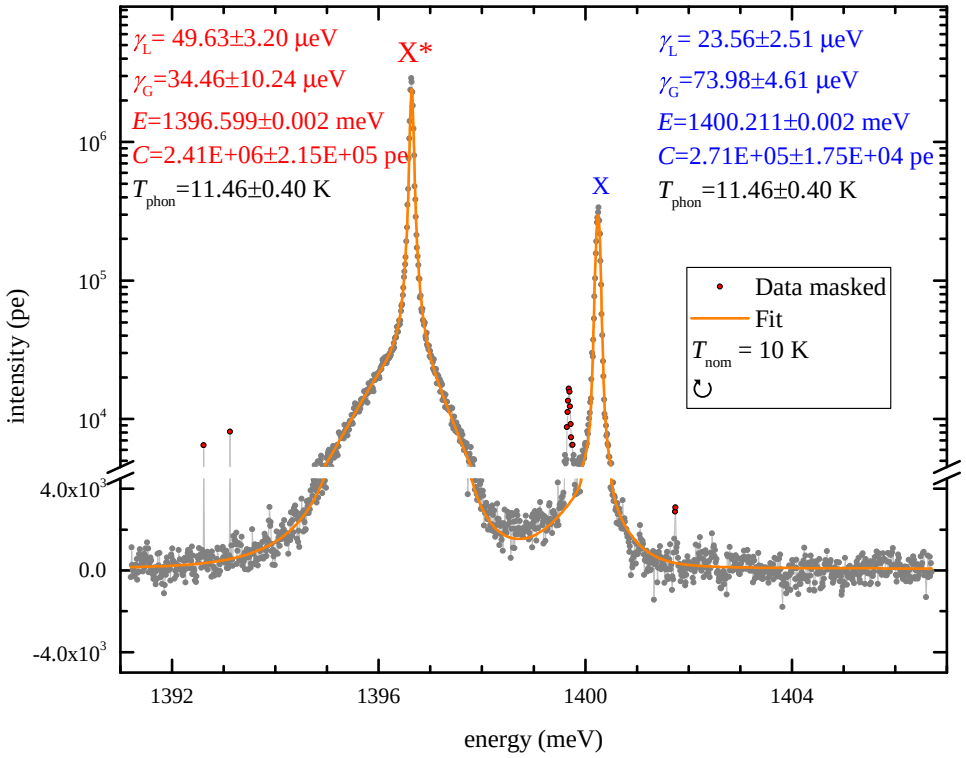

Figure 5.19: As Fig. 5.18, but for a nominal temperature T=10 K. Fit RMSE=2.79. Amy Morreau built and run the model to fit the experimental data; plot produced by the author.

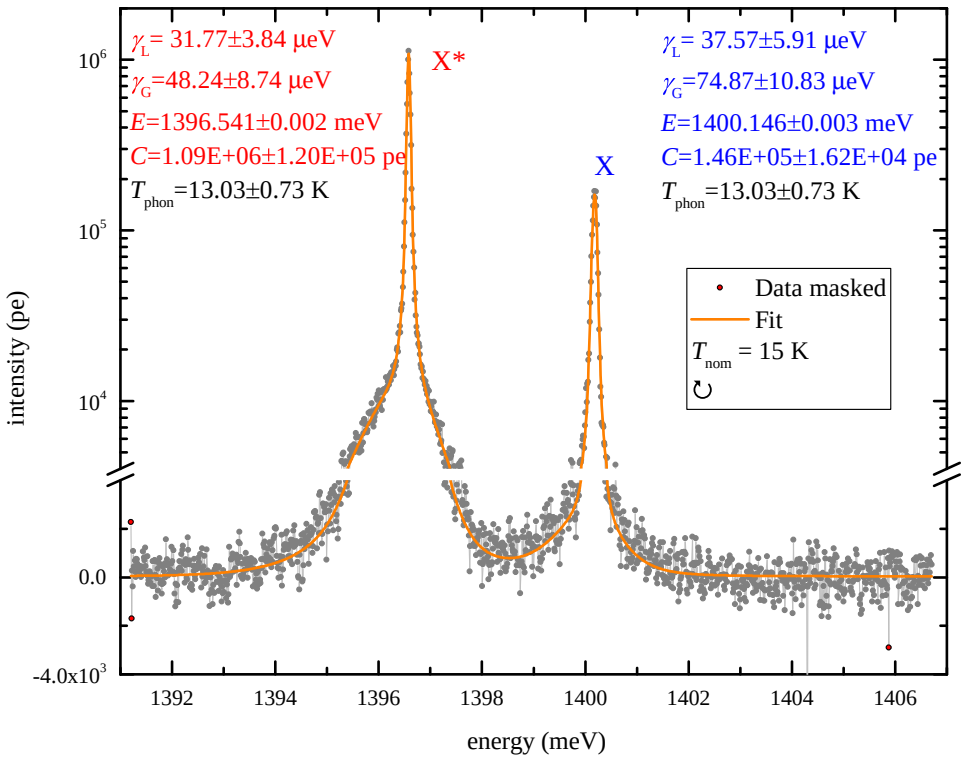

Figure 5.20: As Fig. 5.18, but for a nominal temperature T=15 K. Fit RMSE 2.45. Amy Morreau built and run the model to fit the experimental data; plot produced by the author.

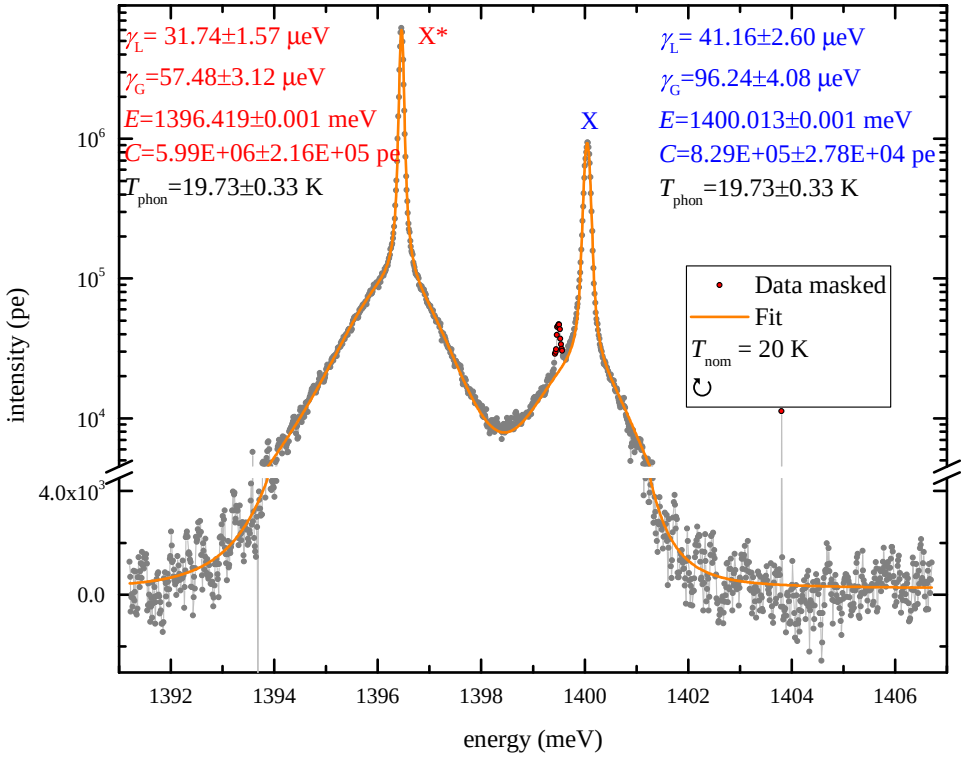

Figure 5.21: As Fig. 5.18, but for a nominal temperature T=20 K. Fit RMSE 2.57. Amy Morreau built and run the model to fit the experimental data; plot produced by the author.

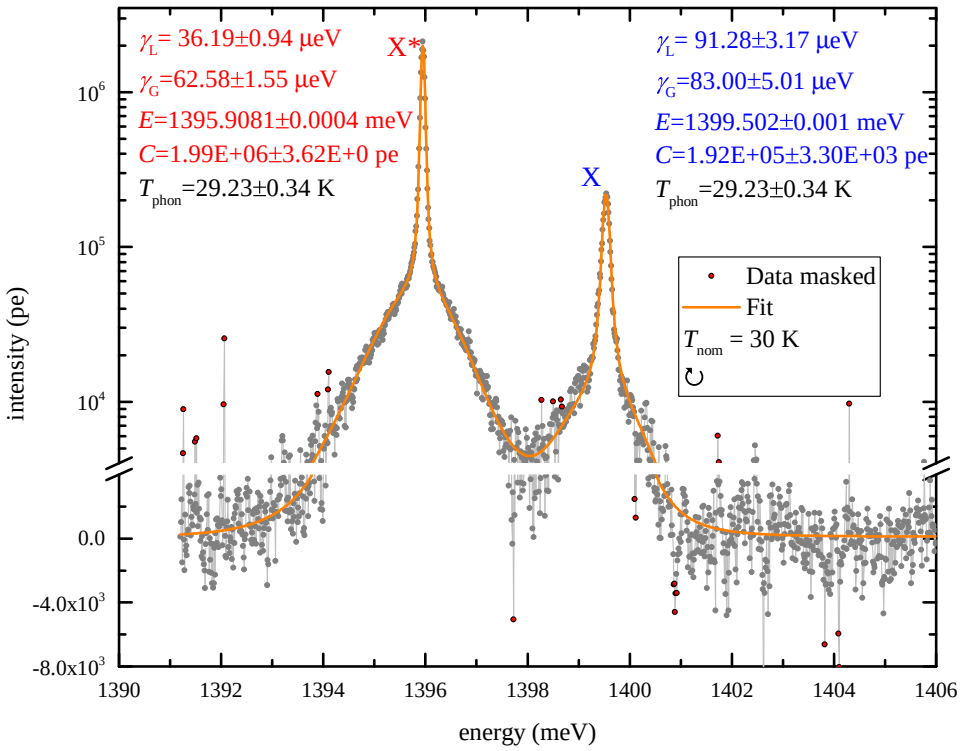

Figure 5.22: As Fig. 5.18, but for a nominal temperature T=30 K. Fit RMSE 4.37. Amy Morreau built and run the model to fit the experimental data; plot produced by the author.

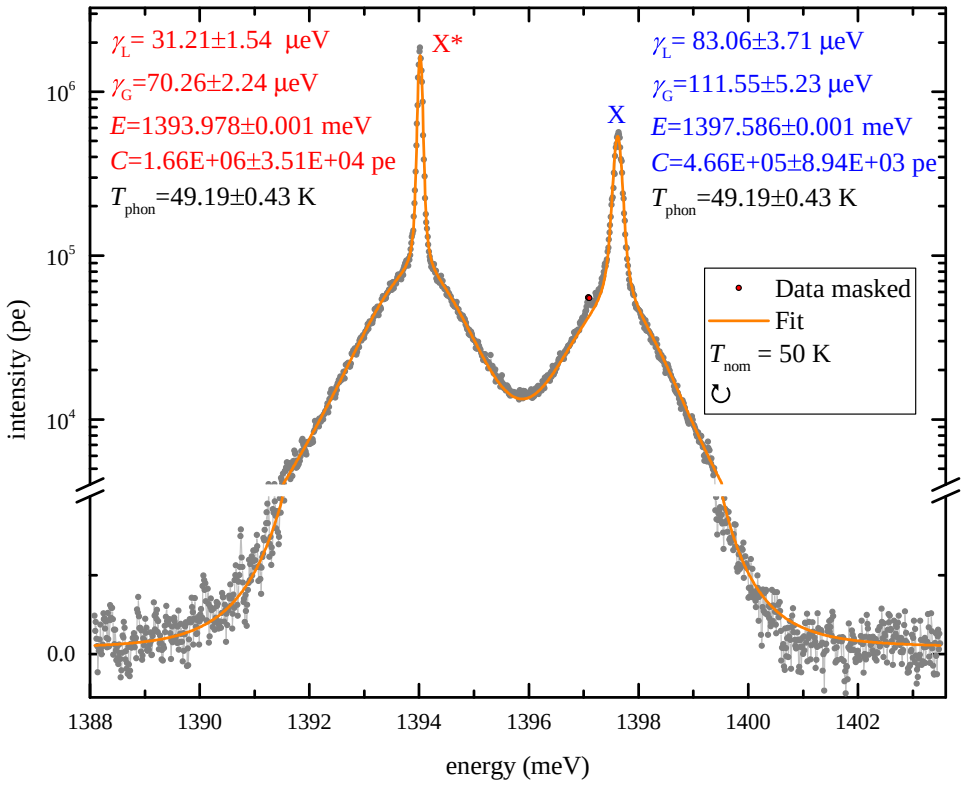

Figure 5.23: As Fig. 5.18, but for a nominal temperature T=50 K. Fit RMSE 2.37. Amy Morreau built and run the model to fit the experimental data; plot produced by the author.

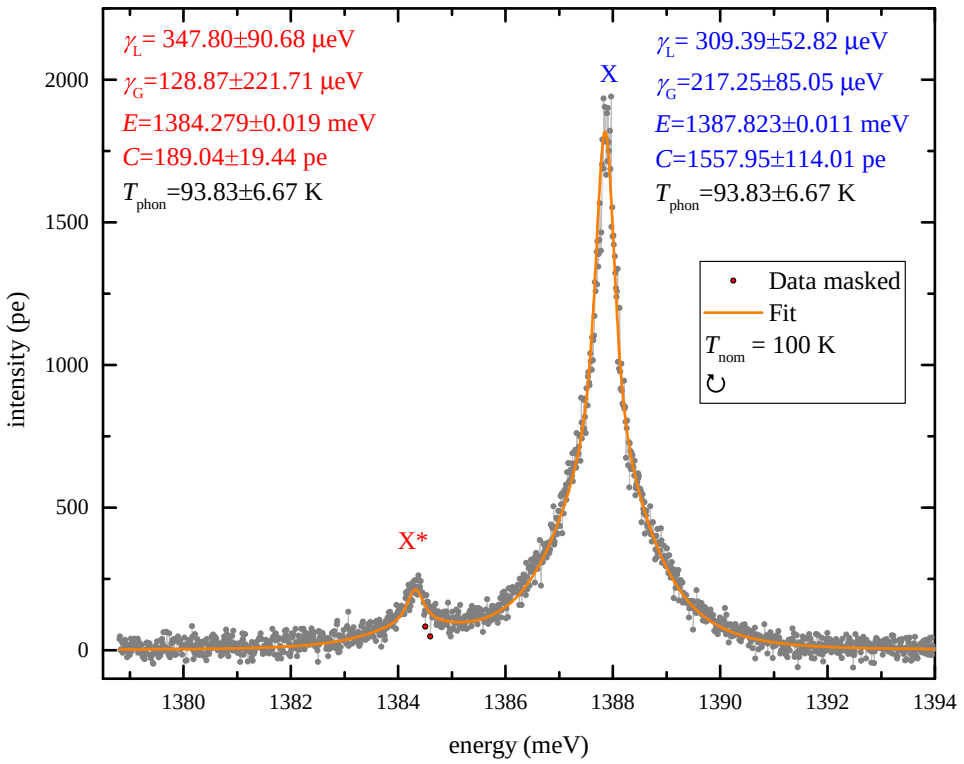

Figure 5.24: As Fig. 5.18, but for a nominal temperature T=100 K. Fit RMSE 0.84. Amy Morreau built and run the model to fit the experimental data; plot produced by the author.

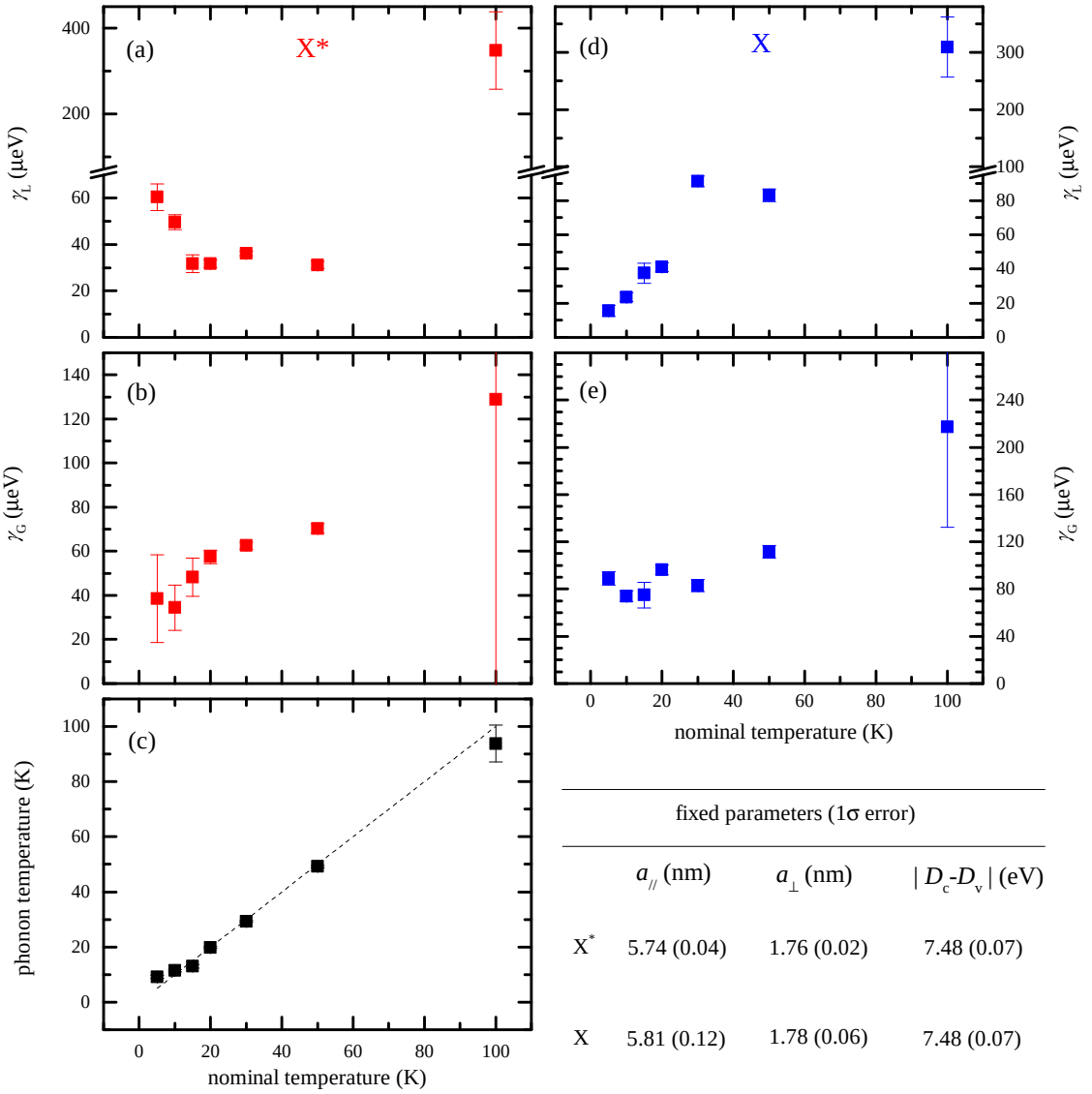

fixed parameters (1σ error)

	$a_{//}$ (nm)	$a_{\perp}$ (nm)	$\lvert D_c\text{-}D_v \rvert$ (eV)
X*	5.74 (0.04)	1.76 (0.02)	7.48 (0.07)
X	5.81 (0.12)	1.78 (0.06)	7.48 (0.07)

Figure 5.25: Fit summary for dQD_1. Red (blue) symbols: results for the trion (exciton) transition; (a) and (d): Lorentzian FWHM; (b) and (e): Gaussian FWHM; (c) phonon temperature as a function of the nominal temperature; table: confinement lengths and deformation potential parameter used in the fit and calculated as explained in the text.

up to about 310 μeV; an increasing of the Gaussian linewidth from about 75 μeV up to roughly 220 μeV. Aside from an offset at $T = 5$ K, of about 4 K, the obtained phonon temperature is in reasonable good agreement, within error bars, with the nominal one, as we would expect. The obtained in-plane ($a_{\parallel}$) and perpendicular ($a_{\perp}$) confinement lengths are 5.74 ± 0.04 nm and 1.76 ± 0.02 nm respectively for the X* state, and 5.81 ± 0.12 nm and 1.78 ± 0.06 nm respectively for the X state. Finally, as for dQD_2 and sQD samples, the deformation potential parameters $|D_c - D_v|$ is fixed to 7.48 ± 0.07 eV.

For dQD_2, when increasing the temperature from 5 K to 100 K, we observe: for the X* state, a roughly constant (within error bars) Lorentzian linewidth, of about 20 μeV, up to 30 K; it then starts to increase, reaching a value of 400 μeV at $T = 100$ K; an increase of the

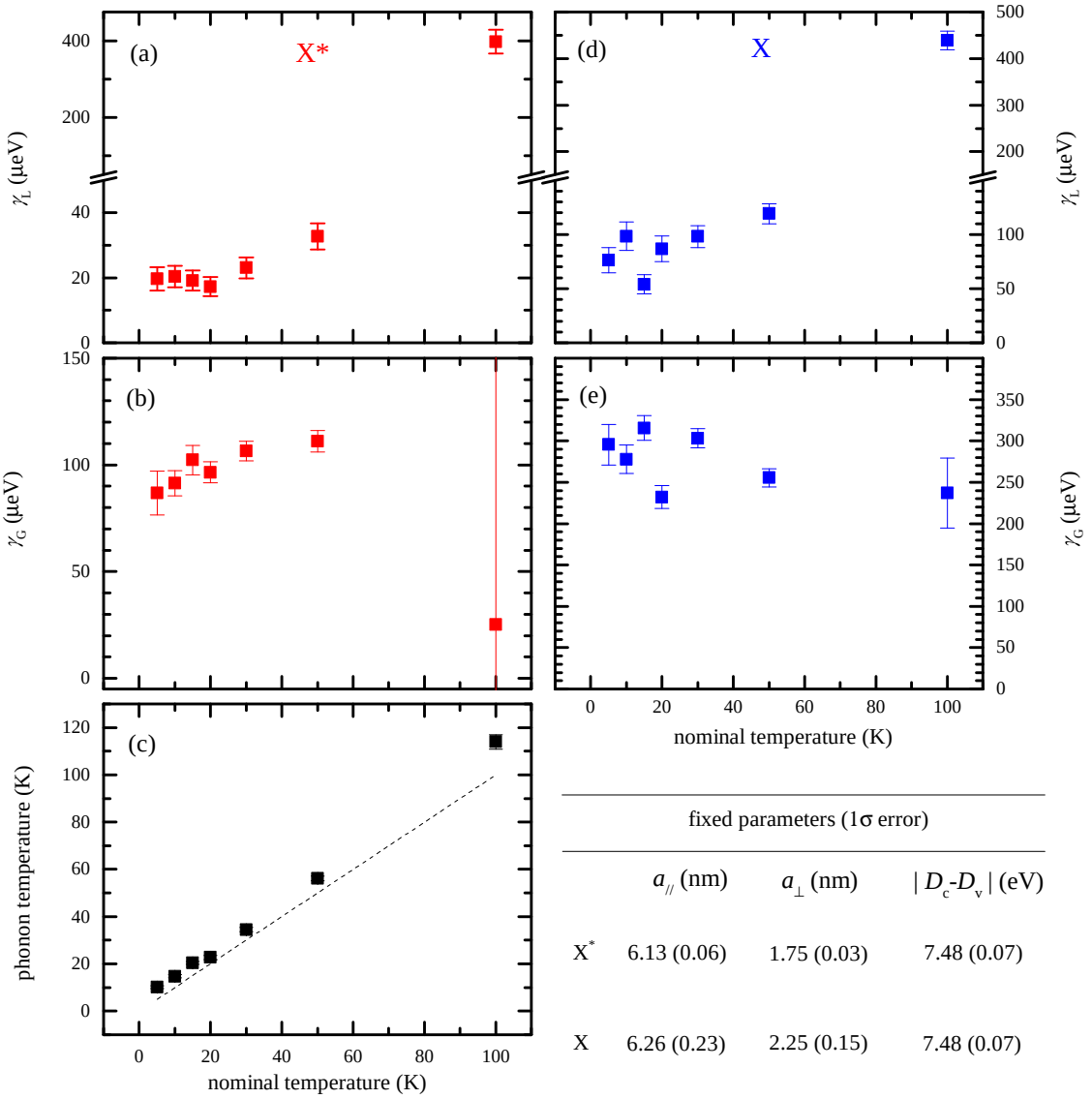

fixed parameters (1σ error)

	$a_{//}$ (nm)	$a_{\perp}$ (nm)	$\lvert D_c\text{-}D_v \rvert$ (eV)
X*	6.13 (0.06)	1.75 (0.03)	7.48 (0.07)
X	6.26 (0.23)	2.25 (0.15)	7.48 (0.07)

Figure 5.26: Fit summary for dQD_2, as Fig. 5.25.

Gaussian linewidth from about 87 μeV, to 111 μeV up to 50 K; the value at 100 K is not well defined due to extremely large error bars, and we do not discuss it further; for the X state, an increasing of the Lorentzian linewidth from 76 μeV to 439 μeV; a roughly constant Gaussian linewidth, which averages to 274 ± 33 μeV. In this case, the obtained phonon temperature shows an offset of about 4-5 K for all the temperatures, with the exception of $T = 20$ K, for which we obtain a phonon temperature of 22.73 ± 0.92 K, and $T = 100$ K, for which we obtain a phonon temperature of $T = 113.97 \pm 3.08$ K. The obtained in-plane and perpendicular confinement lengths are 6.13 ± 0.06 nm and 1.75 ± 0.03 nm respectively for the X^* state, and 6.26 ± 0.23 nm and 2.25 ± 0.15 nm respectively for the X state.

Finally, for the X^* state of the sQD sample, when increasing the temperature from 5 K to 100 K, we observe: an increase of the Lorentzian linewidth from 43 μev to 235 μeV; a not well defined Gaussian linewidth, which averages to 106 ± 58 μeV. The obtained phonon

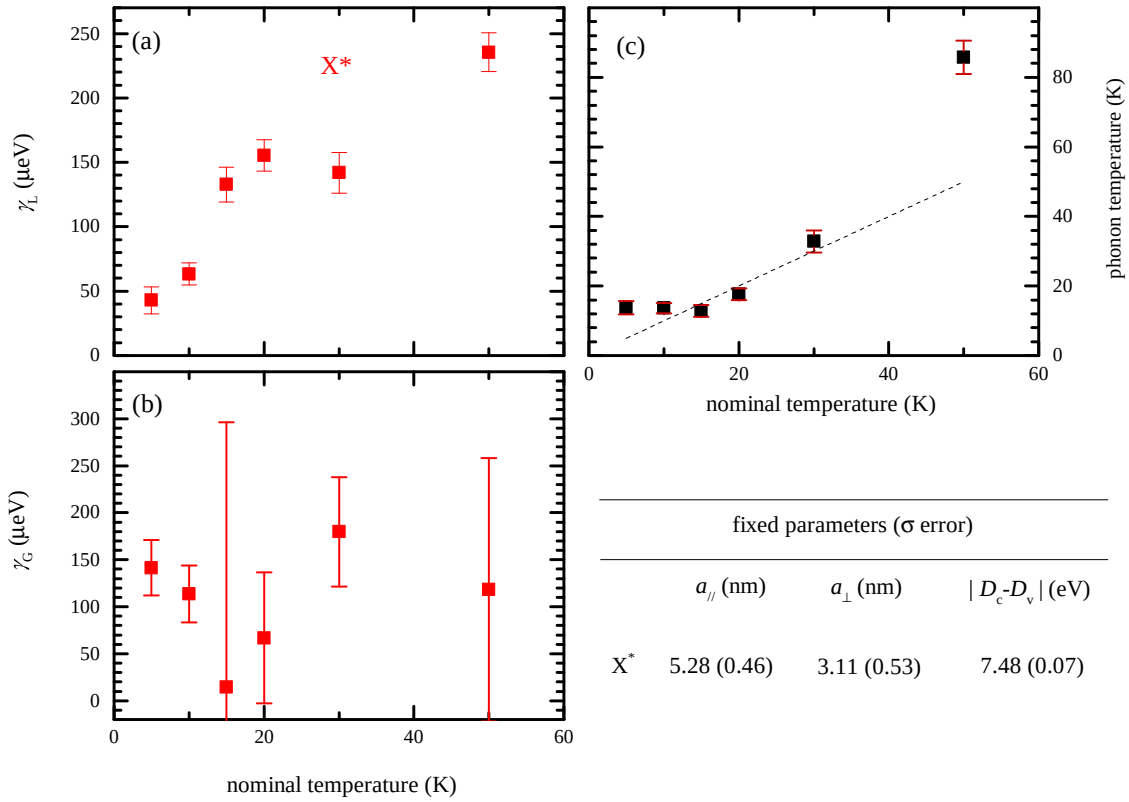

Figure 5.27: Fit summary for sQD, as Fig. 5.25, but only for the X* transition.

temperature stays approximately constant at 13 K up to a nominal temperature of 15 K; it is in agreement, within errors, to the nominal one at 20 K and 30 K; it then reaches a value of about 86 K for a nominal temperature of 50 K. The obtained in-plane and perpendicular confinement lengths are 5.28 ± 0.46 nm and 3.11 ± 0.53 nm respectively.

5.10 Discussion

We now turn into the discussion of the experimental results.

5.10.1 Confinement lengths: comparison with measurement of diamagnetic shift

An important aspect of fitting the phonon sidebands is that it allows to determine the confinement length of an exciton confined in the QD, from a simple PL experiment. Traditionally, the confinement length of excitons is determined from the diamagnetic shift of the corresponding transition [205, 206], which requires magnetophotoluminescence techniques [207]. The diamagnetic shift probes the motion of the charge carriers in the plane orthogonal to the field, and is therefore related to the excitonic wavefunction. In order to characterise a QD, there are mainly two configurations to be considered: magnetic field B aligned along the growth direction (Faraday configuration) and B orthogonal to the growth direction (Voigt configuration). For an exciton strongly confined in a QD, the

diamagnetic shift ΔE as a function of a magnetic field B is given by [205, 206]:

$$\Delta E_j = \frac{e^2}{8}\left(\frac{\langle\rho_{\mathrm{e}}^2\rangle_j}{m_{\mathrm{e}}} + \frac{\langle\rho_{\mathrm{h}}^2\rangle_j}{m_{\mathrm{h}}}\right) B^2, \tag{5.37}$$

where e is the electron charge, $\rho_i = (x_i, y_i, z_i)$, m_{e} (m_{h}) is the electron (hole) effective mass and j=F,V with F (V) labelling Faraday (Voigt) configuration. We use the wavefunction ψ given by Eq. 5.31 for the electron and the hole, therefore $\rho_{\mathrm{e}} = \rho_{\mathrm{h}} \equiv \rho$. We then calculate $\langle\rho^2\rangle_j$ as:

$$\begin{aligned}\langle\rho\rangle_{\mathrm{F}} &= \int dx\, dy\, dz \left(x^2 + y^2\right) |\psi|^2 = a_{\parallel}^2 \\ \langle\rho\rangle_{\mathrm{V}} &= \int dx\, dy\, dz \left(x^2 + z^2\right) |\psi|^2 = \frac{1}{2}\left(a_{\parallel}^2 + a_{\perp}^2\right) \quad .\end{aligned} \tag{5.38}$$

We now make use of Eq. 5.38, together with Eq. 5.37, to estimate $a_{\perp}$ and $a_{\parallel}$ from the measurement of diamagnetic shift presented in the PhD thesis of Barbara Van Hattem [208]. In her work, $\gamma_{\mathrm{F}} = \Delta E_{\mathrm{F}}/B^2 = 22\,\mu\mathrm{eV/T^2}$ and $\gamma_{\mathrm{V}} = \Delta E_{\mathrm{V}}/B^2 = 15\,\mu\mathrm{eV/T^2}$ have been measured. Using the GaAs effective masses with the hole effective mass given by $m_{\mathrm{v}} = (m_{\mathrm{lh}} + m_{\mathrm{hh}})/2$, these values corresponds to $a_{\parallel} \sim 7\,\mathrm{nm}$ and $a_{\perp} \sim 4\,\mathrm{nm}$.

A more correct expression for the diamagnetic shift has been calculated by Muljarov et al. [209], and it is given by:

$$\Delta E_{\mathrm{F}} = \sum_{i=\mathrm{e,h}} \frac{e^2 \langle x_i^2\rangle \langle y_i^2\rangle}{2m_i c^2 \left(\langle x_i^2\rangle + \langle y_i^2\rangle\right)} B^2 \tag{5.39a}$$

$$\Delta E_{\mathrm{V}} = \sum_{i=\mathrm{e,h}} \frac{e^2 \langle x_i^2\rangle \langle z_i^2\rangle}{2m_i c^2 \left(\langle x_i^2\rangle + \langle z_i^2\rangle\right)} B^2 \quad . \tag{5.39b}$$

In this case, we calculate the following expressions for the diamagnetic shift:

$$\Delta E_{\mathrm{F}} = \frac{a_{\parallel} e^2}{8c^2}\left[\frac{1}{m_{\mathrm{e}}} + \frac{1}{m_{\mathrm{h}}}\right] \tag{5.40a}$$

$$\Delta E_{\mathrm{V}} = \frac{e^2}{4c^2}\frac{a_{\parallel}^2 a_{\perp}^2}{a_{\parallel}^2 + a_{\perp}^2}\left[\frac{1}{m_{\mathrm{e}}} + \frac{1}{m_{\mathrm{h}}}\right] \quad , \tag{5.40b}$$

from which we derive $a_{\parallel} \sim 7\,\mathrm{nm}$ and $a_{\perp} \sim 5\,\mathrm{nm}$. In both cases, the values from our fit are slightly smaller. Anyway, we emphasise that we are comparing numbers from samples growth on different chips and at distance of years. Therefore, we can not exclude that the two samples are just different. For a more quantitative comparison, we would need a measurement of the diamagnetic shift on exactly the same QDs we measured.

5.10.2 Deformation potentials

The deformation of the crystal due to hydrostatic pressure changes the lattice potential, resulting in the energy shift of band-edge electronic states [210]. The amount of energy

shift is quantified by the deformation potentials D_c and D_v. These quantities are usually measured in diamond anvil cells [211, 212], which allow to measure PL spectra under high pressure. For InAs, accepted values for the deformation potentials are $D_c = -5.08\,\text{eV}$ and $D_v = 1.00\,\text{eV}$, resulting in $|D_c - D_v| = 6.08\,\text{eV}$ and for GaAs $D_c = -7.17\,\text{eV}$ and $D_v = 1.16\,\text{eV}$, resulting $|D_c - D_v| = 8.33\,\text{eV}$ [210]. For InGaAs, only the parameter $|D_c - Dv|$ has been measured, and it has been found to be $(7.79 \pm 0.40)\,\text{eV}$ at the Γ-point [211], which is in perfect agreement with the value we obtained from our fit of $7.48 \pm 0.07\,\text{eV}$. This is a remarkable result, as it supports the validity of our model, and implies that our fitting model can be used as an alternative powerful tool to determine the deformation potential parameter $|D_c - D_v|$.

5.10.3 Phonon temperature

Contrary to other works where the phonon temperature was fixed to the nominal one [192, 193], having the phonon temperature as a free fit parameter allows us to use our fitting model as a phonon thermometer, as already mentioned in Sec. 5.7, which has not been shown before for QDs. For dQD_1, we find that the phonon temperature is in good agreement with the nominal one, as we would expect. Importantly, contrary to the simple analysis shown in Fig. 5.16, the phonon thermometer works well also at $T > 20\,\text{K}$, as the fit includes the exciton and trion sidebands. For dQD_2, the phonon temperature has a small offset to the nominal one, as observed in Fig. 5.26. The offset is about 1-2 K at $T = 20\,\text{K}$, which could be explained as a local heating effect due to optical excitation and the thermal radiation. At all the other temperatures, the offset is of the order of 4-5 K, and it reaches 10 K at the nominal temperature of 100 K. This is probably too high to be explained by local heating and it might rather be a systematic error of our fit. One could improve the fit by removing the camera sensitivity fluctuations from the data, which in principle are known, rather then including them as a fit weight. This has not been done yet, but we believe it could lead to an improvement. The phonon temperature for the sQD sample fluctuates around the nominal temperature. The reason for the larger fluctuations could be the lower signal to noise ratio, about 1 order of magnitude less than for the dQDs samples at $T = 5\,\text{K}$, which affects the fit of the tails of the phonon sidebands.

5.10.4 Lorentzian and Gaussian lineshapes

The homogeneous linewidth in InGaAs/GaAs QDs has been investigated by FWM spectroscopy, and it was found to be 2 µeV at $T = 7\,\text{K}$ [66]. This value is below our spectrometer resolution, which was measured to be about 8 µeV FWHM at the energy of the QDs emission. The obtained Gaussian broadening is always quite large with respect to the expected homogeneous linewidth at low temperatures, >30 µeV in all the investigated samples and for both the X and X^* transitions, reaching values of the order of 300 µeV in some cases (see for example Fig. 5.26(e)). Therefore, the inhomogeneous broadening due to spectral diffusion is quite strong in these QDs, which also implies charging. Inelastic processes

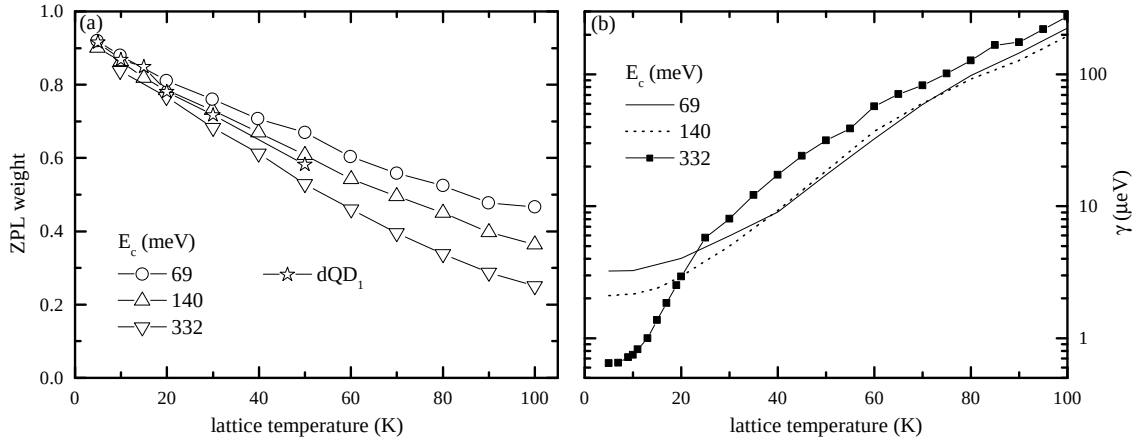

Figure 5.28: (a) ZPL weights as a function of temperature for different confinement energies E_c, measured on InAs QDs by FWM spectroscopy; star symbols: ZPL measured on dQD_1. (b) Homogeneous broadening as a function of temperature measured on InAs QDs by FWM spectroscopy. Both figures are reproduced from Ref. [214].

which occur due to the presence of charge carriers trapped in the QD surrounding seem to give a significant contribution to the observed Lorentzian lineshape at low temperatures, which is always above resolution and >10 μeV in all cases at $T = 5$ K. The Lorentzian linewidth increases with the temperature in all the samples and for both the X and X* transitions, as expected from inelastic scattering with acoustic phonons [66], which populates other spin states of the exciton ground state [213]. The only exception is for the X* of the dQD_1 (Fig. 5.25(a)), for which γ_L decreases form 60 μeV at 5 K down to 30 μeV at 50 K. Importantly, γ_L at $T = 100$ K is of the order of 300-400 μeV, which is higher than what found with FWM spectroscopy in Ref. [66], although γ_L was given only for strongly confined QDs. For a better comparison, we use the data published in Ref. [214]. In the work of Borri et al., the homogeneous broadening of InAs QDs is measured by FWM spectroscopy, as a function of the size dependent confinement energy E_c, measured with respect to the WL absorption peak. For similar materials, the ZPL weight is expected to be determined mainly by the QD size. Therefore, by comparing the measured ZPL weight for dQD_1, with the ZPL weights for different confinement energies, we conclude that the samples investigated here have confinement energies of the order of 140 meV, as shown in Fig. 5.28(a). For these confinement energies, the homogeneous broadening at 100 K is about 200 μeV, as shown in Fig. 5.28(b). Therefore, the homogeneous broadening in our system is about a factor of 2 higher than what expected from inelastic scattering with acoustic phonons, which implies the dynamics is still dominated by scattering with charge carriers. An analysis of power dependence would help to further confirm this conclusion.

5.11 Conclusions

In conclusion, we have presented a fitting model, based on the IBM, which allows us to fit PL emission spectra, where the characteristic lineshape, given by a ZPL plus sidebands

due to phonon-assisted transitions, is visible. From the fit, we are able to determine: deformation potentials, which usually requires anvil cells; QD confinement lengths, whose determination requires measurements of the exciton diamagnetic shift; phonon temperature, which was never done for QDs. Additionally, we also separate the inhomogeneous from the homogeneous broadening using a thermal offset which is not predicted by the IBM. These results are remarkable, as we are able to obtain a series of parameters from a single, and relatively simple, measurement.

As an outlook, high dynamic range measurements for different excitation powers are needed to further investigate on the large homogeneous broadening we observe, as well as measurements of FWM. Additionally, one could further extend the model by the inclusion of Coulomb correlation effects in the wavefunction. Finally, one could model the inhomogeneous broadening as a sum of discrete energy steps, rather then a continuous Gaussian distribution. Indeed, we have measured also a series of data where discrete energy shifts of the lineshape, due to trap states, seem to dominate the spectra. For decreasing energy shifts, the model would then tend to the Gaussian limit. In terms of fitting procedure, the next step would be to remove from the data the sensitivity fluctuations of the CCD camera, which we have measured separately.

Chapter 6

Conclusions

6.1 Summary

This thesis is based on three different experiments: the first one is a study of the exciton density dynamics in MLs of $MoSe_2$; the second one is a study of the coupling of InAs QDs to a PCWG mode; the third one is a study of the spontaneous emission lineshape of InGaAs PQDs.

The exciton density dynamics in ML of $MoSe_2$ is measured by heterodyne detected resonant three-beam FWM spectroscopy. Our detection scheme allows to measure the signal both in amplitude and phase. The dynamics from 100 fs to 10 ns is described by a complex multi-exponential response function, including four exponentially decaying processes. We developed a fitting function to fit the FWM signal simultaneously in amplitude and phase, allowing for quantitative analysis. The dynamics is interpreted in terms of the intrinsic band structure as radiative decay, scattering within the exciton dispersion, and scattering between spin-allowed direct and spin-forbidden indirect exciton states. We exclude exciton-exciton annihilation as a relevant process in the dynamics.

The coupling of InAs QDs to standard PCWGs is investigated by direct spectral imaging. In particular, we measured a maximum beta factor of 0.99 ± 0.01, after correcting for the propagation losses and for the relative coupling efficiencies of the grating out-couplers. All the reported measured beta factors are not corrected for the collection efficiency of free-space and coupler emission, which would increase the beta factor, since the free space emission, according to our simulation, is collected typically twice as efficiently depending on the QD position. We find that low beta factors occur at points of high circularities. Additionally, spectral imaging allows us to observe directional emission of photons, which we use to estimate the electromagnetic field polarisation at the QD location. The QD beta factor and the corresponding mode circularity uniquely define the QD position inside the lattice unit cell. To exploit this property, we performed numerical simulations. In particular, we first measured the PCWG band structure, within the light cone, using Fourier spectroscopy. This measurement is used to calibrate the simulation parameters to the sample structure. We then perform finite-difference time-domain simulations to calculate

beta factor and mode circularity as a function the dipole source position inside the lattice unit cell. We fully simulate the experimental measurements, by including both the collection efficiency, determined in the far-field by microscope objective and in the real-space by the input slit of the imaging spectrometer, and the detection efficiency, determined by the spectrometer grating efficiency for different incident polarisations. From the comparison of experimental data and simulations, we determined the most likely QD position within the lattice unit cell.

The spontaneous emission lineshape of individual InGaAs PQDs is investigated by PL spectroscopy. Using measurements of power dependence, fine-structure splitting and Zeeman splitting, we attribute the emission lines to exciton, trion and biexciton recombinations. We performed high dynamic range measurements to observe phonon sidebands with high signal-to-noise ratio. We developed a fitting model for the lineshape, based on the independent boson model, from which we obtain the absolute value of the difference of the electron and hole deformation potentials, the QD confinement lengths and the phonon temperature. Additionally, we used an observed thermal offset to separate the homogeneous and inhomogeneous contributions in the single QD lineshape.

6.2 Future directions

In the following, we present the future research directions which build upon the results described in this work.

In terms of ensemble measurements of heterodyne-detected FWM, a possible research direction is the development of a microscopic model for the complex multi-exponential response function which is used to fit experimental data. This would be helpful for the understanding of the exciton-exciton interactions and the corresponding scattering channels in TMDs, where the intricate band structure together with strong excitonic effects are responsible for a complicated exciton dynamics.

Another interesting research direction is to use the concepts developed in Ch. 4, together with the fitting routine described in Ch. 5, to investigate the exciton-phonon coupling in PCWGs. In particular, recent theoretical studies [215, 216] demonstrated that the homogeneous linewidth of QDs embedded in nanobeam waveguides is limited by the coupling to vibrational modes of the waveguide and that the coupling depends on the QD position inside the lattice unit cell. On the other hand, another recent study showed that PQDs can be embedded in photonic crystal structures, with measured beta factor up to 88% [217]. Therefore, by applying spectral imaging to PQDs embedded in PCWG, we could investigate the exciton-phonon coupling as a function of the QD position inside the lattice unit cell. This experiment is important in the context of QD-based single photon sources.

The fitting routine presented in Ch. 5 has potential applications also in other physical systems. Although in this work it is tested on a relatively well known system such a InGaAs QDs, it could be used to explore exciton-phonon coupling mechanisms in emerging

physical systems like QD defects in ML-TMDs [218, 219]. Similarly to PQDs, they can be site-controlled, and they are therefore promising for scalable optical quantum information processing. The understanding of the dephasing mechanisms, QD confinement lengths and exciton-phonon coupling parameters in these systems is therefore an important step forward. In this context, our fitting model, combined with single QD FWM, could lead to interesting results.

Appendix A

Additional data for WG_B sample

In Ch. 4 we show data mainly for WG_A. In this section of the appendix, data for WG_B are also shown.

A.1 Waveguide dispersion

In Fig. A.1, we show the simulated dispersion of the PCWG, together with an emission spectrum from an ensemble of QDs. The sample parameters used in the simulation are adjusted to match the measured dispersion, shown by the blue circles. The matching criteria are described in Sec. 4.8.1. Similarly to WG_A, the QDs emit between 1.37 eV and 1.43 eV. The broader emission at around 1.42 eV is due to the QD WL. Sharp lines superimposed to the WL emission are attributed to localized excitons.

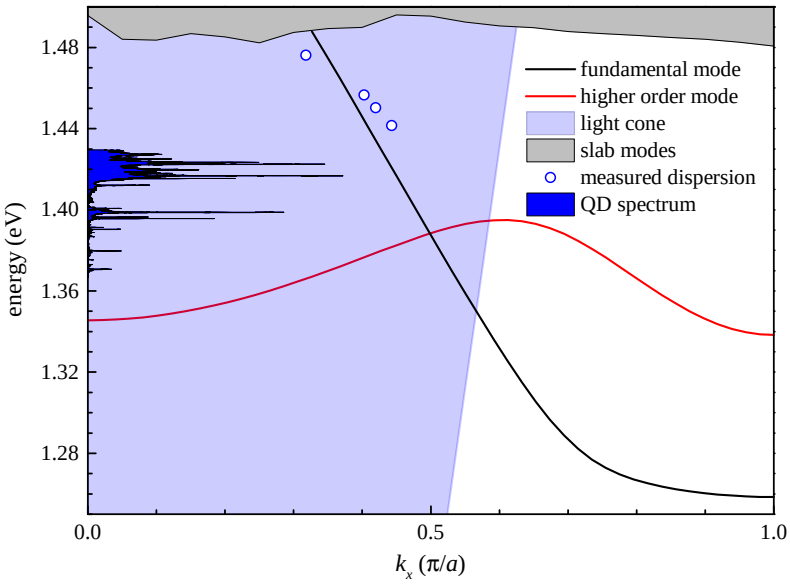

Figure A.1: Simulated photonic band structure for WG_B. Dark blue shaded area: QDs emission spectrum; blue circles: measured dispersion from Fourier-space imaging. Benjamin Lang built and run the model to generate the data of the simulated dispersion; plot produced by the author.

A.2 Real-space and Fourier-space imaging

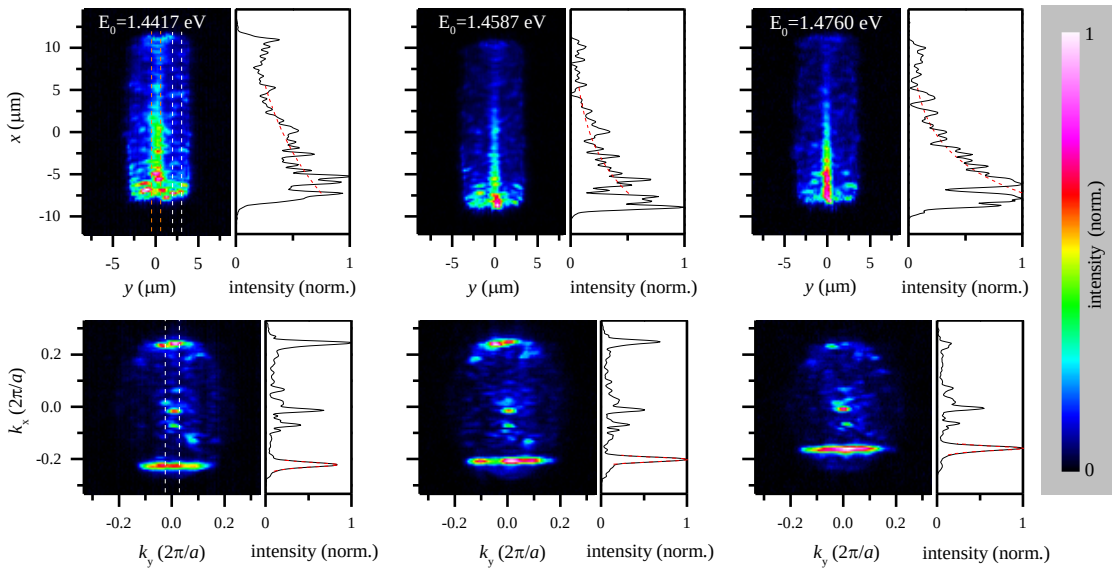

Figure A.2: Top panel: real-space imaging of the out-of-plane losses of the PCWG propagating mode, at the energy indicated. Real-space intensity profiles (black solid line) are obtained as the difference between a cut along the PCWG (orange dashed line) and a reference side cut (white dashed lines). Red dashed line: exponential fit. Bottom panel: corresponding Fourier-space. The profiles (black solid lines) are obtained from a cut highlighted by white dashed line. Dashed line: Lorentzian fit.

In Fig. A.2 we show real-space (upper panel) and Fourier-space (lower panel) images measured for different laser energies. The measurements setting are as described in Sec. 4.4.

A.3 Losses model

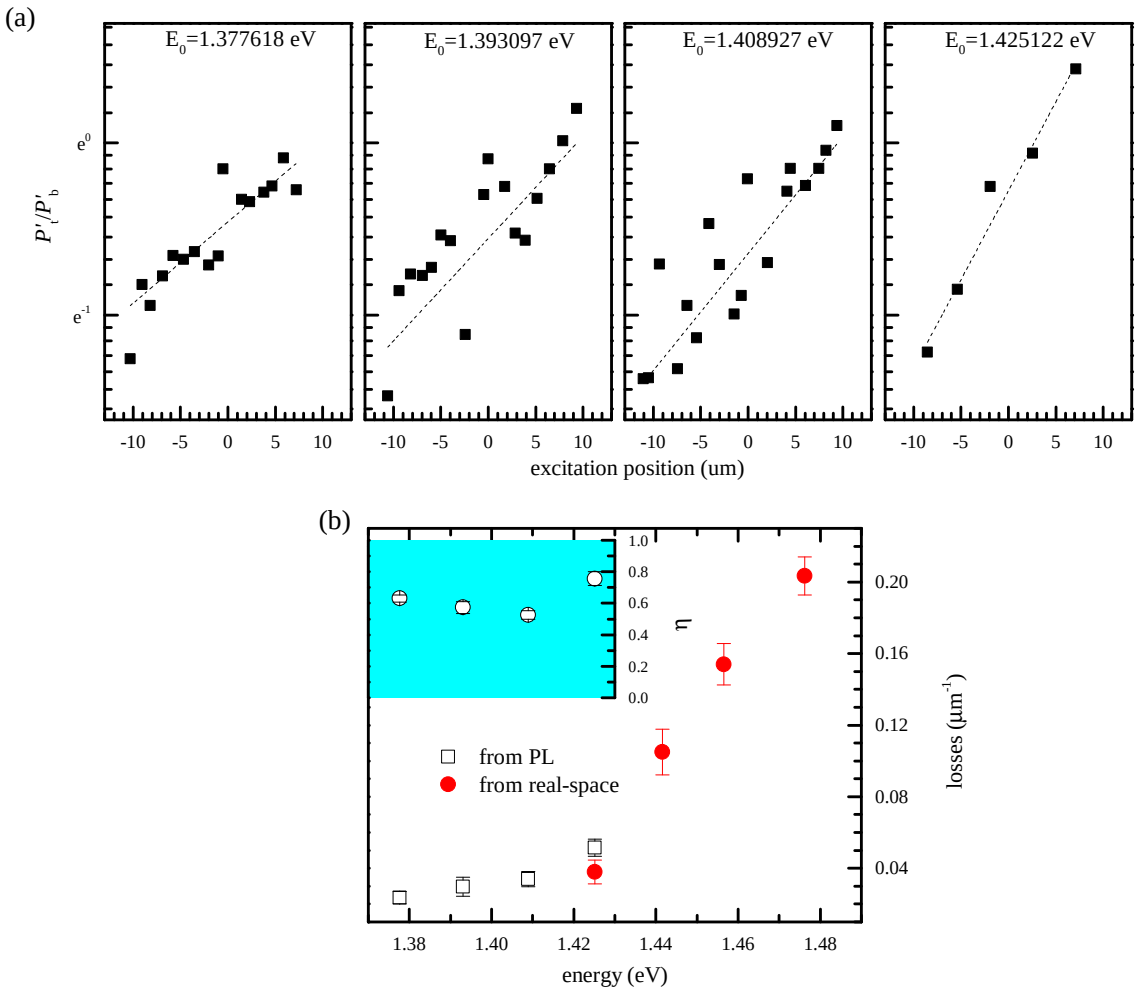

Figure A.3: (a) Ratio P'_t/P'_b as a function of the excitation position for spectral ranges centred at different energies, as indicated. (b) Main: propagation losses as a function of energy measured from PL and from real-space imaging; inset: relative extraction efficiency of the grating out-couplers η as a function of energy as obtained from PL measurements.

In Fig. A.3, we show the propagation losses and the coefficient η, obtained from spectral images as described inSec. 4.7.1. In particular, in Fig. A.3(a) we show the ratio P'_t/P'_b as a function of the excitation position, for spectral ranges centred at four different energies. The large spread around the fit is possibly due to residual directional emission of the QDs. The obtained loss coefficient is shown Fig. A.3(b). At $E_0 = 1.37762\,\text{eV}$, $\alpha = 0.02\,\mu\text{m}^{-1}$. It then increases with energy, up to $\alpha = 0.05157\,\mu\text{m}^{-1}$ at $E_0 = 1.42512\,\text{eV}$. At this energy, the loss calculated from spectral images is consistent with the loss measured from real-space imaging, as visible in the figure. The coefficient η is shown in the inset of Fig. A.3(b). We calculate an average value of $\eta = 0.6 \pm 0.1$.

Appendix B

Additional fitted data for dQD_2 and sQD samples

B.1 Sample dQD_2

In this section, the fit performed on the dQD_2 sample are shown, in the same way as in Sec. 5.9.

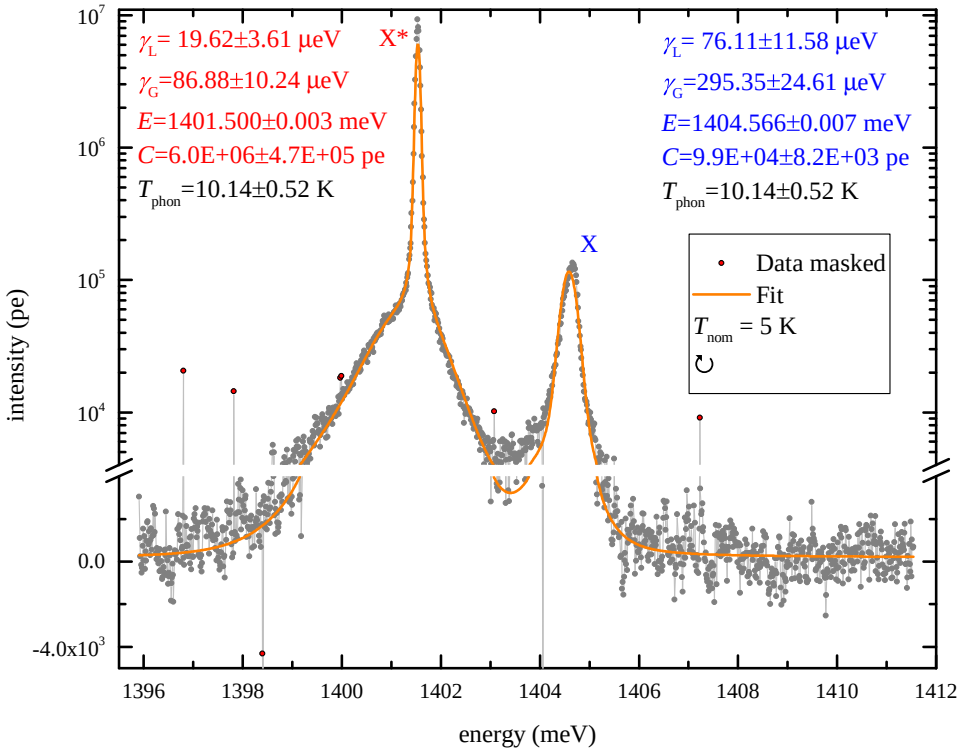

Figure B.1: Experimental and fitted emission spectra for dQD_2 at the nominal temperature of 5 K, showing data manually excluded from the fit in red symbols. RMSE = 2.1. Red: fit parameters for X^*; blue: fit parameters for X. The phonon temperature (black) is a global fit parameter. Amy Morreau built and run the model to fit the experimental data; plot produced by the author.

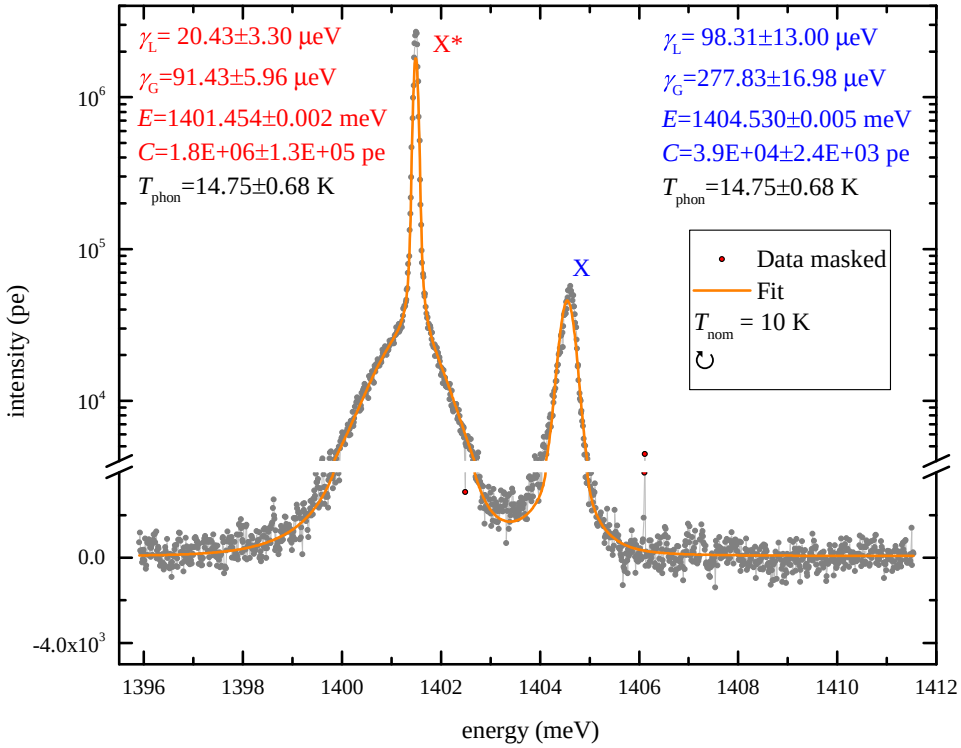

Figure B.2: As Fig. B.1, but for a nominal temperature T=10 K. RMSE = 2.01. Amy Morreau built and run the model to fit the experimental data; plot produced by the author.

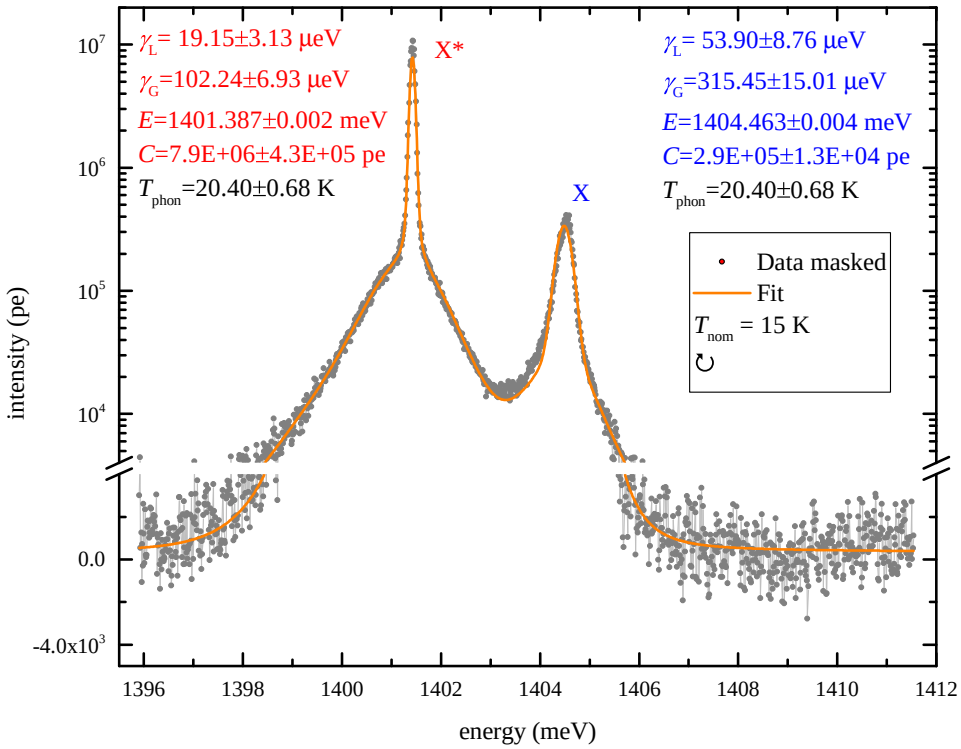

Figure B.3: As Fig. B.1, but for a nominal temperature T=15 K. RMSE = 2.86. Amy Morreau built and run the model to fit the experimental data; plot produced by the author.

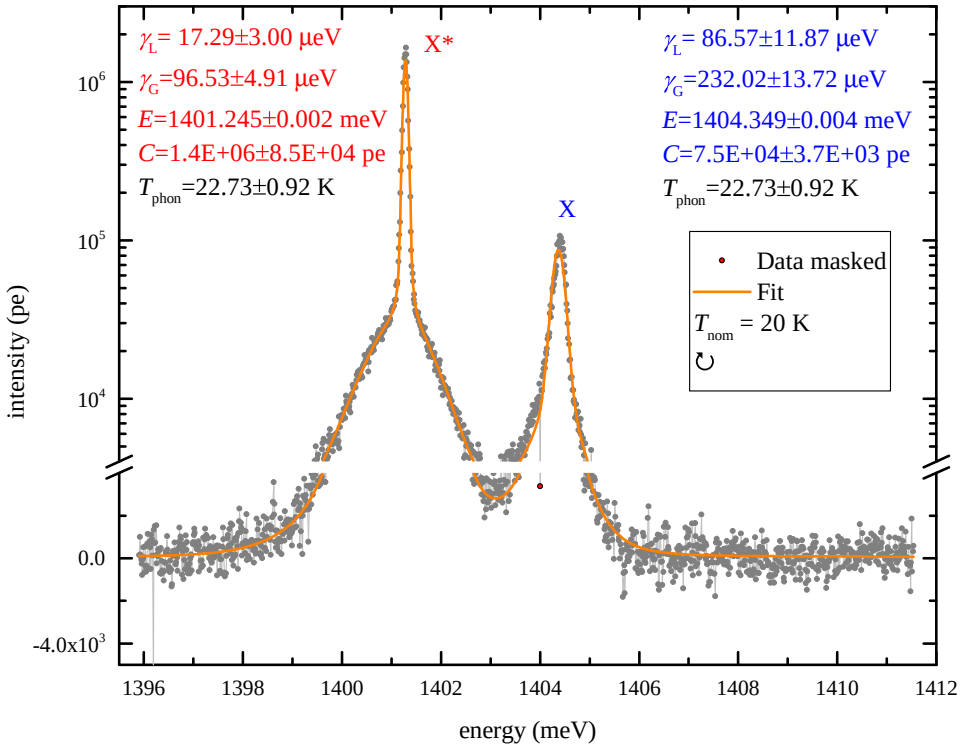

Figure B.4: As Fig. B.1, but for a nominal temperature T=20 K. RMSE = 2.45. Amy Morreau built and run the model to fit the experimental data; plot produced by the author.

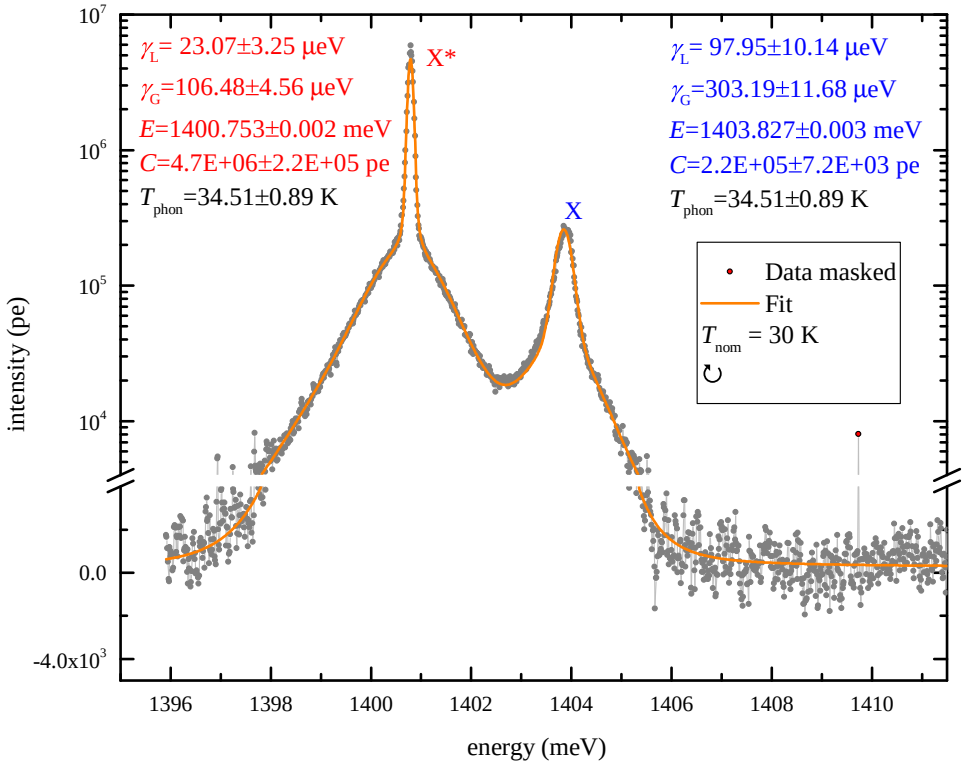

Figure B.5: As Fig. B.1, but for a nominal temperature T=30 K. RMSE = 2.41. Amy Morreau built and run the model to fit the experimental data; plot produced by the author.

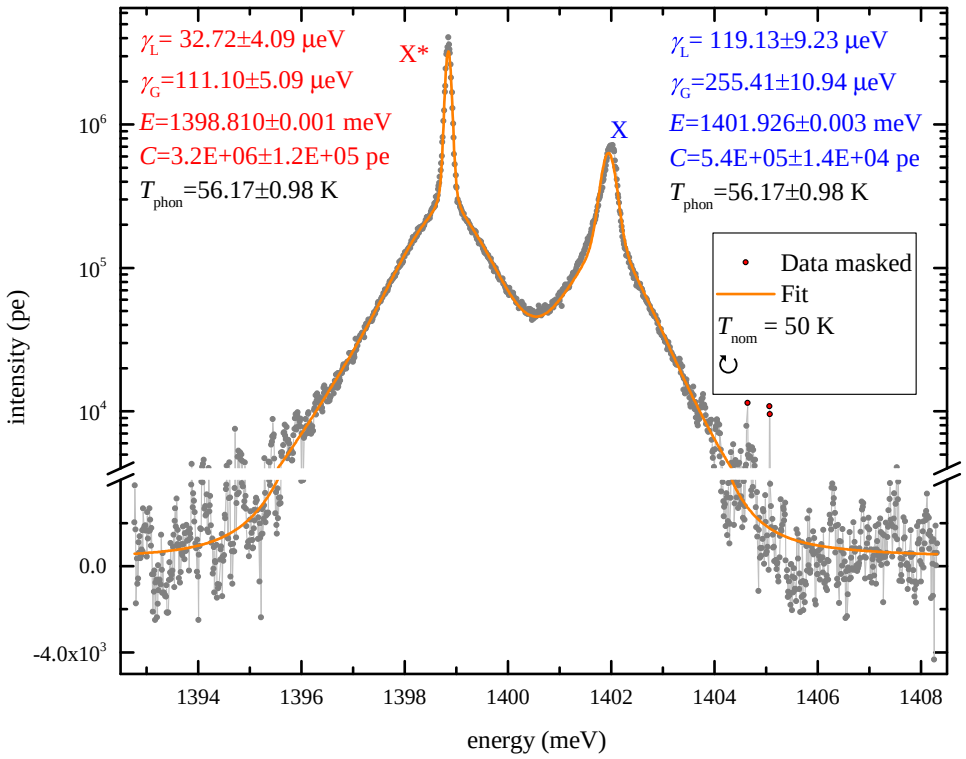

Figure B.6: As Fig. B.1, but for a nominal temperature T=50 K. RMSE = 3.27. Amy Morreau built and run the model to fit the experimental data; plot produced by the author.

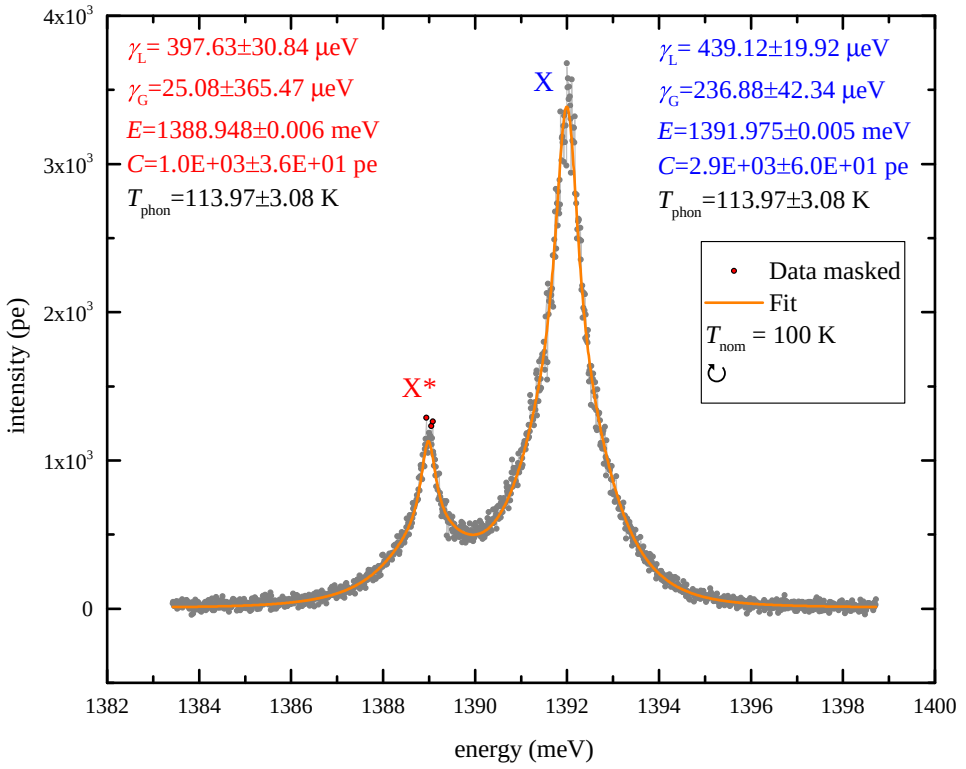

Figure B.7: As Fig. B.1, but for a nominal temperature T=100 K. RMSE = 1.77. Amy Morreau built and run the model to fit the experimental data; plot produced by the author.

B.2 Sample sQD

In this section, the fit performed on the sQD sample are shown, in the same way as in Sec. 5.9.

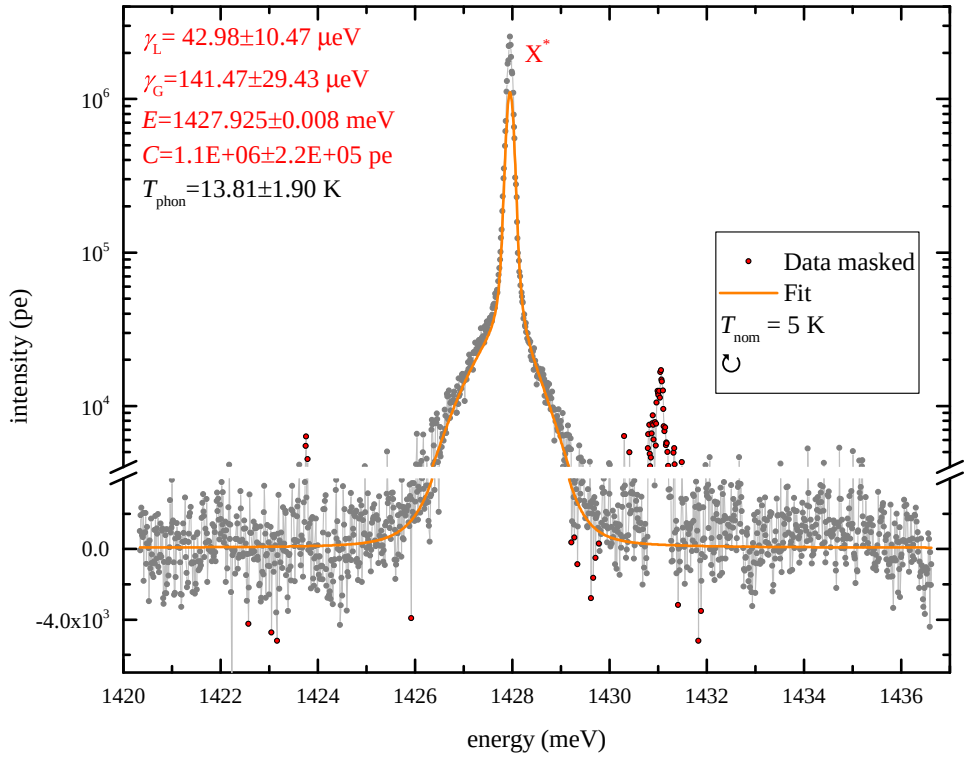

Figure B.8: Experimental and fitted emission spectra for sQD at the nominal temperature of 5 K, showing data manually excluded from the fit in red symbols. RMSE = 6.29. Red: fit parameters for X*; the phonon temperature is given in black. Amy Morreau built and run the model to fit the experimental data; plot produced by the author.

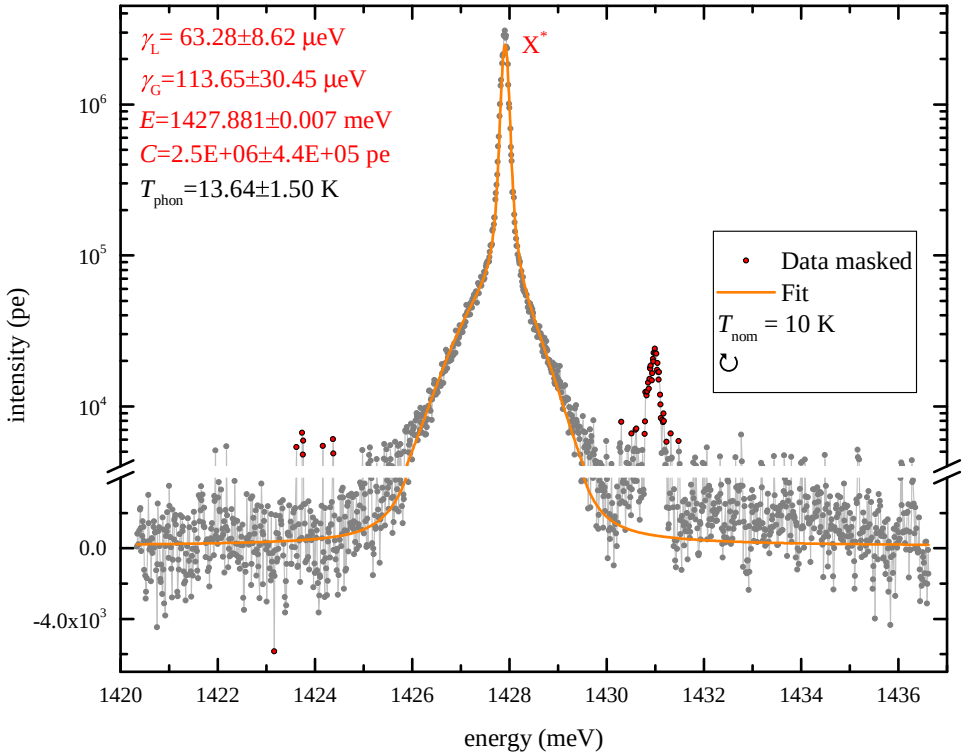

Figure B.9: As Fig. B.8, but for a nominal temperature T=10 K. RMSE = 6.48. Amy Morreau built and run the model to fit the experimental data; plot produced by the author.

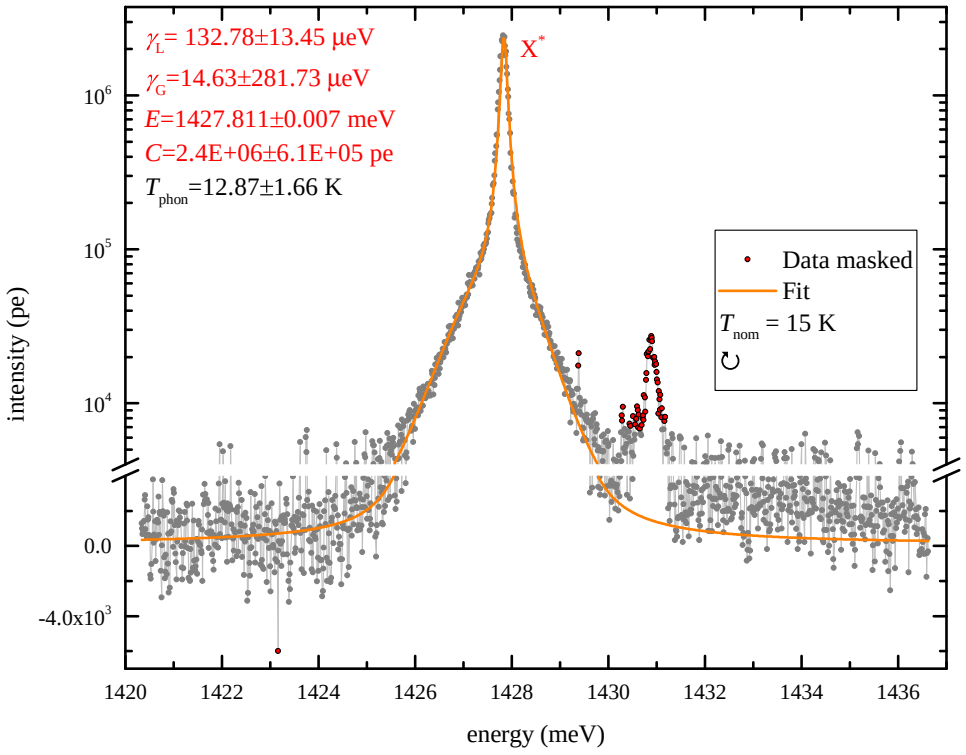

Figure B.10: As Fig. B.8, but for a nominal temperature T=15 K. RMSE = 8.11. Amy Morreau built and run the model to fit the experimental data; plot produced by the author.

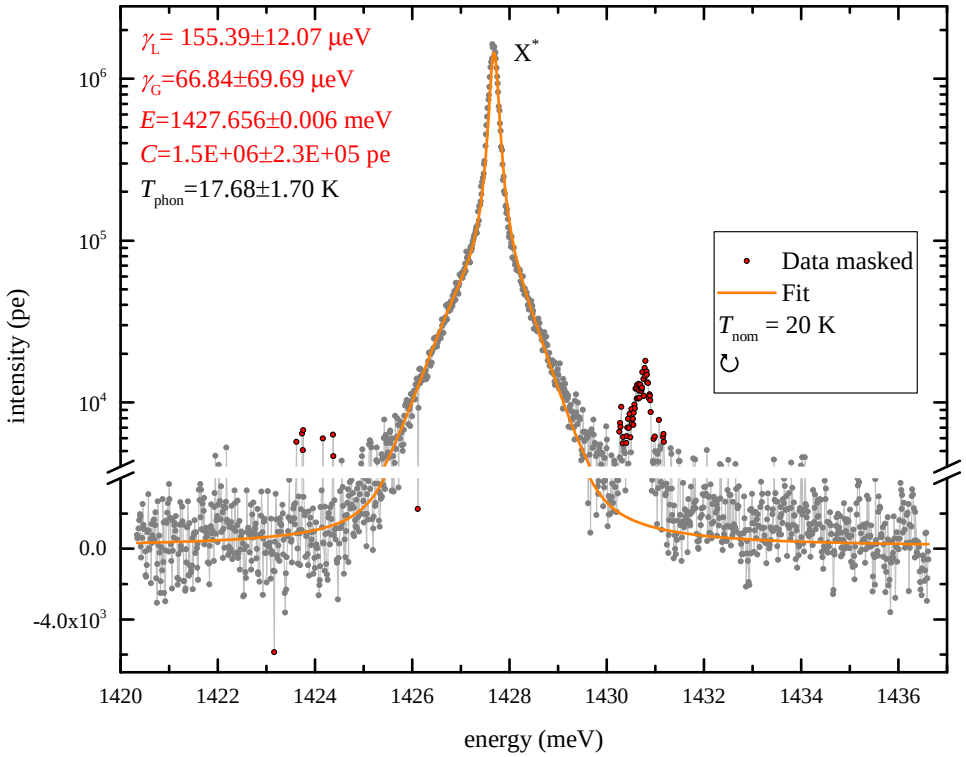

Figure B.11: As Fig. B.8, but for a nominal temperature T=20 K. RMSE = 9.42. Amy Morreau built and run the model to fit the experimental data; plot produced by the author.

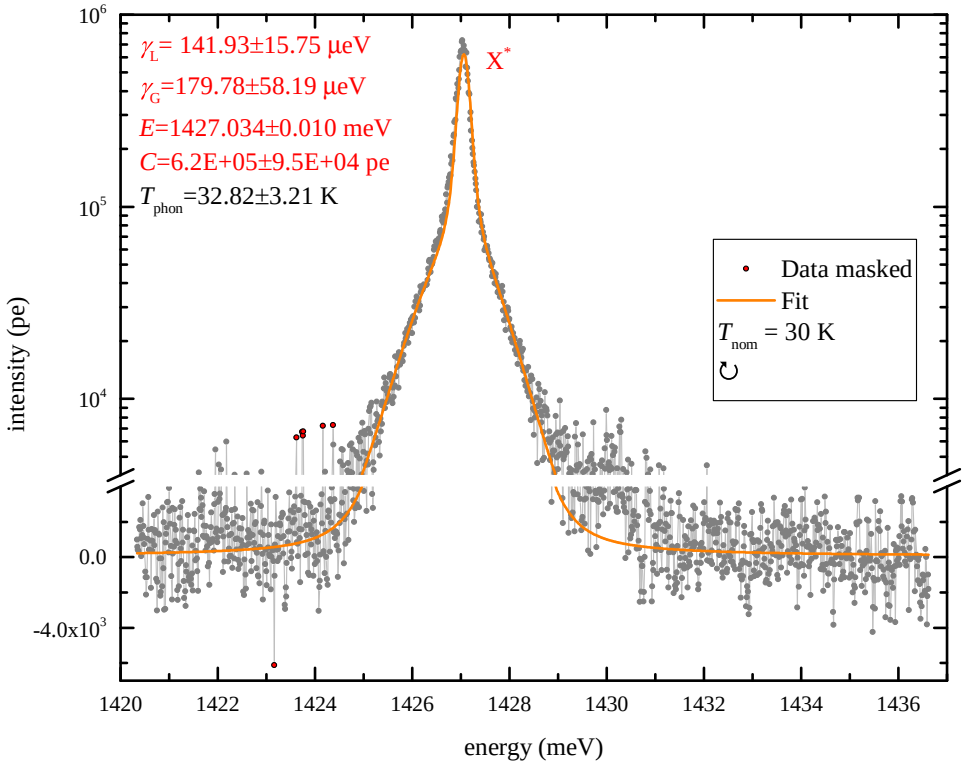

Figure B.12: As Fig. B.8, but for a nominal temperature T=30 K. RMSE = 7.87. Amy Morreau built and run the model to fit the experimental data; plot produced by the author.

Bibliography

[1] N.W. Ashcroft and N.D. Mermin. *Solid State Physics*. Cengage Learning, 2011.

[2] Physical Properties of Semiconductors Ioffe Physico-Technical Institute. http://www.ioffe.ru/SVA/NSM/Semicond/.

[3] P. Y. Yu and M. Cardona. *Fundamental of semiconductors: Physics and Materials Properties*. Springer, Berlin, 2001.

[4] M. Cardona, N. E. Christensen, and G. Fasol. Relativistic band structure and spin-orbit splitting of zinc-blende-type semiconductors. *Physical Review B*, 38:1806, 1988.

[5] P. Kok and B.W.Lovett. *Introduction to Optical Quantum Information Processing*. Cambridge University Press, 2010.

[6] P. Lodahl, S. Mahmoodian, and S. Sobbe. Interfacing single photons and single quantum dots with photonic nanostructures. *Review of Modern Physics*, 87:347–400, 2015.

[7] P. G. Linares, A. Martí, E. Antolín, and A. Luque. III-V compound semiconductor screening for implementing quantum dot intermediate band solar cells. *Journal of Applied Physics*, 109:014313, 2011.

[8] M. Kroner. *Resonant photon-exciton interaction in semiconductor quantum dots*. PhD thesis, Fakultät für Physik der Ludwig-Maximilians-Universität München, 2008.

[9] G. Sęk, J. Misiewicz, D. Radziewict, M. Tłaczała, M Panek, and R Korbutowicz. Study of the nature of light hole excitonic transitions in InGaAs/GaAs quantum well. *Vacuum*, 50:199, 1998.

[10] Y. A. Goldberg and N. M. Shmidt. *Handbook series on semiconductor parameters*, chapter GALLIUM INDIUM ARSENIDE ($Ga_xIn_{1-x}As$), pages 62–88. World Scientific, 1996.

[11] W.W. Chow and S.W. Koch. *Semiconductor-Laser Fundamentals: Physics of the Gain Materials*. Springer-Verlag, 1994.

[12] G.Bastard, J.A.Brum, and R.Ferreira. Electronic states in semiconductor heterostructures. *Solid State Physics*, 44:229–415, 1991.

[13] A. Wojs, P. Hawrylak, S. Fafard, and L. Jacak. Electronic structure and magneto-optics of self-assembled quantum dots. *Physical Review B*, 54:5604, 1996.

[14] R. J. Warburton, B. T. Miller, C. S. Dürr, C. Bödefeld, K. Karrai, J. P. Kotthaus, G. Medeiros-Ribeiro, P. M. Petroff, and S. Huant. Coulomb interactions in small charge-tunable quantum dots: A simple model. *Physical Review B*, 58:16 221, 1998.

[15] M. Bayer, O. Stern, P. Hawrylak, S. Fafard, and A. Forchel. Hidden symmetries in the energy levels of excitonic 'artificial atoms'. *Nature*, 405:923–926, 2000.

[16] S. Raymond, S. Studenikin, A. Sachrajda, Z.Wasilewski, S. J. Cheng, W. Sheng, P. Hawrylak, A. Babinski, M. Potemski, G. Ortner, and M. Bayer. Excitonic energy shell structure of self-assembled InGaAs/GaAs quantum dots. *Physical Review B*, 92:187402, 2004.

[17] P. Petroff. *Single Quantum Dots: Fundamentals, Applications and New Concepts*, chapter Epitaxial Growth and Electronic Structure of Self-Assembled Quantum Dots, pages 1–24. Springer, 2004.

[18] A. V. Koudinov, I. A. Akimov, Yu. G. Kusrayev, and F. Henneberger. Optical and magnetic anisotropies of the hole states in Stranski-Krastanov quantum dots. *Physical Review B*, 70:241305, 2004.

[19] Y. Léger, L. Besombes, L. Maingault, and H. Mariette. Valence-band mixing in neutral, charged, and Mn-doped self-assembled quantum dots. *Physical Review B*, 76:045331, 2007.

[20] T. Belhadj, T. Amand, A. Kunold, C.-M. Simon, T. Kuroda, M. Abbarchi, T. Mano, K. Sakoda, S. Kunz, X. Marie, and B. Urbaszek. Impact of heavy hole-light hole coupling on optical selection rules in GaAs quantum dots. *Applied Physics Letters*, 97:051111, 2010.

[21] M. Chhowalla, H. S. Shin, G. Eda, L.-J. Li, K. P. Loh, and H. Zhang. The chemistry of two-dimensional layered transition metal dichalcogenide nanosheets. *Nature Chemistry*, 5:263–275, 2013.

[22] K. F. Mak, C. Lee, J. Hone, J. Shan, and T. F. Heinz. Atomically thin MoS_2: A new direct-gap semiconductor. *Physical Review Letters*, 105:136805, 2010.

[23] Z. Y. Zhu, Y. C. Cheng, and U. Schwingenschlögl. Giant spin-orbit-induced spin splitting in two-dimensional transition-metal dichalcogenide semiconductors. *Physical Review B*, 84:153402, 2011.

[24] G.-B. Liu, W.-Y. Shan, Y. Yao, W. Yao, and D. Xiao. Three-band tight-binding model for monolayers of group-VIB transition metal dichalcogenides. *Physical Review B*, 88:085433, 2013.

[25] D. Xiao, G.-B. Liu, W. Feng, X. Xu, and W. Yao. Coupled Spin and Valley Physics in Monolayers of MoS_2 and Other Group-VI Dichalcogenides. *Physical Review Letters*, 108:196802, 2012.

[26] X. Xu, W. Yao, D. Xiao, and T. F. Heinz. Spin and pseudospins in layered transition metal dichalcogenides. *Nature Physics*, 10:343–350, 2014.

[27] S.Y. Zhou, G.-H. Gweon, A.V. Fedorov, P.N. First, W.A. De Heer, D.-H. Lee, F. Guinea, A.H. Castro Neto, and A. Lanzara. Substrate-induced bandgap opening in epitaxial graphene. *Nature Materials*, 6:770–775, 2007.

[28] W. Yao, D. Xiao, and Q. Niu. Valley-dependent optoelectronics from inversion symmetry breaking. *Physical Review B*, 77:235406, 2008.

[29] E. V. Castro, K. S. Novoselov, S.V. Morozov, N. M. R. Peres, J. M. B. Lopes dos Santos, Johan Nilsson, F. Guinea, A. K. Geim, and A. H. Castro Neto. Biased bilayer graphene: Semiconductor with a gap tunable by the electric field effect. *Physical Review Letters*, 99:216802, 2007.

[30] K. Kósmider, J. W. González, and J. Fernández-Rossier. Large spin splitting in the conduction band of transition metal dichalcogenide monolayers. *Physical Review B*, 88:245436, 2013.

[31] K. F. Mak, K. L. McGill, J. Park, and P. L. McEuen. The valley Hall effect in MoS_2 transistors. *Science*, 344:1489–1492, 2014.

[32] J. Frenkel. On the transformation of light into heat in solids. ii. *Physical Review*, 37:1276–1294, 1931.

[33] G.H. Wannier. The structure of electronic excitation levels in insulating crystals. *Physical Review*, 52:191–197, 1937.

[34] N.F. Mott. Conduction in polar crystals. II. The conduction band and ultraviolet absorption of alkali-halide crystals. *Transactions of the Faraday Society*, 34:500–506, 1938.

[35] A. V. Kavokin, J. J. Baumberg, G. Malpuech, and F. P. Laussy. *Microcavities*. Oxford University Press, 2017.

[36] A. Naeem, F. Masia, S. Christodoulou, I. Moreels, P. Borri, and W. Langbein. Giant exciton oscillator strength and radiatively limited dephasing in two-dimensional platelets. *Physical Review B*, 91:121302(R), 2015.

[37] R. L. Greene, K. K. Bajaj, and D. E. Phelps. Energy levels of wannier excitons in GaAs-$Ga_{1-x}Al_xAs$ quantum-well structures. *Physical Review B*, 29:1807, 1984.

[38] L. C. Andreani. *Confined Electrons and Photons: New Physics and Applications*, pages 57–112. Plenum Press, 1995.

[39] S. Horzum, H. Sahin, S. Cahangirov, P. Cudazzo, A. Rubio, T. Serin, and F. M. Peeters. Phonon softening and direct to indirect band gap crossover in strained single-layer $MoSe_2$. *Physical Review B*, 87:125415, 2013.

[40] G. Wang, A. Chernikov, M. M. Glazov, T. F. Heinz, X. Marie, T. Amand, and B. Urbaszek. Excitons in atomically thin transition metal dichalcogenides. *Review of Modern Physics*, 90:021001, 2018.

[41] P. Cudazzo, I. V. Tokatly, and A. Rubio. Dielectric screening in two-dimensional insulators: Implications for excitonic and impurity states in graphane. *Physical Review B*, 84:085406, 2011.

[42] A. W. Achtstein, A. Schliwa, A. Prudnikau, M. Hardzei, M. V. Artemyev, C. Thomsen, and U. Woggon. Electronic structure and exciton-phonon interaction in two-dimensional colloidal CdSe nanosheets. *Nano Letters*, 12:3151?3157, 2012.

[43] J. Wang, F. Ma, and M. Sun. Graphene, hexagonal boron nitride, and their heterostructures: properties and applications. *RSC Advances*, 7:16801, 2017.

[44] D. Y. Qiu, F. H. da Jornada, and S. G. Louie. Optical spectrum of MoS_2: Many-body effects and diversity of exciton states. *Physical Review Letters*, 111:216805, 2013.

[45] Z. Ye, T. Cao, K. O'Brien, H. Zhu, X. Yin, Y. Wang, S. G. Louie, and X. Zhang. Probing excitonic dark states in single-layer tungsten disulphide. *Nature*, 513:214, 2014.

[46] A. Chernikov, T. C. Berkelbach, H. M. Hill, A. Rigosi, Y. Li, O. B. Aslan, D. R. Reichman, M. S. Hybertsen, and T. F. Heinz. Exciton binding energy and nonhydrogenic Rydberg series in monolayer WS_2. *Physical Review Letters*, 113:076802, 2014.

[47] K. He, N. Kumar, L. Zhao, Z. Wang, K. F. Mak, H. Zhao, and J. Shan. Tightly bound excitons in monolayer WSe_2. *Physical Review Letters*, 113:026803, 2014.

[48] L. Scarpelli, F. Masia, E. M. Alexeev, F. Withers, A. I. Tartakovskii, K. S. Novoselov, and W. Langbein. Resonantly excited exciton dynamics in two-dimensional $MoSe_2$ monolayers. *Physical Review B*, 96:045407, 2017.

[49] L. C. Andreani and F. Bassani. Exchange interaction and polariton effects in quantum-well excitons. *Physical Review B*, 41:7536, 1990.

[50] F. Tassone, F. Bassani, and L. C. Andreani. Resonant and surface-polaritons in quantum-wells. *Nuovo Cimento Della Societa Italiana Di Fisica D-Condensed Matter Atomic Molecular and Chemical Physics Fluids Plasmas Biophysics*, 12:1673–1687, 1990.

[51] Y. N. Gartstein, X. Li, and C. Zhang. Exciton polaritons in transition-metal dichalcogenides and their direct excitation via energy transfer. *Physical Review B*, 92:075445, 2015.

[52] H. Wang, C. Zhang, W. Chan, C. Manolatou, S. Tiwari, and F. Rana. Radiative lifetimes of excitons and trions in monolayers of the metal dichalcogenide MoS_2. *Physical Review B*, 93:045407, 2016.

[53] Efros A and Al. L. Efros. Interband light absorption in semiconductor spheres. *Soviet physics*, 16:772–775, 1982.

[54] R. J. Warburton, C. Schäflein, D. Haft, F. Bickel, A. Lorke K. Karrai, J. M. Garcia, W. Schoenfeld, and P. M. Petroff. Optical emission from a charge-tunable quantum ring. *Nature*, 405:926–929, 2000.

[55] D.V. Regelman, D. Gershoni, E. Ehrenfreund, W.V. Schoenfeld, and P.M. Petroff. Spectroscopy of single semiconductor quantum dots at negative, neutral, and positive charge states. *Physica Status Solidi (a)*, 190:491–497, 2002.

[56] I. A. Akimov, K. V. Kavokin, A. Hundt, and F. Henneberger. Electron-hole exchange interaction in a negatively charged quantum dot. *Physical Review B*, 71:075326, 2005.

[57] M. Bayer, G. Ortner, O. Stern, A. Kuther, A. A. Gorbunov, A. Forchel, P. Hawrylak, S. Fafard, K. Hinzer, T. L. Reinecke, S. N. Walck, J. P. Reithmaier, F. Klopf, and F. Schäfer. Fine structure of neutral and charged excitons in self-assembled In(Ga)As/(Al)GaAs quantum dots. *Physical Review B*, 65:195315, 2002.

[58] A. V. Kuhlmann, J. Houel, A. Ludwig, L. Greuter, D. Reuter, A. D.Wieck, M. Poggio, and R. J.Warburton. Charge noise and spin noise in a semiconductor quantum device. *Nature Physics*, 9:570–575, 2013.

[59] B. Urbaszek, X. Marie, T. Amand, O. Krebs, P. Voisin, P. Maletinsky, A. Högele, and A. Imamoglu. Nuclear spin physics in quantum dots: An optical investigation. *Review of Modern Physics*, 85:79, 2013.

[60] A. Nazir and D. P. S. McCutcheon. Modelling exciton-phonon interactions in optically driven quantum dots. *Journal of Physics: Condensed Matter*, 28:103002, 2016.

[61] W. Langbein, P. Borri, U. Woggon, V. Stavarache, D. Reuter, and A. D. Wieck. Radiatively limited dephasing in InAs quantum dots. *Physical Review B*, 70:033301, 2004.

[62] T. Jakubczyk, V. Delmonte, M. Koperski, K. Nogajewski, C. Faugeras, W. Langbein, M. Potemski, and J. Kasprzak. Radiatively limited dephasing and exciton dynamics in $MoSe_2$ monolayers revealed with four-wave mixing microscopy. *Nano Letters*, 16:5333–5339, 2016.

[63] D. Gammon, E. S. Snow, B. V. Shanabrook, D. S. Katzer, and D. Park. Homogeneous linewidths in the optical spectrum of a single gallium arsenide quantum dot. *Science*, 273:87–90, 1996.

[64] M. J. Fernée, C. Sinito, Y. Louyer, P. Tamarat, and B. Lounis. The ultimate limit to the emission linewidth of single nanocrystals. *Nanotechnology*, 24:465703, 2013.

[65] T. Ihara and Y. Kanemitsu. Spectral diffusion of neutral and charged exciton transitions in single CdSe/ZnS nanocrystals due to quantum-confined stark effect. *Physical Review B*, 90:195302, 2014.

[66] P. Borri, W. Langbein, S. Schneider, and U. Woggon. Ultralong dephasing time in InGaAs quantum dots. *Physical Review Letters*, 87:157401, 2001.

[67] F. Masia, W. Langbein, I. Moreels, Z. Hens, and P. Borri. Exciton dephasing in lead sulfide quantum dots by X-point phonons. *Physical Review B*, 201309:83, 2011.

[68] F. Masia, N. Accanto, W. Langbein, and P. Borri. Spin-flip limited exciton dephasing in CdSe/ZnS colloidal quantum dots. *Physical Review Letters*, 108:087401, 2012.

[69] S. Mukamel. *Principles of Nonlinear Optical Spectroscopy*. Oxford University Press, 1999.

[70] M. O. Scully and M. S. Zubairy. *Quantum Optics*. Cambridge University Press, 1997.

[71] G. Grynberg, A. Aspect, and C. Fabre. *Introduction to Quantum Optics*. Cambridge University Press, 2010.

[72] J. Shah. *Ultrafast Spectroscopy of Semiconductors and Semiconductor Nanostructures*. Springer, 1996.

[73] P. Borri and W. Langbein. *Semiconductor Quantum Bits*, chapter 12, pages 269–319. Pan Stanford, 2008.

[74] W. Bak, H. Noh, C. Stambaugh, Y. Arakawa, and W. Jhe. Spectral fluctuations of excitonic transitions of InGaAs single quantum dots. *Applied Physics Letters*, 100:022105, 2012.

[75] J. Houel, A.V. Kuhlmann, L. Greuter, F. Xue, M. Poggio, B. D. Gerardot, P. A. Dalgarno, A. Badolato, P. M. Petroff, A. Ludwig, D. Reuter, A. D. Wieck, and R. J. Warburton. Probing single-charge fluctuations at a GaAs/AlAs interface using laser

spectroscopy on a nearby InGaAs quantum dot. *Physical Review Letters*, 108:107401, 2012.

[76] J. D. Joannopoulos, S. G. Johnson, J. N. Winn, and R. D. Meade. *Photonic Crystals: Molding The Flow Of Light*. Princeton University Press, 2008.

[77] S.G. Johnson, S.Fan, P.R. Villeneuve, J. D. Joannopoulos, and L.A. Kolodziejski. Guided modes in photonic crystal slabs. *Physical Review B*, 60:5751, 1999.

[78] B. Lang, D. M. Beggs, and R. Oulton. Time-reversal constraint limits unidirectional photon emission in slow-light photonic crystals. *Philosophical Transactions of the Royal Society A*, 374:1–11, 2016.

[79] Wikipedia. http://en.wikipedia.org/wiki/StokesParameters.

[80] E.M. Purcell. Spontaneous emission probabilities at radio frequencies. *Physical Review*, 69:681, 1946.

[81] M. Fox. *Quantum Optics*. Oxford University Press, New York, 2006.

[82] A. Laucht. *Semiconductor Quantum Optics with Tailored Photonic Nanostructures*. PhD thesis, Fakultät für Physik der Technischen Universität München, 2011.

[83] S. Hughes. Enhanced single-photon emission from quantum dots in photonic crystal waveguides and nanocavities. *Optics Letters*, 29:2659, 2004.

[84] V. S. C. Manga Rao and S. Hughes. Single quantum-dot Purcell factor and β factor in a photonic crystal waveguide. *Phys.Rev. B*, 75:205437, 2007.

[85] A. Mecozzi and J. Mørk. Theory of heterodyne pump-probe experiments with femtosecond pulses. *Journal of the Optical Society of America B*, 13:2437, 1996.

[86] M. Hofmann, S. D. Brorson, J. Mørk, and A. Mecozzi. Time resolved four-wave mixing technique to measure the ultrafast coherent dynamics in semiconductor optical amplifiers. *Applied Physics Letters*, 68:3236, 1996.

[87] P. Borri, W. Langbein, J. Mørk, and J.M. Hvam. Heterodyne pump-probe and four-wave mixing in semiconductor optical amplifiers using balanced lock-in detection. *Optics Communications*, 169:317–324, 1999.

[88] P. Borri, W. Langbein, J. Mørk, J. M. Hvam, F. Heinrichsdorff, M.-H. Mao, and D. Bimberg. Dephasing in InAs/GaAs quantum dots. *Physical Review B*, 60:7784, 1999.

[89] P. Borri, W. Langbein, J. M. Hvam, F. Heinrichsdorff, M.-H. Mao, and D. Bimberg. Time-resolved four-wave mixing in InAs/InGaAs quantum-dot amplifiers under electrical injection. *Applied Physics Letters*, 76:1380, 2000.

[90] W. Langbein and B. Patton. Microscopic measurement of photon echo formation in groups of individual excitonic transitions. *Physical Review Letters*, 95:017403, 2005.

[91] B. Patton, U. Woggon, and W. Langbein. Coherent control and polarization readout of individual excitonic states. *Physical Review Letters*, 95:266401, 2005.

[92] W. Langbein and B. Patton. Heterodyne spectral interferometry for multidimensional nonlinear spectroscopy of individual quantum systems. *Optics Letters*, 31:1151, 2006.

[93] J. Kasprzak and W. Langbein. Coherent response of individual weakly-confned exciton-biexciton system. *Journal of Optical Society of America B*, 29:1766, 2012.

[94] J. Kasprzak, B. Patton, V. Savona, and W. Langbein. Coherent coupling between distant excitons revealed by two-dimensional nonlinear hyperspectral imaging. *Nature Photonics*, 5:5763, 2011.

[95] J. Kasprzak, S. Reitzenstein, E.A. Muljarov, C. Kistner, C. Schneider, M. Strauss, S. Höfling, A. Forchel, and W. Langbein. Up on the Jaynes-Cummings ladder of a quantum dot/microcavity system. *Nature Materials*, 9:304–308, 2010.

[96] A. Naeem. Optical properties and exciton dynamics of colloidal quantum dots, rods, and platelets. PhD thesis, 2016.

[97] J. Kasprzak. Exploring coherence of individual emitters in solids. Habilitation thesis. School of Physics and Astronomy, Cardiff University, 2012.

[98] P. Borri. Coherent light-matter interaction in semiconductor quantum dots. Habilitation thesis. Dortmund University, 2003.

[99] E. Hecht. *Optics*. Addison-Wesley, 2001.

[100] S. Schneider. Aufbau eines hochauflösenden abbildenden spektrometers, 2000.

[101] K. S. Novoselov and A. H. Castro Neto. Two-dimensional crystals-based heterostructures: materials with tailored properties. *Physica Scripta*, T146:014006, 2012.

[102] R. Frisenda, E. Navarro-Moratalla, P. Gant, D. Pérez De Lara, P. Jarillo-Herrero, R. V. Gorbachevc, and A. Castellanos-Gomez. Recent progress in the assembly of nanodevices and van der Waals heterostructures by deterministic placement of 2D materials. *Chemical Society Reviews*, 47:53, 2018.

[103] F. Cadiz, E. Courtade, C. Robert, G. Wang, Y. Shen, H. Cai, T. Taniguchi, K. Watanabe, H. Carrere, D. Lagarde, M. Manca, T. Amand, P. Renucci, S. Tongay, X. Marie, and B. Urbaszek. Excitonic linewidth approaching the homogeneous limit in MoS_2-based van der Waals heterostructures. *Physical Review X*, 7:021026, 2017.

[104] J. Wierzbowski, J. Klein, F. Sigger, C. Straubinger, M Kremser, T. Taniguchi, K. Watanabe, U. Wurstbauer, A. W. Holleitner, M. Kaniber, K Müller, and J. J. Finley. Direct exciton emission from atomically thin transition metal dichalcogenide heterostructures near the lifetime limit. *Scientific Reports*, 7:12383, 2017.

[105] C. Robert, M. A. Semina, F. Cadiz, M. Manca, E. Courtade, T. Taniguchi, K. Watanabe, H. Cai, S. Tongay, B. Lassagne, P. Renucci, T. Amand, X. Marie, M. M. Glazov, and B. Urbaszek. Optical spectroscopy of excited exciton states in MoS_2 monolayers in van der Waals heterostructures. *Physical Review Materials*, 2:011001, 2018.

[106] T. Jakubczyk, G. Nayak, L. Scarpelli, F. Masia, W.-L. Liu, S. Dubey, N. Bendiab, L. Marty, T. Taniguchi, K. Watanabe, G. Nogues, J. Coraux, V. Bouchiat, W. Langbein, J. Renard, and J. Kasprzak. Coherence and density dynamics of excitons in a single-layer MoS_2 reaching the homogeneous limit. *Arxiv*, 1810.00039:1, 2018.

[107] A. C. Akhavan. The quartz page.

[108] Wikipedia. https://en.wikipedia.org/wiki/OpticalRotation.

[109] S. Chandrasekhar. Simple model for optical activity. *American Journal of Physics*, 24:503–506, 1956.

[110] S. Chandrasekhar. Optical rotatory dispersion of crystals. *Proceedings of the Royal Society of London. Series A, Mathematical and Physical Sciences*, 259:531–553, 1961.

[111] G. Wang, I. C. Gerber, L. Bouet, D. Lagarde, A. Balocchi, M. Vidal, T. Amand, X. Marie, and B. Urbaszek. Exciton states in monolayer $MoSe_2$: Impact on interband transitions. *2D Materials*, 2:045005, 2015.

[112] R. Pässler. Temperature dependence of exciton peak energies in multiple quantum wells. *Journal of Applied Physics*, 83:3356, 1998.

[113] J. S. Ross, S. Wu, H. Yu, N. J. Ghimire, A. M. Jones, G. Aivazian, J. Yan, D. G. Mandrus, D. Xiao, W. Yao, and X. Xu. Electrical control of neutral and charged excitons in a monolayer semiconductor. *Nature Communications*, 4:1474, 2013.

[114] B. Stébé, E. Feddi, A. Ainane, and F. Dujardin. Optical and magneto-optical absorption of negatively charged excitons in three- and two-dimensional semiconductors. *Physical Review B*, 58:9926, 1998.

[115] A. Esser, E. Runge, Roland Zimmermann, and W. Langbein. Photoluminescence and radiative lifetime of trions in GaAs quantum wells. *Physical Review B*, 62:8232, 2000.

[116] A. Singh, G. Moody, S. Wu, Y. Wu, N. J. Ghimire, J. Yan, D. G. Mandrus, X. Xu, and X. Li. Coherent electronic coupling in atomically thin $MoSe_2$. *Physical Review Letters*, 112:216804, 2014.

[117] G. Wang, E. Palleau, T. Amand, S. Tongay, X. Marie, and B. Urbaszek. Polarization and time-resolved photoluminescence spectroscopy of excitons in $MoSe_2$ monolayers. *Applied Physics Letters*, 106:112101, 2015.

[118] F. Gao, Y. Gong, M. Titze, R. Almeida, P. M. Ajayan, and H. Li. Valley trion dynamics in monolayers $MoSe_2$. *Physical Review B*, 94:245413, 2016.

[119] M. Sidler, P. Back, O. Cotlet, A. Srivastava, T. Fink, M. Kroner, E. Demler, and A. Imamoglu. Fermi polaron-polaritons in charge-tunable atomically thin semiconductors. *Nature Physics*, 13:255, 2017.

[120] A. Arora, K. Nogajewski, M. Molas, M. Koperski, and M. Potemski. Exciton band structure in layered $MoSe_2$: from a monolayer to the bulk limit. *Nanoscale*, 7:20769–20775, 2015.

[121] M. A. Becker, L. Scarpelli, G. Nedelcu, G. Rainò, F. Masia, P. Borri, T. Stöferle, M. V. Kovalenko, W. Langbein, and R. F. Mahrt. Long exciton dephasing time and coherent phonon coupling in $CsPbBr_2Cl$ perovskite nanocrystals. *Nano Letters*, 18:7546–7551, 2018.

[122] V. Savona and W. Langbein. Realistic heterointerface model for excitonic states in growth-interrupted GaAs quantum wells. *Physical Review B*, 74:075311, 2006.

[123] R. Zimmermann, E. Runge, and V. Savona. Theory of resonant secondary emission: Rayleigh scattering versus luminescence. In *Quantum Coherence, Correlation and Decoherence in Semiconductor Nanostructures*. Elsevier Science, 2003.

[124] T. Jakubczyk, K. Nogajewski, M. R Molas, M. Bartos, W. Langbein, M. Potemski, and J. Kasprzak. Impact of environment on dynamics of exciton complexes in a WS_2 monolayer. *2D Materials*, 5:031007, 2018.

[125] L. C. Andreani. *Confined Electrons and Photons: New Physics and Applications*, pages 57–112. Plenum Press, 1995.

[126] S. Dufferwiel, S. Schwarz, F. Withers, A.A.P. Trichet, F. Li, M. Sich, O. Del Pozo-Zamudio, C. Clark, A. Nalitov, D.D. Solnyshkov, G. Malpuech, K.S. Novoselov, J.M. Smith, M.S. Skolnick, D.N. Krizhanovskii, and A.I. Tartakovskii. Exciton-polaritons in van der Waals heterostructures embedded in tunable microcavities. *Nature Communications*, 6:8579, 2015.

[127] C. Robert, D. Lagarde, F. Cadiz, G. Wang, B. Lassagne, T. Amand, A. Balocchi, P. Renucci, S. Tongay, B. Urbaszek, and X. Marie. Exciton radiative lifetime in transition metal dichalcogenide monolayers. *Physical Review B*, 93:205423, 2016.

[128] H. Dery and Y. Song. Polarization analysis of excitons in monolayer and bilayer transition-metal dichalcogenides. *Physical Review B*, 92:125431, 2015.

[129] T. Cao, G. Wang, W. Han, H. Ye, C. Zhu, J. Shi, Q. Niu, P. Tan, E. Wang, B. Liu, and J. Feng. Valley-selective circular dichroism of monolayer molybdenum disulphide. *Nature Communications*, 3:887, 2012.

[130] T. Yu and M. W. Wu. Valley depolarization due to intervalley and intravalley electron-hole exchange interactions in monolayer MoS_2. *Physical Review B*, 89:205303, 2014.

[131] D. Y. Qiu, T. Cao, and S. G. Louie. Nonanalyticity, valley quantum phases, and lightlike exciton dispersion in monolayer transition metal dichalcogenides: Theory and first-principles calculations. *Physical Review Letters*, 115:176801, 2015.

[132] J. P. Echeverry, B. Urbaszek, T. Amand, X. Marie, and I. C. Gerber. Splitting between bright and dark excitons in transition metal dichalcogenide monolayers. *Physical Review B*, 93:121107, 2016.

[133] A. Singh, G. Moody, K. Tran, M. E. Scott, V. Overbeck, G. Berghäuser, J. Schaibley, E. J. Seifert, D. Pleskot, N. M. Gabor, J. Yan, D. G. Mandrus, M. Richter, E. Malic, X. Xu, and X. Li1. Trion formation dynamics in monolayer transition metal dichalcogenides. *Physical Review B*, 93:041401, 2016.

[134] T. Godde, D. Schmidt, J. Schmutzler, M. Aßmann, J. Debus, F. Withers, E.M. Alexeev, O. DelPozo-Zamudio, O.V. Skrypka, K.S. Novoselov, M. Bayer, and A.I. Tartakovskii. Exciton and trion dynamics in atomically thin $MoSe_2$ and WSe_2: Effect of localization. *Physical Review B*, 94:165301, 2016.

[135] S. Mouri, Y. Miyauchi, M. Toh, W. Zhao, G. Eda, and K. Matsuda. Nonlinear photoluminescence in atomically thin layered WSe_2 arising from diffusion-assisted exciton-exciton annihilation. *Physical Review B*, 90:155449, 2014.

[136] D. Sun, Y. Rao, G. A. Reider, G. Chen, Y. You, L. Brézin, A. R. Harutyunyan, and T. F. Heinz. Observation of rapid exciton exciton annihilation in monolayer molybdenum disulfide. *Nano Letters*, 14:5625, 2014.

[137] N. Kumar, Q. Cui, F. Ceballos, D. He, Y. Wang, and H. Zhao. Exciton exciton annihilation in $MoSe_2$ monolayers. *Physical Review B*, 89:125427, 2014.

[138] Y. Yu, Y. Yu, C. Xu, A. Barrette, K. Gundogdu, and L. Cao. Fundamental limits of exciton-exciton annihilation for light emission in transition metal dichalcogenide monolayers. *Physical Review B*, 96:201111, 2016.

[139] H. Shi, R. Yan, S. Bertolazzi, J. Brivio, B. Gao, A. Kis, D. Jena, H. G. Xing, and L. Huang. Exciton dynamics in suspended monolayer and few-layer MoS_2 2D crystals. *ACS Nano*, 7:1072, 2013.

[140] H. Wang, C. Zhang, and F. Rana. Ultrafast dynamics of defect assisted electron hole recombination in monolayer MoS_2. *Nano Letters*, 15:339, 2015.

[141] A. M. Jones, H. Yu, J. R. Schaibley, J. Yan, D. G. Mandrus, T. Taniguchi, K. Watanabe, H. Dery, W. Yao, and X. Xu. Excitonic luminescence upconversion in a two-dimensional semiconductor. *Nature Physics*, 12:323, 2016.

[142] M. Arcari, I. Söllner, A. Javadi, S. Lindskov Hansen, S. Mahmoodian, J. Liu, H. Thyrrestrup, E.H. Lee, J.D. Song, S. Stobbe, and P. Lodahl. Near-unity coupling efficiency of a quantum emitter to a photonic crystal waveguide. *Physical Review Letters*, 113:093603, 2014.

[143] P. Lodahl, S. Mahmoodian, S. Stobbe, A. Rauschenbeutel, P. Schneeweiss, J. Volz, H. Pichler, and P. Zoller. Chiral quantum optics. *Nature*, 541:473–480, 2017.

[144] A.B. Young, A.C.T. Thijssen, D.M. Beggs, P. Androvitsaneas, L. Kuipers, J.G. Rarity, S. Hughes, and R. Oulton. Polarization engineering in photonic crystal waveguides for spin photon entanglers. *Physical Review Letters*, 115:153901, 2015.

[145] R.J. Coles, D.M. Price, J.E. Dixon, B. Royall, E. Clarke, P. Kok, M.S. Skolnick, A.M. Fox, and M.N. Makhonin. Chirality of nanophotonic waveguide with embedded quantum emitter for unidirectional spin transfer. *Nature Communitcations*, 7:11183, 2016.

[146] R. J. Coles, D. M. Price, B. Royall, E. Clarke, M. S. Skolnick, A. M. Fox, and M. N. Makhonin. Path-dependent initialization of a single quantum dot exciton spin in a nanophotonic waveguide. *Physical Review B*, 95:121401, 2017.

[147] L. Goldstein, F. Glas, J. Y. Marzin, M. N. Charasse, and G. Le Roux. Growth by molecular beam epitaxy and characterization of InAs/GaAs strained-layer superlattices. *Applied Physics Letters*, 47:1099, 1985.

[148] D. Leonard, K. Pond, and P. M. Petroff. Critical layer thickness for self-assembled InAs islands on GaAs. *Physical Review B*, 50:11687, 1994.

[149] P. Offermans, P. M. Koenraad, R. Nötzel, J. H. Wolter, and K. Pierz. Formation of InAs wetting layers studied by cross-sectional scanning tunneling microscopy. *Applied Physics Letters*, 87:111903, 2005.

[150] T. Lund-Hansen, S. Stobbe, B. Julsgaard, H. Thyrrestrup, T. Sünner, M. Kamp, A. Forchel, and P. Lodahl. Experimental realization of highly efficient broadband coupling of single quantum dots to a photonic crystalwaveguide. *Physical Review Letters*, 101:113903, 2008.

[151] H. Thyrrestrup, L. Sapienza, and P. Lodahl. Extraction of the β-factor for single quantum dots coupled to a photonic crystal waveguide. *Applied Physics Letters*, 96:231106, 2010.

[152] S. J. Dewhurst, D. Granados, D. J. P. Ellis, A. J. Bennett, R. B. Patel, I. Farrer, D. Anderson, G. A. C. Jones, D. A. Ritchie, and A. J. Shields. Slow-light-enhanced single quantum dot emission in a unidirectional photonic crystal waveguide. *Applied Physics Letters*, 96:031109, 2010.

[153] A. Laucht, S. Pütz, T. Günthner, N. Hauke, R. Saive, S. Frédérick, M. Bichler, M.-C. Amann, A.W. Holleitner, M. Kaniber, and J. J. Finley. A waveguide-coupled on-chip single-photon source. *Physical Review X*, 2:011014, 2012.

[154] T. B. Hoang, J. Beetz, L. Midolo, M. Skacel, M. Lermer, M. Kamp, S. Höfling, L. Balet, N. Chauvin, and A. Fiore. Enhanced spontaneous emission from quantum dots in short photonic crystal waveguides. *Applied Physics Letters*, 100:061122, 2012.

[155] A. Kurzmann, A. Ludwig, A. D. Wieck, A. Lorke, and M. Geller. Auger recombination in self-assembled quantum dots: Quenching and broadening of the charged exciton transition. *Nano Letters*, 16(5):3367–3372, 2016.

[156] W. Langbein, P. Borri, U. Woggon, V. Stavarache, D. Reuter, and A. D. Wieck. Radiatively limited dephasing in InAs quantum dots. *Physical Review B*, 70:033301, 2004.

[157] A. Javadi, S. Mahmoodian, I. Söllner, and P. Lodahl. Numerical modeling of the coupling efficiency of single quantum emitters in photonic-crystal waveguides. *Journal of the Optical Society of America B*, 35:514, 2018.

[158] I. Söllner, S. Mahmoodian, S. L. Hansen, L. Midolo, A. Javadi, G. Kiršanskė, T. Pregnolato, H. El-Ella, E. H. Lee, J. D. Song, S. Stobbe, and P. Lodahl. Deterministic photon-emitter coupling in chiral photonic circuits. *Nature Nanotechnology*, 10:775, 2015.

[159] S. Barik, A. Karasahin, C. Flower, T. Cai, H. Miyake, W. DeGottardi, M. Hafezi, and E. Waks. A topological quantum optics interface. *Science*, 359:666–668, 2018.

[160] D. L. Hurst, D. M. Price, C. Bentham, M. N. Makhonin, B. Royall, E. Clarke, P. Kok, L. R. Wilson, M. S. Skolnick, and A. M. Fox. Nonreciprocal transmission and reflection of a chirally coupled quantum dot. *Nano Letters*, 18:5475, 2018.

[161] A. Faraon, I. Fushman, D. Englund, N. Stoltz, P. Petroff, and J. Vučković. Dipole induced transparency in waveguide coupled photonic crystal cavities. *Optics Express*, 16:12154, 2008.

[162] A. A. Sukhorukov, S. Ha, I. V. Shadrivov, D. A. Powell, and Y. S. Kivshar. Dispersion extraction with near-field measurements in periodic waveguides. *Optics Express*, 17:3716, 2009.

[163] H. Gersen, T.J. Karle, R.J.P. Engelen, W. Bogaerts, J.P. Korterik, N.F. van Hulst, T.F. Krauss, and L. Kuipers. Real-space observation of ultraslow light in photonic crystal waveguides. *Physical Review Letters*, 94:073903, 2005.

[164] A. Laucht, T. Günthner, S. Pütz, R. Saive, S. Frédérick, N. Hauke, M. Bichler, M.-C. Amann, A. W. Holleitner, M. Kaniber, and J. J. Finley. Broadband Purcell enhanced emission dynamics of quantum dots in linear photonic crystal waveguides. *Journal of Applied Physics*, 112:093520, 2012.

[165] W. Langbein, J. M. Hvam, and R. Zimmermann. Time-resolved speckle analysis: A new approach to coherence and dephasing of optical excitations in solids. *Physical Review Letters*, 82:1040, 1999.

[166] W. Langbein and J. M. Hvam. Elastic scattering dynamics of cavity polaritons: Evidence for time-energy uncertainty and polariton localization. *Physical Review Letters*, 88:047401, 2002.

[167] N. Le Thomas, R. Houdré, M. V. Kotlyar, D. O'Brien, and T. F. Krauss. Exploring light propagating in photonic crystals with Fourier optics. *Journal of the Optical Society of America B*, 24:2964, 2007.

[168] Y. Benny, Y. Kodriano, E. Poem, D. Gershoni, T. A. Truong, and P. M. Petroff. Excitation spectroscopy of single quantum dots at tunable positive, neutral, and negative charge states. *Physical Review B*, 86:085306, 2012.

[169] A.F. Oskooi, L. Zhang, Y. Avniel, and S.G. Johnson. The failure of perfectly matched layers, and towards their redemption by adiabatic absorbers. *Optics Express*, 16:11376, 2008.

[170] S. Gehrsitz, F. K. Reinhart, C. Gourgon, N. Herres, A. Vonlanthen, and H. Sigga. The refractive index of $Al_xGa_{1-x}As$ below the band gap: Accurate determination and empirical modeling. *Journal of Applied Physics*, 87:7825, 2000.

[171] G. C. DeSalvo, C. A. Bozada, J. L. Ebel, D. C. Look, J. P. Barrette, C. L. A. Cerny, R. W. Dettmer, J. K. Gillespie, C. K. Havasy, T. J. Jenkins, K. Nakano, C. I. Pettiford, T. K. Quach, J. S. Sewell, and G. D. Via. Wet chemical digital etching of GaAs at room temperature. *Journal of The Electrochemical Society*, 143:3652–3656, 1996.

[172] Y. Chen, T. R. Nielsen, N. Gregersen, P. Lodahl, and J. Mørk. Finite-element modeling of spontaneous emission of a quantum emitter at nanoscale proximity to plasmonic waveguides. *Physical Review B*, 81:125431, 2010.

[173] Y. Sugiyama, Y. Sakuma, S. Muto, and N. Yokoyama. Novel InGaAs/GaAs quantum dot structures formed in tetrahedral-shaped recesses on (111)B GaAs substrate using metalorganic vapor phase epitaxy. *Applied Physics Letters*, 67:2, 1995.

[174] A. Hartmann, Y. Ducommun, L. Loubies, K. Leifer, and E. Kapon. Structure and photoluminescence of single AlGaAs/GaAs quantum dots grown in inverted tetrahedral pyramids. *Applied Physics Letters*, 73:2322, 1998.

[175] M. H. Baier, E. Pelucchi, E. Kapon, S. Varoutsis, M. Gallart, I. Robert-Philip, and I. Abram. Single photon emission from site-controlled pyramidal quantum dots. *Applied Physics Letters*, 84:648, 2004.

[176] O. Benson, C. Santori, M. Pelton, and Y. Yamamoto. Regulated and entangled photons from a single quantum dot. *Physical Review Letters*, 84:2513, 2000.

[177] A. J. Hudson, R. M. Stevenson, A. J. Bennett, R. J. Young, C. A. Nicoll, P. Atkinson, and K. Cooper. Coherence of an entangled exciton-photon state. *Physical Review Letters*, 99:266802, 2007.

[178] G. Juska, V. Dimastrodonato, L. O. Mereni, A. Gocalinska, and E. Pelucchi. Towards quantum-dot arrays of entangled photon emitters. *Nature Photonics*, 7:527, 2013.

[179] S. T. Moroni, T. H. Chung, G. Juska, A. Gocalinska, and E. Pelucchi. Statistical study of stacked/coupled site-controlled pyramidal quantum dots and their excitonic properties. *Applied Physics Letters*, 111:083103, 2017.

[180] T. Chung. *Arrays of quantum-light-emitting diodes with site-controlled pyramidal quantum dots*. PhD thesis, University College Cork, 2016.

[181] E. Kapon, E. Pelucchi, S. Watanabe, A. Malko, M.H. Baier, K. Leifer, B. Dwir, F. Michelini, and M.-A. Dupertuis. Site- and energy-controlled pyramidal quantum dot heterostructures. *Physica E*, 25:288–297, 2004.

[182] V. Dimastrodonato, E. Pelucchi, and D. D. Vvedensky. Self-limiting evolution of seeded quantum wires and dots on patterned substrates. *Physical Review Letters*, 108:256102, 2012.

[183] A Hartmann, Y Ducommun, K Leifer, and E Kapon. Structure and optical properties of semiconductor quantum nanostructures self-formed in inverted tetrahedral pyramids. *Journal of Physics: Condensed Matter*, 11:5901–5915, 1999.

[184] S. T. Moroni, V. Dimastrodonato, T.-H. Chung, G. Juska, A. Gocalinska, D. D. Vvedensky, and E. Pelucchi. Indium segregation during III-V quantum wire and quantum dot formation on patterned substrates. *Journal of Applied Physics*, 117:164313, 2015.

[185] M. I. Dyakonov. *Spin Physics in Semiconductors*. Springer, 2008.

[186] K.V. Kavokin. Fine structure of the quantum-dot trion. *Physica Status Solidi (a)*, 1958:592–595, 2003.

[187] B. Urbaszek, R. J.Warburton, K. Karrai, B. D. Gerardot, P.M. Petroff, and J.M. Garcia. Fine structure of highly charged excitons in semiconductor quantum dots. *Physical Review Letters*, 90:247403, 2003.

[188] N. I. Cade, H. Gotoh, H. Kamada, H. Nakano, and H. Okamoto. Fine structure and magneto-optics of exciton, trion, and charged biexciton states in single InAs quantum dots emitting at 1.3 μm. *Physical Review B*, 73:115322, 2006.

[189] G. Mahan. *Many-Particle physics.* Plenum, 1990.

[190] S. Schmitt-Rink, D. A. B. Miller, and D. S. Chemla. Theory of the linear and nonlinear optical properties of semiconductor microcrystallites. *Physical Review B*, 35:8113, 1987.

[191] B. Krummheuer, V. M. Axt, and T. Kuhn. Theory of pure dephasing and the resulting absorption line shape in semiconductor quantum dots. *Physical Review B*, 65:195313, 2002.

[192] L. Besombes, K. Kheng, L. Marsal, and H. Mariette. Acoustic phonon broadening mechanism in single quantum dot emission. *Physical Review B*, 63:155307, 2001.

[193] I. Favero, G. Cassabois, R. Ferreira, D. Darson, C. Voisin, J. Tignon, C. Delalande, G. Bastard, Ph. Roussignol, and J. M. Gérard. Acoustic phonon sidebands in the emission line of single InAs/GaAs quantum dots. *Physical Review B*, 68:233301, 2003.

[194] E. Peter, J. Hours, P. Senellart, A. Vasanelli, A. Cavanna, J. Bloch, and J. M. Gérard. Phonon sidebands in exciton and biexciton emission from single GaAs quantum dots. *Physical Review B*, 69:041307, 2004.

[195] R. Zimmermann and E. Muljarov. Dephasing of optical transitions in quantum dots - where exact solutions meet sophisticated experiments. In *12th Int. Symp. "Nanostructures: Physics and Technology" St Petersburg, Russia*, 2004.

[196] F. Vialla, Y. Chassagneux, R. Ferreira, C. Roquelet, C. Diederichs, G. Cassabois, Ph. Roussignol, J. S. Lauret, and C. Voisin. Unifying the low-temperature photoluminescence spectra of carbon nanotubes: The role of acoustic phonon confinement. *Physical Review Letters*, 057402:2014, 113.

[197] T. Takagahara. Electron-phonon interactions and excitonic dephasing in semiconductor nanocrystals. *Physical Review Letters*, 71:3577, 1993.

[198] T. Takagahara. Theory of exciton dephasing in semiconductor quantum dots. *Physical Review B*, 60:602638, 1999.

[199] F. Grosse, E.A. Muljarov, and R. Zimmermann. *Semiconductor Nanostructures.* Springer, 2008.

[200] E. A. Muljarov and R. Zimmermann. Dephasing in quantum dots: Quadratic coupling to acoustic phonons. *Physical Review Letters*, 93:237401, 2004.

[201] S. Berciaud, M.Y. Han, K.F. Mak, L.E. Brus, P. Kim, and T.F. Heinz. Electron and optical phonon temperatures in electrically biased graphene. *Physical Review Letters*, 104:227401, 2010.

[202] C. Faugeras, B. Faugeras, M. Orlita, M. Potemski, R.R. Nair, and A.K. Geim. Thermal conductivity of graphene in corbino membrane geometry. *ACSNano*, 4:1889, 2010.

[203] A. Kuther, M. Bayer, A. Forchel, A. Gorbunov, V. B. Timofeev, F. Schäfer, and J. P. Reithmaier. Zeeman splitting of excitons and biexcitons in single $In_{0.60}Ga_{0.40}As$/GaAs self-assembled quantum dots. *Physical Review B*, 58:R7508, 1998.

[204] A. Morreau. *Phonon-induced dephasing of quantum dot excitons and microcavity-embedded quantum dot polaritons*. PhD thesis, Physics and Astronomy, Cardiff University, 2019.

[205] K. J. Nash, M. S. Skolnick, P. A. Claxton, and J. S. Roberts. Diamagnetism as a probe of exciton localization in quantum wells. *Physical Review B*, 39:10943, 1989.

[206] S. N. Walck and T. L. Reinecke. Exciton diamagnetic shift in semiconductor nanostructures. *Physical Review B*, 57:9088, 1998.

[207] T. Kehoe, M. Ediger, R. T. Phillips, and M. Hopkinson. Cryogenic confocal microscopy with rotation in a magnetic field. *Review of Scientific Instruments*, 81:013906, 2010.

[208] Barbara Van Hattem. *Orientation-dependent magneto-photoluminescence of excitons confined in semiconductor nanostructures*. PhD thesis, Hughes Hall College, University of Cambridge, 2014.

[209] E. A. Muljarov and S. G. Tikhodeev. Exciton diamagnetic shift in confined and anisotropic systems. Unpublished material, 1998.

[210] I. Vurgaftman, J. R. Meyer, and L. R. Ram-Mohan. Band parameters for III-V compound semiconductors and their alloys. *Journal of Applied Physics*, 89:5815, 2001.

[211] R. People, A. Jayaraman, K.W. Wecht, D.L. Sivco, and A.Y. Cho. Measurement of the pressure dependence of the direct band gap of $In_{0.53}Ga_{0.47}As$ using stimulated emission. *Applied Physics Letters*, 52:2124, 1988.

[212] V. A. Wilkinson, A. D. Prins, J. D. Lambkin, E. P. O'Reilly, D. J. Dunstan, L. K. Howard, and M. T. Emeny. Hydrostatic pressure coeffcients of the photoluminescence of InGaAs/GaAs strained-layer quantum wells. *Physical Review B*, 42:3113, 1990.

[213] M. Bayer, A. Kuther, A. Forchel, A. Gorbunov, V. B. Timofeev, F. Schäfer, J. P. Reithmaier, T. L. Reinecke, and S. N. Walck. Electron and hole g factors and exchange interaction from studies of the exciton fine structure in $In_{0.60}Ga_{0.40}As$ quantum dots. *Physical Review Letters*, 82:1748, 1999.

[214] P. Borri, W. Langbein, U. Woggon, V. Stavarache, D. Reuter, and A. D. Wieck. Exciton dephasing via phonon interactions in InAs quantum dots: Dependence on quantum confinement. *Physical Review B*, 71:115328, 2005.

[215] P. Tighineanu, C. L. Dreeßen, C. Flindt, P. Lodahl, and A. S. Sørensen. Phonon decoherence of quantum dots in photonic structures: Broadening of the zero-phonon line and the role of dimensionality. *Physical Review Letters*, 120:257401, 2018.

[216] L. Dreeßen, C. Ouellet-Plamondon, P. Tighineanu, X. Zhou, L. Midolo, A. S. Sørensen, and P. Lodahl. Suppressing phonon decoherence of high performance single-photon sources in nanophotonic waveguides. *Quantum Science and Technology*, 4:015003, 2019.

[217] B. Rigal, B. Dwir, A. Rudra, I. Kulkova, A. Lyasota, and E. Kapon. Single photon extraction and propagation in photonic crystal waveguides incorporating site-controlled quantum dots. *Applied Physics Letters*, 112:051101, 2018.

[218] A. Srivastava, M. Sidler, A. V. Allain, D. S. Lembke, Andras Kis, and A. Imamoğlu. Optically active quantum dots in monolayer WSe_2. *Nature Nanotechnology*, 10:491, 2015.

[219] A. Branny, S. Kumar, R. Proux, and B. D. Gerardot1. Deterministic strain-induced arrays of quantum emitters in a two-dimensional semiconductor. *Nature Communications*, 8:15053, 2017.